UNIVERSITÀ DEGLI STUDI DI PADOVA

DIPARTIMENTO DI FISICA E ASTRONOMIA "GALILEO GALILEI"

CORSO DI DOTTORATO DI RICERCA IN ASTRONOMIA
Ciclo XXXV

UNVEILING THE DYNAMICS OF YOUNG STAR CLUSTERS AND THEIR BLACK HOLE POPULATION

Coordinatore: Ch.mo Prof. Giovanni Carraro
Supervisore: Ch.ma Prof.ssa Michela Mapelli
Co-supervisori: Dr. Alessandro Ballone
Dr. Mario Pasquato

Dottorando: Stefano Torniamenti

Contents

Abstract

Young star clusters are key objects to interpret a large number of astrophysical processes, from star and binary formation to the hierarchical assembly of the Milky Way. The spatial distribution and motions of young stars reflect the processes of cluster formation, while the kinematics of more evolved systems and the age dependence of their mass function inform us on how star clusters progressively dissolve into the field of the Galaxy. Finally, being the place where the most massive stars form, star clusters are building blocks for our comprehension of the formation of compact objects, which we can detect through gravitational-wave observations.

Direct $N-$body simulations are usually adopted to integrate the evolution of star clusters since their earliest phases, but we often assume quite unrealistic initial conditions for such simulations. In particular, young star clusters display highly non-trivial spatial and velocity distributions, with the presence of sub-structures, sub-clump relative motions, mergers, rotation, and are far from virial and thermal equilibrium. Hydro-dynamical simulations are an accurate method to obtain realistic initial conditions for star forming regions. However, producing large sets of hydro-dynamical simulations is prohibitively expensive in terms of computational time.

In Chapter 2, I introduce a novel algorithm to generate new star clusters from a given set of star masses, positions and velocities from a hydro-dynamical simulation. This method is based on a hierarchical clustering algorithm that learns a tree representation of the cluster phase-space. This is later turned into new realizations by modifying the initial branches of the tree (encoding the relations between the biggest sub-clumps), while preserving the characteristics of small scale structure responsible for most of the dynamical evolution. The new realizations qualitatively resemble the original simulation, and show a realistic evolution at all scales. This method results in a promising way to generate new mass and phase-space distributions from existing hydro-dynamical simulations, thus increasing our sample of initial conditions for $N-$body simulations, at a tiny computational cost.

In Chapter 3, I provide an accurate modeling of the very first phases of the cluster's life. First, I make use of hydro-dynamical simulations of collapsing molecular clouds, which, coupled with appropriate recipes for star formation, yield realistic initial conditions. Then, I introduce a new algorithm to associate a primordial binary star population to the obtained stellar distributions. Finally, I quantify the impact of primordial binaries on the global evolution of the cluster. I find that primordial binaries accelerate the star cluster dissolution, and enhance the formation of a hot core of massive objects. At the same time, the stellar environment dynamically creates additional binary systems with binding energy of the order of its kinetic energy. In the absence of primordial binaries, these dynamically formed binaries reach a binary fraction that spontaneously reproduces the relation between the binary fraction and stellar mass found in observations.

Young star clusters are an ideal environment for the formation of compact objects. Being the place where a large fraction of massive stars form, evolve, and eventually die, they are expected to host populations of black holes (BHs). Such BHs encode valuable information on their progenitor stars, which can otherwise only be observed during their short lifetime. Over the last seven years, our knowledge of stellar-mass BHs has drastically improved thanks to the detection of binary black hole (BBH) mergers through gravitational waves. Thanks to these signals, we can now study BHs with unprecedented precision, but our theoretical understanding of their formation is still hampered by large model uncertainties and degeneracies.

Dynamical interactions in dense star clusters are considered one of the most effective formation channels for BBH mergers. Also, they leave recognizable imprints on the BBH population, which can be used to disentangle them from other formation pathways (e.g., mergers from isolated binaries). In Chapter 4, I explore how dynamical interactions within young star clusters affect the properties of BBH mergers. I find that dynamically active environments produce more massive BBH mergers thanks to the high rate of dynamical exchanges, which favor the coupling of the most massive BHs. Also, the high initial cluster densities trigger a large number of stellar collisions. This, in turn, leads to a non-negligible number of BBH mergers with primary mass in the pair-instability mass gap, where BHs are not expected to form via isolated stellar evolution.

In massive star clusters, BHs born by the merger of other BHs can be retained, dynamically form new BBHs, and merge again. This hierarchical merger process can repeat several times and lead to a significant BH mass growth. Hierarchical mergers are crucial to understand how stellar-mass black holes produce pair-instability and intermediate-mass BHs, and to unveil the correlation between the BH properties and those of their host stellar system. In Chapter 5, I explore the process of hierarchical mergers in globular clusters, whose high escape velocities allow the clusters to retain a large fraction of BBH merger remnants. I focus on the impact of star cluster evolution on the efficiency of hierarchical mergers. In particular, I investigate the importance of stellar evolution, two-body relaxation and tidal stripping by the host galaxy. My results indicate that globular clusters can only host hierarchical BBH mergers up to the third generation, i.e. at least one generation less than what previously thought.

If, on the one hand, dynamical encounters in young star clusters shape the properties of BBHs, on the other hand BHs affect the structure of the host cluster. In particular, the internal dynamical evolution tends to progressively segregate the most massive objects at the cluster center, with increasingly lighter stars pushed further and further away. BHs, being among the most massive objects within the cluster, tend to concentrate at its center, quenching the segregation of massive stars. As a consequence, the presence of a population of BHs in a given star cluster has a direct and measurable impact on the observational properties of the cluster' stellar population. In Chapter 6, I look for signatures of the presence of BHs the Hyades cluster, by comparing accurate $N-$body models to precise measurements from *Gaia*. I find that even a few BHs can affect the properties of visible stars in a quantifiable way, leading to less concentrated distributions. For the case of the Hyades, ~ 3 BHs (total mass $M_{\rm BH} \approx 25\,{\rm M}_{\odot}$) are favored to match the observed properties of the cluster.

Symbols

$M_\odot$	solar mass	1.98892×10^{30} kg
$R_\odot$	solar radius	6.957×10^{8} m
au	astronomical unit	$1.495978707 \times 10^{11}$ m
pc	parsec	$3.08567758149137 \times 10^{16}$ m
Myr	megayear	3.1536×10^{13} s
c	speed of light in vacuum	$2.99792458 \times 10^{8}\,\mathrm{m\,s^{-1}}$
G	gravitational constant	6.6743×10^{-11} $\mathrm{m^3\ kg^{-1}\ s^{-2}}$

Acronyms

BBH	Binary black hole
BH	Black hole
CE	Common envelope
GC	Globular cluster
GW	Gravitational wave
IMBH	Intermediate-mass black hole
NS	Neutron star
NSC	Nuclear star cluster
OC	Open cluster
PI	Pair Instability
PPI	Pulsational Pair Instability
SN	Supernova
YSC	Young star cluster

Chapter 1

Star clusters and their black hole populations

1.1 Star clusters in the Milky Way

Young stars are generally observed to be located near other young stars (Blaauw 1952, 1964). For this reason, it has long been assumed that stars are born in groups (Lada & Lada 2003; Portegies Zwart et al. 2010). In the Milky Way Galaxy, evidence for this comes from the global clustering of spectral O-type stars (Parker & Goodwin 2007), which mainly ($\sim 70\%$) reside in young clusters or associations (Gies 1987). In the nearby Orion B star-forming region, where star formation is still ongoing, $\sim 96\%$ of the stars are clustered (Clarke et al. 2000). These groups subsequently disperse, and most stars in the Milky Way follow lonely orbits, unrelated to their temporary neighbours, in what is commonly referred to as the Galactic field. In some cases, stars might remain gravitationally bound to their siblings, forming what is usually referred to as a star cluster (Portegies Zwart et al. 2010).

As groups of coeval stars (born at the same time) sharing the same initial chemical composition (born from the same molecular cloud), star clusters represent ideal laboratories to test stellar evolution models. Also, since estimating the age of and distance to a cluster is easier than for individual field stars, clusters have long been used as tracers of the structure and evolution of the Milky Way and its metallicity gradient (e.g., Cantat-Gaudin et al. 2016; Spina et al. 2021). Understanding how clusters (and stars) form, and how clusters are disrupted by the tidal forces of the Milky Way and by encounters with giant molecular clouds is also crucial to reconstruct the evolution of our Galaxy (Gieles et al. 2006). The velocity fields within the youngest clusters reveal their formation history, while the kinematics of the older clusters and the age dependence of their mass function test theories of cluster destruction Gilmore et al. (2022). Furthermore, each star cluster provides a (near-)coeval snapshot of the stellar mass function, and a detailed study of their stellar content is therefore important for understanding possible variations in the initial mass function (Elmegreen 2004). Finally, being the place where the most massive stars form, star clusters are building blocks for our comprehension of the formation of compact objects, which we can detect through gravitational-wave observations.

1.1.1 What is a star cluster?

Star clusters represent a broad and in-homogeneous class of objects, spanning ages from a few Myr to ~ 10 Gyr, and masses from a few hundreds to several millions of solar masses. As shown in Fig. 1.1, some star clusters are so compact and rich that stars become lost in confusion in the frame shown, while others are so sparse and extended that most cluster members are outside the frame. Still, objects like the Orion Nebula Cluster are forming and, depending on the author, might not even be classified as a cluster (Krumholz et al. 2019).

Traditionally, star clusters have been identified as stellar over-densities: wherever a group of stars appeared tightly distributed in the sky, it was assumed they formed a physical cluster. In their review, Portegies Zwart et al. (2010) define a star cluster as a set of stars that are gravitationally bound to one another, while the earlier review by Lada & Lada (2003) defines a cluster as a collection of stars with a mass density large enough ($\gtrsim 1\,\mathrm{M}_\odot\,\mathrm{pc}^{-3}$) to resist tidal disruption in Solar neighborhood conditions, and numerous enough to avoid evaporation for at least 100 Myr.

Modern datasets, e.g. from *Gaia* (Gaia Collaboration et al. 2022), now allow us to verify that these stars are indeed travelling together through the Milky Way (they share a common proper motion and radial velocity) and are physically close enough to each other to be considered physically related (their parallaxes indicate they are all the same distance away from us). In particular, additional information from velocities is critical for the census of sparser and less massive clusters: many apparent stellar over-densities are not made of related stars and despite being located in the same region of the sky, and do not share a common origin (the so called asterisms, Cantat-Gaudin & Anders 2020). For example, NGC 1252 was previously classified as an open cluster, but it was later shown to be merely an asterism (Krumholz et al. 2019).

1.1.2 Star clusters flavors

Star clusters are classified according to their age, density and mass. In general, we distinguish among four different kinds of star cluster.

Globular clusters (GCs) are old (~ 12 Gyr), very massive ($\geq 10^4\,\mathrm{M}_\odot$) and dense (central density $\rho_\mathrm{c} \geq 10^4\,\mathrm{M}_\odot\,\mathrm{pc}^{-3}$) stellar systems. Our Galaxy hosts about 150 globular clusters, and more than one half of them are within 10 kpc from the Galaxy center (Harris 1996, 2010). Globular clusters are evolved systems which do not contain gas, dust or young stars. Because of their mass and high central density, they are sites of intense dynamical processes, which play a relevant role in the formation and merger of compact-object binaries (Portegies Zwart & McMillan 2000; Downing et al. 2010).

Young star clusters (YSCs) are young (< 100 Myr) systems, thought to be the most common birthplace of massive stars (Lada & Lada 2003; Portegies Zwart et al. 2010). In some cases, they are still (partially) embedded in their parent molecular cloud. The central density of YSCs can be as high as that of GCs, although the former ones have smaller sizes (see Fig. 1.2). Some YSCs have also comparable masses to present-days GCs. However, because of the large stellar mass loss during their life, most YSCs are not massive enough to evolve into present-day GCs. In particular, gas expulsion by stellar winds and supernova (SN) explosions can eject the gas in which the cluster is embedded, decreasing its gravitational binding and potentially causing its disruption - a process referred to as infant mortality. A fraction of YSCs might survive this violent gas

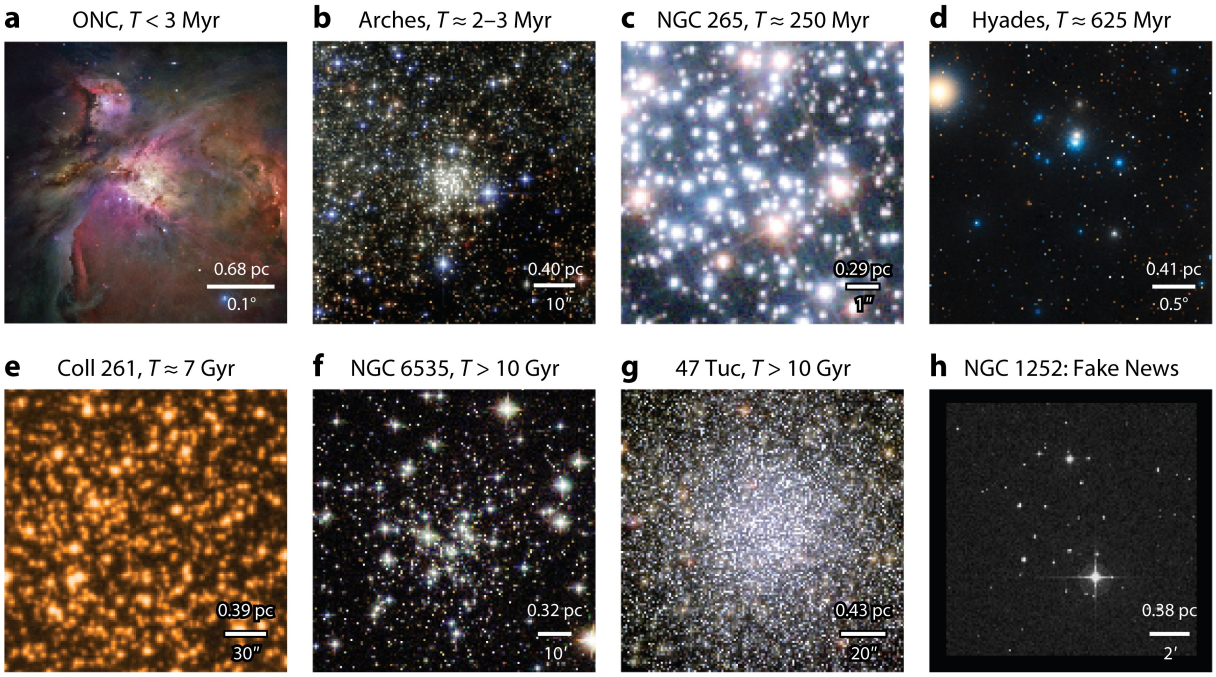

Figure 1.1: Images of a range of star clusters, along with NGC 1252, an object previously classified as a cluster but now known to be an asterism. Figure from Krumholz et al. (2019).

evaporation and evolve into open clusters.

Open clusters (OCs) are irregular star clusters composed from 10 to a few thousands of stars (e.g., see the recent catalog from Tarricq et al. 2022). Open clusters are not long-lived because they inevitably disrupt into the tidal field of their host galaxy as they lose mass during their evolution. When YSCs and OCs dissolve into the Galaxy, their stellar content is released into the field. Thus, it is reasonable to expect that a large fraction of binaries, black holes, and binary black holes that are now in the field may have formed in young star clusters, where they participated in the dynamics of the cluster.

Nuclear star clusters (NSCs) are rather common in the nuclei of galaxies, including our own (Neumayer et al. 2020). These clusters are usually more massive and denser than GCs, and may host a super-massive black hole (SMBH) at their center. Stellar-mass BHs formed in the innermost regions of a galaxy could even be "trapped" in the accretion disc of the central SMBH, triggering their merger (Gondán et al. 2018; Mapelli 2021).

1.1.3 Physical scales

On a theoretical point of view, an effective description of the star cluster size can be given in terms of its Lagrangian radii, defined as distances from the center containing specific fractions of the total cluster mass. In particular, the global scale of the system is generally given by the half-mass radius ($r_{\rm hm}$, the 50% Lagrangian radius), that is is the distance from the cluster center containing half of the total mass. For observers, a similar definition can be formulated in terms of isophotes containing given fractions of the total luminosity, and the projected half-light radius, the effective radius $r_{\rm eff}$, is often used. The relation between the half-mass and the effective radii, however, may not be

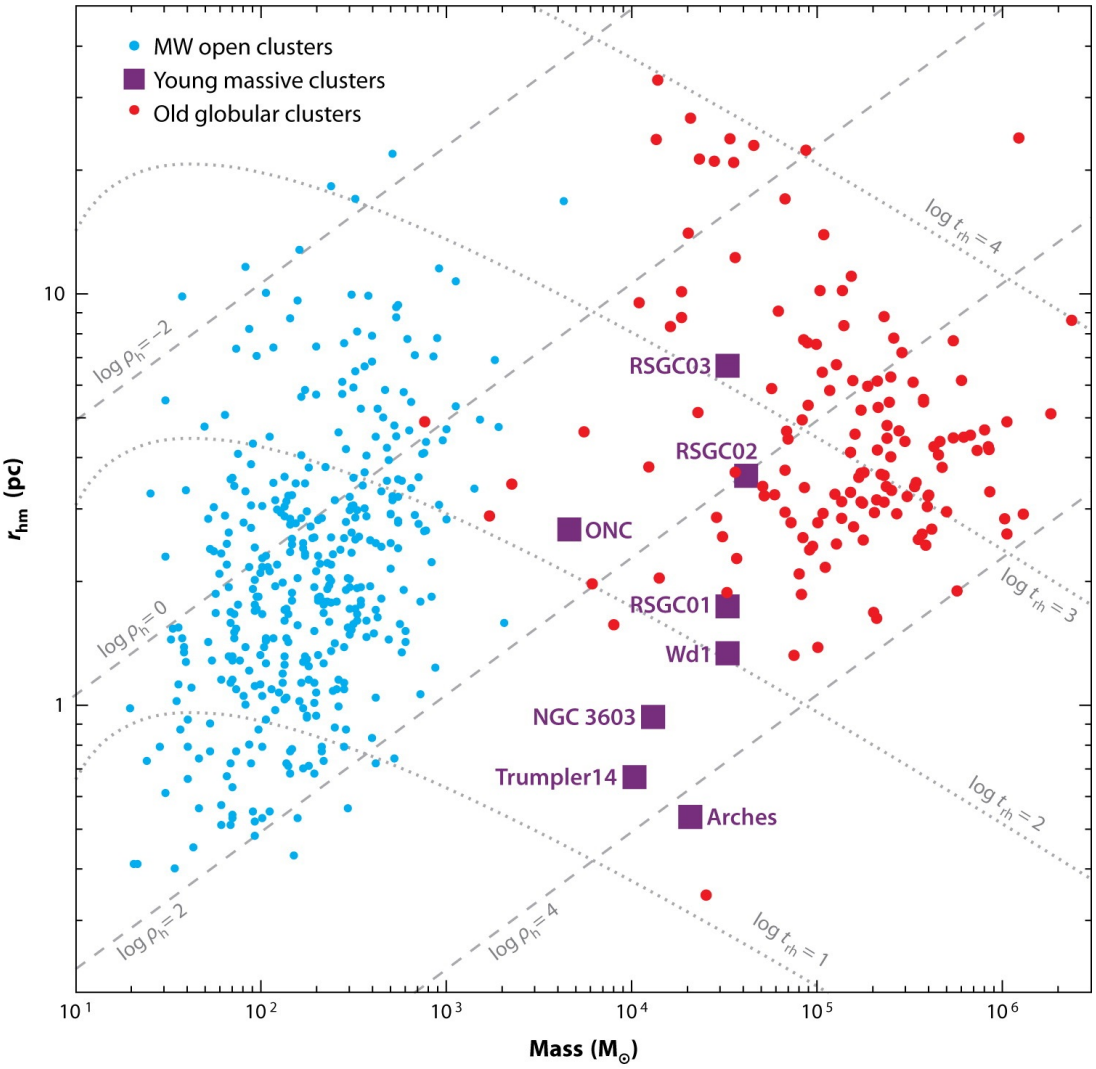

Figure 1.2: Mass-radius diagram of Milky Way open clusters, massive young star clusters (here labelled as young massive clusters), and old globular clusters. Gray dashed and dotted lines represent lines of constant half-mass density ($\rho_{\rm h} = 3M_{\rm tot}/(8\pi r_{\rm hm}^3)$) and relaxation time ($t_{\rm rlx}$, see eq. 1.8), respectively. Figure from Portegies Zwart et al. (2010).

trivial, as in the case where the mass-to-light ratio of the cluster varies with the distance to the cluster center, because of the presence of mass segregation and/or dark components (Hurley 2007; Bianchini et al. 2017).

The tidal radius $r_{\rm t}$ is the distance from the center of a star cluster where the gravitational acceleration due to the cluster equals the tidal acceleration of the parent Galaxy. As a practical matter, the Jacobi radius, that is the distance from the cluster center to the lagrangian point L_1, is commonly used to quantify the tidal boundary. For clusters on circular orbits, this can be defined from the cluster mass M, and the orbital angular frequency in the galaxy ω (Gieles & Baumgardt 2008):

$$r_{\rm t} = \left(\frac{GM}{3\omega^2}\right)^{1/3}, \tag{1.1}$$

where $\omega = V_{\rm G}/R_{\rm G}$, $R_{\rm G}$ is the galactocentric distance and $V_{\rm G}$ is the circular orbital speed around the galaxy center.

To identify the star cluster central regions, observers generally define the cluster core radius $r_{\rm c}$ as the distance from the cluster center at which the surface brightness drops by a factor of two from the central value. On a theoretical point of view, at least two distinct definitions of $r_{\rm c}$ can be used, depending on the context. When the central density ρ_0 and velocity dispersion σ_0 are easily and stably defined, like in analytic models (e.g., King 1966 models), the core radius is given by:

$$r_{\rm c} = \sqrt{\frac{3\sigma_0^2}{4\pi G\rho_0}} \tag{1.2}$$

For typical cluster models, this corresponds roughly to the radius at which the three-dimensional stellar density drops by a factor of 3, and the surface density by ~ 2 (King 1966).

In $N-$body simulations, however, both ρ_0 and σ_0 are difficult to determine, as they are subject to substantial stochastic fluctuations. As a result, a density-weighted core radius is used instead. Specifically, for each star a local density ρ_i is defined using the star's k nearest neighbors (Casertano & Hut 1985), where $k = 12$ is a common choice. A density center is then determined, as simply the location of the star having the greatest neighbor density. The core radius, then, is the ρ_i^2-weighted root-mean-square stellar distance from the density center:

$$r_{\rm c} = \sqrt{\frac{\sum_i \rho_i^2 r_i^2}{\sum_i \rho_i^2}}. \tag{1.3}$$

Despite their rather different definitions, the two "theoretical" core radii behave quite comparably in simulations (Portegies Zwart et al. 2010).

The dynamical timescale is the time required for a typical star to cross the system; it is also the timescale on which the system re-establishes dynamical equilibrium (Binney & Tremaine 2008):

$$t_{\rm dyn} = \frac{r_{\rm hm}}{\sigma}, \tag{1.4}$$

where σ is the velocity dispersion within the half-mass radius.

As for velocities, a relevant scale for the retention of black holes and compact objects is given by the escape velocity (Georgiev et al. 2009a,b; Fragione et al. 2020):

$$v_{\rm esc} = 40\,{\rm km\,s^{-1}} \left(\frac{M}{10^5\,{\rm M_\odot}}\right)^{1/3} \left(\frac{\rho_{\rm hm}}{10^5\,{\rm M_\odot\,pc^{-3}}}\right)^{1/6}, \tag{1.5}$$

where $\rho_{\rm hm}$ is the density within the half-mass radius. The relevant time, mass, size, and velocity scales for different star clusters types are reported in Tab. 1.1.3.

Cluster	$t_{\rm age}$ [Gyr]	$m_{\rm to}$ [$M_\odot$]	M [$M_\odot$]	$r_{\rm hm}$ [pc]	$\rho_{\rm c}$ [$M_\odot\,{\rm pc}^{-3}$]	$t_{\rm rlx}$ [Myr]	$v_{\rm esc}$ [$\rm km\,s^{-1}$]	location
YSC	$\lesssim 0.1$	$\gtrsim 5$	$\gtrsim 10^3$	$0.1-10$	$\gtrsim 10^3$	$\lesssim 100$	~ 1	disk
OC	$\lesssim 0.3$	$\lesssim 4$	$\lesssim 10^3$	$\lesssim 10$	$\lesssim 10^3$	$\lesssim 100$	$\lesssim 1$	disk
GC	$\gtrsim 10$	~ 0.8	$\gtrsim 10^5$	$\lesssim 50$	$\gtrsim 10^3$	$\gtrsim 10^4$	$\gtrsim 10$	halo
NSC	$\gtrsim 10$	–	10^6-10^9	$\lesssim 50$	10^6-10^7	$\gtrsim 10^5$	$\gtrsim 100$	galactic center

Table 1.1: Column 1: SC type; column 2: SC age; column 3: turn-off mass; column 4: total SC mass; column 5: half-mass radius (for NSCs we refer to the effective radii reported in Neumayer et al. 2020); column 6: density within the core; column 7: escape velocity; column 8: relaxation time scale (defined in eq. 1.8); column 9: location where these clusters are found.

1.2 Young star clusters

The majority of star formation occurs in embedded clusters (Lada & Lada 2003), but only a small fraction of stars in the Galactic disk currently reside in clusters. This indicates that most clusters and associations are relatively short-lived, as confirmed by the scarcity of OCs with ages $\gtrsim 1$ Gyr (Tarricq et al. 2022; Gilmore et al. 2022).

The evolution of YSCs can be split into three phases: the first few Myr, during which stars are still forming and the cluster contains significant amounts of ambient gas; a subsequent period when the cluster is largely gas-free, but stellar mass loss plays an important role in the overall dynamics; a late stage, during which purely stellar dynamical processes dominate the long-term evolution of the cluster. An upper limit on the dividing line between the first two phases is the time of the first supernovae in the cluster, about 3 Myr after formation, since these expel any remaining gas not already ejected by winds and radiation from O- and B- type stars. The dividing line between the last two phases may be anywhere between 100 Myr and 1 Gyr, depending on the initial mass, radius, and density profile of the cluster and the stellar mass function.

1.2.1 Birth properties

The spatial distributions and motions of young stars reflect the processes of star cluster formation. YSCs that are embedded or partially embedded in star-forming clouds typically display clumpy distributions (e.g., Lada & Lada 2003; Kuhn et al. 2019; Cantat-Gaudin et al. 2019). These groups, known as sub-clusters, typically form quite compact ($r_{\rm hm} \approx 0.1-0.3$ pc), with small radii comparable to the observational lower end of the sizes of dense cores in giant molecular clouds (Marks & Kroupa 2011).

It is still unclear whether the sub-clusters will disperse once the molecular gas disperses, or if they will merge into larger, possibly bound clusters that survive gas expulsion. Two principal paths from theoretical studies are: "monolithic" cluster formation, in which a YSC is born in a single molecular cloud core, and "hierarchical" cluster formation, in which larger clusters are built via the assembly of smaller sub-clusters (Bonnell et al. 2003; Banerjee & Kroupa 2015). Examination of the motions of these sub-clusters

can help to reconstruct the formation scenarios of star clusters. The relative motions of clusters within massive star forming regions generally show random motions (as displayed in Fig. 1.3), likely inherited from the parent molecular clouds (Kuhn et al. 2019). They do not generally have the convergent motions expected from hierarchical assembly, indicating that any cluster merger occurred during an embedded phase before the clusters were observed.

Also, the massive YSC R136 is rotating with a rotational velocity amplitude of about 3 $\mathrm{km\,s^{-1}}$, which implies that at least $\sim$ 20% of its total kinetic energy is in rotation (Hénault-Brunet et al. 2012). As confirmed from the combination of hydro-dynamical and $N-$body simulations, this feature can be explained as due to angular momentum conservation in the collapse of the densest gas forming the stellar substructures, as well as angular momentum transport by torques from the gas to the already formed substructures (Mapelli 2017; Ballone et al. 2020). Some of these natal properties might even survive the successive evolution of the stellar system, and leave an imprint on the observed properties of older, relaxed stellar clusters (e.g., they may contribute to the signatures of rotation visible in some globular clusters, van Leeuwen et al. 2000; Bianchini et al. 2013; Kamann et al. 2018).

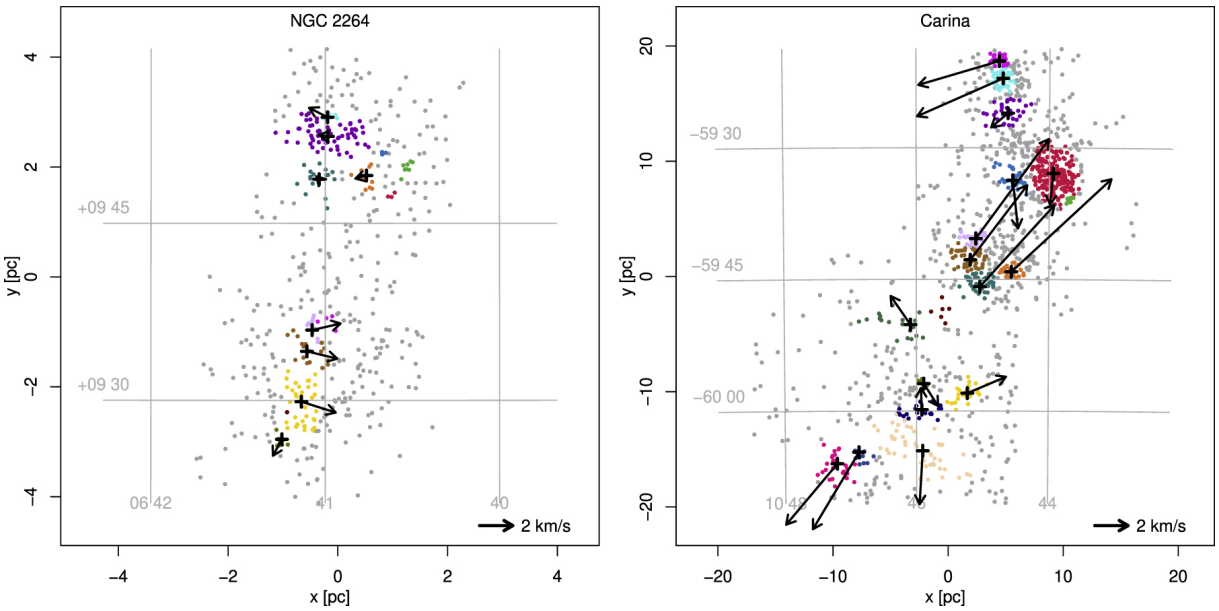

Figure 1.3: Kinematics of subclusters in NGC 2264 (left) and the Carina OB1 association (right). The crosses mark sub-cluster centers, and the vectors indicate velocities of the sub-clusters, as indicated by the velocity scale. Sub-cluster velocities in Carina tend to be much larger than in the smaller, nearby NGC 2264 region. In both NGC 2264 and Carina, nearby groups of stars tend to move in similar directions, but there is no overall sign of sub-cluster mergers. Figure from Kuhn et al. (2019).

1.2.2 Early gas expulsion

The evolution of the cluster during the first phase is a complex mix of gas dynamics, stellar dynamics, stellar evolution, and radiative transfer, and is currently poorly understood. At the end of the star formation process, as a consequence of the developing winds of the

most massive stars or the first supernovae, the residual gas is ejected from the embedded cluster. The gas expulsion phase is expected to be short - on the order of some dynamical times - and might place the remaining stellar population in a super-virial state, making the young cluster vulnerable to dissolution (Goodwin & Bastian 2006; Baumgardt & Kroupa 2007). The sharp decrease in the number of young and embedded star clusters at an age of a few Myr is thought to be a consequence of this early process, and is often referred to as "infant mortality" (Lada & Lada 2003). The response of the cluster to the loss of the residual gas depends on the gas expulsion time scale relative to the dynamical time scale of the cluster. However, the local dynamical time depends strongly on the distance to the cluster center. Real star-forming regions are hierarchically-structured, containing both dense parts for which mass removal is slow compared to the local dynamical time, and diffuse parts for which it is fast; this configuration may give rise to a gravitationally-bound central region and an unbound periphery (Elmegreen 2008).

On the observational point of view, bulk expansion is commonly seen for young stellar systems during the first few million years, with expansion velocities that can range up to $2\,\mathrm{km\,s^{-1}}$ (Portegies Zwart et al. 2010). The *Orion* complex, which still hosts ongoing star formation, and is perhaps the most studied and characterized nearby stellar complex (Kounkel et al. 2018), exhibits kinematic substructures, and one in particular (λ Ori) shows strong signs of radial expansion, attributed to a supernova explosion. In general, stellar systems that are no longer embedded in their natal molecular clouds or only partially embedded are statistically more likely to be in a state of expansion than systems that are still embedded. This result is consistent with expansion as a consequence of gas expulsion, but it is also possible that cloud dispersal and expansion of stellar systems occur simultaneously but independently (Portegies Zwart et al. 2010).

1.2.3 Stellar mass losss

Young star clusters that survive the early gas expulsion continue to lose mass through stellar evolution. During this phase, the most massive ($\gtrsim 50\,\mathrm{M_\odot}$) stars leave the main-sequence within ($\lesssim 4$ Myr), and can lose up 90% of their mass by the time they collapse to a black hole. For a Kroupa (2001) IMF between $0.1\,\mathrm{M_\odot}$ and $100\,\mathrm{M_\odot}$ the total cluster mass decreases by roughly 10%, 20%, and 30% during the first 10, 100, and 500 Myr (Portegies Zwart et al. 2010).

For YSCs, the expansion due to stellar mass loss can even result in its complete disruption, and is stronger if the most massive stars are more segregated at the cluster center (Vesperini et al. 2009, see Sect. 1.3.3 for more details about mass segregation). In particular, when the half-mass radius becomes comparable to its tidal radius ($r_\mathrm{t} \sim 2\,r_\mathrm{hm}$), the clusters loses equilibrium and most of its stars become unbound (Takahashi & Portegies Zwart 2000; Baumgardt & Makino 2003). In Chap. 3, I will quantify the impact of stellar evolution on the mass loss and the global evolution of young star clusters, by comparing $N-$body simulations with and without stellar evolution. Also, I will study the impact of primordial populations of binaries (see Sect. 1.2.4), which, in this phase, play a relevant role.

Eventually, the cluster can continue to expand until it completely dissolves or until its core starts to contract again due to internal dynamical effects. At this point, the evolution of the cluster is completely dominated by dynamical interactions (see Sect. 1.3).

1.2.4 Primordial binaries

A large fraction of O- and B- type stars form as members of binary and higher order systems, with typical separations $\lesssim 0.1$ pc (Moe & Di Stefano 2017; Offner et al. 2022). To quantify the fraction of multiple systems, we may refer to the multiplicity fraction (sometimes simply named binary fraction), defined as the as the fraction of primaries with at least one companion:

$$f_{\rm mult} = \frac{N_{\rm bin} + N_{\rm trip} + N_{\rm quad} + ...}{N_{\rm sing} + N_{\rm bin} + N_{\rm trip} + N_{\rm quad} + ...}, \tag{1.6}$$

where $N_{\rm bin}, N_{\rm trip}, N_{\rm quad}$ are the number of binary, triple, and quadruple systems, respectively. Also, we can define the companion frequency is the average frequency of companions per primary:

$$f_{\rm comp} = \frac{N_{\rm bin} + 2N_{\rm trip} + 3N_{\rm quad} + ...}{N_{\rm sing} + N_{\rm bin} + N_{\rm trip} + N_{\rm quad} + ...}. \tag{1.7}$$

Figure 1.4 displays how the multiplicity and the companion fractions vary with the spectral type of the primary star.

Given the high densities of young stellar clusters, binary and multiple systems can actively interact with the surrounding stars since the very beginning of their life. On the one hand, binary stars contain a large reservoir of internal energy, which can be transferred to other stars in the host star cluster, through three- and multi-body encounters (e.g., Heggie 1975; Hut 1983). On the other hand, the global evolution of the cluster shapes the properties of the binary population and of the resulting population of binary compact objects. When dealing with binary stars in star clusters, we usually distinguish between two fundamental types of binaries:

- **original** (or "primordial") binaries, which formed simultaneously with the stars in the cluster, as a crucial part of the star-formation process (Goodman & Hut 1989),
- **exchanged** (or "dynamical") binaries, which formed later via stellar interactions.

Binary stars within star clusters are also closely related to the formation of exotic objects, as they often form via internal binary evolution or during dynamical interactions between binaries and other stars. For example, the formation of blue straggler stars, colliding wind binaries, and anomalous X-ray pulsars, all require the presence of binary stars in the system (Portegies Zwart et al. 2010).

1.2.5 Not all stars are born in clusters?

While many stars form in gravitationally-bound clusters, and some clusters likely do undergo a ordered bulk expansion, recent results from OB associations (e.g., see Wright 2020 for a recent review) hint at the possibility of alternative formation scenarios. In particular, a number of observational studies with *Gaia* have shown that OB associations are born extended and highly sub-structured, and only exhibit slow expansion patterns (Mel'nik & Dambis 2017; Kuhn et al. 2019). Also, their proper motions reveal many kinematic substructures, and are not compatible with models that trace radial expansion (Ward & Kruijssen 2018; Ward et al. 2020). As a consequence, these OB associations are likely not be the expanded remnants of dense clusters.

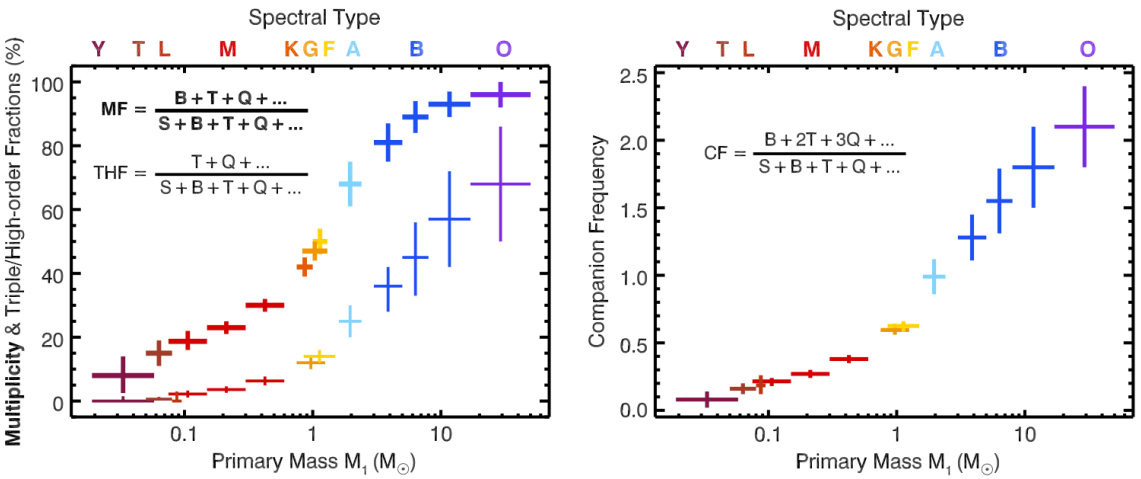

Figure 1.4: Multiplicity fraction $f_{\rm mult}$, here named MF (left; thick), triple/high-order fraction (THF, left; thin), and companion frequency $f_{\rm comp}$, here named CF (right), of brown dwarfs and main sequence stars. The indicated spectral types at the top roughly correspond to the mean primary masses of field dwarfs. Figure from Offner et al. (2022).

Further support for this scenario comes from the observation of coeval populations that are spatially too extended to be the result of expansion (Kruijssen 2012), as in the case of the *Vela-Puppis* region (e.g., see Cantat-Gaudin et al. 2019). Finally, the distribution of sizes and densities between the structures once called associations and those called clusters actually show a continuous distribution, making the distinction somehow arbitrary (Cantat-Gaudin 2022). All these results suggest that a fraction of stars may form across continuous density distributions throughout molecular clouds, rather than exclusively within clusters.

1.3 Dynamical evolution of star clusters

When the cluster is largely gas-free, its evolution is driven by individual stellar encounters, which main effect is to modify the stellar velocities, both in magnitude and direction, and to perturb stars away from their original trajectories. After many such encounters, the star eventually loses its memory of the original orbit, and finds itself on a wholly unrelated one. The characteristic time over which this loss of memory occurs is called the relaxation time $t_{\rm rlx}$ (Spitzer 1987):

$$t_{\rm rlx} = 0.138 \frac{M\, r_{\rm hm}^{3/2}}{m^{1/2}\, G^{1/2}\, \ln(\Lambda)}, \tag{1.8}$$

where M is the total mass of the cluster, $r_{\rm hm}$ is the half-mass radius, m is the the mean cluster mass, and $\ln(\Lambda)$ is the Coulomb logarithm, which depends weakly on the number of cluster stars. In particular, $\ln(\Lambda) = \ln(\gamma {\rm N})$, with $\gamma = 0.02$ for multi-mass systems (Giersz et al. 2008) and can be roughly considered as constant $\ln(\Lambda) = 10$. The relaxation time is longer for stellar systems with larger number of stars. For a star cluster in virial equilibrium, it scales with the number of particles as (Bertin 2014):

$$\frac{t_{\rm rlx}}{t_{\rm dyn}} \sim \frac{N}{\ln(N)}, \tag{1.9}$$

where $t_{\rm dyn}$ is defined in eq. 1.4.

Figure 1.2 and Tab. 1.1.3 display the typical mass, size and relaxation timescales for different cluster types. YSCs typically display relaxation timescales of $10 - 100$ Myr, an order of magnitude shorter than old and more massive GCs. This peculiarity allows relaxation processes to affect the cluster structure since the early phases of its life.

1.3.1 Gravothermal instability

For timescales longer than $t_{\rm rlx}$, the cumulative effect of two-body encounters on stellar motions is a random walk in the velocity space. In particular, if the velocity distribution is not in kinetic equilibrium, there will be a net diffusion in the velocity space, in the direction of reducing the deviations from this equilibrium, i.e. from the Maxwellian distribution. This process has a fundamental impact on the internal structure of the cluster. More specifically, two-body relaxation drives a flux of kinetic energy, carried by stars, from the center of the cluster to its outskirts. According to the virial theorem, for a self-gravitating system with a total energy E:

$$E = -K = \frac{W}{2}, \tag{1.10}$$

where K is the total kinetic energy and W is the total gravitational energy. If the system loses energy (E is negative, so its absolute value increases), W becomes more negative and K increases: the system becomes hotter as it loses energy and cools as it is heated: the system has negative specific heat. If such a bound system is in thermal contact with a heat sink (a colder system), heat flows into the sink and the kinetic energies of the particles in the gravitationally bound system increase steadily as the system contracts, losing energy.

Within a single cluster, when stars move from the hotter core to the colder halo, they carry heat with them. As the core loses energy, it collapses, thus it increases its velocity dispersion (it becomes hotter). Thus, the core loses energy to the outer regions, contracts and heats up in the process. The increase of mean square random velocity in the core then encourages additional flow of heat to the surrounding regions, increasing the rate of core collapse (Spitzer 1987). This results in a runaway process called gravothermal catastrophe, and is a consequence of the negative heat capacity typical of every self-gravitating system (Spitzer 1987). As the stellar halo expands, some stars reach high enough velocities to escape the cluster, in a process called **evaporation**. This process is further accelerated if stars have a mass spectrum.

1.3.2 Energy equipartition

As a consequence of dynamical encounters stars with different masses tend to erase their kinetic energy differences and reach a condition of thermodynamical equilibrium, in which their temperatures (the mean kinetic energies) are constant. If we consider two generic components i and j, energy equipartition can be expressed as a condition of isothermality between them ($T_i = T_j$):

$$m_i \sigma_i^2 = m_j \sigma_j^2, \tag{1.11}$$

where $m_{i,j}$ and $\sigma_{i,j}$ are the mass and velocity dispersion of the i, j component, respectively.

For realistic initial mass functions (e.g. $N(m) \propto m^{-2.3}$, Kroupa 2001), the pathway towards equipartition breaks, and the population of the most massive objects (massive

stars first, then black holes) dynamically decouples from the lightest objects (Spitzer 1969). This leads to the formation of a independent sub-cluster of massive objects, which interact only among themselves. This sub-cluster, being hotter than the surrounding cluster, acts as an additional internal energy source for the whole system, accelerating its disruption, as described in detail in Sect. 1.5.2.

1.3.3 Mass segregation

As the temperature of the heavier stars approaches that of the lighter stars, the former ones will tend to acquire lower random velocities and sink towards the center of the cluster. On the other hand the lighter stars, which acquire higher random velocities, move outwards and populate the outermost regions of the cluster. The system will thus tend to be characterized by a stratification in mass, usually called mass segregation. The timescale on which mass segregation sets in for a star of mass $m_\star$ in a cluster of stars with mean mass $\langle m \rangle$ is given by the dynamical friction timescale:

$$t_{\rm df} = \frac{\langle m \rangle}{m_\star} t_{\rm rlx}. \tag{1.12}$$

The presence of a mass spectrum accelerates the tendency towards core collapse. In star clusters with a mass spectrum, the core collapse occurs on the dynamical friction timescale, rather than the two-body relaxation one. Also, the steeper is the mass spectrum, the faster is the core collapse (Fujii & Portegies Zwart 2014). For YSCs, the typically short relaxation timescales (Sect. 1.3) allow the most massive stars to segregate at the cluster center before evolving into black holes. This triggers dynamical interactions and even direct collisions between stars and binary stars (see Capt. 4).

1.3.4 Halting core collapse with binaries

The tendency towards core collapse (see Sect. 1.3.1) increases the cluster central density, and produces an ideal environment for dynamical interactions between stars and binaries to take place at high rates. In particular, the rate of encounters between a binary and a single star depends on the density as (Binney & Tremaine 2008):

$$\Gamma_{1+2} = 4\sqrt{\pi} n \sigma r_{\rm ra}^2 \left[1 + \frac{G(m_{\rm bin} + m)}{2\sigma r_{\rm ca}} \right], \tag{1.13}$$

where n, m, and σ are the single stars number density, average mass, and velocity dispersion, $m_{\rm bin}$ is the mass of the binary, and $r_{\rm ca}$ is the closest approach distance. For the encounter to result in energy exchange between the single and the binary star, the encounter needs to be close enough to perturb the binary orbital parameters. This happens only if the single star approaches the binary by few orbital separations. As shown in eq. 1.13, for this to happen with a non-negligible frequency, the binary must be in a dense environment, because the rate of three-body encounters scales with the local density of stars. If in the cluster core no binaries are present, they can be formed via three-body encounters of single stars. The timescale to form a binary star by this process is (Goodman & Hut 1993):

$$t_{\rm 3bb} = 5.5 \times 10^6 \left(\frac{10^6\,{\rm pc}^{-3}}{n} \right)^2 \left(\frac{\sigma_{\rm 1D}}{30\,{\rm km/s}} \right)^9 \left(\frac{20\,{\rm M}_\odot}{m} \right)^5 \frac{1}{N}\ {\rm Myr}, \tag{1.14}$$

where σ_{1D} is the 1-dimensional velocity dispersion, and N is the number of interacting objects in the core. As the system approaches core collapse, binary stars form (if they are not already present) and interact with the surrounding stars via thee-body encounters. Hereafter, we will define a three-body encounter as a close encounter between a binary and a single star.

Hard binaries

During a three-body encounter, a fraction of the binary internal energy is redistributed as energy among the interacting bodies. Statistically, three-body encounters can have different outcomes depending on the kinetic energy of the single and the binding energy of the binary (Heggie 1975; Heggie & Hut 2003):

$$E_{\rm bin} = \frac{Gm_1m_2}{2a}, \tag{1.15}$$

where, m_1, m_2 are the masses of the binary members and a is the binary semi-major axis. In the context of stellar clusters, a binary is considered as hard if its binding energy $E_{\rm bin}$ is greater than the average kinetic energy of neighboring stars, while it is soft in the opposite case. On average, subsequent encounters make hard binaries harder (i.e. their semi-major axis shrinks), while soft binaries tend to become softer (i.e. wider semi-major axis) until they break up (Heggie 1975). Hardness is a property of the binary relative to its environment. Due to the higher velocity dispersion, the same binary in the core of a cluster might be soft, whereas in the halo it would be hard.

The kinetic energy released by hard binaries through three-body encounters can be used to reverse core collapse. During this core bounce, the thermal energy generated builds up in and around the core faster than it can be conducted away. This causes an expansion and cooling of the core and its immediate surroundings, because of the negative specific heat. If the core collapse is sufficiently deep, the expanding core can actually cool to temperatures below that of its surroundings (Heggie & Hut 2003).

1.3.5 Tidal stripping

Despite being bound by gravity, YSCs and OCs slowly dissolve over time scales of several hundred million years (See Sect 1.2), and stars progressively disperse into the Galactic field. As explained in Sect. 1.3.1, relaxation processes accelerate stars to velocities higher than the cluster's escape velocity, leading to cluster evaporation. This is a consequence of the steady loss of stars from the cluster driven by the continuous re-population of the high-velocity tail of the Maxwellian velocity distribution. At the same time, the expansion of the cluster, as a consequence of early gas expulsion (Sect. 1.2.2), stellar mass loss, or relaxation (Sect. 1.3.1) exposes its outermost regions to the tidal field of the host galaxy.

Tidal stripping is the prompt removal of stars that find themselves outside the cluster tidal radius (eq. 1.1) due to internal processes such as stellar mass loss or a change in the external tidal field (e.g., as the cluster approaches pericenter in its orbit around the parent galaxy). On a $\sim$ 100 Myr time scale, and for clusters with masses $\gtrsim 10^4 M_\odot$, relaxation is unlikely to be important, and so tidal stripping dominates the cluster mass loss (Portegies Zwart et al. 2010). When tidal stripping is effective, clusters preferentially lose stars through their Lagrange points L_1 an L_2 (e.g., Küpper et al. 2008; Portegies

Zwart et al. 2010), leading to the formation of two so-called tidal tails, made up of stellar escapers.

Until few years ago, tidal tails had mainly been observed in GCs (e.g., Gieles et al. 2021), which are denser, more massive, older, and often further from the Galactic plane than OCs. Recently, it has been possible to detect these spatial elongations in a clear way for a number of OCs, like the Hyades or the Praesepe cluster (Röser et al. 2011, see Fig. 1.5). For the Hyades (Reino et al. 2018; Röser et al. 2019) it has been possible to trace tidal tails over a distance of 800 pc (Jerabkova et al. 2021). This additional information, when combined with proper dynamical modeling, can provide information to predict the final fate of OCs. For example, the Hyades cluster are predicted to become entirely unbound within the next 30 Myr (Oh & Evans 2020).

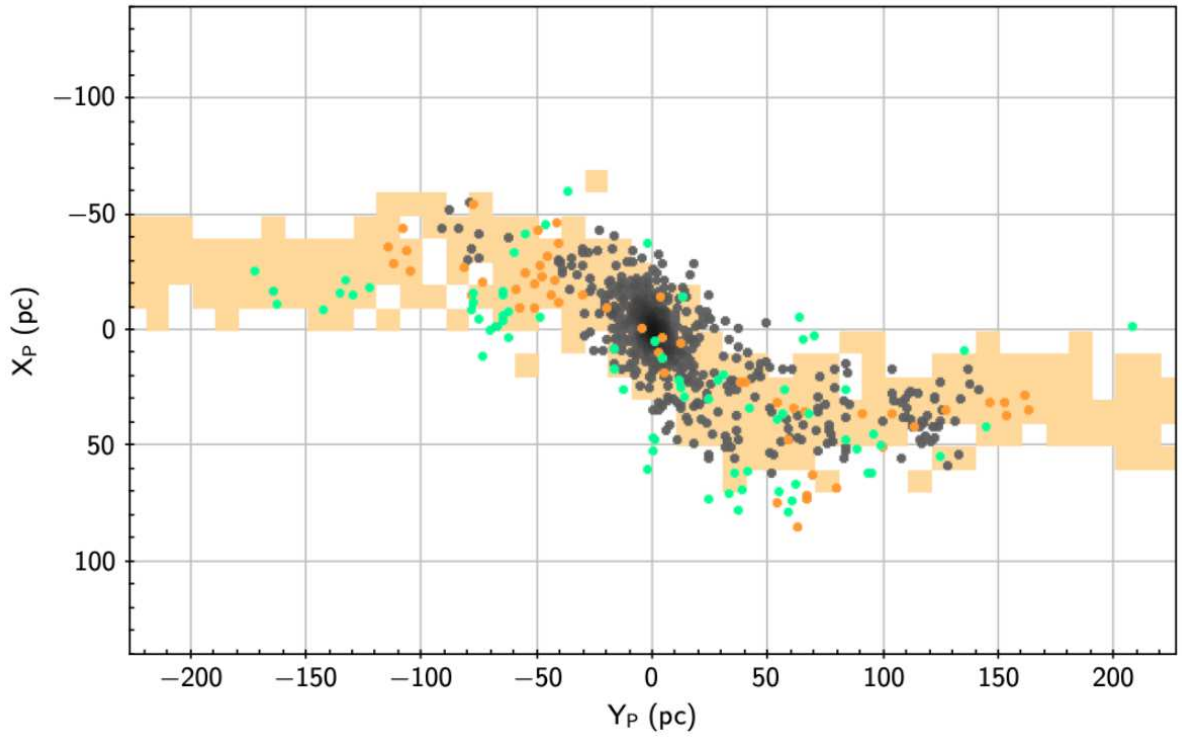

Figure 1.5: Members of the Praesepe cluster (NGC 2632) identified by Röser et al. (2011), displayed in Cartesian Galactic coordinates centerd on the cluster. The grey, orange, and cyan points are secure, likely, and possible members of the cluster, respectively. The shaded background is the tidal tail model from Kharchenko et al. (2009). Figure from Cantat-Gaudin (2022).

1.4 Stellar-mass black holes

A black hole (BH) can be defined as a region of the space-time that cannot communicate with the external Universe. The boundary of this region is called the surface of the BH, or event horizon (Shapiro & Teukolsky 1983). In principle, any mass $m_{\rm BH}$ can become a BH, provided that there is a process able to confine it inside the event horizon. The radius of this boundary depends on the mass of the collapsed object, and is given by its

Schwarzschild radius:

$$r_{\rm sch} = \frac{2Gm_{\rm BH}}{c^2}. \tag{1.16}$$

As a reference, the Schwarzschild radius for $1\,{\rm M}_\odot$ is ≈ 3 km.

The possibility that the evolution of a star could lead to the formation of a BH was first recognized in the 1930's, soon after Chandrasekhar's discovery of a maximum value for the mass of a white dwarf. The existence of this maximum implied that a massive stellar core could collapse into a region of space in which gravity was overwhelming. Many astrophysicists found this outcome for stellar evolution unacceptable, if not absurd. In 1935, Eddington made this view very clear when he wrote:
"The star apparently has to go on radiating and radiating and contracting and contracting until, I suppose, it gets down to a few kilometers radius when gravity becomes strong enough to hold the radiation and the star can at last find peace... I felt driven to the conclusion that this was almost a reductio ad absurdum of the relativistic degeneracy formula. Various accidents may intervene to save the star, but I want more protection than that. I think that there should be a law of Nature to prevent the star from behaving in this absurd way."

At the present day, it is well established that stellar evolution provides a valid mechanism for generating such exotic objects: stars with initial mass in excess of $\approx 8\,{\rm M}_\odot$ end their lives in a violent supernova (SN) explosion, leaving behind a compact remnant in the form of either a neutron star (NS) or, if the star initial mass exceeds $\approx 20\,{\rm M}_\odot$, a BH. However, prior to the detection of gravitational waves (GWs), our knowledge of stellar-mass BHs lacked of a strong observational counterpart. In particular, we were limited to electromagnetic observations of Galactic BH X-ray binaries, that is binary systems consisting of a visible star and and invisible compact object. X-rays are produced by mass flowing from the star into the strong gravitational field of the invisible compact object. Observations from X-ray binaries lead to the discovery of a handful of known BHs with confirmed dynamical mass measurements, most of them with mass $\lesssim 15{\rm M}_\odot$ (Özel et al. 2010; Farr et al. 2011), as shown in Fig. 1.6. Also, only few theoretical models predicted the existence of BHs with masses $\gtrsim 20{\rm M}_\odot$ (Heger et al. 2003; Mapelli et al. 2009, 2013; Belczynski et al. 2010; Spera et al. 2015).

1.4.1 Black holes in the gravitational wave era

On September 14 2015, the LIGO interferometers captured a gravitational wave (GW) signal from two merging BHs (Abbott et al. 2016). The event, named GW150914, was attributed to the coalescence of two stellar-mass BHs with masses $m_1 = 36^{+5}_{-4}\,{\rm M}_\odot$ and $m_2 = 29^{+4}_{-4}\,{\rm M}_\odot$. GW150914 established the existence of binary black holes (BBHs) and that stellar-mass BHs can merge in a Hubble time, becoming detectable sources of GWs. Also, it laid the foundations of a new way to investigate the Universe, by studying the properties of compact objects with unprecedented precision.

At the present day, the Ligo-Virgo-Kagra collaboration (LVK) has completed three observing runs and detected the merger of several tens (~ 90) of compact object binaries (e.g., Abbott et al. 2016b, 2019, 2021f,d,e). The catalog already contains a many events that challenge up-to-date theoretical models. For instance, GW190814 (Abbott et al. 2020c) is an event with very asymmetric masses, a merger that most theoretical models find very difficult to explain. Furthermore, the lightest member is of uncertain nature: it can be the heaviest NS or the lightest BH ever observed. GW190521 (Abbott et al.

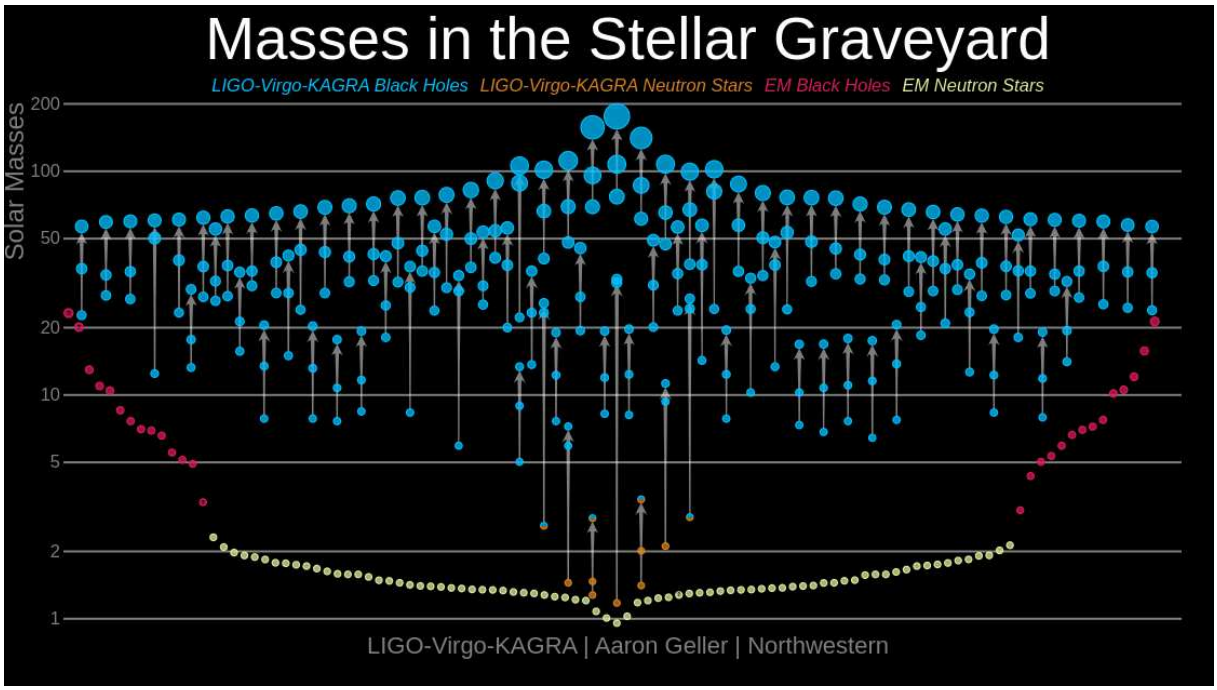

Figure 1.6: Masses of all the detected and observed NSs and BHs so far. Credits: LIGO-Virgo-KAGRA / Aaron Geller / Northwestern. Image from this link.

2020) is the event[1] with the heaviest BHs, with at least one of the two falling in the pair-instability mass gap (see Sect. 1.4.4). Its merger product, a BH with mass $148^{+28}_{-16}\mathrm{M}_{\odot}$, is the first confirmation of the existence of intermediate-mass BHs. GW200105_162426 and GW200115_042309 are the first BH - NSs ever observed (Abbott et al. 2021a). GW170817 (Abbott et al. 2017c) is associated with a merger of two NSs and it is the only event observed not only through GWs but also throughout the whole electromagnetic spectrum, a crucial milestone for multi-messenger astronomy Abbott et al. (2017d).

All these detections are contributing to improve our understanding the formation and evolution of compact-object binaries and their progenitor stars. The discovery of GWs gave an unprecedented boost to the development of new theoretical models, with a new goal: providing an astrophysical interpretation to GW sources.

1.4.2 Formation channels of gravitational waves sources

Many stars, especially the more massive ones, are born in binaries or higher multiple stellar systems (see Sect. 1.2.4), with a multiplicity fraction that increases with the mass of the primary star (Moe & Di Stefano 2017; Offner et al. 2022). Thus, most BH progenitors form as members of binaries, triples, and even quadruple stellar systems. Studying the interactions between these close stars is crucial to reconstruct the evolutionary history of GW mergers.

The timescales of GW coalescence for a BBH with component mass m_1 and m_2 was

[1]With signal-to-noise ratio $S/N > 10$ and a probability of being of astrophysical origin $> 90\%$.

derived analytically by Peters (1964)[2]:

$$t_{\rm GW} = \frac{3}{85}\frac{a^4 c^5}{G^3 m_1 m_2 (m_1+m_2)}(1-e^2)^{7/2}, \tag{1.17}$$

where e and a are the eccentricity and semi-major axis of the binary, respectively. Based on this formula, two BHs of $10\,{\rm M}_\odot$ in a circular orbit, must have an initial semi-major axis smaller than ~ 0.1 au to merge within a Hubble time. At solar metallicity, the stellar progenitors have about $30\,{\rm M}_\odot$ zero-age main sequence mass and a radius of $\sim 20\,{\rm R}_\odot$, corresponding to ~ 0.18 au. The members of this binary system could not form at such small separation, because they would have collided during the main-sequence phase, even without considering the following giant phase. The progenitors of merging BBHs, thus, must have been born at wider separations, and subsequently brought closer to each other by various mechanisms (Spera et al. 2022).

From the theoretical point of view, two main formation channels have been proposed to explain merging compact objects. In the isolated formation channel (Sect. 1.4.3), two progenitor stars are bound since their formation, evolve, and then turn into (merging) compact objects at the end of their life, without experiencing any kind of external perturbation. This scenario is driven mainly by single and binary stellar evolution processes. In the dynamical formation channel (Sect. 1.6), two compact objects get very close to each other after one (or more) gravitational interactions with other stars or compact objects. This evolutionary scenario is quite common in dense stellar environments (e.g. YSCs, GCs, NSCs), and is driven mainly by stellar dynamics.

1.4.3 The isolated formation scenario

Naively, one could think that if two massive stars are members of a binary system, they will eventually become a BBH and the mass of each BH will be the same as if its progenitor star was a single star. This is true only if the binary system is sufficiently wide (detached binary) for its entire evolution. If the binary members are close enough, they will evolve through several processes which might significantly change their final fate. In particular, the nature and mass of the stellar remnant depends crucially on the final properties of the stellar core, which, in turn, depend on the amount of mass a star has lost or accreted during its life.

Mass transfer

An efficient way to transfer mass from a star to its companion is via Roche lobe overflow. The Roche lobe of a star in a binary system is the maximum equipotential surface around the star within which matter is bound. If the stellar radius is relatively large compared to the size of the binary, the external layers of the star may be stripped out by the gravity of the companion and the centrifugal force of the binary motion.

Roche-lobe overflow can be caused by either the primary star entering the giant phase and increasing in radius, or by the shrinking of the binary orbit due to tides. If the radius of one of the stars exceeds its Roche radius, part of the material will be accreted by the companion star, while some material may be dispersed in a circumbinary disk. If all the

[2]This formula is a zeroth order approximation to describe the evolution of unperturbed BBHs. Also, it assumes that the eccentricity does not change with time.

mass lost by one star is accreted by the other and no mass is dispersed, we are in the case of conservative mass transfer. The material that is lost during non-conservative mass transfer will carry out not only mass but also angular momentum from the binary. If mass transfer is dynamically unstable or both stars overfill their Roche lobe, then the binary is expected to merge – if the donor lacks a steep density gradient between the core and the envelope –, or to enter common envelope (CE) – if the donor has a clear distinction between core and envelope (Mapelli 2021).

Common envelope (CE)

If two stars enter in CE, their envelope(s) stop corotating with their cores. The two stellar cores (or the compact remnant and the core of the star, if the binary is already single degenerate) are embedded in the same non-corotating envelope, which exerts a drag force. Because of the drag, the two cores begin an inspiral phase, during which orbital energy and angular momentum are transferred to the envelope, which heats up and expands. After the inspiral sets in, only two outcomes are possible. If the envelope is too tightly bound, the inspiral continues until the two cores are tidally disrupted and the binary merges into a single star. If, instead, the envelope is ejected, a short-period binary forms (Eggleton 2006).

The most commonly adopted formalism to model common envelope in population-synthes codes is the so-called $\alpha-\lambda$ model, which is based on energy balance considerations (Webbink 1984). The main idea of this approach is to compare the orbital energy of the binary at the onset of CE with the binding energy of the envelope. By comparing these two energies, it is possible to determine whether or not the binary will survive the CE and to estimate the final size of the binary. The model depends on two unknown parameters, α and λ, which parameterize the CE efficiency (i.e. how efficiency orbital energy is used to unbind the envelope) and the envelope binding energy, respectively. The λ parameter measures the concentration of the envelope: the smaller λ, the more concentrated the envelope (Mapelli 2021):

$$E_{\rm env} = \frac{G}{\lambda}\left[\frac{m_{\rm env,1}m_1}{R_1} + \frac{m_{\rm env,2}m_2}{R_2}\right] \tag{1.18}$$

here m_1 (m_2) is the mass of the primary (secondary) member of the binary, and $m_{\rm env,1}$ ($m_{\rm env,2}$) and R_1 (R_2) are the mass of the envelope and the radius of the primary (secondary) member of the binary. The envelope binding energy is then compared to the difference in orbital energy due to the inspiral. The parameter α quantifies the fraction of the removed orbital energy that is transferred to the envelope (Mapelli 2021):

$$\Delta E = \alpha(E_{\rm b,f} - E_{\rm b,i}) = \alpha\frac{Gm_{\rm c1}m_{\rm c2}}{2}\left(\frac{1}{a_{\rm f}} - \frac{1}{a_{\rm i}}\right) \tag{1.19}$$

where $E_{\rm b,i}$ ($E_{\rm b,f}$) is the orbital binding energy of the two cores before (after) the CE phase, $a_{\rm i}$ ($a_{\rm f}$) is the semi-major axis before (after) the CE phase, $m_{\rm c1}$ and $m_{\rm c2}$ are the masses of the two cores. If the primary is already a compact object, $m_{\rm c2}$ is the mass of the compact object.

By setting $\Delta E = E_{\rm env}$, we can derive the value of the final semi-major axis $a_{\rm f}$ for which the envelope is ejected:

$$\frac{1}{a_{\rm f}} = \frac{1}{\alpha\lambda}\frac{2}{m_{\rm c1}m_{\rm c2}}\left[\frac{m_{\rm env,1}m_1}{R_1} + \frac{m_{\rm env,2}m_2}{R_2}\right] + \frac{1}{a_{\rm i}} \tag{1.20}$$

If $a_{\rm f}$ is lower than the sum of the radii of the two cores (or the sum of the Roche lobe radii of the cores), then the binary will merge during CE, otherwise it will survive and eq. 1.20 quantify us the final orbital separation (Claeys et al. 2014).

The $\alpha-\lambda$ model is a very simplistic approach, because it hides behind two parameters the complex physics processes that happen during CE evolution. Because of this, large (and seemingly nonphysical) values of the α parameter in population-synthesis simulations ($\gtrsim 3$) seem to be necessary to match the merger rate of binary NSs inferred by LVK detections (e.g., see Giacobbo & Mapelli 2018).

BBH mergers from isolated binaries

Figure 1.7 illustrates schematically how the evolution of an isolated stellar binary can give birth to merging BHs like GW150914 and other massive BHs observed by the LVK collaboration (Belczynski et al. 2016a).

Initially, the two stars are both on the main sequence. When the most massive one leaves the main sequence, which happens usually on a time-scale of few Myr for massive stars with zero-age main sequence mass $m_{\rm ZAMS} > 30{\rm M}_\odot$, its radius starts inflating and can grow by a factor of a hundreds. The most massive star becomes a giant star with a helium core and a large hydrogen envelope. If its radius equals the Roche lobe, the system starts a stable mass-transfer episode (Sect. 1.4.3). Some mass is lost by the system, some is transferred to the companion. After several additional evolutionary stages, the primary star collapses to a BH (a direct collapse is preferred with respect to a SN explosion if we want the BH to be rather massive). At this stage the system is still quite large (hundreds to thousands of $\rm R_\odot$).

When also the secondary star leaves the mains sequence, growing in radius, the system enters a CE phase (Sect. 1.4.3): the BH and the helium core spiral in. If the orbital energy is not sufficient to unbind the envelope, then the BH merges with the helium core leaving a single BH. In contrast, if the envelope is ejected, we are left with a new binary, composed of the BH and of a stripped naked helium star. The new binary has a much smaller orbital separation (tens of $\rm R_\odot$) than the pre-CE binary, because of the spiral-in. If this new binary remains bound after the naked helium star undergoes a SN explosion or if the naked helium star is sufficiently massive to directly collapse to a BH, the system evolves into a close BBH, which might merge within a Hubble time (Mapelli 2021).

1.4.4 Black holes in the pair-instability mass gap

Theoretical models of single-star evolution predict the existence of a gap in the mass spectrum of compact remnant, which extends from $\sim 60\,{\rm M}_\odot$ to $\sim 120\,{\rm M}_\odot$. The main mechanisms behind the formation of this gap are the pulsational pair-instability supernova (PPISN) and the pair-instability supernova (PISN) (Fryer et al. 2001).

In massive stars, if the core temperature rises above $\sim 7\times10^8$ K, photons become energetic enough to create electron-positron pairs. This process converts energy (gamma photons) into rest mass (electrons and positrons), and thus lowers the radiation pressure, triggering stellar collapse (Rakavy & Shaviv 1967; Fraley 1968). In stars with helium core masses between $\sim 30\,{\rm M}_\odot$ and $\sim 60\,{\rm M}_\odot$, the collapse is reversed by O- or Si- core burning, which shows up as a pulse and makes the core expand and cool. The flash is not energetic enough to disrupt the star but it significantly enhances mass loss, especially from the outermost stellar layers. The core then begins a series of contractions and expansions (i.e.

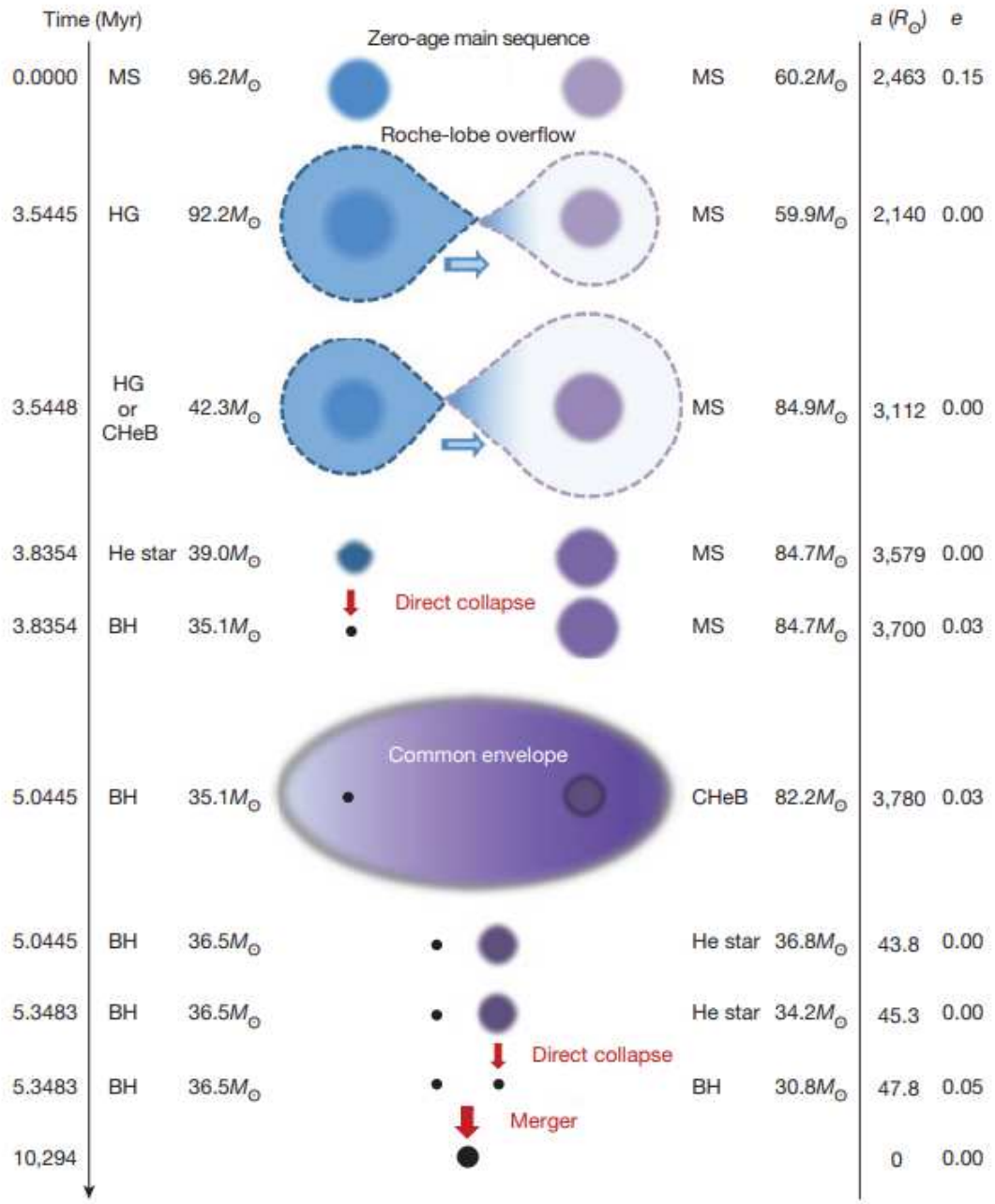

Figure 1.7: Formation and evolution of a binary system that results in a merger with similar masses as GW150914 (Abbott et al. 2016). Legend: MS, main-sequence star; HG, Hertzsprung-gap star; CHeB,core-helium-burning star; BH, black hole; a, orbital semi-major axis; e, eccentricity. Figure from Belczynski et al. (2016a).

PPISN) that continue until the entropy becomes low enough to avoid the pair instability (PI) and stabilize the core until the core-collapse SN explosion. In contrast, in stars with helium core masses between $\sim 60\,M_\odot$ and $\sim 120\,M_\odot$, the first pulse is energetic enough to completely disrupt the entire star (i.e. PISN). Stars with helium cores above $\sim 120M_\odot$ experience a rapid PI-induced collapse but the energy released by nuclear burning is not enough to reverse the collapse before photodisintegration (endothermic) becomes the dominant photon-interaction mechanism (Fryer et al. 2001).

Figure 1.8 shows a typical example of a BH mass spectrum, obtained from a population of single stars, at various metallicities (Spera & Mapelli 2017). The net effect brought about by PPISNe and PISNe is to create a gap in the BH mass spectrum from $\sim 60M_\odot$ to $\sim 120M_\odot$. The values of the lower and upper limit are highly uncertain because they strongly depend on metallicity, on the adopted stellar-wind models, on the boundaries of helium core masses or the occurrence of PPISNe and PISNe, on nuclear reaction rates, on stellar rotation, on the treatment of convection, and on the SN explosion mechanism (Farmer et al. 2020; Mapelli et al. 2021b; Farrell et al. 2021; Belczynski et al. 2020; Costa et al. 2022). Overall, considering all the main known uncertainties so far, the lower limit ranges between $M_{\rm low} \in [40M_\odot; 75M_\odot]$. As for the upper limit, $M_{\rm high}$, the scenario is more complex, and the range for $M_{\rm high} \in [120M_\odot; 200M_\odot]$ (Spera et al. 2022).

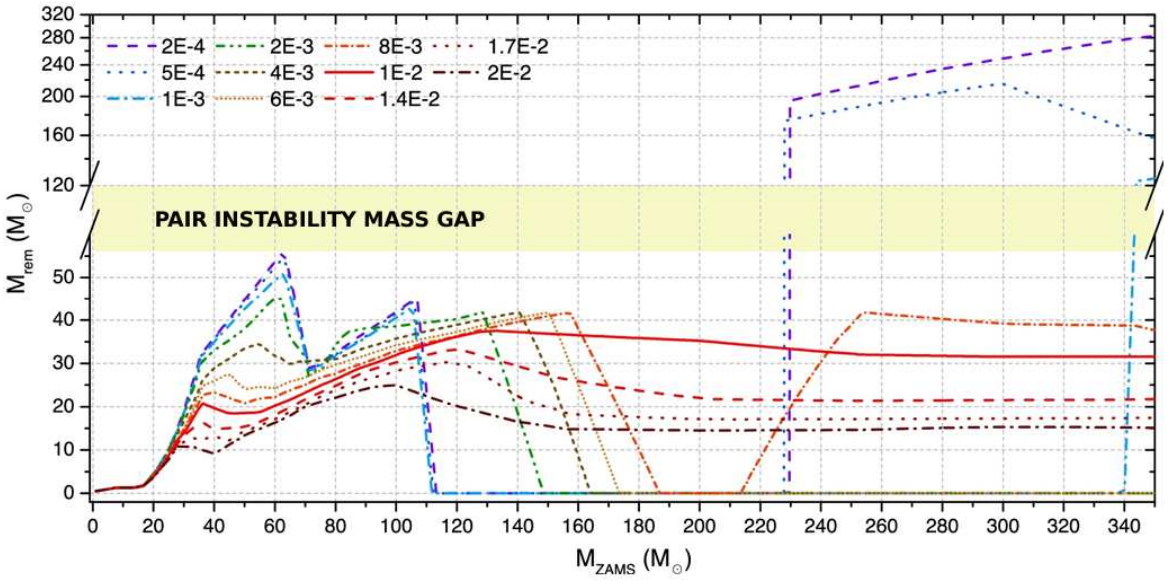

Figure 1.8: Mass of the BH as a function of the zero-age main sequence (here, ZAMS) mass of its progenitor star, for different values of metallicity $Z \in [2 \times 10^{-4}, 2 \times 10^{-2}]$. The shaded yellow area shows the location of the pair-instability mass gap. Figure from Spera & Mapelli (2017).

1.5 Black holes in star clusters

1.5.1 Supernova kicks and black hole retention

Some, if not all, compact objects receive quite high kicks at birth (Gunn & Ostriker 1970). From the theoretical point of view, these kicks are imparted by asymmetries in the SN

ejecta (e.g., Wongwathanarat et al. 2013). Natal kicks can vary from $\sim 10\,\mathrm{km\,s^{-1}}$ to $\sim 1000\,\mathrm{km\,s^{-1}}$, depending mainly on the steepness of the density profile at the outer edge of the stellar core, and on the stochastic variations of non-radial instabilities associated with the SN engine. Thus, shallow (steep) density profiles are more (less) prone to SN shock stalling, thus neutrinos will be able to interact with more (less) material and produce more- (less-)asymmetric ejecta (Spera et al. 2022).

On the observational point of view, most information about supernova kicks come from Galactic pulsars, which are observed to display fairly large spatial velocities, as high as $\sim 1000\,\mathrm{km\,s^{-1}}$. Their three-dimensional speeds are well fit by a Maxwell-Boltzmann distribution with $\sigma_{1\mathrm{D}} = 265\,\mathrm{km\,s^{-1}}$ (Hobbs et al. 2005). Assuming that BHs share the same formation mechanism as NSs and that kicks are driven by the asymmetries in the SN ejecta, BH kicks are expected to be smaller than NSs', with differences coming mainly from the heavier mass of BHs and the smaller amounts of ejecta.

This theoretical argument is poorly supported by observations, because BH kicks lack strong observational constraints. Studies on distances from the Galactic plane (Repetto et al. 2012; Repetto & Nelemans 2015) and on the motions (Atri et al. 2019) of some BH X-ray binaries can only be explained if BHs acquire high kicks at birth. In particular, Atri et al. (2019) suggest that an unimodal Gaussian distribution with a mean of $\sim 100\,\mathrm{km\,s^{-1}}$ is favored to match the observed kicks. In contrast, the recently-discovered massive X-ray-faint binary VFTS 243 can be explained by little or no ejected material or BH kick (Shenar et al. 2022).

Velocity kicks have multiple consequences for the formation of merging compact objects. Besides breaking binaries, they can re-align the binary orbital plane, or misalign it with respect to the stellar spin vectors. In fact, SN kicks can tilt and even flip the orbital plane of the binary, resulting in spin-orbit misalignment (Steinle & Kesden 2021). Also, natal kicks can eject compact objects and binaries from their birth star clusters, depending on the cluster escape velocity. Thus, they have a relevant impact on the BH retention within the cluster (Pavlík et al. 2018). This, in turn, has a fundamental impact on the cluster evolution (Breen & Heggie 2013).

1.5.2 Black hole sub-systems in star clusters

In star clusters, BHs (and even more BBHs), are the most massive objects, and lose energy to the other components as the cluster tends towards energy equipartition (see Sect. 1.3.2). More specifically, the BH component eventually decouples from the bulk of the cluster, and forms a dynamically independent sub-cluster, which is hotter, denser and more compact than the rest of the cluster. Most importantly, the core of this sub-system represents a dynamically active environment where BBHs can efficiently exchange energy and momentum with the single BHs in the sub-system core (Breen & Heggie 2013). Since most BBHs are hard binaries (BHs are among the most massive bodies in star clusters), the net effect of dynamical interactions within the BH sub-system is to extract energy from BBHs. In turn, this energy is conducted via two-body relaxation, and spreads throughout the bulk of the cluster (Hénon 1961; Breen & Heggie 2013).

Since the presence of a BH sub-system provides an additional energy source for the cluster, it accelerates its expansion and dissolution in the tidal field. Figure 1.9 shows the impact of this BH sub-system on the global evolution of star clusters with different tidal radii (Giersz et al. 2019). In particular, it highlights the comparison between two

SN kick prescriptions: in the first, BHs receive the same kicks as NSs (see Sect. 1.5.1), and are thus easily ejected during SN explosions; in the second a fallback mechanism is implemented to reduce the SN kicks for BHs, resulting in a non-negligible retention for these objects. Initially, all the models behave in a similar way, because the cluster mass loss is due to stellar and binary evolutionary processes. When relaxation comes into play and BHs start to segregate, the evolution of the cluster shows a dependency on the strong energy generation by the BH sub-system. In particular, the high flow of escaping stars decreases the cluster mass and, as a consequence, the escape velocity (eq. 1.5). This, in turn, enhances the tidal stripping. The resulting high mass-loss rate removes the cluster from dynamical equilibrium and produces, in the final stages of its life, an abrupt dissolution (Giersz et al. 2019).

1.5.3 Dynamical ejections

During three-body encounters, the difference between the initial and final internal binary energy is redistributed as kinetic energy between the single and binary star, due to momentum conservation. As a consequence, both the star and the binary undergo a recoil, which is generally of the order of few $\mathrm{km\,s^{-1}}$, but can be up to several hundred $\mathrm{km\,s^{-1}}$. The injected kinetic energy might thus be sufficiently high to eject the binary from the core and even from the cluster itself, decreasing the number of BHs within the system. This process, called dynamical ejection, causes the decrease of the BH number shown in Fig. 1.9.

After a BBH forms, it hardens because of dynamical interactions, thus undergoing more and more energetic encounters. When the BBH is tight enough, the energy transferred by the successive three-body encounters will produce a recoil that is high enough to eject it from the cluster. The semi-major axis at which this happens can be estimated by equating the dynamical recoil to the cluster escape velocity (Miller & Hamilton 2002):

$$a_{\rm ej} = \frac{2}{5}\frac{\langle m\rangle^2}{(m_1+m_2)^3}\frac{Gm_1m_2}{v_{\rm esc}^2}. \tag{1.21}$$

When all BHs have the same mass, a BBH ejects on average ~ 4 BHs before ejecting itself (Goodman 1984).

The rate of dynamical ejections has a deep impact on the cluster evolution, as well as on its present-day observed properties. In dense clusters, most BHs are generally ejected before the cluster dissolves, because of their higher interaction rates. Clusters with lower initial densities have instead longer relaxation times, resulting in fewer BH ejections, while tidal stripping of stars (see Sect. 1.3.5) is more efficient. In principle, this could even lead to the formation of star clusters made entirely of BHs (the so-called dark star clusters, Banerjee & Kroupa 2011). Simple two-component models (Breen & Heggie 2013) suggest that in idealized single-mass star clusters that fill their tidal radius, there exists a critical BH mass fraction $f_{\rm BH} \approx 10\%$ at which the mass-loss rate of stars and BHs is the same and $f_{\rm BH}$ remains constant. For higher (lower) $f_{\rm BH}$, stellar mass is lost at a higher (lower) rate by tidal stripping than BH mass is lost by ejections from the core. $N-$body simulations with a realistic mass function suggest that this fraction may be lower, $f_{\rm BH} \approx 2.5\%$ (Gieles et al. 2021).

When the BBH and/or the BH intruder are ejected, they become field objects and cannot participate in the dynamics of the star cluster anymore. Thus, not only does the

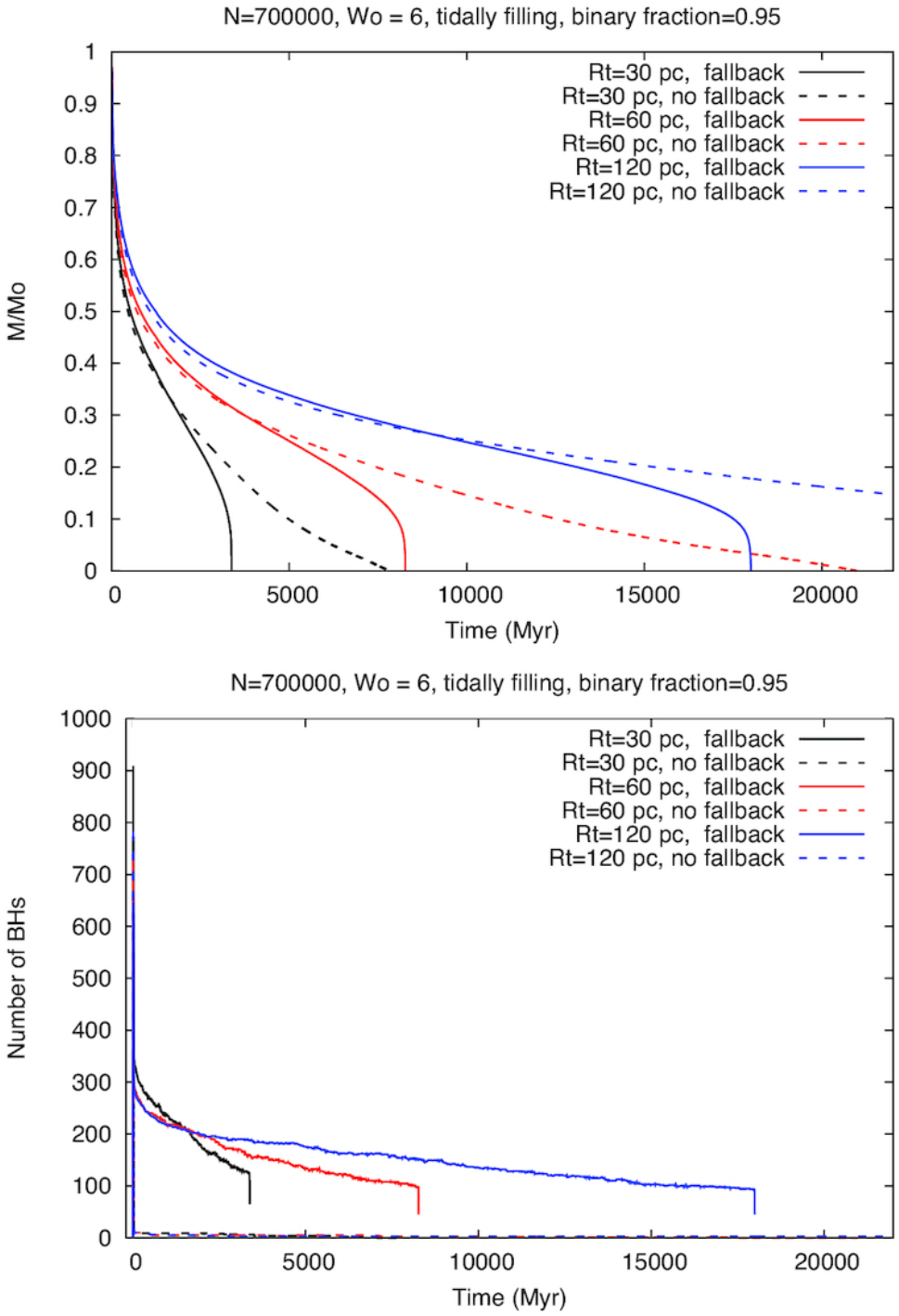

Figure 1.9: Evolution of the fraction of cluster bound mass (top panel) and of the number of BHs (bottom panel) as a function of time for different $r_{\rm t}$ (eq. 1.1) and for SN natal kicks mass fallback set to ON (solid lines) or OFF (dashed lines). Different colours represent different initial tidal radii $r_{\rm t}$ = 30 pc (black), $r_{\rm t}$ = 60 pc (red) line, $r_{\rm t}$ = 120 pc (blue). Figure from Giersz et al. (2019).

ejected BBH stop hardening, but also the ejected intruder loses any chance of entering a new binary by dynamical exchange (see Sect. 1.6). This, in turn, affects the dynamical production of BBH mergers, as described in detail in Sect. 1.6.

1.6 Star clusters as gravitational-wave factories

During a three-body encounter between a hard BBH and an intruder, the BBH semi-major axis generally shrinks because a fraction of its internal energy is redistributed among the interacting bodies (Heggie 1975). Shrinking the semi-major axis of compact object binaries can dramatically shorten their coalescence time for GW emission, which scales as $t_{\rm GW} \propto a^4$ (see eq. 1.17). Thus, the hardening process may be sufficiently effective to harden a BH binary till it enters the regime where GW emission is efficient: a BH binary which is initially too loose to merge may then become a GW source thanks to dynamical hardening.

Another important consequence of three-body encounters is that they tend to excite the orbital eccentricity of binaries. In fact, the probability distribution of binary eccentricities after in dynamically active environments tends to a thermal distribution, $N(e) \propto e$ (Heggie 1975), and can be even super-thermal in the case of low angular momentum encounters (Ginat & Perets 2023). The orbital eccentricity has an even greater impact on the GW coalescence timescale, because, for eccentricities close to 1, the coalescence timescale shortens as $t_{\rm GW} \propto (1-e^2)^{7/2}$ (see eq. 1.17). Although the formation of high-eccentric BBHs is one of the most peculiar imprints of dynamical encounters, by the time they reach the LVK band, GW emission circularizes them. Therefore, most binaries are not expected to have any residual eccentricity at > 10 Hz (Abbott et al. 2016a). Only binaries with an extreme eccentricity ($e_0 > 0.999$) can retain some eccentricity at 10 Hz, but their coalescence time will be extremely small ($\sim$ days).

1.6.1 Exchanges

Dynamical exchanges are three-body encounters during which one of the binary members swaps with the initial single body. Exchanges lead to the formation of new BBHs. This is a very important difference between BHs in the field and in star clusters: a BH which forms as a single object in the field has negligible chances to become member of a binary system, while a single BH in the core of a star cluster has good chances of becoming member of a binary by exchanges (Mapelli 2021).

Statistically, exchanges are expected to produce many more BBHs than they can destroy. As shown in Fig. 1.10, the probability for an intruder to replace one of the members of a binary is ≈ 0 if the intruder is less massive than both binary members, while it suddenly jumps to ≈ 1 if the intruder is more massive than one of the members of the binary (Hills & Fullerton 1980). Since BHs are among the most massive bodies in a star cluster, they are very efficient in acquiring companions through dynamical exchanges (Ziosi et al. 2014). BBHs formed through dynamical exchange will have some distinctive features with respect to those formed through the isolated formation channels.

1. As a consequence of the tendency to acquire massive companions, BBHs formed by exchanges will be (on average) more massive than the isolated ones.

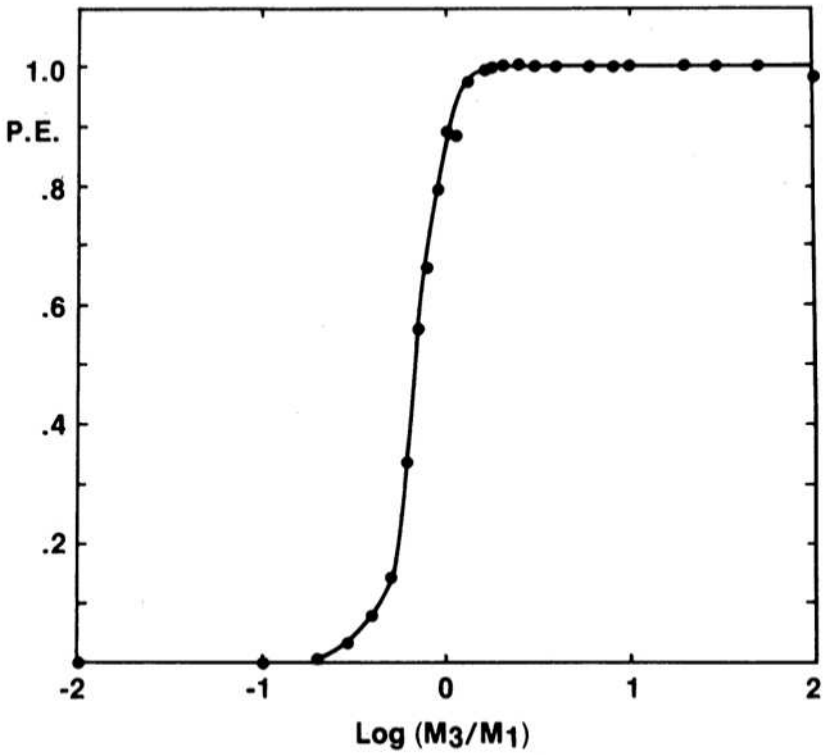

Figure 1.10: Exchange probability, defined as the fraction of post-encounter binaries containing the initial single star, as a function of the mass of the intruder. Figure from Hills & Fullerton (1980).

2. Dynamically-assembled binaries should not have any correlation between the orientation of the BHs spins. We expect that an isolated binary in which the secondary becomes a BH by direct collapse results in a BBHs with aligned spins (i.e. the spins of the two BHs have the same orientation, which is approximately the same as the orbital angular momentum direction of the binary), because tidal evolution and mass transfer in a binary tend to synchronise the spins (Hurley et al. 2002). For dynamically-formed BBHs (through exchange) we expect misaligned, or even nearly isotropic spins, because any original spin alignment is completely reset by three-body encounters (Mapelli 2021).

1.6.2 Star–star collisions

Dynamical interactions within star clusters provide a channel to produce BHs in the pair-instability (PI) mass gap (Sect. 1.4.4). In particular, two mechanisms can lead to the formation of BHs between $60M_\odot$ and $120M_\odot$: star–star collisions and hierarchical mergers.

Direct collisions of stars in dense stellar environments, can lead to large masses, thus filling the PI mass gap (Spera et al. 2019; Di Carlo et al. 2020a). In particular, if a massive star with a well-developed helium core merges with a non-evolved companion (a main sequence or an Hertzsprung-gap star), it might give birth to an evolved star with an over-sized hydrogen envelope. If the helium core remains below $\sim 30\,M_\odot$ and the star collapses to a BH before growing a much larger core and before losing a significant

fraction of its envelope. This scenario, represented in Fig. 1.11, has demonstrated to explain the formation of BHs in the pair-instability mass gap in detailed stellar evolution models (Spera et al. 2019; Renzo et al. 2020; Costa et al. 2022; Ballone et al. 2022).

If such a BH forms from a stellar merger form in the field, it remains a single object and cannot produce any BBH mergers. In contrast, if it forms in a dense stellar cluster, it might capture a new companion through a dynamical exchange, possibly becoming a BBH and, then, producing a BBH merger (Di Carlo et al. 2019, 2020a). In Chap. 4, I will describe in detail the formation of BHs in the PI mass gap in YSCs, where the short relaxation times trigger dynamical interactions and direct collisions between stars when they have not evolved into BHs yet.

1.6.3 Hierarchical mergers

In star clusters, stellar-origin BHs can undergo repeated mergers with other BHs, thus building up to form more massive ones (Miller & Hamilton 2002; Fishbach et al. 2017; Gerosa & Berti 2017; Doctor et al. 2020): this scenario is referred to as hierarchical merger scenario (see Gerosa & Fishbach 2021 for a recent review on this topic).

The hierarchical assembly of BHs is a complex process, because it involves a complex interplay between the properties of the BBH population (mass ratios, spins) and the structure and evolution of the host cluster (escape velocity, central density). In particular, what mainly hampers the formation of hierarchical merger chains is the relativistic kick that the merger remnant receives at birth (e.g., Fitchett 1983; Favata et al. 2004; Campanelli et al. 2007; Lousto & Zlochower 2011). When two BH merge, asymmetric dissipation of linear momentum via GWs imparts a recoil (or "kick") to the post-merger remnant. These merger recoils range from 0 (for the case of highly symmetric configurations) to $\sim 5000\,\mathrm{km\,s^{-1}}$, depending on the BBH mass ratio and on the spins of the two BHs. In order to produce hierarchical mergers, the escape speed of the host cluster needs to be larger than the typical kick imparted to the BH remnant. Due to their high escape velocity ($v_{\rm esc} \gtrsim 100\,\mathrm{km\,s^{-1}}$, NSCs are more likely to retain BBH merger remnants than other star clusters (e.g., Antonini & Rasio 2016a; Arca Sedda & Benacquista 2019; Arca Sedda et al. 2020), and to lead to the production of hierarchical mergers, as shown in Fig. 1.12. The BH growth can become substantial enough to fill the PI mass gap, and even to lead to the formation of intermediate-mass BHs (IMBHs) (Antonini et al. 2019; Mapelli et al. 2021a).

The process of hierarchical mergers involves a large number of parameters for both the compact objects' populations and the stellar clusters. SN kicks have an impact on the BH retention fraction (see Sect. 1.5.1). Also, both spins and mass ratios play a fundamental role in determining the magnitude of the relativistic kicks. Furthermore, the cluster mass, density (and thus escape velocity) and metallicity affect the hardening and the dynamical ejection of BBHs. Exploring this huge parameter space is not feasible by means hybrid Monte-Carlo and/or N-body codes. To overcome this difficulty, a number of semi-analytic codes has been developed, to investigate hierarchical mergers, by probing the parameter space including BBH masses, spins, delay times, orbital eccentricities, and star cluster properties, e.g. `cBHBd` (Antonini et al. 2019; Antonini & Gieles 2020b; Antonini et al. 2022), `Fastcluster` (Mapelli et al. 2021a, 2022), `B-POP` (Arca Sedda et al. 2021), and `Rapster` (Kritos et al. 2022b,a).

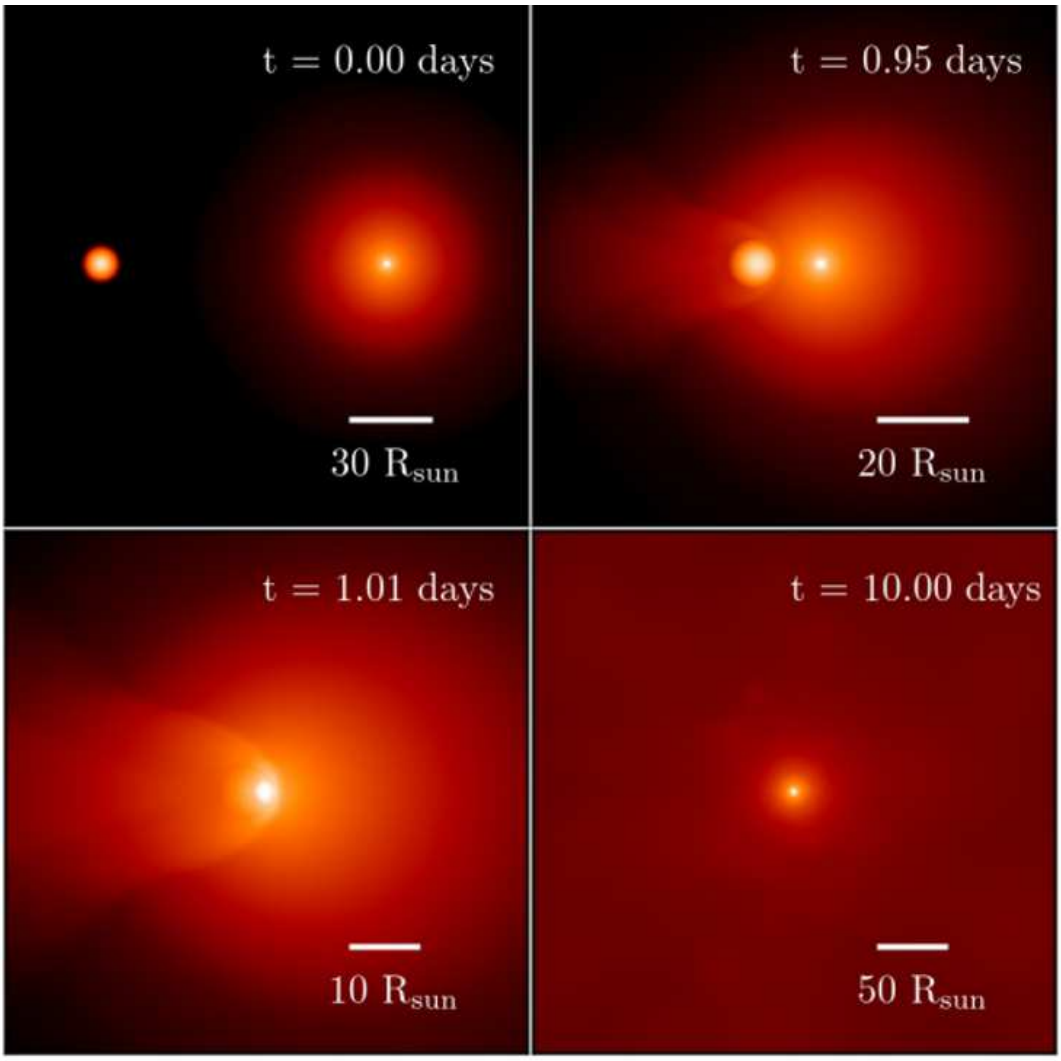

Figure 1.11: Column mass density maps of a edge-on collision between a core helium burning star and a main sequence star, from the beginning to 10 days of evolution. As the two stars move on their radial orbit, the secondary star enters the much larger envelope of the primary, and gets disrupted when reaching the inner parts of the core helium burning star after about 1 day of evolution. At the end of the simulation, the stellar remnant relaxes to a much larger envelope, generated by the inflation of the outer layers of the primary star. Figure adapted from Ballone et al. (2022).

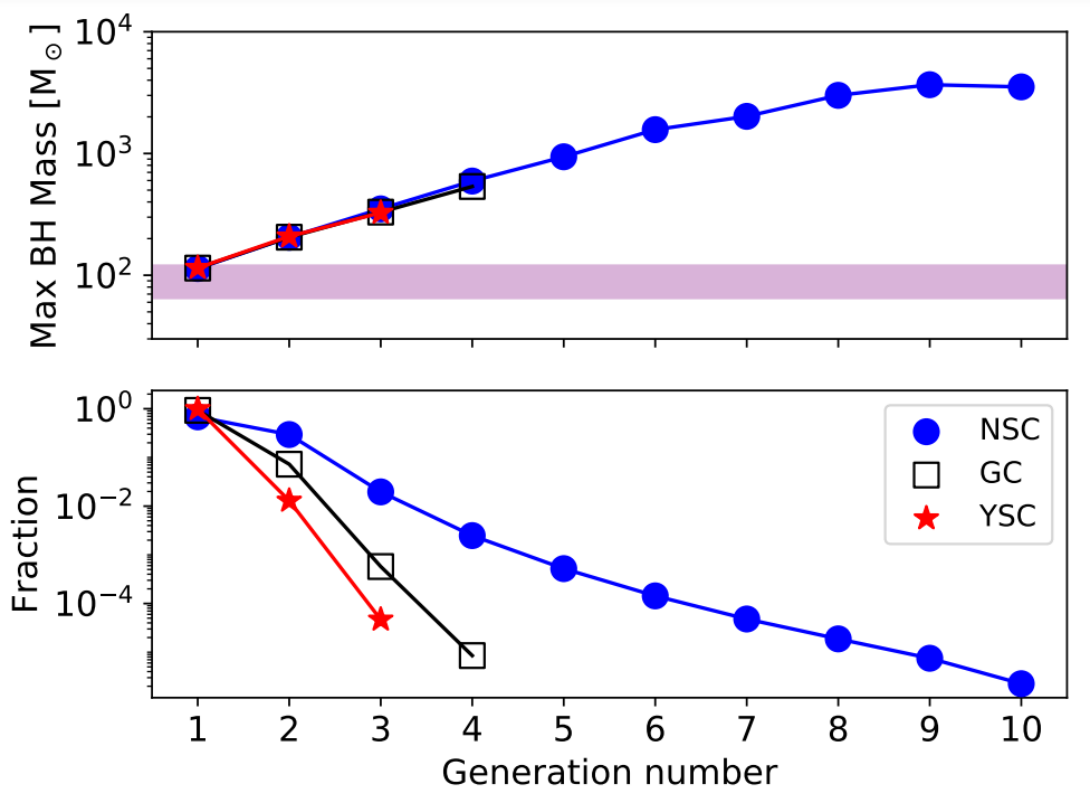

Figure 1.12: Upper panel: maximum merger remnant mass in each generation as a function of the generation number (where 1 means first generation). Lower panel: Fraction of mergers belonging to a given generation with respect to all BBH mergers in the considered model as a function of the generation number. Figure from Mapelli et al. (2021a).

Thesis outline

This thesis is organized as follows:

In Chapter 2, I introduce a new approach to generate many sets of initial conditions from a given set of star masses, positions and velocities from a hydro-dynamical simulation, which incorporates the observed complexity of star forming regions. This method is based on a hierarchical clustering algorithm that learns a tree representation of the cluster phase-space. This tree encodes instructions to generate new realizations, by simply modifying the initial branches of the tree (encoding the relations between the biggest sub-clumps), while preserving the characteristics of the small scale structure responsible for most of the dynamical evolution. I investigate the mass spectrum, velocity distribution, and fractal scheme of the newly-generated clusters. Finally, I compare their evolution at different scales to that of the original cluster.

In Chapter 3, I address the impact of original binary populations on the evolution of young star clusters. In particular, I generate initial conditions from hydro-dynamical simulations of collapsing molecular clouds. Then, I introduce a new algorithm to associate a primordial binary star population to these stellar distributions. Through this study, I quantify how original binaries affect the global evolution of the cluster. Also, I investigate how star clusters produce dynamical populations of binaries, depending on their global properties. Finally, I compare the evolution of star clusters generated through hydro-dynamical simulations to that of spherical, more idealized models.

In Chapter 4, I explore how dynamical interactions within young star clusters affect the properties of BBH mergers. In particular, I compare the populations of BBH in two different star cluster families: low-mass ($\sim 500 - 800\,\mathrm{M}_\odot$) and relatively high-mass star clusters ($\geq 5000\,\mathrm{M}_\odot$). I explore how the tidal disruption of the cluster quenches the formation and hardening of BBHs. Also, I investigate how star-star collisions, which are triggered by the high initial densities of young star clusters, can lead to the formation of BHs in the PI mass gap and of IMBHs.

In Chapter 5, I explore the process of hierarchical mergers in globular clusters. To do this in a realistic framework, I implemented the relevant processes that drive the evolution of globular clusters, namely stellar evolution, two-body relaxation, and tidal stripping from the host galaxy, in the semi-analytic code FASTCLUSTER. I investigate how these processes

quench the production of hierarchical mergers. Also, I study how the BH spins and the BBH orbital angular momentum build up to increase the BH spins at higher generations.

In Chapter 6, I look for signatures of the presence of BHs the Hyades cluster. More specifically, I compare a large suite on $N-$body models, run with the precise intent to reproduce the present-day state of the Hyades, to accurate radial density profiles obtained from *Gaia*. I study how the presence of BHs affect the radial distribution of visible stars, with particular attention to the most massive ones, which cannot segregate at the cluster center because of the presence of a heavier component. Also, I study the period distribution of dynamically formed BH-star binaries. Finally, I look for stars with potential BH companions through large *Gaia* astrometric and spectroscopic errors.

Finally, Chapter 7 summarizes my conclusions and outlook.

Chapter 2

Hierarchical generative models for star clusters from hydro-dynamical simulations

Based on:
Torniamenti S., Pasquato M., Di Cintio, P., Ballone, A., Iorio G., Artale M. C., Mapelli M.,
"Hierarchical generative models for star clusters from hydrodynamical simulations", 2022, MNRAS 510, 2097

Abstract

Star formation in molecular clouds is clumpy, hierarchically subclustered. Fractal structure also emerges in hydro-dynamical simulations of star-forming clouds. Simulating the formation of realistic star clusters with hydro-dynamical simulations is a computational challenge, considering that only the statistically averaged results of large batches of simulations are reliable, due to the chaotic nature of the gravitational N-body problem. While large sets of initial conditions for N-body runs can be produced by hydro-dynamical simulations of star formation, this is prohibitively expensive in terms of computational time. Here we address this issue by introducing a new technique for generating many sets of new initial conditions from a given set of star masses, positions and velocities from a hydro-dynamical simulation. We use hierarchical clustering in phase space to inform a tree representation of the spatial and kinematic relations between stars. This constitutes the basis for the random generation of new sets of stars which share the clustering structure of the original ones but have individually different masses, positions, and velocities. We apply this method to the output of a number of hydro-dynamical star-formation simulations, comparing the generated initial conditions to the original ones through a series of quantitative tests, including comparing mass and velocity distributions and fractal dimension. Finally, we evolve both the original and the generated star clusters using a direct N-body code, obtaining a qualitatively similar evolution.

keywords: ISM: kinematics and dynamics – open clusters and associations: general – ISM: clouds – methods: numerical – methods: statistical

2.1 Introduction

A large fraction of star formation happens in clusters (Lada & Lada 2003; but see also the recent findings by Reina-Campos et al. 2019a and Ward et al. 2020), which are are clumpy and hierarchically sub-structured (Larson 1995; Bastian et al. 2009; Dib & Henning 2019). Young star clusters often show signatures of fractality (Cartwright 2009; Kuhn et al. 2019), complex motions between sub-clumps (Cantat-Gaudin et al. 2019), and possibly rotation (Hénault-Brunet et al. 2012). In addition, the early expulsion of gas due to stellar winds and supernova explosions brings young clusters out of dynamical equilibrium, causing an expansion phase (Hills 1980; Goodwin & Bastian 2006; Baumgardt & Kroupa 2007; Pfalzner 2009). The comprehension of the early evolution of star clusters is of fundamental importance to interpret the later phases of their life. For example, Corsaro et al. (2017) have shown that the rotation signature from the parent molecular cloud persists in the alignment of stellar spins in some open clusters, even today. Rotation in young and open star clusters is confirmed by numerical simulations (e.g., Lee & Hennebelle 2016; Mapelli 2017; Ballone et al. 2020). Also, observations of globular clusters show signatures of rotation, sometimes with significant dynamical effects (Bianchini et al. 2013; Fabricius et al. 2014; Ferraro et al. 2018; Kamann et al. 2018; Dalessandro et al. 2021) that may have been imprinted in the first phases of their evolution.

Gravitational $N-$body simulations are a key tool to model the early star cluster evolution, but they often start from rather idealized initial conditions, sampled from equilibrium models, such as Plummer (1911) or King (1966) models. Even though more sophisticated models are available (e.g., Lynden-Bell 1962; Michie & Bodenheimer 1963; Prendergast & Tomer 1970; Wilson 1975; Bertin & Stiavelli 1984; Lupton & Gunn 1987; Trenti & Bertin 2005; An & Evans 2006; Varri & Bertin 2012; Gieles & Zocchi 2015; Daniel et al. 2017; Claydon et al. 2019), these were developed with the goal of describing the current, quasi-equilibrium state of star clusters, and do not perform well in describing the early and out-of-equilibrium structure of the clusters. Thus, by design, they bear little resemblance to observed original conditions in embedded clusters.

A seemingly obvious but computationally demanding way to generate realistic initial conditions for star clusters is to run suites of hydro-dynamical simulations, coupled with appropriate recipes for handling star formation and other sub-grid physics (e.g., Klessen & Burkert 2000; Bonnell et al. 2003; Bate 2009b; Federrath 2013; Krumholz et al. 2012; Dale et al. 2015; Fujii & Portegies Zwart 2016; Geen et al. 2016; Seifried et al. 2017; Zamora-Avilés et al. 2019; Lee & Hennebelle 2019; Wall et al. 2019). Despite these efforts, large sets of simulations including all the relevant physics are at present hard to come by, notwithstanding ever-advancing hardware capabilities. This is compounded by the fact that $N-$body simulations, even direct-summation ones, eventually diverge from the true solution of the $N-$body problem for most initial conditions due to numerical errors and the chaotic nature of the problem (e.g. see Goodman et al. 1993; Hemsendorf & Merritt 2002; Kandrup & Sideris 2003; Boekholt & Portegies Zwart 2015; Di Cintio & Casetti 2019, 2020; Manwadkar et al. 2020; Wang & Hernandez 2021 and references therein), with the consequence that only ensemble-averaged results are considered reliable within the current consensus. To obtain such averages, multiple $N-$body runs are needed, each with its own initial conditions.

The usage of clustering algorithms is widespread in cosmology, where different methods have been developed to identify over-dense gravitationally bound systems (i.e., groups

or dark matter haloes and subhaloes). There is a huge variety of group-finding algorithms, which perform clustering in different ways. For example, density-peak locators and spherical over-density finders identify density peaks in the particle distribution and draw spheres of decreasing density around them, down to a density threshold (see, e.g., Press & Schechter 1974). Direct particle collectors, instead, connect particles based on a linking length criterion. Such scheme is the basis of the friend-of-friends prescription, which is used in the context of halo-finding in cosmological simulations (Davis et al. 1985) and in galaxy clusters from observational data (Murphy et al. 2012; see also Feng & Modi 2017 and references therein). Other group finders extend these two approaches to include particle velocity information (see, e.g., Diemand et al. 2006; Maciejewski et al. 2009).

Here, we adopt a hierarchical clustering algorithm. As opposed to the aforementioned algorithms, hierarchical clustering does not rely on the definition of a density threshold or a length scale, but is provided with a definition of similarity between groups. In particular, it proceeds in a hierarchical way, by connecting the most similar pair of clusters, starting from individual instances, until a certain number of groups is reached. This hierarchical construction allows not only to identify over-densities in the distribution of stars, but also to draw information about the structure of star systems at different scales. New stellar clusters can thus be obtained by modifying selected nodes in the hierarchical structure, depending on the properties we want to preserve or modify.

Our generative model is meant to produce new large-scale distributions of sink particles, by preserving the properties that make them so realistic, such as their complex fractal structure. The goodness of our method is evaluated by comparing the fractal structure of the new realizations to that of the original cluster. Also, we check if the new velocity distributions are consistent with the original distribution. Finally, we run N-body simulations of the newly generated clusters to test if they are consistent with the stochastic fluctuations of the original simulations.

The paper is organized as follows. In Section 2.2, we recap the properties of the hydrodynamical simulations we used to generate our original initial condition sets; Section 2.3 presents our approach for generating new realizations, while in Section 2.4 we describe our results and run various checks to compare the generated realizations to the original simulations. In Section 2.5, we discuss and draw conclusions.

2.2 Smoothed-particle hydro-dynamical simulations

2.2.1 Initial conditions and simulation set-up

As a starting point for this work, we used the sink particles from 10 smoothed-particle hydro-dynamics (herafter SPH) simulations of molecular clouds performed by Ballone et al. (2020) using the GASOLINE2 code (Wadsley et al. 2004, 2017). In the following, we may refer to these sink particles as 'stars' for convenience.

The initial conditions of the SPH simulations are spherical molecular clouds with total gaseous mass in the range $10^4 \leq M_{\rm mc}/{\rm M}_\odot \leq 10^5$ (see the last column of Table 2.1), uniform temperature $T_0 = 10$ K and uniform density $\rho_0 = 2.5 \times 10^2$ cm^{-3}. All runs have a fixed number of initial SPH particles equal to 10^7, corresponding to a gas mass resolution of 10^{-3} to 10^{-2} M$_\odot$, depending on the cloud mass. Stars form during the simulation by means of a sink particle algorithm based on the same prescriptions as Bate et al. (1995). The spatial resolution (kernel size) of the simulation can get as small as 0.001 pc in the

densest regions.

In order to induce a non-isotropic evolution, the SPH gas particles are initially given a turbulent, divergence-free, Gaussian random velocity field with a different random seed for each simulation of the set, following a Burgers (1948) velocity power-law spectrum with index -4 (Bate 2009a). With respect to the classical Kolmogorov (1941) power spectrum (with index $-11/3$), the Burgers power spectrum better matches turbulence in compressive flows, where shocks are present (Federrath 2013). The clouds are in an initial marginally bound state, so that their initial virial ratio $\alpha_{\rm vir} \equiv 2K/|W| = 2$, where K and W are the gas kinetic and potential energy, respectively.

During the hydro-dynamical simulation, the gas equation of state has been set to be adiabatic, while radiative cooling by dust has been modeled as in Boley (2009) and Boley et al. (2010). The amount of energy lost by cooling was calculated through the divergence of the heat flux

$$\nabla \cdot F_{\rm cool} = -\frac{(36\pi)^{1/3}\sigma(T^4 - T_{\rm irr}^4)}{s(\Delta\tau + 1/\Delta\tau)}. \tag{2.1}$$

In the Equation above, σ is the Stefan-Boltzmann constant, T the gas temperature, $T_{\rm irr}$ the irradiation temperature, $s = (m/\rho)^{1/3}$ and $\Delta\tau = s\,k\,\rho$, where m and ρ are the gas particle mass and density and k is the local opacity. The dust-to-gas ratio has been fixed to a constant value for each different dust species. For k, the adopted Planck and Rosseland dust opacities are taken from D'Alessio et al. (2001). The irradiation temperature, which represents the minimum temperature allowed by the dust that acts as a thermostat for the gas, is set to $T_{\rm irr} = 10\,{\rm K}$.

No stellar feedback was included in this set of simulations, and we simply decided to assume that our clusters are the result of instantaneous gas removal at 3 Myr after the beginning of the hydro-dynamical simulation to roughly simulate the effect of the first supernova explosions. Indeed, Dale et al. (2015) have shown that the pre-supernova gas removal is expected to play a minor effect on the survival and dynamics of stellar clusters and we also checked that at 3 Myr the gas accounts for a small fraction of the mass where most of the stellar mass is residing. Furthermore, at 3 Myr all the clouds converted about 30-40% of their gas mass into sink particles, in agreement with previous hydro-dynamical simulations showing that stellar feedback should lead to a maximum star formation efficiency of about this amount (e.g., Vázquez-Semadeni et al. 2010; Dale et al. 2015; Gavagnin et al. 2017; Li et al. 2019). For more details on such choices, we refer the reader to Ballone et al. (2020).

2.2.2 Structural properties of the SPH simulations

Independently of the specific initial value of $M_{\rm mc}$, our SPH simulations present a clumpy structure with $N_{\rm s} \approx 3 \times 10^3$ stars[1], organized in a maximum of $N_{\rm c} = 9$ main sub-clumps for `m7e4` to a minimum of 2 for `m4e4`. Sub-clumps are identified heuristically as groups of neighbouring stars containing more than $0.05\,N_{\rm s}$, which self potential energy exceeds that of the rest of the system. Figure 2.1 shows the $x-y$, $y-z$ and $z-x$ projections of the stars position on the three coordinate planes for the system `m1e4`, with their masses m

[1]The approximately constant value of $N_{\rm s}$ follows from the fact that the star formation efficiency is roughly independent of $M_{\rm mc}$ (see Table 1 in Ballone et al. 2020). The star formation efficiency is indeed rather dictated by the physical processes involved in the simulations, which, in all cases, start from the same values of cloud temperature and density.

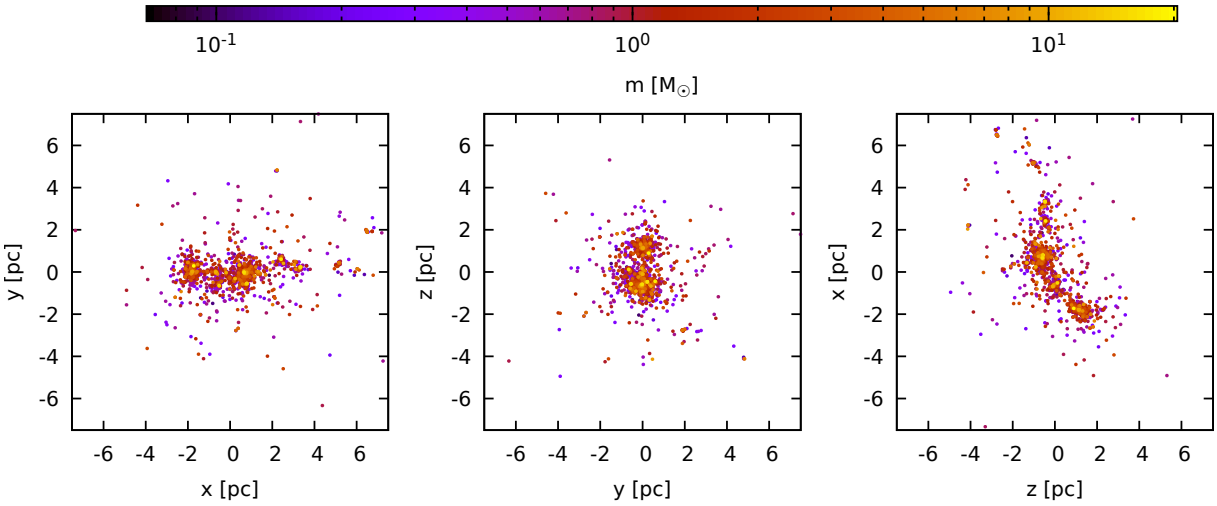

Figure 2.1: From left to right, projections in the $x-y$, $y-z$ and $z-x$ planes of the end state of the `m1e4` simulation. The colour map marks the mass of the individual stars in units of $M_\odot$.

shown in colour. We find a rather prominent primordial mass segregation, with heavier stars typically well within the central regions of the main clumps and lighter stars at larger distances from the geometric centers of such subsystems. All systems are above the virial condition, with $\alpha_{\rm vir}$ ranging from 1.19 for the `m1e4` case, to 1.69 for `m6e4`.

In order to quantify the properties of the end states of the SPH simulations, we have evaluated their distributions of inter-particle distances $f(d)$, mass spectra $f(m)$, and velocity distributions $f(v)$. Figure 2.2 shows these distributions for the sink particles of the simulations `m1e4`, `m3e4`, `m5e4`, `m7e4` and `m9e4`. The distribution of inter-particle distances shows a quite complex structure with several slope changes. The clumpy structure of the particles' spatial distribution gives rise to several peaks in $f(d)$, corresponding to the distances between the clumps themselves. For the specific case of `m1e4`, the peaks are located roughly at 0.1, 0.45, 1.75 and 3 pc (as highlighted by the vertical dotted lines), that can be identified as the distances between the approximate centers of the main clumps of the particles shown in Fig. 2.1.

The mass spectra of sink particles approximately follow the same power-law structure between a low-mass and a high-mass cut-off. The differences in the lower mass limit are due to the different mass resolution of the hydro-dynamical simulations, which are initialized with different total masses but the same number of particles, as explained in Sect. 2.2.1. At higher masses, where the physical processes involved in the simulation become the dominant factor in shaping the mass function, all the spectra recover the same slope. We have fitted the numerically recovered mass spectra with the *bona-fide* function:

$$f(m) = \frac{C}{(m^2 + m_*^2)^{\gamma/2}}, \tag{2.2}$$

where C is a normalization constant, m_* is a scale mass, that for the explored systems is always in the range between 0.8 and 4 $M_\odot$, while exponent γ ranges from ≈ 1.8 to ≈ 2.3.

The velocity distributions $f(v)$ do not show a relevant dependence on the specific initial value of $M_{\rm mc}$, as shown in the right hand panel of Fig. 2.2. Qualitatively, the velocity distribution is well described by a Maxwell-Boltzmann distribution from $v = 0$

Table 2.1: Properties of the end states of the SPH simulations of Ballone et al. (2020).

Name	N_s	N_c	α_{vir}	γ	M_{sink} [$M_\odot$]	M_{mc} [$M_\odot$]
`m1e4`	2523	6	1.19	2.30	4.22×10^3	10^4
`m2e4`	2571	4	1.32	2.12	6.69×10^3	2×10^4
`m3e4`	2825	5	1.48	2.20	1.03×10^4	3×10^4
`m4e4`	2868	2	1.47	2.17	1.44×10^4	4×10^4
`m5e4`	2231	4	1.47	1.80	1.41×10^4	5×10^4
`m6e4`	3054	5	1.69	2.15	2.04×10^4	6×10^4
`m7e4`	4214	9	1.50	2.20	3.15×10^4	7×10^4
`m8e4`	2945	6	1.60	1.86	2.83×10^4	8×10^4
`m9e4`	3161	4	1.52	1.90	3.05×10^4	9×10^4
`m1e5`	3944	6	1.46	2.20	3.80×10^4	10^5

After the name of each simulation (Col. 1), we report the number of stars generated (Col. 2), the number of macroscopic subclumps (Col. 3), the virial ratio ($\alpha_{vir} \equiv 2K/|W|$, Col. 4), the γ coefficient of the mass-spectrum fitting function of (Eq. 2.2, Col. 5), the total mass of the stars (Col. 6), and the mass of the parent molecular cloud (Col. 7).

to 5 km s^{-1} (value corresponding to the peak of $f(v)$) and then shows a v^{-3} power-law trend. The properties of the SPH simulations are summarized in Table 2.1.

2.3 Methods

In the following, we describe our new procedure to build a generative model of star cluster initial conditions. In principle, a generative model's goal is to learn a representation of an intractable distribution given an usually finite number of samples. The generator typically maps from a latent domain on which a simple distribution is defined, such as a multivariate Gaussian on R^n, to the complex data domain (e.g. Ruthotto & Haber 2021). Recently, most of the interest in generative models is driven by deep learning approaches, such as generative adversarial networks (Goodfellow et al. 2014). However, in principle, much simpler models such as hidden Markov models (Rabiner & Juang 1986; Eddy 2004) or grammars (e.g., Chomsky 1959; Jelinek et al. 1992; Beaumont & Stepney 2009) meet the definition of generative model in the broader sense defined above. The latter have proved useful in the description and generation of objects displaying fractal structure, as in the case of Lindenmayer systems applied to plant growth (Lindenmayer 1968a,b; Prusinkiewicz & Hanan 2013).

Our generative approach focuses on reproducing the complex fractal structure of embedded star clusters from hydro-dynamical simulations (see, e.g., Fig 4 in Ballone et al. 2020) by capturing the relations between sub-clusters at different scales through a hierarchical clustering algorithm. This will eventually allow us to generate new realizations by modifying their macro structure, i.e. the relations between large sub-clusters. The parameters that characterize the relevant properties of these clumps and their relations can be treated as the latent domain of our generative model.

We proceed in two steps. First, we use a hierarchical clustering algorithm to identify clumps of stars at different scales in the phase space of the original hydro-dynamical simulation output. The clumps are organized by the algorithm into a hierarchical tree $\mathcal{T}$, where the root node contains the whole set of stars and each subsequent node represents a

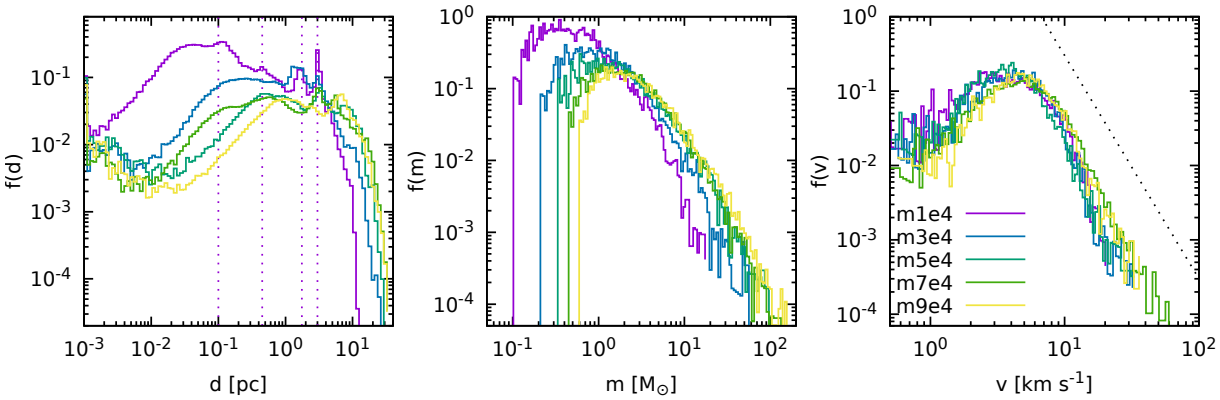

Figure 2.2: Distributions of inter-particle distances $f(d)$ (left-hand panel), mass spectra $f(m)$ (middle panel), and velocity distribution $f(v)$ (right-hand panel) for the sink particles taken from the simulations `m1e4`, `m3e4`, `m5e4`, `m7e4`, `m9e4`. The vertical dotted lines in the left-hand panel mark the position of the main peaks of $f(d)$, corresponding to the distances between the main sub-clusters, for the `m1e4` case. The thin dotted line in the right-hand panel marks the v^{-3} power-law trend of the velocity distributions.

two-way split with each branch being a clump of stars, down to the leaf nodes representing individual stars. For each node $\mathcal{T}_i$, we describe the relevant physical properties of the cluster in terms of the distance vector between the centers of mass of the clumps $\mathbf{l}_i$, their relative velocity vector $\mathbf{u}_i$, and the mass ratio between the two clumps. To describe how the mass is split at each node we refer to q_i, defined as the ratio between the lightest of the two resulting groups and the total mass of the node. With this definition, mass ratios fall between 0 (maximally unequal split) and 0.5 (equal-mass split). The description of the star clusters in terms of the hierarchical clustering algorithm is given in Sect. 2.3.2, but its goal in short is to capture structure as a function of scale, similarly to what was done in, e.g., Elmegreen et al. (2006) by applying smoothing kernels of different sizes.

Second, we generate a new realization of particle positions and velocities by placing clumps of stars (and sub-clumps down to the individual stars) in phase space. To build a new realization of total mass M (details in Sect. 2.3.3), we start with one particle at rest in the origin of our coordinate system, initially containing the total mass of the cluster M. Then, we iteratively split it into new particles and place them, at each step i, at a distance $\mathbf{l}_i$ from each other, moving with relative velocity $\mathbf{u}_i$. The relevant variables $\mathbf{l}_i$, $\mathbf{u}_i$, and the relevant mass ratio q_i are taken from the tree $\mathcal{T}$ except for the first step(s), which are drawn from a tree $\mathcal{T}'$ built on a different simulation. While this does not guarantee that the outcome will be described by a tree with statistical properties that match those of $\mathcal{T}$, it is at least heuristically convincing in the case of very hierarchical distributions. Moreover, we will check ex post that the realizations generated in this way have a set of desirable properties with respect to the original cluster. The details about the generative procedure are given in Sect. 2.3.3.

2.3.1 Hierarchical clustering

Hierarchical clustering algorithms arrange data into a tree-like structure representing nested groups, capturing clustering structure at different scales. In particular, we use an agglomerative clustering algorithm (see the chapter on AGNES in Kaufman & Rousseeuw

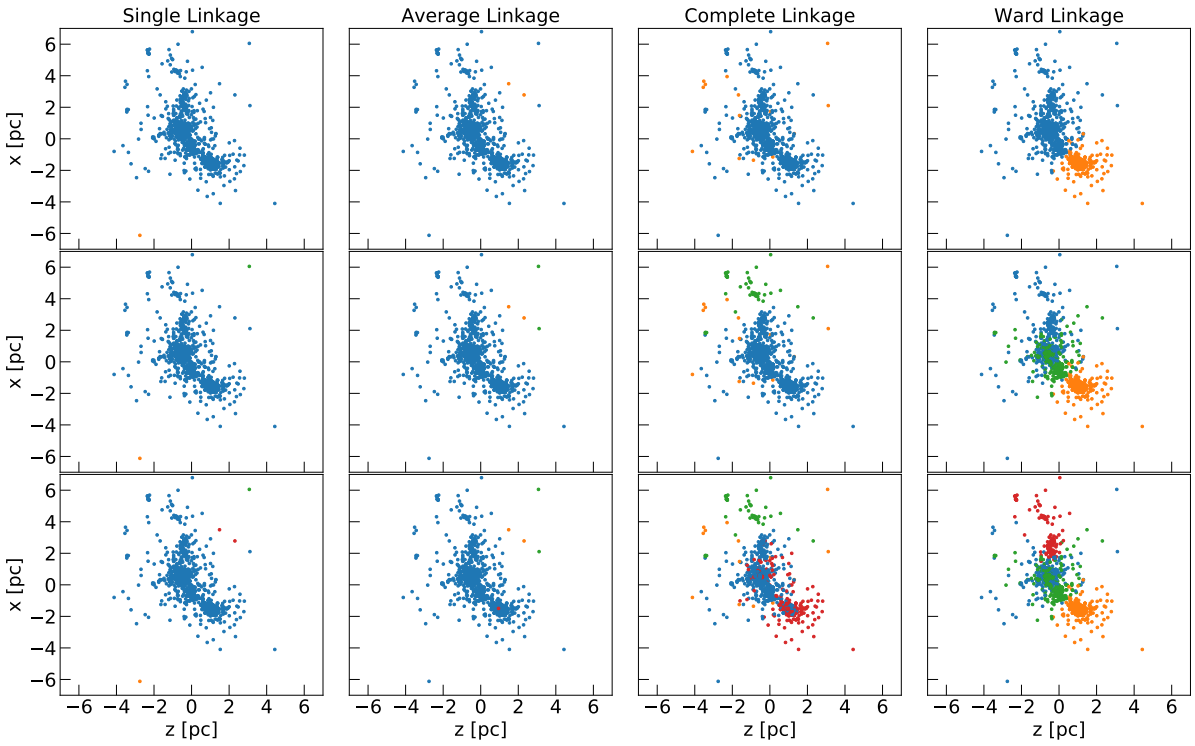

Figure 2.3: First nodes from the trunk in the hierarchical tree for the `m1e4` simulation, obtained by considering different linkages: single (first column), average (second column), complete (third column), and Ward (last column) linkage. The panels in the first row show the first node of the tree, that splits the sink particles of the simulation into two groups (blue and orange). In the second node, the blue group is split further into two subgroups (blue and green, panels in the second row). The third node splits the blue group into the blue and the red groups (panels in the lower row).

1990). This means that the tree-like hierarchy of clusters is built from the bottom up: the algorithm starts from individual points, and merges the most similar ones into clusters until some stopping criterion is satisfied (e.g., until only a specified number of clusters are left). This way of proceeding can be thought as drawing a tree with a branch for every pair of clusters that merge[2]. A dendrogram can be used to display the resulting tree structure, with leaf nodes corresponding to individual points and the root corresponding to the whole data set. We refer the interested reader to Pasquato & Milone (2019) for an illustration of this and other clustering algorithms in an astronomical context. Here, we selected this algorithm because it is well suited for studying the complex structure of the hydro-dynamical simulations described in Section 2.2, since it is informative on very different scales and it can capture clusters (and sub-clusters) of various sizes. We use the implementation offered by the SCIKIT-LEARN library (Pedregosa et al. 2011)[3].

[2]The procedure of drawing a hierarchy of merging sub-structures may recall the merger tree history, which is used in cosmology to track the assembly of sub-structures across time (see, e.g., Rodriguez-Gomez et al. 2015). Agglomerative clustering algorithms, however, do not imply any evolution in time, but use the tree-like structure to identify groups of instances at different scales.

[3]The details about the implementation of the algorithm can be found at this link.

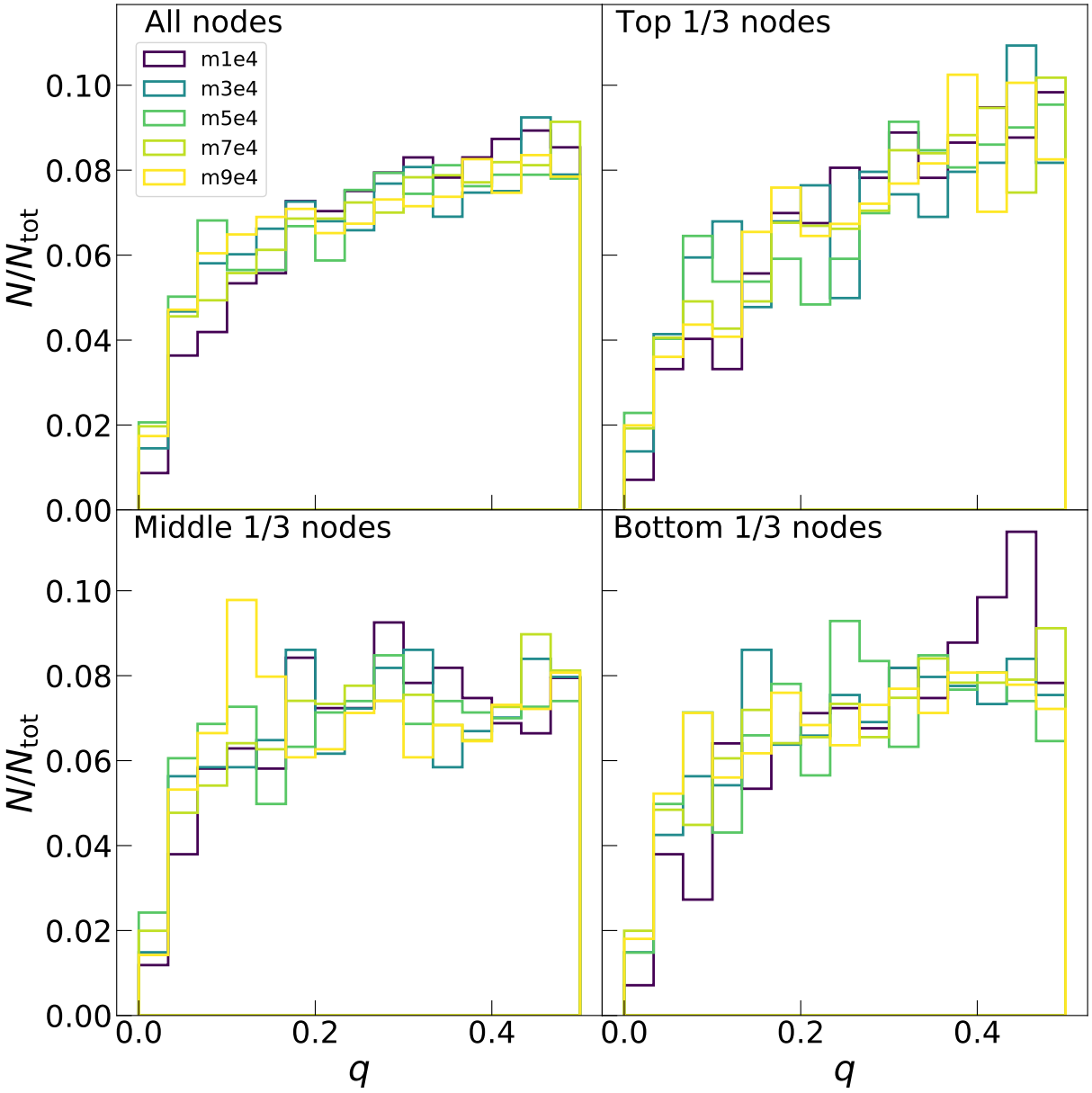

Figure 2.4: Distribution of the mass of the lightest of the two resulting groups at any given split, in units of the parent group. The top left panel shows the distribution calculated for all nodes in the learned tree. The top right panel shows the distribution for the top 1/3 of the nodes from the root (big clumps), the bottom left for the middle 1/3 of the nodes (intermediate-size clumps), and the bottom right for the lower 1/3 of the nodes (small clumps to individual stars).

Linkage

Moving towards the root of the tree, an agglomerative clustering algorithm merges at each node either two groups with each other or a lone point into a group. This process is based on a notion of (dis)similarity between groups which may be defined in multiple ways, or linkages. We considered four different linkages and evaluated their performance in clustering the sink particle spatial distribution.

- The *single linkage* merges the two clusters that have the minimum distance between any points in the two groups:

$$\Delta_{AB} \coloneqq \min\left(l_{i\in A,\, j\in B}\right), \tag{2.3}$$

  where i and j represent sink particles belonging to group A and B, respectively, and $l_{i,j}$ is the distance between two such particles.

- The *average linkage* merges the two clusters that have the smallest average distance between all their points:

$$\Delta_{AB} \coloneqq \mathrm{mean}(l_{i\in A,\, j\in B}). \tag{2.4}$$

- The *complete linkage* (also known as maximum linkage) merges the two clusters that have the smallest maximum distance between their points:

$$\Delta_{AB} \coloneqq \max\left(l_{i\in A,\, j\in B}\right). \tag{2.5}$$

- *Ward's linkage* merges two clusters such that the variance within all clusters increases the least. This often leads to clusters that are relatively equally sized. Ward's linkage is defined as follows:

$$\Delta^2_{AB} = \sum_{i\in A\cup B} l^2_{i,c_{A\cup B}} - \left(\sum_{i\in A} l^2_{i,c_A} + \sum_{i\in B} l^2_{i,c_B}\right), \tag{2.6}$$

  where the index i denotes the generic $i-$th particle and c_A, c_B, and $c_{A\cup B}$ denote the centroids of sets A, B, and $A\cup B$ respectively. Equation 2.6 corresponds to the increase in variance with respect to the relevant centroids as groups A and B are merged. Merging groups decreases the number of centroids by one, so variance is bound to increase, but using Ward's linkage results in cluster mergers that minimize its increase at each step.

Figure 2.3 shows how the choice of the linkage affects the structure of the first three nodes of the tree of `m1e4`. The single linkage approach leads to a single, big sub-clump, separated from a few isolated stars. In fact, following this prescription, two blobs that just touch in one point are considered similar and get merged into one pretty quickly, even if their centers-of-mass are far from each other. In contrast, single isolated stars are merged only in the final branches. The average and complete linkage perform poorly as well, likely because their merging criterion is too simple to fit the complex structure of the hydro-dynamical clusters. Finally, Ward's linkage performs well in describing the large scale structure of the cluster, as it correctly identifies the main clumps and is thus informative about the structure of the cluster. For this reason, hereafter we will consider only Ward's linkage.

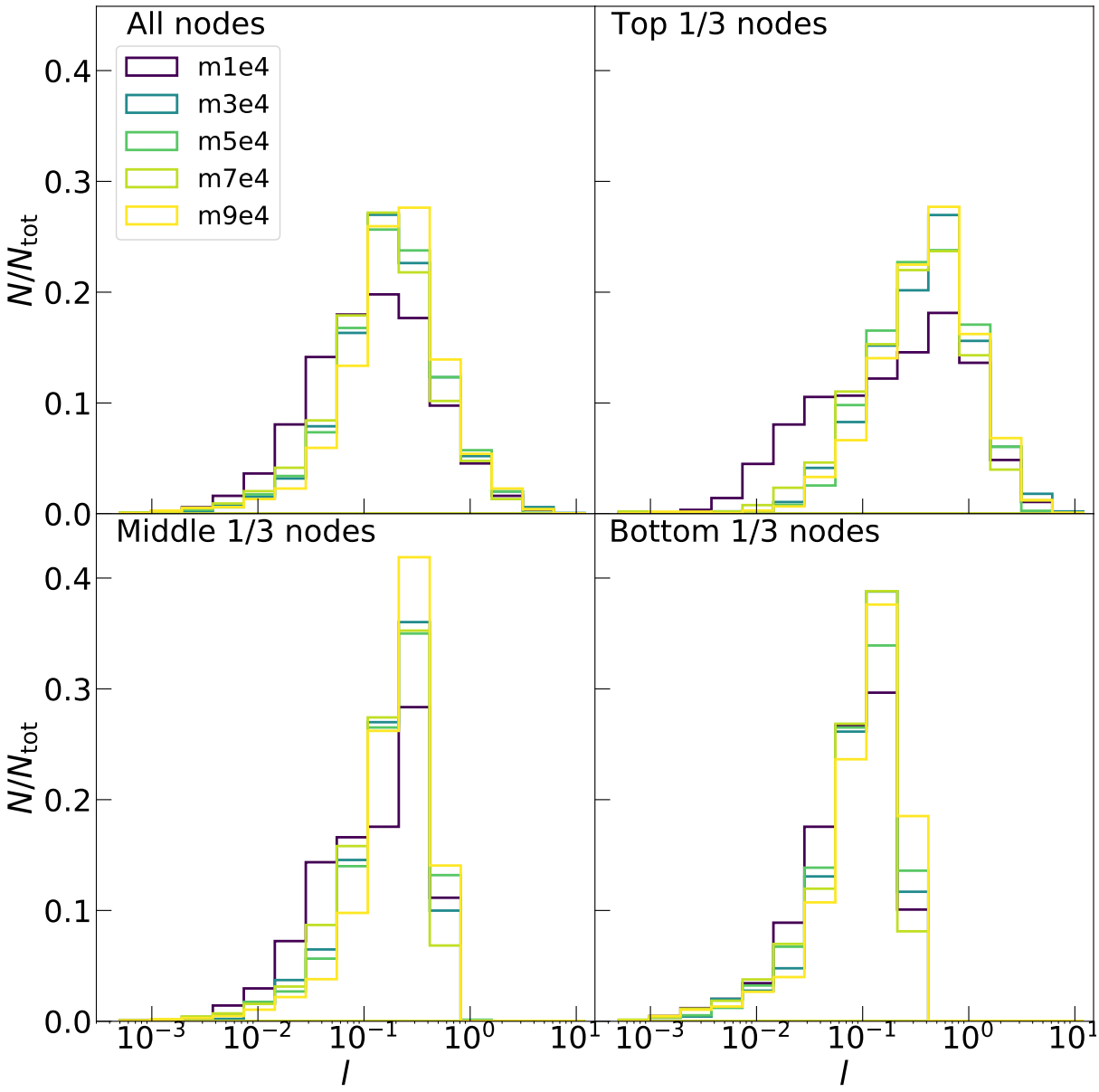

Figure 2.5: Same as Figure 2.4 but for the distribution of the distances (scaled by their variance) between the centers-of-mass of two resulting groups at any given split of the agglomerative clustering hierarchical tree.

2.3.2 Application of hierarchical clustering to stellar clusters

We applied agglomerative clustering to the stellar clusters from hydro-dynamical simulations introduced in Section 2.2. The trees are built by relying on euclidean distance between sink particles in the phase space as a measure of dissimilarity, so that particles sharing both similar positions and similar velocities tend to be grouped together. Before applying the algorithm, we scaled the positions and the velocities by their standard deviations. This step or some such is necessary so that the result of our clustering does not depend on the arbitrary choice of the unit of measurement of time.

The right column of Fig. 2.3 shows the groups of sink particles corresponding to the first two nodes of the learned tree (starting from the root). The first node splits the sinks into two big chunks, and the second node splits off a smaller clump from one of these[4]. Our choice of using Ward linkage results in the splitting off of the most massive sub-clumps in the first branches of the tree, leading to an overall balanced tree. The first splitting thus gives information about the distribution of the sub-clumps at large scales and, moving towards the leaves of the trees, sub-clusters are split in smaller and smaller sub-clumps, as desired for our task.

Figure 2.4 shows the mass ratios between sub-clumps branching off at different depths within the tree. The distribution of mass ratios is not particularly affected by the tree depth. This is expected if the structure of the sink particle distribution is scale invariant, as moving down the tree (towards the leaves) probes smaller scales by construction. Additionally, Fig. 2.4 shows that the distribution is similar across different simulations, spanning a range of total mass of an order of magnitude. To assess if the mass ratios can be considered as drawn from the same distribution (after properly rescaling the mass), we performed pairwise Kolmogorov–Smirnov tests. Despite multiple testing we never obtain a p-value below 10^{-2}, so we have no reason to suspect that the distributions are different. Also, we performed the same test on the sub-distributions shown in Fig. 2.4 separately. Our test always obtains p-values above 10^{-1}, with the only exception for the comparison between the middle nodes of `m1e4` and `m9e4`, where p-value $= 10^{-1.2}$. This result suggests that, despite some statistical fluctuations, the splitting in mass is performed in the same way at different scales for all the simulations.

Similar information on the scaling behavior of our simulations can be extracted from Figures 2.5 and 2.6, where we show the distribution of the distances between the clumps ($l = |\mathbf{l}|$) and that of their relative velocities ($u = |\mathbf{u}|$). In particular, the positions of the maxima of the distributions shift towards lower values by moving from the top to the bottom nodes, confirming that the tree is considering smaller and smaller scales. Also in this case, all the simulations show very similar distributions at each level for both the distances and the relative velocities. The distribution of the angles between the relative velocity and the distance, $\theta = \arccos\left(\mathbf{l} \cdot \mathbf{u}\,(l\,u)^{-1}\right)$, is shown in Figure 2.7. This distribution appears flat except for a rise at $\cos\theta \approx 1$ which corresponds to relative velocity parallel to the separation vector between clumps, which is expected in a supervirial cluster undergoing overall expansion.

Relevant physical information can be drawn by considering the relation between quantities of the same node in the agglomerative clustering tree. Figure 2.8 shows the relation between the distance of the sub-clumps and their relative velocity, for each node. The

[4]Even as we describe the tree from the root up (writing occasionally in terms of splits/splitting) agglomerative methods build the tree from the leaves, i.e. the individual sink particles.

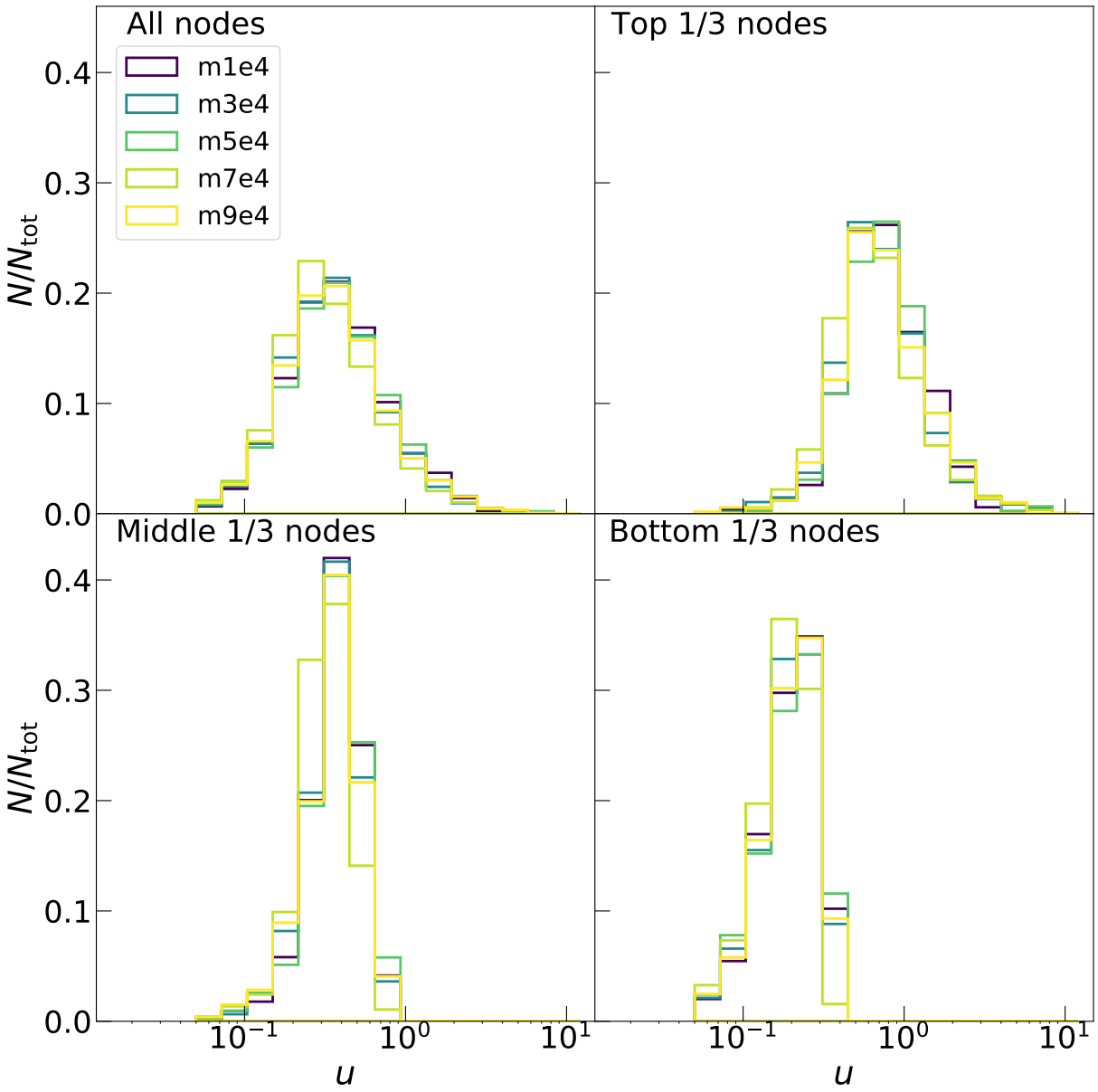

Figure 2.6: Same as Figure 2.4 but for the distribution of the relative velocities (scaled by their variance) between the centers-of-mass of two resulting groups at any given split of the agglomerative clustering hierarchical tree.

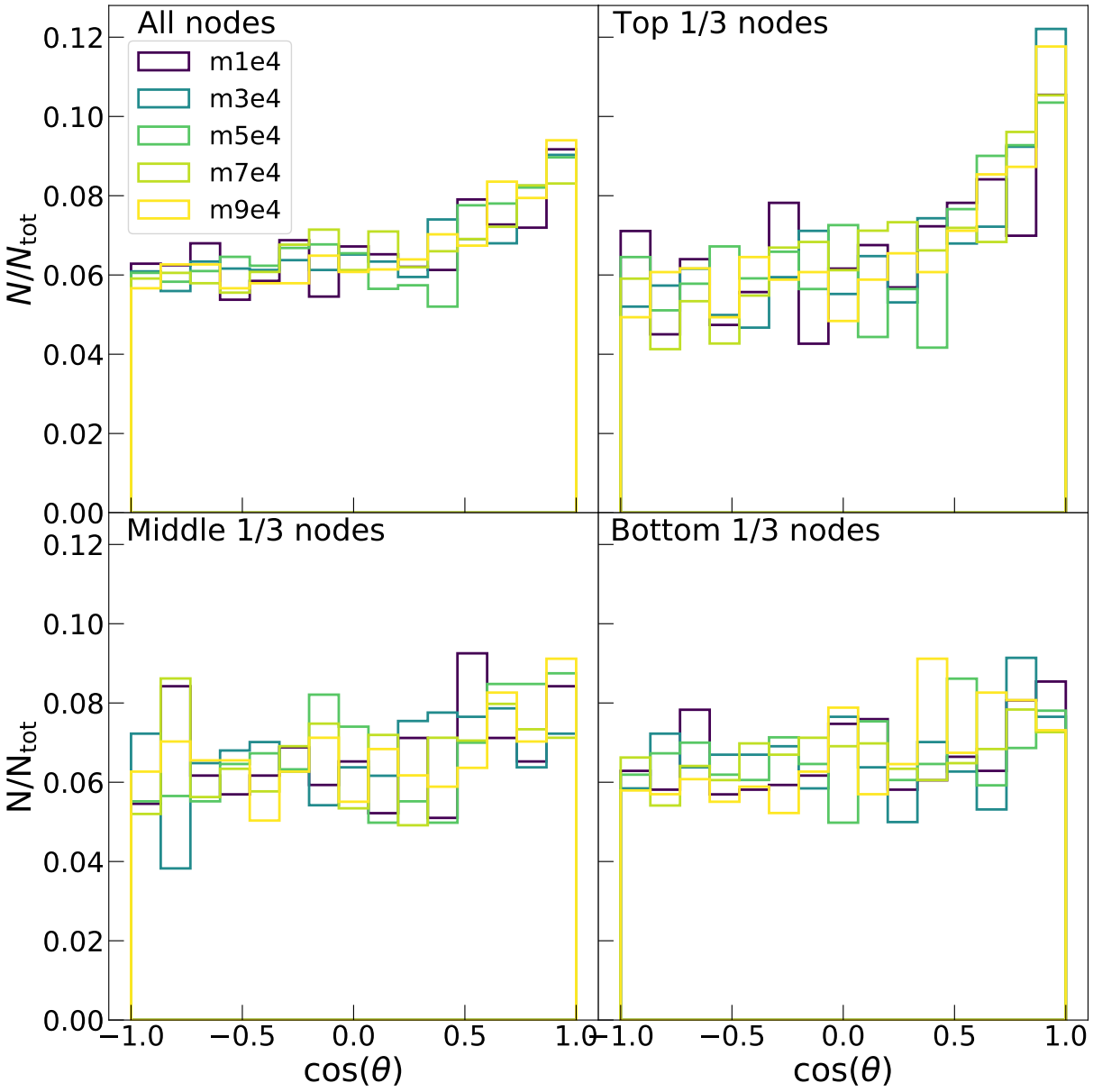

Figure 2.7: Same as Figure 2.4 but for the distribution of the cosine of the angle between the relative velocity and the distance of the centers-of-mass of two resulting groups at any given split of the agglomerative clustering hierarchical tree.

main sub-clumps, that correspond to the nodes closest to the root, show a direct proportionality between these two quantities, possibly due to rigid rotation. In contrast, on the smallest scales, the single particle relative velocity shows a tendency to decline with the square root of their distance, as would happen for two clumps (or even two individual stars) orbiting one another under the influence of each other's monopole potential. Interestingly, all relative motions between clumps take place between the rigid and Keplerian extremes.

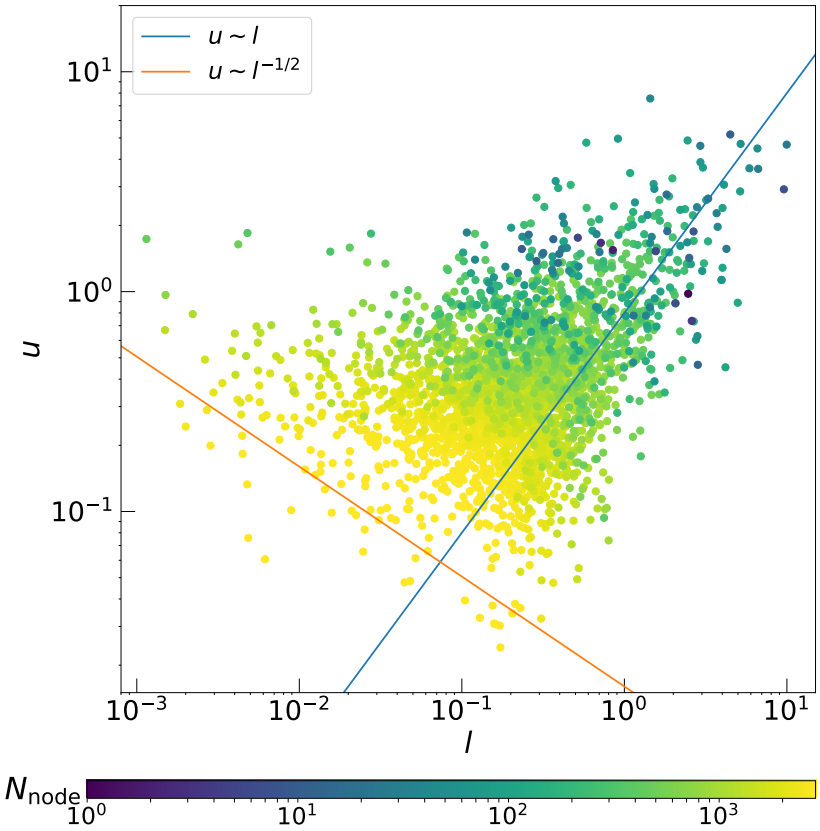

Figure 2.8: Scatter plot of the relative velocity between the centers-of-mass of two different sub-clumps corresponding to a given node in the agglomerative clustering tree as a function of their distance. The colour gradient maps the depth of the node (from the root, in blue, to the leaves, in yellow) within the hierarchical tree, N_{node}. The superimposed lines represent two limit slopes corresponding to rigid rotation (blue) and Keplerian motion (orange).

2.3.3 Generating new realizations

As explained in Section 2.3.2, the application of the agglomerative clustering algorithm to stellar clusters allows us to inform a tree $\mathcal{T}$ encoding their hierarchical structure. Each node of the three $\mathcal{T}_i$ is associated to the relevant properties $\mathbf{l}_i$, $\mathbf{u}_i$, and q_i, which quantify the relations between the sub-clumps corresponding to the branches departing from the node. Thus the tree essentially encodes instructions to generate a new star cluster, as it

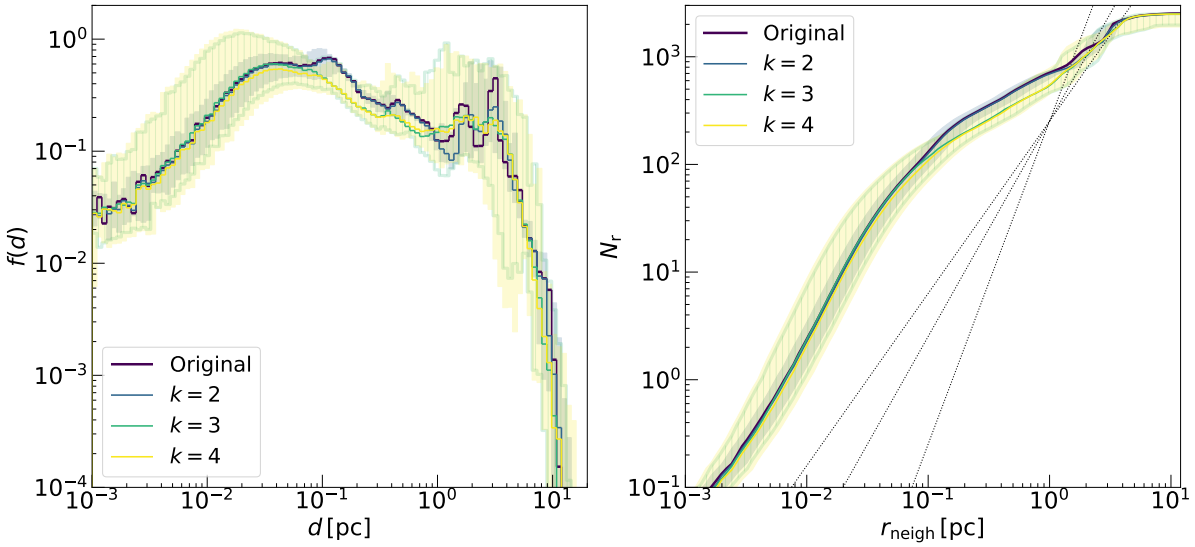

Figure 2.9: Left-hand panel: distribution of inter-particle distances $f(d)$ for the sink particles taken from the `m1e4` simulation (thick magenta line) and three distributions of new generations obtained by replacing the first 1 (blue), 2 (green, hatched area) and 3 (yellow) nodes, corresponding to $k = 2$, 3, and 4 in the notation used above. The shaded area encloses the distribution of the new generations, and the solid line is the median of the distribution. Right-hand panel: average number of neighbours $N_{\rm r}$ around a star, within a sphere with radius $r_{\rm neigh}$, for different values of $r_{\rm neigh}$. Lines and colors are the same as in the left-hand panel. The black dotted lines represent the trend expected for distributions with a uniform fractal dimension, for $\beta = 1.6$, 2, and 3 .

can be traversed from the top, iteratively splitting an intial particle until the leaf level is reached, where individual stars have been produced. In our case, the goal is to change the cluster at the global structure level -nearest to the trunk of the tree-, thus creating different sub-clumps configurations while preserving the small scale properties of the sub-clumps (such as their fractal structure). We thus take the quantities $\mathbf{l}_i$, $\mathbf{u}_i$, and q_i associated to the nodes $\mathcal{T}_i$ for $i < k$ and replace them with the quantities $\mathbf{l}'_i$, $\mathbf{u}'_i$, and q'_i associated to the nodes $\mathcal{T}'_i$ of another tree $\mathcal{T}'$, learned from a different set of sink particles. This grafting procedure represents a way to combine the large scale properties of one simulation with the small scale properties of another. For the results presented in Sect. 2.4, these nodes are sampled randomly from other simulations.

The generation procedure is implemented as follows. First, we consider a particle with a mass M_1 equal to the total mass of the cluster considered, placed at the centerof mass of the cluster. The particle is first split into two particles of masses M_{11} and M_{12} such that $M_{11} + M_{12} = M_1$ and $\min(M_{11}, M_{12})/M_1 = q'_1$. The positions and velocities of the new particles are assigned such that their center of mass is at rest in the origin of the system, their distance vector is $\mathbf{l}'_i$, and their relative velocity $\mathbf{u}'_1$. This splitting procedure is then repeated until a cluster with the same number of particles as the reference one is obtained. At each step, the particle-to-split is chosen by considering the same order of splitting as the original reference tree. This procedure may at times result in very low mass particles. We remove these planet-sized objects with a cutoff at the minimum mass of the original stars on which $\mathcal{T}$ was learned.

Grafting depth

In the procedure described above, the choice of the grafting depth k determines how different the new realizations are from the original system. A low value of k produces generations that are very similar to the original one at all scales. In contrast, when k is high, also the small scales are modified substantially. In our case, we want to generate new clusters that are similar to the original one but, at the same time, cannot be considered as its copies. We evaluated how the choice of the grafting depth affects the spatial structure of the new generations. In particular, we considered the distributions of distances and the fractal dimensions obtained by generating sets of one hundred new realizations for `m1e4`, at different values of k. The left panel of Fig. 2.9 shows the general shape of the distributions of inter-particle distances. Predictably, the realizations obtained by modifying just one node match the original distribution better than those that change two or three nodes, and present the smallest spread. The peaks correspond to sub-clumps of sinks, that are formed in different numbers and sizes in each realization. At small distances, the new realizations recover the the general trend of the original distribution, as meant for our method. For the case with $k = 1$, this happens at about 1 pc, meaning that only the very large scales (the distance between the main sub-clumps) are modified. By increasing k, also the smaller scales are altered, and the original shape is recovered later. This suggests that very few changes are sufficient to produce generations that can be defined as different from the original cluster. The distributions for $k \leq 3$ are consistent with the original simulation throughout the range of distances.

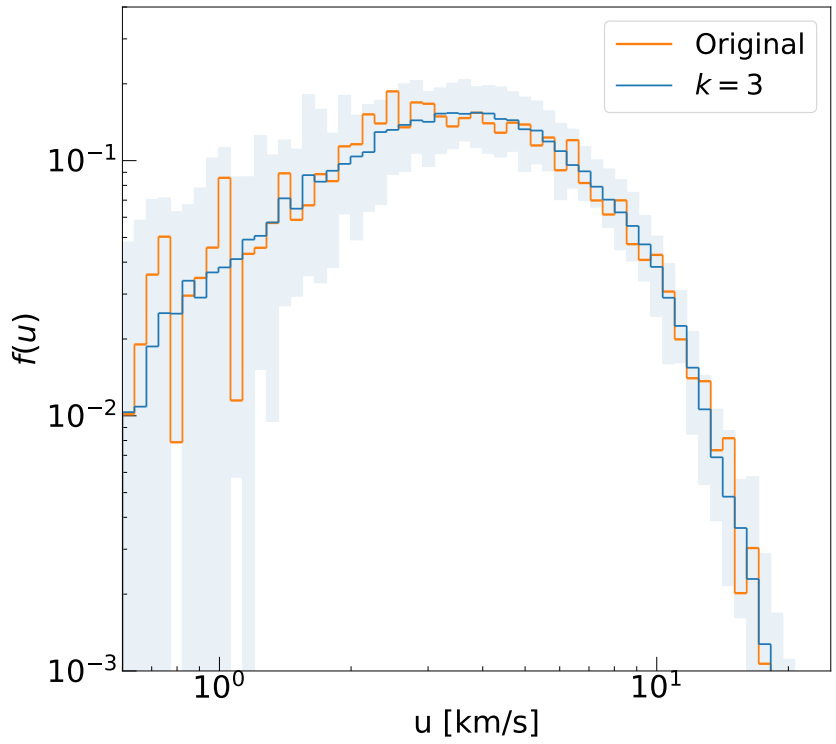

Figure 2.10: Distribution of velocities $f(u)$ for the sink particles taken from the `m1e4` simulation (orange line) and for a distribution of new generations obtained by considering $k = 3$ (blue). The shaded area encloses the distribution of the new generations, and the solid line is the median of the distribution.

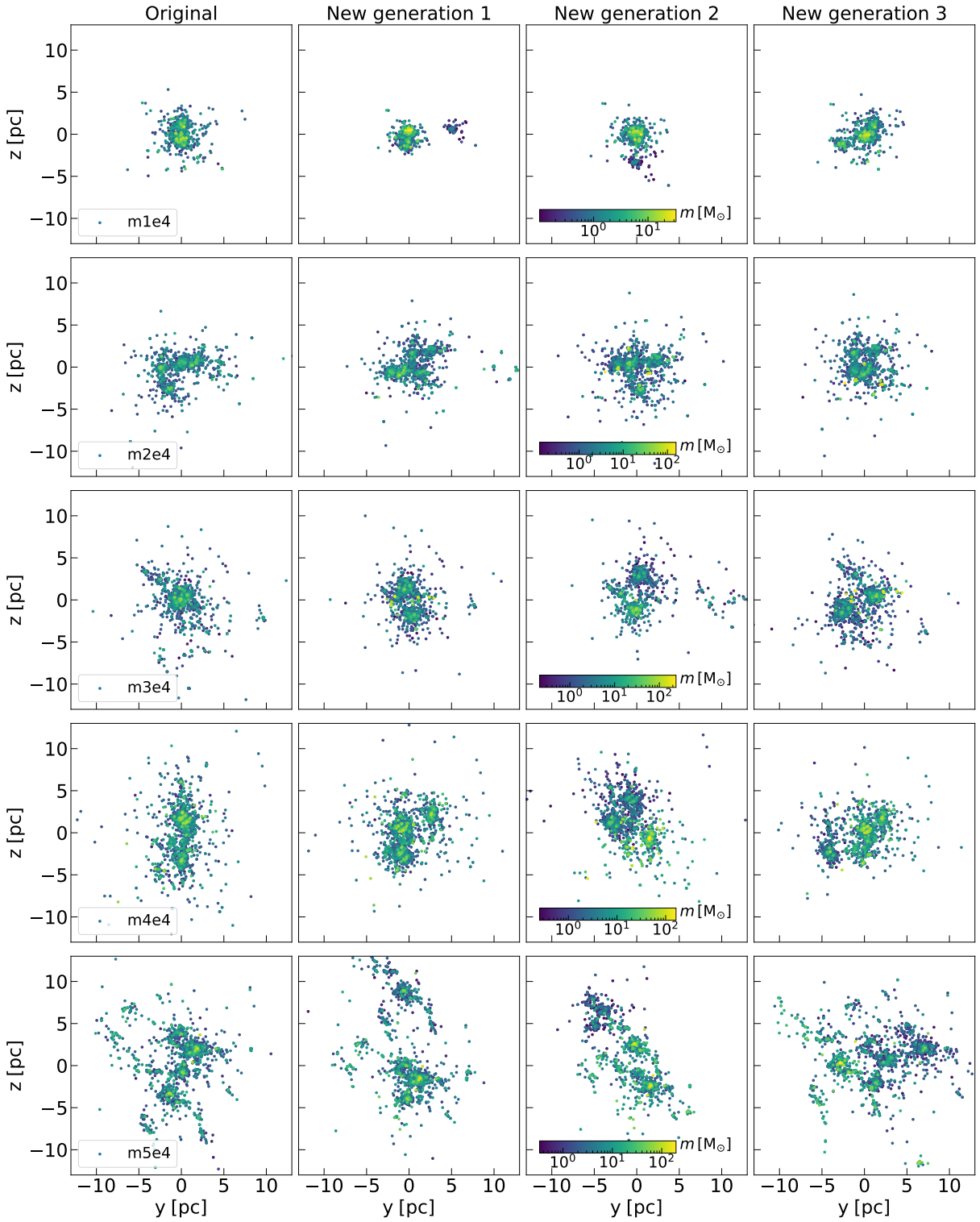

Figure 2.11: Projections in $y - z$ of the 5 least massive star clusters (left), and of three different generated clusters per each. The colour map marks the mass of the individual stars.

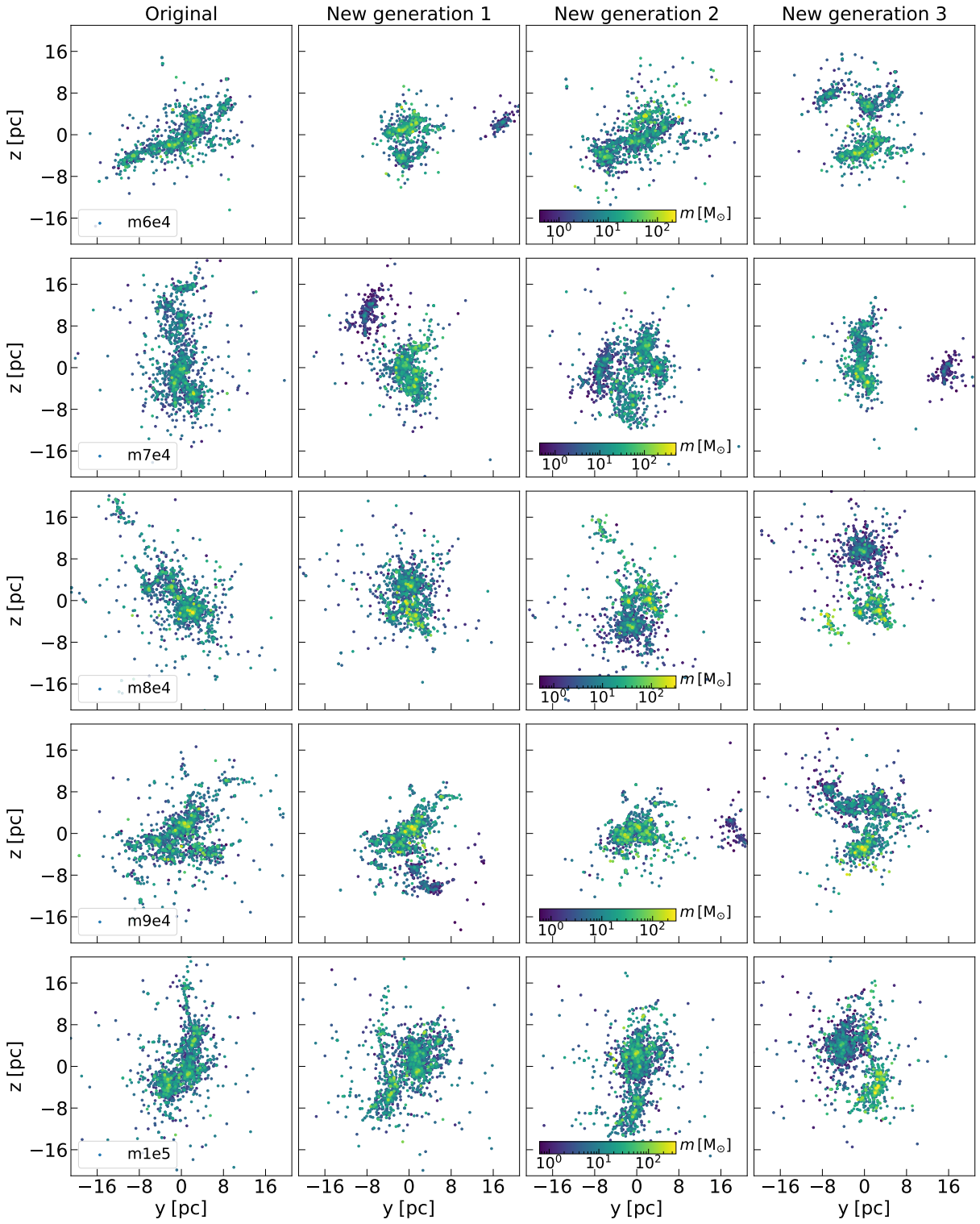

Figure 2.12: Same as Fig. 2.11, but for the 5 most massive star clusters.

In the right-hand panel of Fig. 2.9, we have computed the fractal dimension by means of the average number of neighbours of the stars within a given distance, following Ballone et al. (2020). The distribution of neighbours of `m1e4` is not described by a single power law of non integer index β, as one would expect in a simple fractal structure, but presents two slope changes at around $\approx 10^{-1}$ and ≈ 2 pc (see also Ballone et al. 2020). To guide the eye, the three dotted lines mark the theoretical distance distributions in the case of a pure fractal distribution with $N_{\rm r} \propto r_{\rm neigh}^{\beta}$, for $\beta = 1.6$, 2, and 3. The generated distributions match the general trend and the changes in the slope of the original simulation very well, showing that our method captured the underlying structure of the particle distribution in the 3D space at all scales. Like for the inter-particle distance distribution, the choice of $k = 2$ produces only minimal differences from the original `m1e4` profile. In the following, we will focus on generations with $k = 3$, which allows to produce a distribution of clusters that are distinguishable but still consistent with the original one at all scales.

Figure 2.10 shows the distribution of velocities for the new generations obtained by setting $k = 3$, as compared to the original sink particle trend. The median of the new generations matches the original distribution at all velocities, both on the low-velocity tail, where the Maxwell-Boltzmann trend seems to be preserved, and on the sharper power-law trend at high velocities. At very low values ($u < 1\,\mathrm{km/s}$), the very low number of stars causes large fluctuations in the distribution of new generations, but their median trend is still well consistent with the original one.

2.4 Results

Figure 2.11 and 2.12 show the spatial distributions of the original cluster and of three new generations per each, for all the sink particle distributions of our sample. The new generations are qualitatively indistinguishable from the original clusters (e.g., see also Torniamenti 2022).

2.4.1 Properties of the newly generated systems

In this Section, we discuss the properties of the systems generated using our procedure starting from the simulation `m1e4`, which presents the highest resolution. Figure 2.13 shows the spatial distributions of five new generations obtained with the method described in Section 2.3.3, compared to the original one. The new generations show a strong sub-structured configuration, with a different number of clumps, depending on the single realization, which has drawn branches from different simulations. Also, a strong degree of mass segregation is still present in the single sub-clumps, as highlighted by the colour coding. This primordial mass segregation in the individual realizations qualitatively matches the one present in the original cluster.

In Fig. 2.14, we compare the mass distribution of `m1e4` to those of the new generations. In this case, our method leaves the slope of the mass function largely unaltered for most of the mass spectrum. At the boundaries of the mass spectrum, some discrepancies are present. This is due to the fact that the change in the first nodes may split up a relatively small particle more times than in the original cluster, and leaves more massive particles less split. This explains the higher number of particles at the boundaries of the mass spectrum with respect to the original one. The sharper cut-off at $m \approx 10^{-1}\,\mathrm{M}_{\odot}$ is due to the fact that all masses below this threshold are systematically removed. In general, the

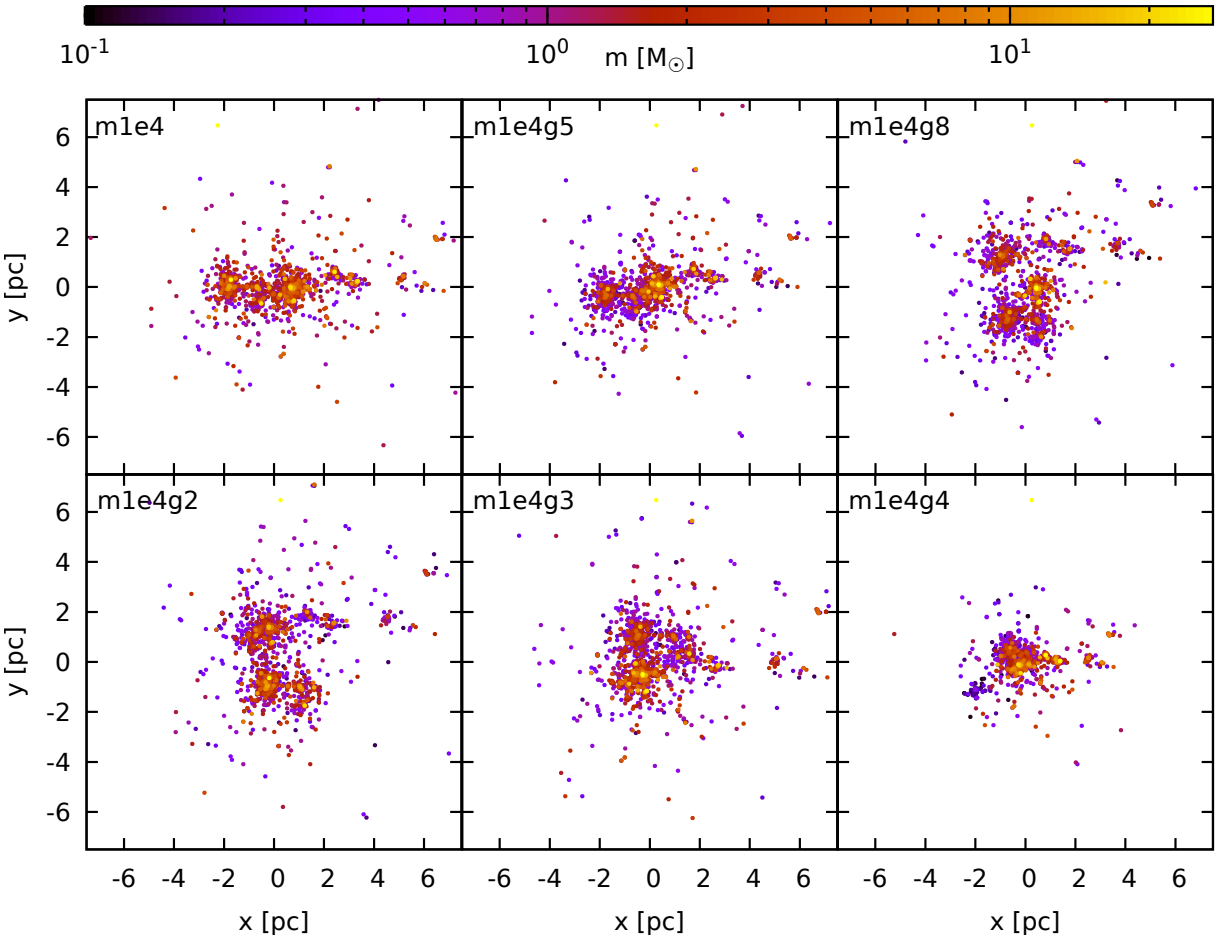

Figure 2.13: $x - y$ projection of the `m1e4` system (top left panel, see also Fig. 2.1) and five different new generations. The colour code marks the different masses of the sink particles and their new generations.

fit with Eq. 2.2 is rather good, yielding values of γ around 2.3, reminiscent of a Salpeter (1955) slope.

Due to the redistribution of particle positions, velocities and masses in the generation process, the value of the total virial ratio $\alpha_{\rm vir}$ may be significantly altered (with respect, in this case, to the value of 1.19 for the `m1e4` case) ranging from a minimum of 0.46 to a maximum of 2.08. Clearly, the future dynamical evolution depends heavily on the virial ratio, which, in turn, is heavily affected by the left tail of the particle pairwise distances. There is indeed a margin of variation in short distances between realizations, as shown in Fig. 2.9. However, the shortest distances in any stellar system essentially correspond to binary-star semiaxes. Our hydro-dynamical simulations were not designed to faithfully reproduce an observational initial mass function (Ballone et al. 2021) nor to capture binary properties. In Torniamenti et al. (2021), we introduce a realistic binary distribution with a separate procedure. While binary binding energy is a large fraction of the total binding energy in many realistic scenarios, the time scale over which this energy is exchanged with the cluster at large is much longer than the dissolution time for the typical system under consideration: hard binaries are dynamically inert in the short term. To check that this is the source of the observed virial ratio mismatch, we have operated two diagnostics. First of all, we have recomputed the virial ratio $\alpha_{\rm vir}$ for

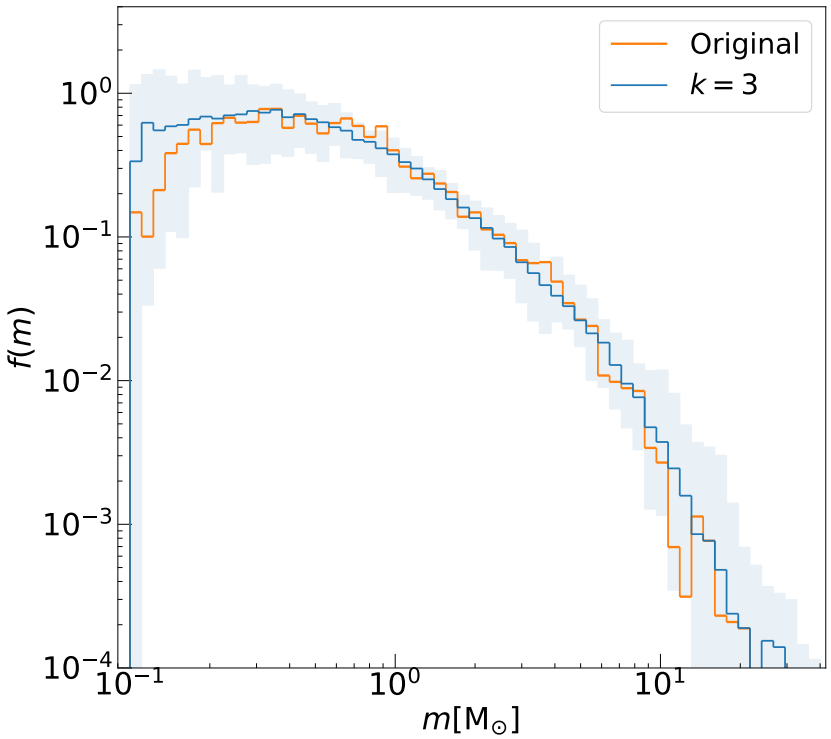

Figure 2.14: Distribution of masses $f(m)$ for the sink particles taken from the `m1e4` simulation (orange line) and for a distribution of new generations obtained by considering k = 3 (blue). The shaded area encloses the distribution of the new generations, and the solid line is the median of the distribution.

N_s times excluding each time a different particle. This gives us a robust way to quantify the virial ratio, as the spread in the resulting distribution will be driven by instances in which a member of a very close binary was excluded. In all cases, the value of $\alpha_{\rm vir}$ of the original system lies well inside the distribution of $\alpha_{\rm vir}$ obtained by removing one particle at time from a given generation.

Second, we have also computed the $\alpha_{\rm vir}$ by excluding the binding energy of stars with separation under a varying threshold between one tenth and one half of the average inter-particle distance. We found that the large variations in the value of $\alpha_{\rm vir}$ observed for the generated clusters is essentially due to the different distributions of tightly bound particles in the generated clusters and the parent sink particle system produced by our SPH simulations. Thus, different values of the virial ratio will result in a similar dynamical evolution on the time scales of interest, as shown below by evolving our realization through direct $N-$body simulations. We list the nominal virial coefficients of our generated realizations together with other properties in Table 2.2.

2.4.2 *N*-body simulations

Our method aims to generate large samples of initial conditions for $N-$body simulations. To test that our realizations are indeed suitable for this use, we evolve via direct N-body simulations the three original clusters (`m1e4`, `m3e4` and `m6e4`) and 10 different generated clusters per each of the three original ones. Finding that the evolution of the generated

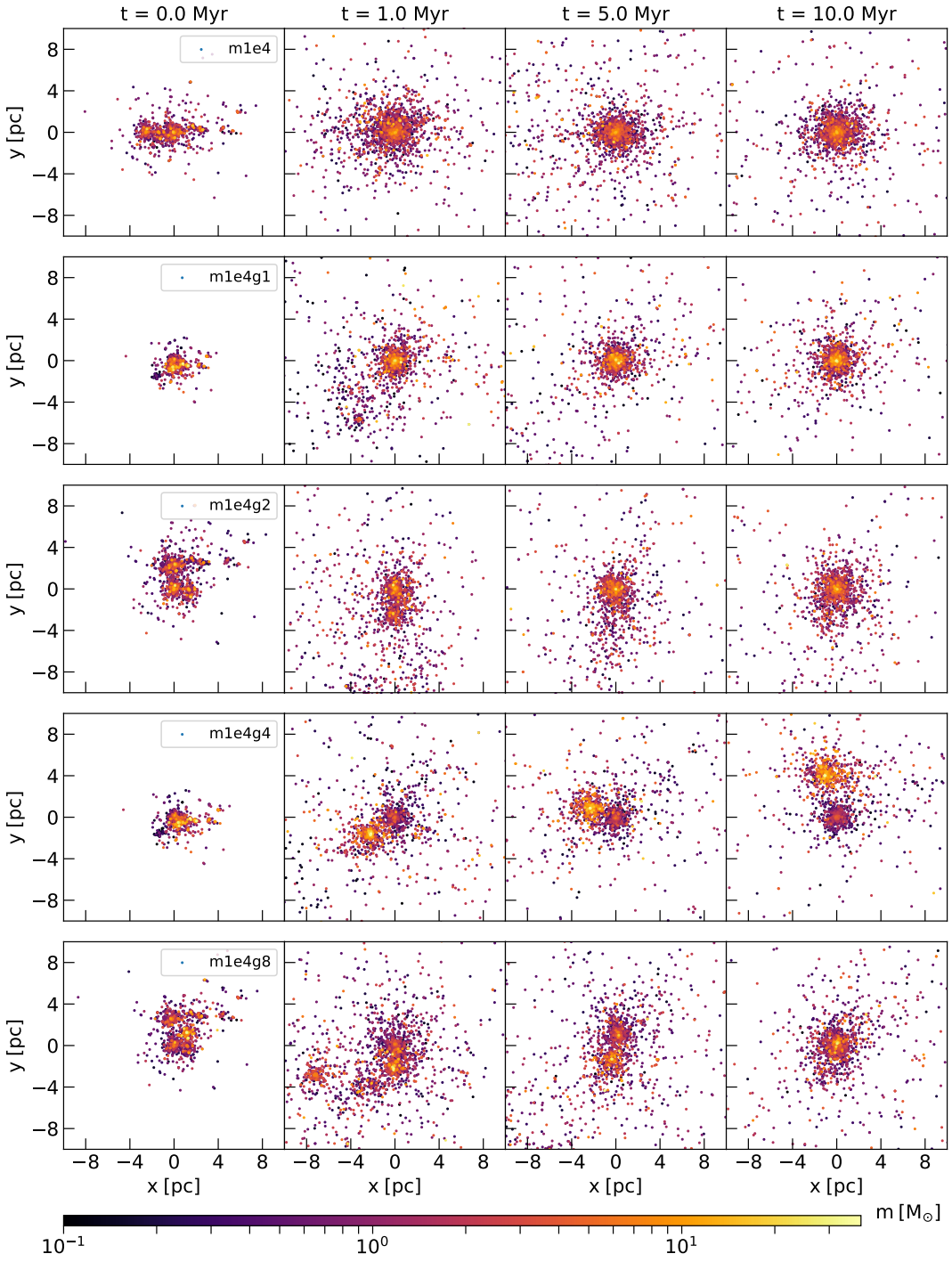

Figure 2.15: Projection in the $x - y$ plane of the evolution of the original cluster (`m1e4`, upper panel) and four different generated clusters (lower panels) as a function of time. The clusters are shown at their initial configuration (first column) and at three different time steps: 1 Myr (second column), 5 Myr (third column) and 10 Myr (last column). The colour code marks the different masses of the sink particles and their generations.

clusters is neither identical nor dramatically different with respect to the original cluster is one of the main test-beds of our method. In fact, our method can be successfully used only if the new clusters evolve in a similar way as the original one, but are sufficiently different not to be an exact copy. Ideally, the generated clusters should behave as different random realizations of the same underlying physical distributions.

We ran our simulations with the direct N-body code NBODY6++GPU (Wang et al. 2015). Thanks to a neighbour scheme (Nitadori & Aarseth 2012), NBODY6++GPU efficiently handles the collisional force contributions at short time scales as well as those at longer time intervals, to which all the members in the system contribute. The force integration also includes a solar neighbourhood-like static external tidal field (Wang et al. 2016). Stellar evolution is not included in our runs, for the sake of simplicity and to make the comparison with the original cluster more straightforward. We evolved the clusters for 10 Myr.

Table 2.2 shows the main initial properties of the generated clusters for which we ran the $N-$body simulations. Figure 2.15 shows the projection in the $x-y$ plane of the original `m1e4` cluster and of four generations, at different times. The global evolution of the new generated clusters shows a variety of configurations depending on the different distribution of mass. In some cases, distinct sub-clumps are present at $t > 1\,\mathrm{Myr}$ and tidally interact with each other before eventually merging. In the case of `m1e4g4`, two distinct sub-clumps are still present at 10 Myr.

A more quantitative description of the global evolution of the clusters can be given in terms of the evolution of the 10% and 50% Lagrangian radii (r_{10} and r_{50}), centered in the center of density[5]. Figure 2.16 shows the evolution of r_{10} and r_{50} for the original clusters and the generated ones. In all the cases, the original evolution lies within the limits of the distribution of the generated clusters, which shows a large spread. This spread is consistent with the large stochastic fluctuations that we expect in the evolution of such low-mass clusters (see, e.g., Torniamenti et al. 2021).

2.5 Discussion and Conclusions

We introduced a new method for generating a number of new realizations from a given set of initial conditions (particle masses, positions and velocities) produced by hydrodynamical simulations. The realizations are built to display a different large scale structure, but share similar properties at smaller scales, preserving in particular the fractal dimension of the original simulation. We have shown that they can be used as initial conditions for $N-$body simulations, producing a comparable evolution to the original cluster. This suggests that our method is suitable for drawing the initial conditions of a large set of $N-$ body simulations at an infinitesimal fraction of the computational cost of generating initial conditions from a hydro-dynamical simulation.

Our novel approach relies on informing a hierarchical clustering structure (represented as a tree) from the original initial condition data through agglomerative clustering. This is later turned into new realizations by modifying the initial branches of the tree (encoding the relations between the biggest sub-clumps in the simulation). This results in realizations with different macroscopic properties from the original one (e.g., the number

[5]The local density around each star was calculated as the density of the sphere that includes the 300 closest stars.

Table 2.2: Properties of the generated clusters starting from `m1e4`, `m3e4` and `m6e4`.

Name	N_s	N_c	α_{vir}	γ	M_{sink} [$M_\odot$]
`m1e4g1`	2006	6	0.60	2.3	4.20×10^3
`m1e4g2`	2509	6	1.41	2.3	4.20×10^3
`m1e4g3`	2512	6	1.57	2.3	4.20×10^3
`m1e4g4`	1998	8	0.60	2.3	4.20×10^3
`m1e4g5`	2512	5	1.68	2.3	4.20×10^3
`m1e4g6`	2491	7	1.50	2.3	4.20×10^3
`m1e4g7`	2081	8	0.48	2.3	4.20×10^3
`m1e4g8`	2512	9	1.81	2.3	4.20×10^3
`m1e4g9`	2196	4	0.46	2.3	4.20×10^3
`m1e4g10`	2496	7	1.57	2.3	4.20×10^3
`m3e4g1`	2765	5	0.80	2.2	1.03×10^4
`m3e4g2`	2805	7	1.39	2.2	1.03×10^4
`m3e4g3`	2811	5	1.16	2.2	1.03×10^4
`m3e4g4`	2719	5	1.20	2.2	1.03×10^4
`m3e4g5`	2747	7	1.48	2.2	1.03×10^4
`m3e4g6`	2774	6	1.40	2.2	1.03×10^4
`m3e4g7`	2750	6	1.46	2.2	1.03×10^4
`m3e4g8`	2770	7	1.13	2.2	1.03×10^4
`m3e4g9`	2628	7	0.94	2.2	1.03×10^4
`m3e4g10`	2764	6	0.94	2.2	1.03×10^4
`m6e4g1`	2747	7	1.65	2.1	2.04×10^4
`m6e4g2`	2823	7	1.80	2.1	2.04×10^4
`m6e4g3`	2900	5	1.82	2.1	2.04×10^4
`m6e4g4`	2718	6	1.66	2.1	2.04×10^4
`m6e4g5`	2967	6	1.75	2.1	2.04×10^4
`m6e4g6`	2752	5	1.30	2.1	2.04×10^4
`m6e4g7`	2998	6	1.55	2.1	2.04×10^4
`m6e4g8`	2833	6	1.36	2.1	2.04×10^4
`m6e4g9`	3001	6	1.82	2.1	2.04×10^4
`m6e4g10`	3015	5	1.82	2.1	2.04×10^4

After the name of the generated cluster (Col. 1), we report the total number of stars (Col. 2), the number of macroscopic sub-clumps (Col. 3), the virial ratio (Col. 4), the γ coefficient of the mass-spectrum fitting function (Eq. 2.2, Col. 5), and the total mass of the stars (Col. 6).

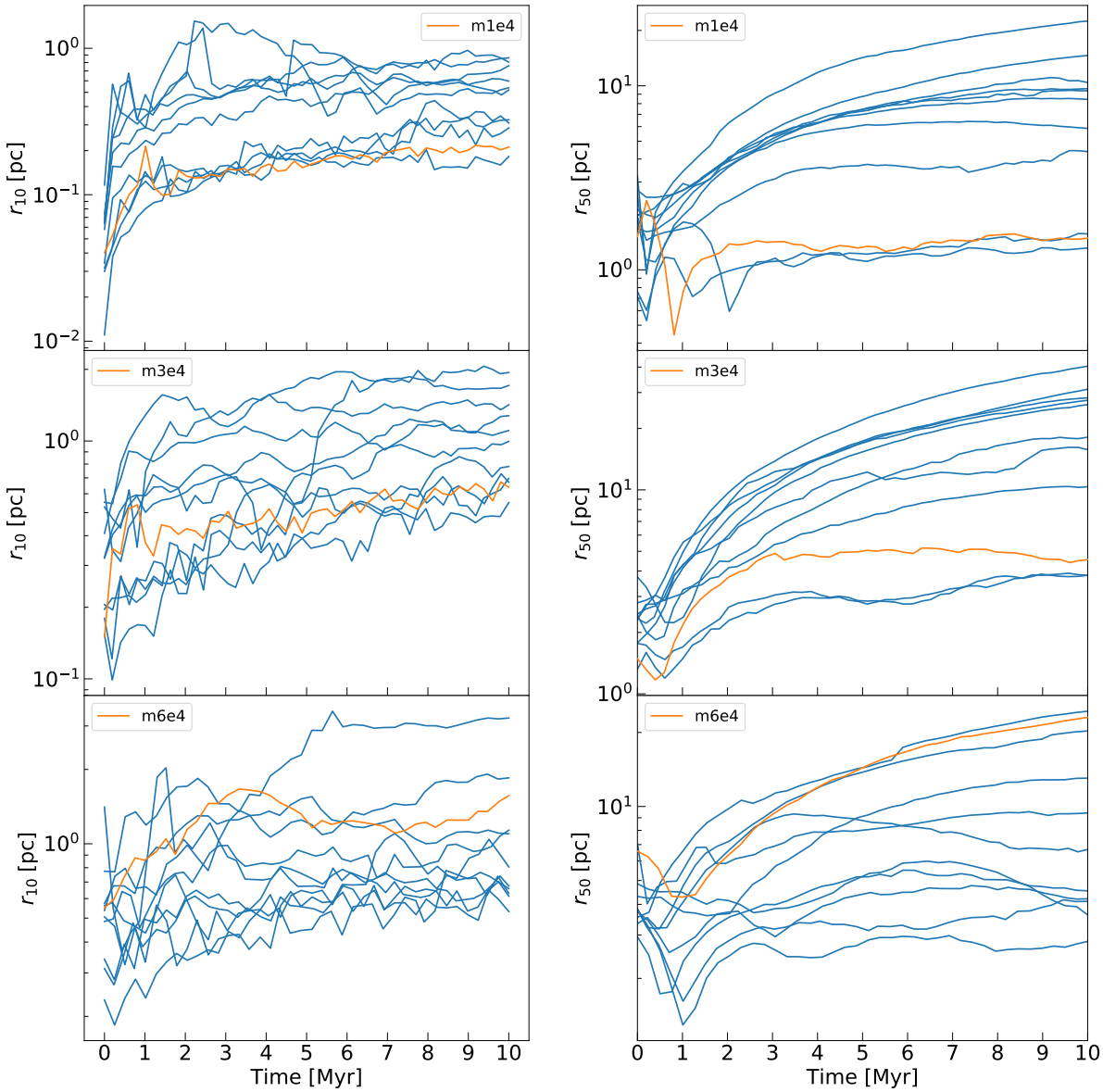

Figure 2.16: Evolution of the 10% Lagrangian radius (left) and the 50% Lagrangian radius (right) for the original sink particles and for ten different generations of `m1e4` (upper panel), `m3e4` (middle panel), and `m6e4` (lower panel). The orange line represents the original sink particle system, and the blue lines are the generated clusters.

of big clumps and their distances), while approximately preserving the characteristics of small scale structure responsible for most of dynamical evolution (e.g., the distribution of pairwise distances between individual stars). In principle, this scheme is very flexible, allowing to choose how much of the large scale structure we control directly, by choosing the number of initial branches we modify.

The realizations we obtained with our method qualitatively resemble the original simulation when visualized in three-dimensional space. In our case, the original distribution of stars was generated by hydro-dynamical simulations of embedded clusters, so our new realizations appear qualitatively indistinguishable from the output of these simulations. The mass spectrum and the velocity distribution are also very similar to the original simulation. The distribution of the number of neighbours as a function of distance reveals that the fractal dimension of our realizations and that of the original simulation match on different scales (they both show a similar complex fractal pattern).

Finally, we ran direct $N-$body simulations of a sample of generated initial conditions for three different original star clusters. In all the cases, the new generations show a realistic evolution on all scales, bracketing that of the original one, as shown by the trend of the 10% and 50% Lagrangian radii. Our analysis suggests that this method is a promising way to generate new mass and phase-space distributions from existing hydro-dynamical simulations, thus increasing our sample of initial conditions for $N-$body simulations. The speedup in computation obtained by our new method is tremendous: generating initial conditions from hydro-dynamical simulations requires about 1.5×10^5 core hours per simulation, while our procedure takes about 10 core seconds to train the initial tree distribution and generate a new realization.

Acknowledgements

We thank the anonymous referee for their useful comments, which helped to improve this work. This project has received funding from the European Unions Horizon 2020 research and innovation programme under the Marie Skłodowska-Curie grant agreement No. 896248. MP's initial contribution to this material is based upon work supported by Tamkeen under the NYU Abu Dhabi Research Institute grant CAP^3. MM, AB and GI acknowledge financial support from the European Research Council for the ERC Consolidator grant DEMOBLACK, under contract no. 770017. PFDC acknowledges financial support from MIUR-PRIN2017 project *Coarse-grained description for non-equilibrium systems and transport phenomena (CO-NEST)* n.201798CZL. MM and MCA acknowledge financial support from the Austrian National Science Foundation through FWF stand-alone grant P31154-N27.

Chapter 3

The impact of binaries on the evolution of star clusters from turbulent molecular clouds

Based on:
Torniamenti S., Ballone A., Mapelli M., Gaspari N., Di Carlo U. N.,
Rastello S., Giacobbo, N., Pasquato M.,
"The impact of binaries on the evolution of star clusters from turbulent molecular clouds", 2021, MNRAS 507, 2253

Abstract

Most of massive stars form in binary or higher-order systems in clumpy, substructured clusters. In the very first phases of their life, these stars are expected to interact with the surrounding environment, before being released to the field when the cluster is tidally disrupted by the host galaxy. We present a set of $N-$body simulations to describe the evolution of young stellar clusters and their binary content in the first phases of their life. To do this, we have developed a method that generates realistic initial conditions for binary stars in star clusters from hydrodynamical simulations. We considered different evolutionary cases to quantify the impact of binary and stellar evolution. Also, we compared their evolution to that of King and fractal models with different length scales. Our results indicate that the global expansion of the cluster from hydrodynamical simulations is initially balanced by the sub-clump motion and accelerates when a monolithic shape is reached, as in a post-core collapse evolution. Compared to the spherical initial conditions, the ratio of the 50% to 10% Lagrangian radius shows a very distinctive trend, explained by the formation of a hot core of massive stars triggered by the high initial degree of mass segregation. As for its binary population, each cluster shows a self-regulating behaviour by creating interacting binaries with binding energies of the order of its energy scales. Also, in the absence of original binaries, the dynamically-formed binaries display a mass-dependent binary fraction, spontaneously reproducing the trend of the observed binary fraction.

keywords: stars: kinematics and dynamics – galaxies: star clusters: general – open clusters and associations: general – binaries: general – methods: numerical

3.1 Introduction

Most stars form as members of clusters or associations, that show a clumpy spatial distribution and may also contain sub-structures (Larson 1995). Understanding the early evolution of these star-forming complexes is of fundamental importance for the comprehension of the properties of young (< 100 Myr) and open clusters (Portegies Zwart et al. 2010), where the presence of sub-structures and fractality is observed (e.g., Cartwright & Whitworth 2004; Sánchez & Alfaro 2009; Parker & Meyer 2012; Kuhn et al. 2019). Also, these systems are characterized by complex internal kinematics, such as sub-clump relative motions and mergers, cluster expansion, gas dispersal (Kuhn et al. 2019; Cantat-Gaudin et al. 2019) and rotation (Hénault-Brunet et al. 2012). In particular, gas dispersal due to stellar winds and supernova explosions drives the cluster out of dynamical equilibrium, leading to an expansion phase, where most stars become unbound and disperse into the field (Hills 1980; Goodwin & Bastian 2006; Baumgardt & Kroupa 2007; Pfalzner 2009). Some of these natal properties might even survive the successive evolution of the stellar system and leave an imprint on the observed properties of older, relaxed stellar clusters (e.g., they may contribute to the signatures of rotation visible in some globular clusters, van Leeuwen et al. 2000; Pancino et al. 2007; Bianchini et al. 2013; Kamann et al. 2018; Bianchini et al. 2018).

In the first phases of their life, the dynamical evolution of young stellar clusters is deeply influenced by their stellar and binary content, and vice versa. In particular, a large fraction of the most massive stars is part of binary and higher order systems (Moe & Di Stefano 2017) that can actively exchange energy and angular momentum with the host environment, thanks to the very high density ($\rho \sim 10^4$ $M_\odot$ pc^{-3}) of the cluster core. On the one hand, original binary stars (i.e., stars that form as members of a binary system)[1] contain a large reservoir of internal energy, that can be transferred to other stars in the host star cluster, through three- and multi-body encounters (e.g., Heggie 1975; Hut 1983), preventing or reversing the gravothermal collapse of the core of the cluster (Tanikawa & Fukushige 2009; Chatterjee et al. 2013; Fujii & Portegies Zwart 2014). On the other hand, the global evolution of the cluster affects the properties of the binary population: for example, core collapse leads to the formation of new binary systems and to their dynamical hardening (Spitzer & Hart 1971a). On top of this, binary stars are also affected by mass transfer, common envelope, supernova kicks, tides and other evolutionary processes (e.g., Hut 1981; Webbink 1984; Portegies Zwart & Verbunt 1996; Hurley et al. 2002). All these processes are crucial for the ejection of stars from their host star cluster (e.g., runaway stars, Fujii & Portegies Zwart 2011, Oh et al. 2015; Oh & Kroupa 2016), and for the formation of intermediate-mass black holes (e.g., Ebisuzaki et al. 2001; Portegies Zwart et al. 2004; Giersz et al. 2015; Mapelli 2016). Finally, the interplay between dynamical interactions and binary evolution (Banerjee et al. 2010; Ziosi et al. 2014; Banerjee 2017; Fujii et al. 2017; Di Carlo et al. 2020b; Kumamoto et al. 2019; Antonini & Gieles 2020b; Trani et al. 2021) can explain the properties of the binary compact objects observed through gravitational wave detection by LIGO and Virgo (Abbott et al. 2021b,c).

Direct $N-$body simulations are usually adopted to integrate the collisional dynamics of gas-free star clusters, where length-scales of different orders of magnitude, from bi-

[1] Although the binaries present in the initial conditions of a star cluster simulation are often referred to as *primordial*, here we use the term *original* to avoid any confusion with primordial stars or black holes formed in the early Universe.

nary separations of some solar radii to several parsecs, need to be included. However, studies of this type often lack realistic initial conditions. For example, state-of-the-art direct $N-$body simulations of star clusters include realistic stellar mass functions and stellar evolution, but most of them start from spherical idealized models, such as Plummer (1911) or King (1966) models. In some recent work, fractal initial conditions were adopted to mimic the initial clumpiness of star clusters (e.g., Goodwin & Whitworth 2004; Schmeja & Klessen 2006; Allison et al. 2010; Küpper et al. 2011; Parker et al. 2014; Di Carlo et al. 2019; Daffern-Powell & Parker 2020). Few studies tried to re-simulate with a direct $N-$body code the initial conditions obtained from hydrodynamical simulations of star cluster formation (Moeckel & Bate 2010; Moeckel et al. 2012; Parker & Dale 2013; Fujii & Portegies Zwart 2015), but most of them do not include stellar evolution or realistic stellar mass functions or original binary populations. A recent attempt to couple magneto-hydrodynamics and direct $N-$body star cluster formation simulations, also considering the presence of original binaries, was proposed by Cournoyer-Cloutier et al. (2021), who developed a binary generation algorithm consistent with observations of mass dependent binary fraction and distributions of orbital periods, mass ratios and eccentricities. They found that binary systems formed dynamically do not have the same properties as the original ones, and that the presence of an initial population of binaries affects the properties of dynamically-formed binaries. An adequate modelling of the original binary population is thus necessary for a realistic description of dynamical interactions in the early stages of star clusters' evolution.

Recently, Ballone et al. (2020) and Ballone et al. (2021) proposed a new approach to connect hydrodynamics and stellar dynamics that can be used to provide more realistic initial conditions for direct $N-$body simulations. This approach includes a number of the ingredients necessary to self-consistently study this problem: realistic phase-space distributions of stars, drawn from sink particle distributions of collapsing molecular clouds, and a realistic stellar mass function, which is fundamental to assess the impact of stellar evolution. This method is based on the assumption that the gas, in which the newly formed star cluster is embedded, is almost instantaneously expelled by feedback (radiation, winds and, most of all, supernova explosions) from the young most massive stars (e.g., Vázquez-Semadeni et al. 2010; Dale et al. 2014; Pfalzner et al. 2014; Gavagnin et al. 2017; Chevance et al. 2020b,a; Pang et al. 2020). From that moment on, the evolution of the newly born stellar system is mainly driven by gravitational dynamics. A necessary step towards a more realistic description is the insertion of binary stars in the original stellar population.

The aim of this paper is to offer a realistic, self-consistent description of the complex interplay between binaries and their host cluster in the first phases of a cluster's life after gas expulsion, by considering the effects of dynamics, stellar and binary evolution simultaneously. To do this, we insert original binaries in the joining/splitting method introduced in Ballone et al. (2021), to generate realistic initial conditions for $N-$body simulations starting from hydrodynamical simulations. Also, we study the evolution of the phase-space distribution of star clusters generated by hydrodynamical simulations and we compare it to other, more idealized, initial configurations.

This paper is organized as follows. In Sect. 3.2, we introduce our binary generation algorithm. Section 3.3 describes the initial conditions of the $N-$body simulations. In Sect. 3.4, we report the results of the simulation of a stellar cluster under different evolutionary conditions and compare it to other initial phase-space distributions. In Sect. 3.5,

we discuss the peculiar aspects of the evolution of the stellar clusters from hydrodynamical simulations. Finally, in Sect. 3.6 we report our conclusions.

3.2 Methods

3.2.1 Binary generation algorithm

We developed a new algorithm to generate a realistic initial mass function (IMF) and a realistic population of original binaries, based on observations (Sana et al. 2012; Moe & Di Stefano 2017). This algorithm can be easily coupled to different phase-space generation codes to obtain a variety of initial conditions for $N-$body simulations. The method consists of the following steps.

1. First, the algorithm randomly draws a population of stars from a Kroupa (2001) IMF between 0.1 $M_\odot$ and 150 $M_\odot$, for an assigned value of the total mass of the population.

2. The stars are paired up to each other in order to obtain a distribution of mass ratios $q = m_2/m_1$ following Sana et al. (2012):

$$\mathcal{F}(q) \propto q^{-0.1}, \text{ with } q \in [0.1, 1]. \tag{3.1}$$

   The coupling is set to generate a binary fraction $f_{\rm bin} = N_{\rm bin}/(N_{\rm sing} + N_{\rm bin})$, where $N_{\rm bin}$ is the number of binary systems and $N_{\rm sing}$ is the number of single stars, which depends on the mass of the primary star, following the observational results of Moe & Di Stefano (2017). For simplicity's sake, we do not include triple systems, but we take into account their presence when evaluating the binary fraction by labeling a certain number of single stars as third components of the existing binary systems (following Moe & Di Stefano 2017). This results in a fraction of binaries counted as triples ($f_{\rm trip}$), and prevents from having an excessive number of binary systems among the most massive stars. By this procedure, we obtain a distribution of single stars and of binary particles. For this work, we assume the binary fraction goes to zero in the mass range $0.1 - 0.8$ $M_\odot$: the observations indicate that the percentage of binary stars in this mass range is low anyway (Moe & Di Stefano 2017), and including these low-mass binary stars would have dramatically increased the computational cost of the simulations. The resulting binary fraction for stars with mass $m > 0.8$ $M_\odot$ is 0.4.

3. The single and binary particles are assigned a phase-space distribution by coupling the aforementioned algorithm to a phase-space distribution generator. For this work, we considered two choices of the phase-space distribution generator. In the first case, we coupled our algorithm with the joining/splitting procedure summarized in the next sections and described in detail in Ballone et al. (2021). In the second case, the phase-space distribution is created with the code McLuster (Küpper et al. 2011).

4. Finally, the binary particles are split into separate stars and their orbital period (P) and eccentricity (e) distributions are generated following Sana et al. (2012):

$$\mathcal{F}(\mathcal{P}) \propto \mathcal{P}^{-0.55}, \text{ with } \mathcal{P} = \log_{10}(P/\text{days}) \in [0.15, 5.5], \tag{3.2}$$

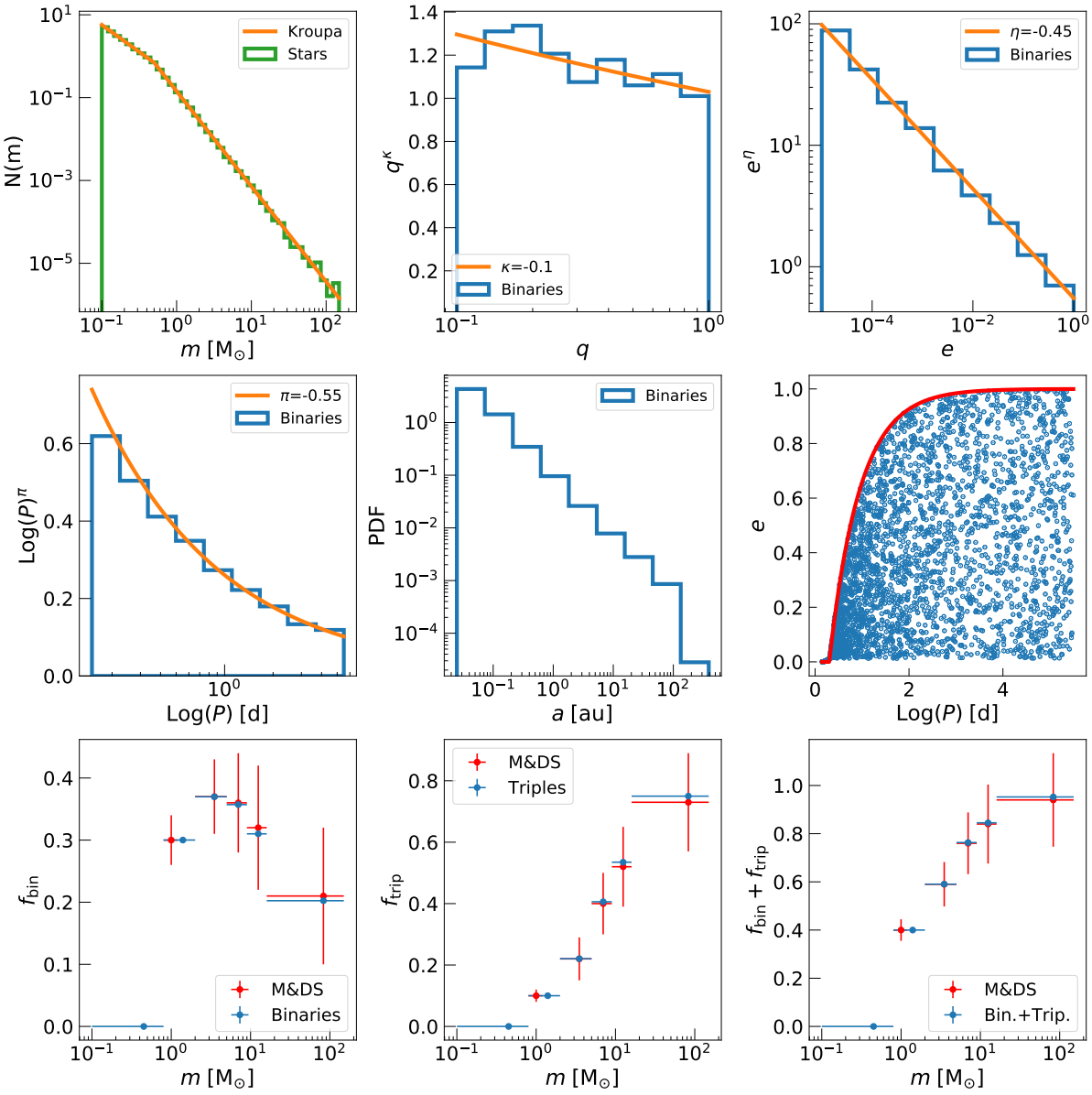

Figure 3.1: Properties of binary stars generated with the algorithm described in Section 3.2.1. **Upper panel:** Kroupa (2001) IMF (left), mass ratio (center) and eccentricity (right) distributions, following Sana et al. (2012). **Central panel:** period distribution (left) from Sana et al. (2012), the resulting semi-major axis distribution (center), and the eccentricity−period relation (right) from Moe & Di Stefano (2017). **Lower panel:** fraction of binaries not counted as triples ($f_{\rm bin}$, left), fraction of binary stars counted as triples ($f_{\rm trip}$, center) and the resulting binary fraction ($f_{\rm bin} + f_{\rm trip}$, right). Red data points labelled as M&DS: observations from Moe & Di Stefano (2017). Blue data points: simulated binaries and triples from this work.

and

$$\mathcal{F}(e) \propto e^{-0.45}, \text{ with } e \in [10^{-5}, e_{\max}(P)], \tag{3.3}$$

where, for a given orbital period, we set the upper limit of the eccentricity distribution $e_{\max}(P)$ according to eq. (3) of Moe & Di Stefano (2017):

$$e_{\max}(P) = 1 - \left(\frac{P}{2\,\text{days}}\right)^{-2/3}. \tag{3.4}$$

The orbital properties of the binaries are then converted into positions and velocities by considering an isotropic distribution for the orbital planes.

Figure 3.1 shows an example of the binary populations generated by means of this algorithm. These initial conditions can be used to study the evolution of binary stars at the early and later stages of their host stellar cluster's life with a great variety of initial configurations. In addition, the generation of initial conditions through this algorithm has negligible computational cost. Finally, the described procedure is also suited to generate initial conditions for population synthesis studies.

3.2.2 Hydrodynamical simulations

The star clusters studied in this work are obtained by applying our algorithm to the output of the hydrodynamical simulations of turbulent molecular clouds presented in Ballone et al. (2020) and Ballone et al. (2021). These hydrodynamical simulations are performed with the smoothed-particle hydrodynamics code GASOLINE2 (Wadsley et al. 2004, 2017). For this work, we consider the hydrodynamical simulation initialized with a total mass of $2 \times 10^4\ M_\odot$. The cloud has an initial uniform density of 250 cm^{-3}, an initial temperature of 10 K and it is in an initial marginally bound state, with a virial ratio $\alpha_{\text{vir}} \equiv 2T/|V| = 2$, where T and V are the kinetic and potential energy, respectively. The turbulence consists of a divergence-free Gaussian random velocity field, following a Burgers (1948) power spectrum. The gas thermodynamics has been treated by adopting an adiabatic equation of state with the addition of radiative cooling (Boley 2009). Stellar feedback was not included. Star formation is implemented through a sink particle algorithm adopting the same criteria as in Bate et al. (1995).

At 3 Myr (for a discussion of this choice see Ballone et al. 2021), we instantaneously remove all the gas from the simulations, mimicking the impact of a supernova explosion. We apply the joining/splitting algorithm to the properties of the sink particles at 3 Myr, as detailed in the next sub-section. We refer to Ballone et al. (2020) and Ballone et al. (2021) for more details on the hydrodynamical simulations.

3.2.3 The joining/splitting algorithm

Ballone et al. (2021) introduced a new algorithm to generate stellar populations from sink particles obtained through hydrodynamical simulations. This algorithm consists in either joining or splitting the sink particle masses, which are affected by non-physical effects (such as the simulation resolution and the adopted sink particle algorithm), so to obtain a new, more realistic mass function of "children" stars. In this way the obtained stellar population inherits the turbulent phase space distribution generated from hydrodynamical

Table 3.1: Initial conditions of the $N-$body simulations.

Name	$M_{\rm tot}$ ($M_\odot$)	r_{50} (pc)	r_{10} (pc)	$\alpha_{\rm vir}$	$f_{\rm bin}$
Hydro	6.69×10^3	1.70	0.06	1.53	0.06
King	6.69×10^3	0.42	0.06	1.53	0.06
Loose Fract	6.69×10^3	1.70	0.30	1.53	0.06
Dense Fract	6.69×10^3	0.32	0.07	1.53	0.06

First column: name of the simulation set; second column: total mass $M_{\rm tot}$; third column: half-mass radius r_{50}; fourth column: core radius r_{10}; fifth column: virial ratio $\alpha_{\rm vir}$; sixth column: binary fraction $f_{\rm bin}$ (if original binaries are present).

simulations, but features a realistic mass function. Here we summarize the main steps of the joining/splitting process.

First, a population of stars with a chosen IMF is created, for an assigned value of their total mass. The joining algorithm is used when a star is more massive than the most massive sink particle. According to the joining algorithm, we select the densest region of the sink particle distribution and merge the neighbour sinks until we obtain the mass of the star. The position and the velocity of the star are assigned as the position and the velocity of the center of mass of the joined sinks. The joining algorithm tends to enforce mass segregation in the central regions of the simulated star clusters.

The splitting branch of the algorithm, instead, is applied if a massive sink is more massive than any left star. In this case, we subtract the mass of individual stars from the massive sink particle, until a mass smaller than 0.1 $M_\odot$ is left. The leftover mass is reassigned to the closest sink, so to enforce local and total mass conservation. The children stars of each sink particle are then distributed around the position and velocity of their parent sink according to a virialized Plummer distribution (for this step we make use of the NEW_PLUMMER_MODEL module in AMUSE, Pelupessy et al. 2013). In Ballone et al. (2021), we considered a Plummer half-mass radius of 10^{-3} pc, that allowed a good energy and virial ratio conservation for all the hydrodynamical simulations of the sample. For this work, we prefer a Plummer half-mass radius of 10^{-2} pc because, for this specific star cluster, this choice allows a better conservation of the total energy and a smaller variation of the virial ratio.

The process of joining/splitting is cycled until either all the sink particles or the stars are consumed.

3.2.4 Direct *N*-body simulations

For our direct $N-$body simulations, we made use of the direct summation $N-$body code NBODY6++GPU (Wang et al. 2015) coupled with the population synthesis code MOBSE (Mapelli 2017; Giacobbo et al. 2018; Giacobbo & Mapelli 2018, 2019; Mapelli & Giacobbo 2018), an upgraded version of BSE (Hurley et al. 2000, 2002). NBODY6++GPU implements a 4th-order Hermite integrator, individual block timesteps (Makino & Aarseth 1992) and a Kustaanheimo-Stiefel regularization of close encounters and few-body subsystems (Stiefel et al. 1965; Mikkola & Aarseth 1993). A neighbour scheme (Nitadori & Aarseth 2012) is used to compute the force contributions at short time intervals (irregular force/time steps), while at longer time intervals (regular force/time steps) all the members in the

system contribute to the force evaluation. The irregular forces are evaluated using CPUs, while the regular forces are computed on GPUs using the CUDA architecture. The force integration includes a solar neighbourhood-like static external tidal field (Wang et al. 2016). In all our cases, we consider a star as an escaper if it reaches a distance from the center of density greater than four times the tidal radius of the cluster. The value chosen for the removal distance avoids the presence of potential escapers in the calculation (Takahashi & Baumgardt 2012; Moyano Loyola & Hurley 2013). MOBSE includes up-to-date prescriptions for massive star winds (Giacobbo et al. 2018), for core-collapse supernova explosions (Fryer et al. 2012; Giacobbo & Mapelli 2020) and for pair instability (Mapelli et al. 2021b). NBODY6++GPU and MOBSE are integrated, as described by Di Carlo et al. (2019, 2020b).

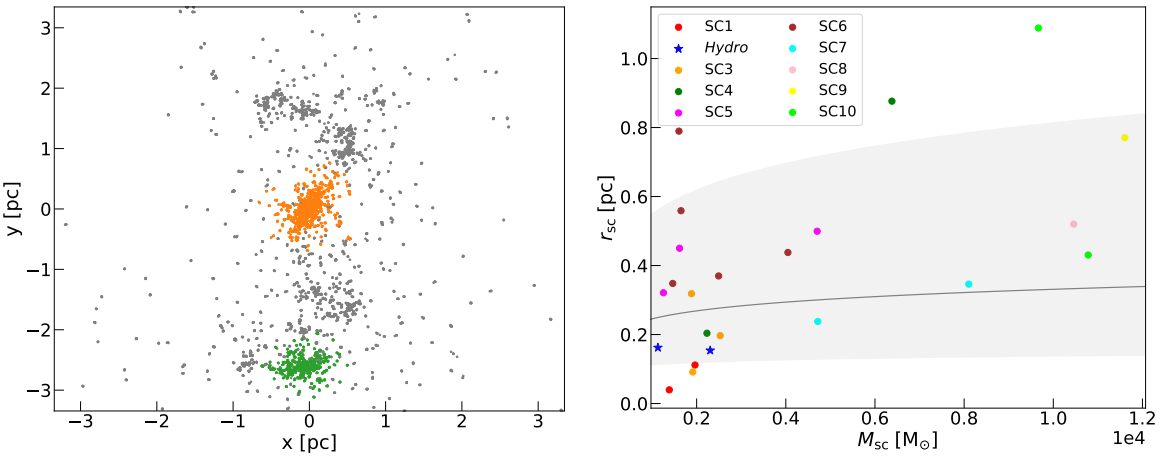

Figure 3.2: **Left panel:** initial spatial distribution of a realization of the *Hydro* stellar cluster after the joining/splitting procedure. The coloured points are the stars that belong to the main (orange) and secondary sub-clump (green). The grey points are the stars that are catalogued as noise points by the DBSCAN algorithm. **Right panel:** relation between the mass ($M_{\rm SC}$) and half-mass radius ($r_{\rm SC}$) of all the sub-clumps of the stellar clusters presented in Ballone et al. (2021). The two sub-clumps of the *Hydro* stellar cluster, which corresponds to SC2 in Ballone et al. (2021), are marked as blue stars. The grey region is the interval defined by the Marks & Kroupa (2012) relation (grey solid line).

3.3 Initial conditions for *N*-body simulations

The initial conditions for the $N-$body simulations from hydrodynamical simulations (hereafter labeled as *Hydro*) are obtained by combining the binary generation algorithm described in Sect. 3.2.1 and the the joining/splitting procedure (Sect. 3.2.3). The main properties of the initial conditions for the star cluster are reported in Table 3.1. The system has a total mass of $M_{\rm tot} = 6687\ M_\odot$, a half-mass radius (defined as the 50% Lagrangian radius centered in the center of density) $r_{50} = 1.70$ pc, and a core radius (defined as the 10% Lagrangian radius centered in the center of density) $r_{10} = 0.06$ pc. After the instantaneous removal of the gas, the system is left in a super-virial state, with $\alpha_{\rm vir} \equiv 2\,T/|V| = 1.53$.

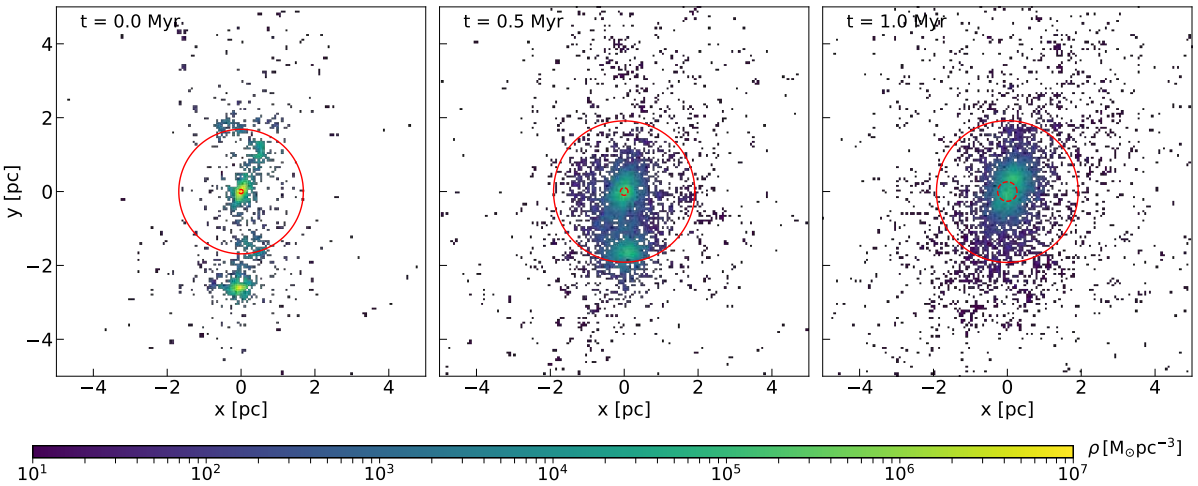

Figure 3.3: Evolution of the cluster in the first Myr. The red solid line is the half-mass radius, and the red dashed line is the core radius. The left-hand panel shows the initial configuration of the system. The central panel shows the system at 0.5 Myr, when the second sub-clump enters the sphere of the half-mass radius, making it decrease. The right-hand panel shows the system at 1 Myr, when the two main sub-clumps are almost merged and start expanding as a monolithic cluster. Every point is weighted with its local density, calculated as the density of the sphere that includes the 500 closest stars.

In order to quantify the impact of different physical ingredients on the dynamical evolution of a stellar cluster, we take into account four different evolutionary cases:

- *Bin*: evolution with original binary stars and without stellar evolution.
- *Bin+SE*: evolution with original binary stars and with stellar evolution. We assumed solar metallicity ($Z = 0.02$, Anders & Grevesse 1989), in order to match the young star clusters of the Milky Way (Portegies Zwart et al. 2010) and to maximize the difference with respect to the case without stellar evolution, because mass loss by stellar winds is extremely high at solar metallicity (e.g., Vink et al. 2001; Kudritzki 2002).
- *NoBin*: case with no original binary stars and no stellar evolution.
- *NoBin+SE*: case without original binary stars but with stellar evolution.

The comparison between the aforementioned four different cases allows us to have a complete view of the impact of binaries and of stellar evolution on the dynamical evolution of a cluster with a realistic phase-space distribution of stars.

For each case, we ran 10 simulations of different joining/splitting realizations in order to filter out stochastic fluctuations.

3.3.1 Comparison with other initial conditions

We compared the evolution of the *Hydro* initial conditions to that of other initial phase-space distributions, which are commonly used in studies of star cluster dynamics. In order to have a fair comparison, we set initial conditions that match the mass scale and either the central length scale (r_{10}) or the global length scale (r_{50}) of our *Hydro* clusters. All the initial conditions are generated by coupling our binary generation code to McLuster (Küpper et al. 2011) as descibed in Section 3.2.1. We considered three cases:

- *King*: a King (1966) model matching the core radius of the hydrodynamical initial conditions. To match the core radii of the two cases, we generated a King model with a reduced half-mass radius, $r_{50} = 0.25$ pc, and a high value for the central concentration, $W_0 = 9$. The chosen value for the central concentration is typical of clusters that are believed to have undergone core-collapse. For this reason a post-core collapse evolution may be expected for both this case and for the central regions of the hydrodynamical case.

- *Loose Fract*: a fractal sphere, with the same total mass and half-mass radius as the *Hydro* case. For this case, we selected a fractal dimension $D = 1.6$, which gives a good description of the sink particle distribution from which the *Hydro* clusters are generated, as shown in Ballone et al. (2020).

- *Dense Fract*: a fractal sphere with the same mass and fractal dimension as the previous case, but with a half-mass radius set according to the Marks & Kroupa (2012) relation:

$$r_{50} = 0.10^{+0.07}_{-0.04}\,\mathrm{pc}\left(\frac{M_{\mathrm{tot}}}{\mathrm{M}_\odot}\right)^{0.13\pm0.04} \tag{3.5}$$

  In this case, we have $r_{50} \approx 0.3$ pc and $r_{10} \approx 0.07$ pc. Interestingly, the core radius results very similar to that of the *Hydro* initial conditions.

For all these initial conditions we set the same virial ratio as the *Hydro* case. The physical properties for all the initial conditions are summarized in Table 3.1.

3.4 Results

3.4.1 Initial clumpiness of the stellar cluster

The initial space distribution of the *Hydro* simulation is clumpy and sub-structured, as can be seen in Fig. 3.2. The stellar cluster mainly consists of two very dense main sub-clumps and some minor and irregular clusters and filaments. We first defined the two main sub-clumps by using the DBSCAN (Density-Based Spatial Clustering of Applications with Noise) algorithm (Ester et al. 1996)[2]. This algorithm allows to group together points in high-density regions: these are labeled as core points and are distinguished from points

[2]The implementation we referred to is that of the python library Scikit-learn (sklearn.cluster.DBSCAN, Pedregosa et al. 2011). DBSCAN requires to define two parameters, ϵ and $minPts$. The parameter $minPts$ is the number of points within the reference distance ϵ needed for a point to be considered as a core point. Otherwise, it is labeled as noise. For our case, we set these parameters based on the half-mass radius of the cluster and on the total number of stars: $minPts = N_{tot}/10$ and $\epsilon = r_{50}/5$.

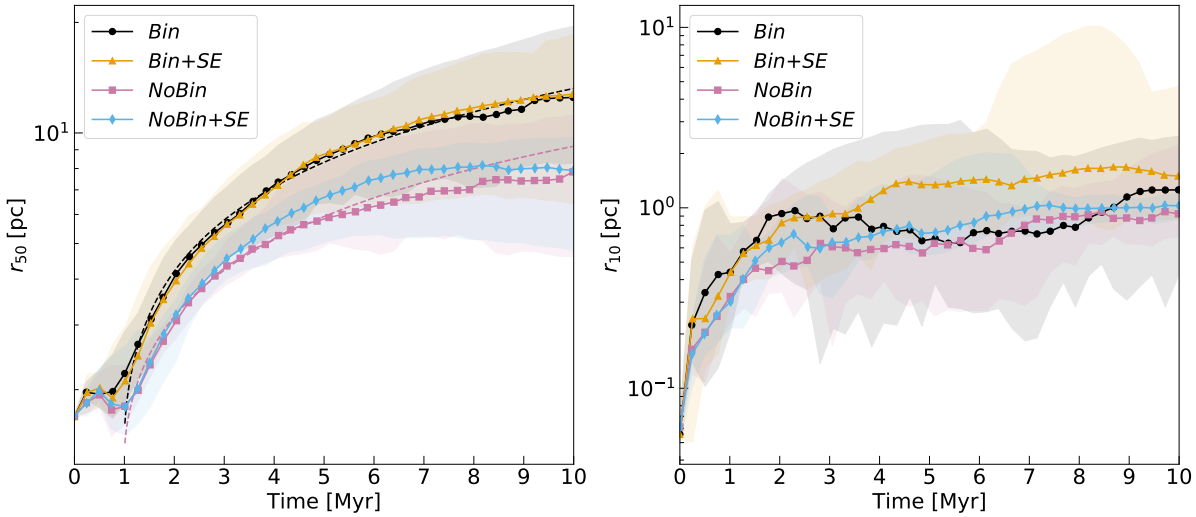

Figure 3.4: Early evolution of the 50% Lagrangian radius (r_{50}, left-hand panel) and 10% Lagrangian radius (r_{10}, right-hand panel) for our set of $N-$body simulations. Different lines represent different evolutionary configurations: with original binary stars and without stellar evolution (*Bin*, black circles), with original binary stars and with stellar evolution (*Bin+SE*, ochre triangles), without original binary stars and without stellar evolution (*NoBin*, pink squares), without original binary stars but with stellar evolution (*NoBin+SE*, cyan diamonds). For each case, the shaded areas define the range of variation (over the 10 different realizations of each model) of r_{50} (left) and r_{10} (right), while solid lines and markers are the median values. The dashed black and pink lines are our best fit according to eq. (3.6).

in low density areas, that are labeled as noise. The result of the clustering procedure is shown in the top panel of Fig. 3.2: the algorithm manages to identify the two main sub-clusters.

The main sub-clump has a mass of $M_{\rm sc} \approx 2304\,{\rm M}_\odot$ (35% of the total mass) and a half-mass radius of $r_{\rm SC} = 0.15\,{\rm pc}$, while the second sub-clump has a mass of $M_{\rm sc} \approx 1132\,{\rm M}_\odot$ (17% of the total mass) and a half-mass radius of $r_{\rm SC} = 0.16\,{\rm pc}$. We checked if the sub-clump masses and half-mass radii are consistent with eq. (3.5), that is the relation between total mass and half-mass radius found in star-forming cloud cores by Marks & Kroupa (2012). Recently, Fujii et al. (2021) found that this relation holds in N-body/SPH simulations for embedded clusters with mass up to about $10^3\,{\rm M}_\odot$ and it is preserved after gas expulsion. In the lower panel of Fig. 3.2, we show the two sub-clumps together with the other stellar clusters simulated by Ballone et al. (2021), that extend to higher masses (between 10^3 and $10^4\,{\rm M}_\odot$). As Fig. 3.2 shows, this sample is well consistent with eq. (3.5).

3.4.2 Global evolution

Early evolution ($t < 1\,{\rm Myr}$)

Figure 3.3 shows the very first phase ($t \leq 1\,{\rm Myr}$) of the evolution for one representative cluster. At $t = 0$ Myr, the center of density is located well within the main clump, while the second main sub-clump is out of the sphere defined by the half-mass radius. At $t = 0.5$

Myr, the cluster structure has significantly evolved. On the one hand, at small scales, each sub-clump rapidly expands, as a consequence of the instantaneous gas removal, thus lowering its local density. On the other hand, the two main sub-clumps get closer to each other, thus balancing the small scale expansion on a larger scale. These competing mechanisms characterize the first ≈ 1 Myr of the simulation.

At $t = 1$ Myr the cluster has nearly a monolithic shape. The half-mass radius is slightly larger ($r_{50} \approx 2$ pc) than at the beginning of the simulation (when $r_{50} \approx 1.7$ pc), while the core radius has grown much faster, as can be easily seen from Fig. 3.3. Typically, a realization reaches a monolithic shape after $1 - 1.5$ Myr (only in a limited number of cases, this condition is fulfilled at about $2 - 2.5$ Myr), after a short period in which the two sub-clumps tidally interact without merging. The resultant cluster has an elongated shape, as a consequence of the strong tidal interaction and the relative motion between the sub-clumps.

The range of merger timescales is in agreement with the results by Fujii (2015), whose simulations can simultaneously reproduce the properties of different types of young star clusters, from massive and dense ones to open clusters and looser OB associations. In this sense, when N-body simulations are exploited to study the early evolution of stellar clusters, the timescale of sub-clump mergers is strongly dependent on the initial energetic state of the molecular cloud, as can be inferred by comparing the results in Fujii & Portegies Zwart (2015) and Ballone et al. (2021), who initialized their clouds in a marginally bound state. On the observational side, this kind of mergers between sub-clumps seems to be disfavoured to explain the formation of young star clusters like NGC 3603 (Banerjee & Kroupa 2013;2015), whose observational properties require either a monolithic formation channel or a prompt assembly in $t < 1$ Myr. However, the results by Sabbi et al. (2012) hint that ongoing mergers between very young clusters (such as R136 and the Northeast Clump in NGC 2070) may also occur.

Cluster expansion

In order to consider both the initial clumpy evolution and the successive monolithic expansion, we evolved the clusters for 10 Myr. Figure 3.4 shows the expansion of the cluster, described by r_{50} and r_{10}, for all the four evolutionary cases. As a consequence of the mechanism described in Section 3.4.2, the half-mass radius initially grows, reaches a peak at about 0.5 Myr, that is when the secondary sub-clump enters the sphere of the half-mass radius of the main sub-clump, and then decreases. At 1 Myr, r_{50} reaches a minimum and then grows monotonically. The expansion of r_{50} is no longer influenced by the relative sub-clump motion, which at this time have merged or are very close to each other, but is due to the small scale expansion that has now reached larger scales. In contrast, the core radius grows rapidly since the very beginning of the simulation, because the sub-clump motion has no effect at these small scales.

The impact of binary stars is evident in the second phase of the evolution of the cluster, during the monolithic expansion. In fact, clusters with original binaries expand faster after 1 Myr: at this point the large-scale interaction of the sub-clumps is no longer present, and the density in the central region is still high enough (of the order of $10^3 - 10^4$ $M_\odot$ pc^{-3}) to allow efficient interactions and energy exchange between the binary stars and their surrounding environment. In the very first phases, instead, the faster expansion due to binary stars is balanced by the global evolution of the sub-clumps.

As explained in Sect. 3.3.1, the central regions of the cluster are matched by a King

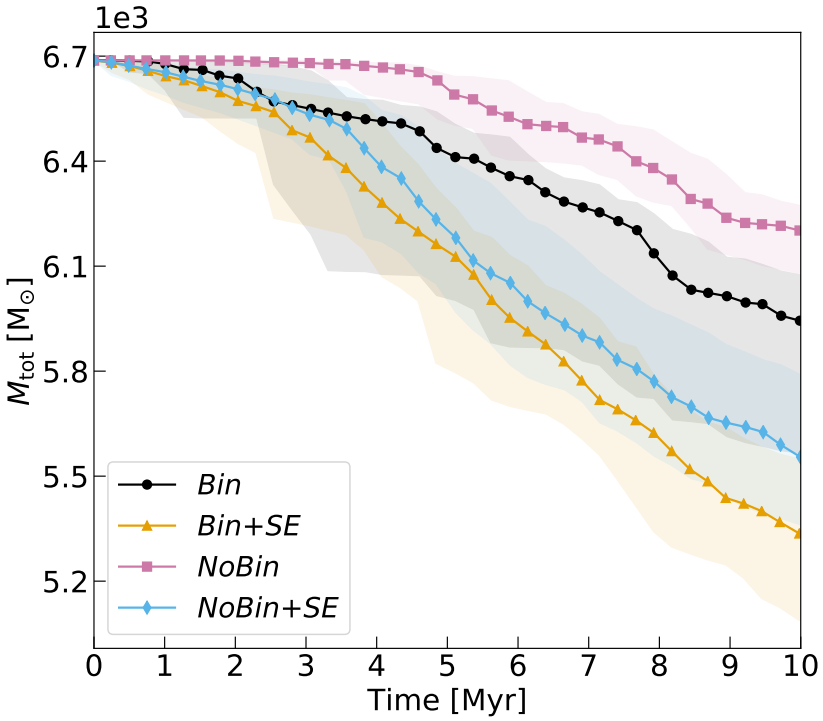

Figure 3.5: Mass variation in the four evolutionary cases we considered. Lines and colours are the same as in Fig. 3.4.

model with $W_0 = 9$, that is typical of stellar clusters that are thought to have undergone core-collapse. We thus compared the monolithic expansion of the cluster with that expected based on a self-similar evolution, at constant mass (Spitzer 1987):

$$r_{50} = \mathcal{B}\, t^{2/3}, \tag{3.6}$$

where $\mathcal{B}$ is a proportionality constant. If the evolution of the cluster is a post-core collapse expansion, the time increase of r_{50} should be roughly consistent with eq. (3.6). We performed a fit to the median values of r_{50} from 1 Myr curves by using eq. (3.6). The resulting best-fit curves are the dashed lines in the left-hand panel of Fig. 3.4. We show the curves for the cases *Bin* and *NoBin*, where the lack of stellar evolution should avoid the presence of additional effects (e.g., mass loss) and make the dynamical effect by binaries more evident. The curves of both cases seem to be consistent with a post-core collapse phase until 10 Myr.

Mass loss

As the cluster expands, stars get further away from its center, until they are eventually removed from the cluster dynamics by the tidal field of the host galaxy. This makes the total mass of the stellar system decrease. The presence of binary stars enhances the number of escaping stars, by powering a faster expansion. Also, close interactions between binary stars and single (or other binary) stars may lead to the ejection of stars, and possibly also of binary systems. In addition, stellar evolutionary processes (e.g. stellar winds, supernova explosions) make single stars, and thus the cluster, lose mass.

Figure 3.5 shows the variation of the total mass of the cluster (the details about the removal of the escapers are given in Sect. 3.2.4). Stellar evolution gives the main contribution to mass loss in the early stages of the simulation, resulting in a steeper slope of the mass evolution. After 10 Myr, the mass loss in the cases with stellar evolution is twice as large as that in the cases without stellar evolution. The absence of original binaries delays the mass loss, because the cluster needs to form its binaries dynamically before they start ejecting other stars.

Energy variation

Figure 3.6 shows the evolution of the total kinetic energy ($E_{\rm k}$), the total potential energy ($E_{\rm g}$) of the centers of mass and the total binding energy of binary systems ($E_{\rm b}$). Binary stars produce an initial sharp increase of the kinetic energy by yielding their internal energy to the surrounding stars. This results in the fast cluster expansion seen in Fig. 3.4. After this initial sharp increase, the kinetic energy of the clusters with original binaries decreases at a fast rate as a consequence of the ejection or evaporation of high velocity stars. After the first ~ 5 Myr, the kinetic energy of the star clusters with original binary systems becomes similar to that of the other clusters, and they evolve in the same way for the rest of the simulation.

The total binding energy of the initial binary population is much higher than the typical gravitational energy of the centers of mass. Our original binary stars are, in fact, mostly hard and a small fraction of their total internal energy is sufficient to deeply affect the evolution of the cluster. The decrease of the total binding energy springs from two factors. Firstly, some binary stars escape from the system. This causes the slow decrease of the black line in Fig. 3.6. Secondly, stellar and binary evolution tend to remove binary stars from the population, via mergers, supernova explosions but also direct collisions between stars. This process is important since the very first stages, because the binary fraction is very high for the most massive stars and because the initial semi-major axes from Sana et al. (2012) are skewed to small values. By comparing the *Bin* models and the *Bin+SE* models, one can infer that this second factor is the main responsible for the variation of the total binding energy.

If there are no original binary systems (*NoBin* and *NoBin+SE* models), the cluster creates its own population, with binding energies of the order of the gravitational energy scale. The case without stellar evolution is characterized by a monotonic increase of the binding energy, where binaries form and the hardest ones tend to harden. In the end, the total binding energy is dominated by the binding energy of a very few binaries. In presence of stellar and binary evolution, after an initial increase, the total binding energy decreases when stellar and binary evolution processes take over.

3.4.3 Binary populations

In order to understand how binary populations evolve and interact with the host cluster, we must estimate how their binding energy distribution is related to the mean energy of the cluster. Figure 3.7 shows the distribution of binding energies for one representative simulation at four different snapshots, in presence of original binary systems and stellar evolution.

At the beginning of the simulation, binding energies are very large if compared to the mean kinetic energy. In particular, the hardest part of the distribution is about five

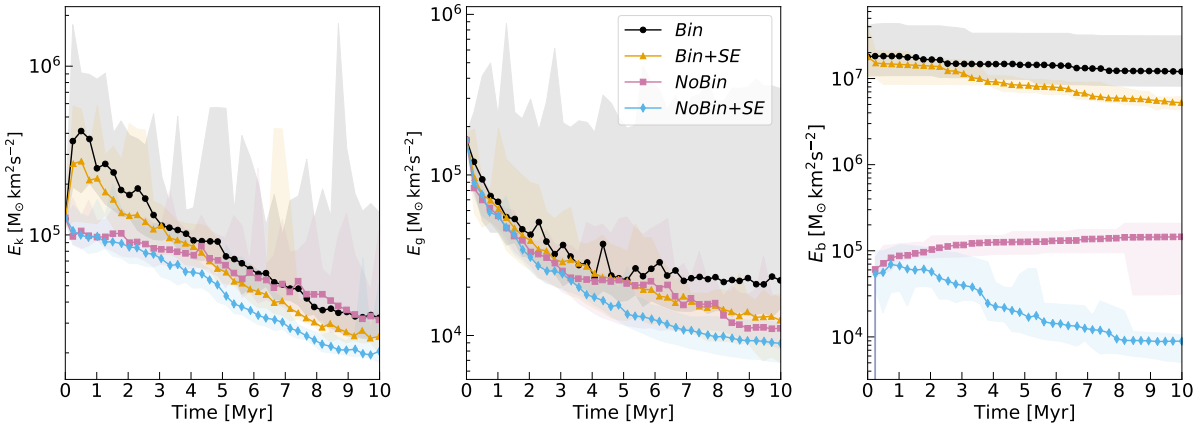

Figure 3.6: Evolution of the total kinetic energy (E_k, left), of the total gravitational energy of the centers of mass (E_g, middle) and of the total binding energy of the binary systems (E_b, right). Lines and colours are the same as in Fig. 3.4.

orders of magnitude higher than the typical energy scale of the star cluster. This means that the other stars in the cluster "see" the hardest binary systems as if they were single stars: the cross section of the hardest binary systems is so small that these can hardly interact with single stars.

In absence of original binary systems with a sufficiently large cross section, the star cluster creates new binary systems, with a larger semi-major axis and, thus, a large cross section for three-body encounters. This is the reason behind the large number of binary systems created at successive snapshots, that are close to the mean kinetic energy of the cluster. Finally, the loosely bound tail of the binary distribution consists of soft binaries that are continuously created and destroyed by dynamical interactions with their neighbours.

Orbital parameters and multiplicity fraction

Figure 3.8 shows the evolution of the probability density function (PDF) of the binary semi-major axes and of the mass ratios and the multiplicity fraction, defined as the sum of the fraction of binaries and the fraction of bound triple systems. We consider two representative populations, one for simulations with original binaries (the same as in Fig. 3.7) and one for simulations without original binaries, in presence of stellar evolution.

In presence of original binaries, the PDFs significantly change with time, because of the creation of a large number of dynamical binaries. In particular, the distribution of semi-major axes extends to higher values, and shows a secondary peak at 10^3 AU, the typical value at which dynamical binaries form. This value corresponds to $\approx 5 \times 10^{-3}$ pc, that is the lowest distance scale (it is the typical distance of stars split into Plummer spheres). As explained above, the cluster responds to the absence of interacting binaries by creating its own. This also explains why the distributions of the dynamically formed semi-major axes and mass ratios are very similar to those that form in absence of original binaries (as shown in the lower-left panel of Fig. 3.8).

As for the mass ratios' (q) distribution, dynamical interactions produce a steep increase of the PDF at high values, because the new binaries are typically formed by the low mass

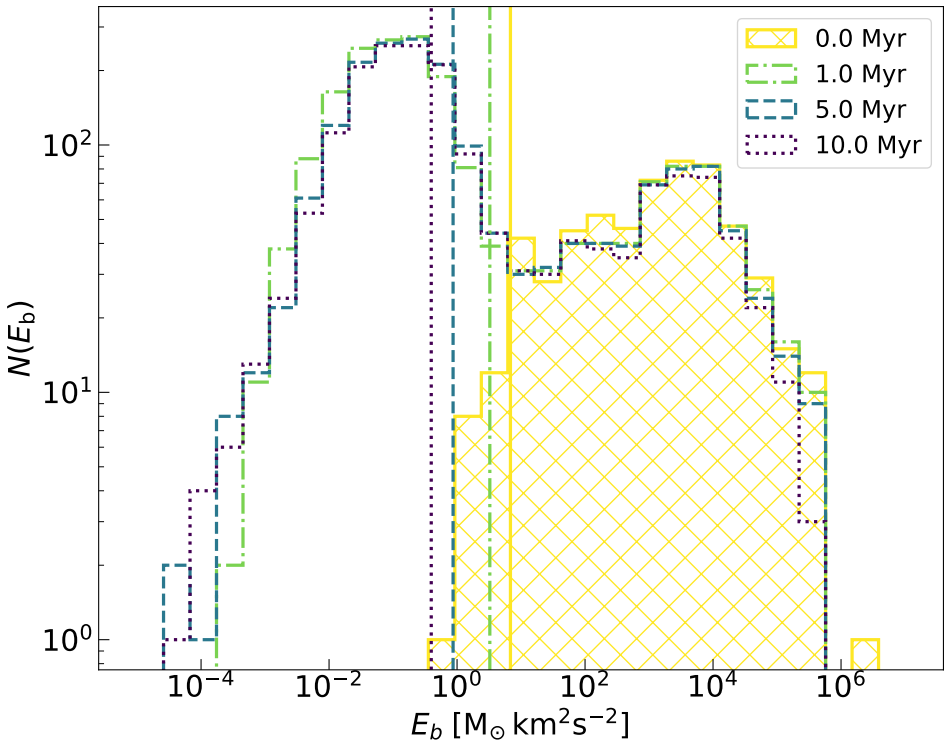

Figure 3.7: Distribution of binding energies for a cluster, in presence of original binaries and stellar evolution. Four different snapshots are shown: $t = 0$ Myr (yellow solid line, hatched area), $t = 1$ Myr (green dot-dashed line), $t = 5$ Myr (blue dashed line), $t = 10$ Myr (magenta dotted line). The vertical lines represent the mean kinetic energy of the cluster, defined as the mean kinetic energy of the centers of mass within two half-mass radii (where binaries are more likely to interact).

stars in the Plummer spheres. Also, the distribution of mass ratios extends towards lower values than the initial lower limit ($q = 0.1$). Most of the variations in the PDFs take place in the first 1 Myr, that is when the environment is dynamically active. Since then, the binary distributions remain almost unchanged. Also, the large number of dynamically-created small-mass binaries increases the total multiplicity fraction from $\approx 6\%$ to $\approx 26\%$. In particular, these systems populate the lowest mass bin of Figure 3.1, by increasing the binary fraction from 0 to 20%.

In the absence of original binaries (*NoBin+SE* case), dynamical interactions produce a distribution of semi-major axes that is similar to the distribution of dynamically formed binary systems in the *Bin+SE* case, but cannot reproduce the hardest part of the Sana et al. (2012) binary distribution. Also, dynamical mechanisms tend to create equal-mass binaries. Remarkably, the binary fraction of dynamically formed binaries in the *NoBin+SE* case is mass-dependent: it grows with the mass of the primary star and mimics the trend of the observed distribution (Moe & Di Stefano 2017).

Hence, in the absence of original binary stars, the cluster is able to produce a mass-dependent binary fraction. However, there is not sufficient energy at small scales to reproduce the hardest part of the initial distribution of Sana et al. (2012).

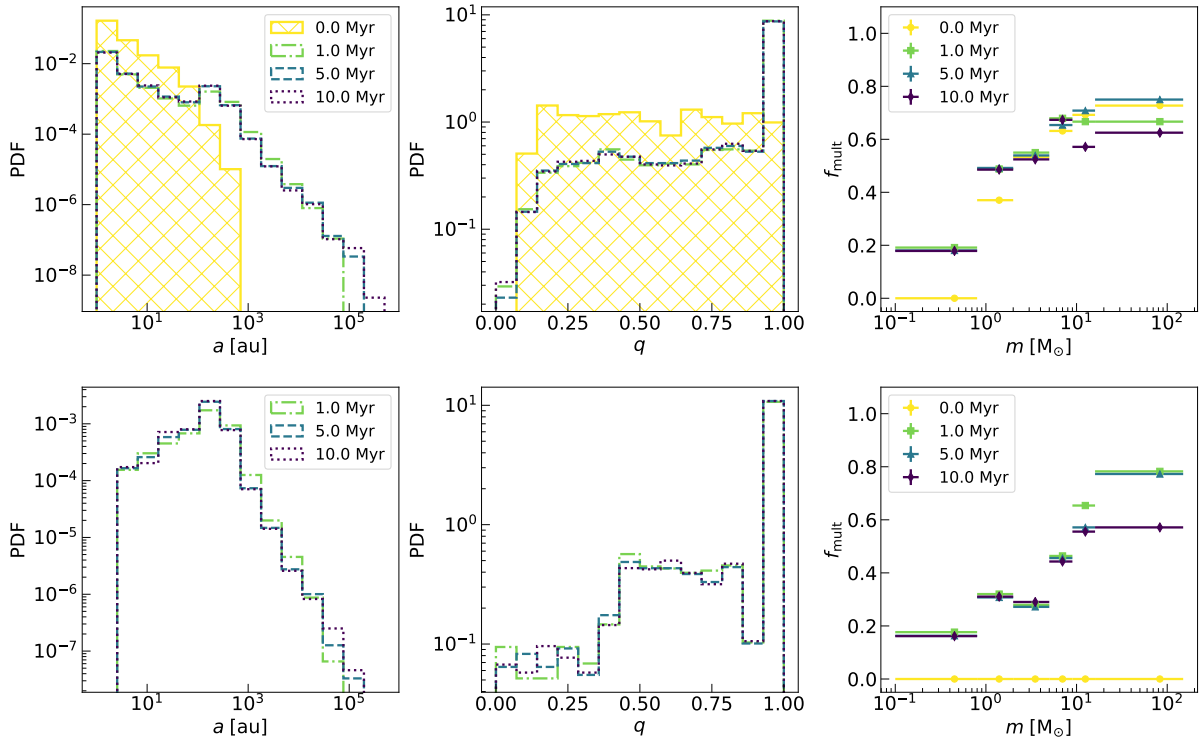

Figure 3.8: Distribution of semi-major axes (left), mass ratios (center) and multiplicity fractions (right) for a cluster with (upper panels) and without (lower panels) original binaries. Four different snapshots are shown: $t = 0$ Myr (yellow solid line, hatched area, circles), $t = 1$ Myr (green dot-dashed line, squares), $t = 5$ Myr (blue dashed line, triangles), $t = 10$ Myr (magenta dotted line, diamonds). The lower right panel shows that, in the absence of original binary stars, the cluster is able to dynamically produce a mass-dependent binary fraction, reminiscent of the observed one.

Exchanges

The degree of interactions between the binary systems and their host cluster can be quantified by evaluating the number of exchanges that take place. Fig. 3.9 shows the variation of the incremental number of exchanges. The original binaries take part in a limited number of exchanges, most of which are in the first 2 Myr of the cluster's life, when densities allow an efficient interaction with the other stars. In the following evolution, the original binaries interact much less, as indicated by the flatness of the curve. Nonetheless, because the original binaries are very hard, the few interactions they undergo exchange a sufficient amount of energy to affect the global evolution of the cluster, as shown by the evolution of r_{50} (Fig. 3.4).

Interestingly, the total number of exchanges is about two orders of magnitude higher than that of original binaries and does not depend on the presence of an initial population of binary stars. This aspect indicates that the cluster under consideration is a very active environment for binary interactions and confirms that the most interacting binaries are dynamically created by the cluster itself. However, most of these exchanges involve binaries that are loosely bound (see also Fig. 3.7) and thus their energy exchange is quite low with respect to that of the original binaries.

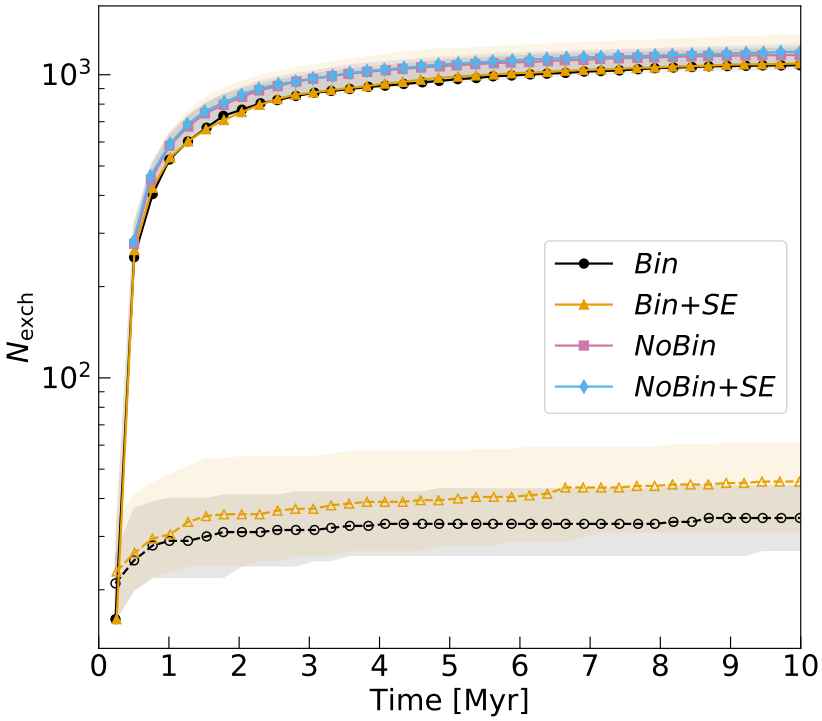

Figure 3.9: Number of exchanges $N_{\rm exch}$ as a function of time for the entire population of binaries (solid lines, filled markers) and for the sub-population of original binaries (dashed lines, empty markers). $N_{\rm exch}$ is calculated at steps of 0.25 Myr. Lines and colours are the same as in Fig. 3.4.

3.4.4 Comparison with other initial conditions

The novelty of the *Hydro* initial conditions can be better understood if we compare their evolution to that of other, more idealized initial conditions. To this purpose, we ran simulations with the initial conditions presented in Section 3.3.1. Since we want to focus on the dynamical evolution with different initial phase-space distributions, we decided to run these simulations without stellar evolution.

Cluster Expansion

Figure 3.10 shows the evolution of the medians of the distributions of r_{50}, of r_{10}, and of the ratio r_{50}/r_{10}, that measures the concentration of the system. In the initial conditions, the *Hydro* clusters have a much larger ratio r_{50}/r_{10} than the other models. Hence, they have very dense cores and rather extended halos, because of the scale of the sub-structures. For these intrinsic differences, the evolution of the characteristic radii of the *Hydro* simulations is considerably different from that of the other distributions.

In the first Myr, the *Hydro* case is the only one that does not show a monotonic increase of r_{50} because of the initial sub-cluster motion (as discussed in Section 3.4.2). All of the other initial conditions develop a monotonic increase of r_{50} and r_{10}, but with different slopes. The *Loose Fract* case, that is initialized with the same half-mass radius as the *Hydro* case, shows a mild expansion on both scales, due to its supervirial state. The low density of the central regions (the initial value of r_{10} is larger than in the *Hydro* case

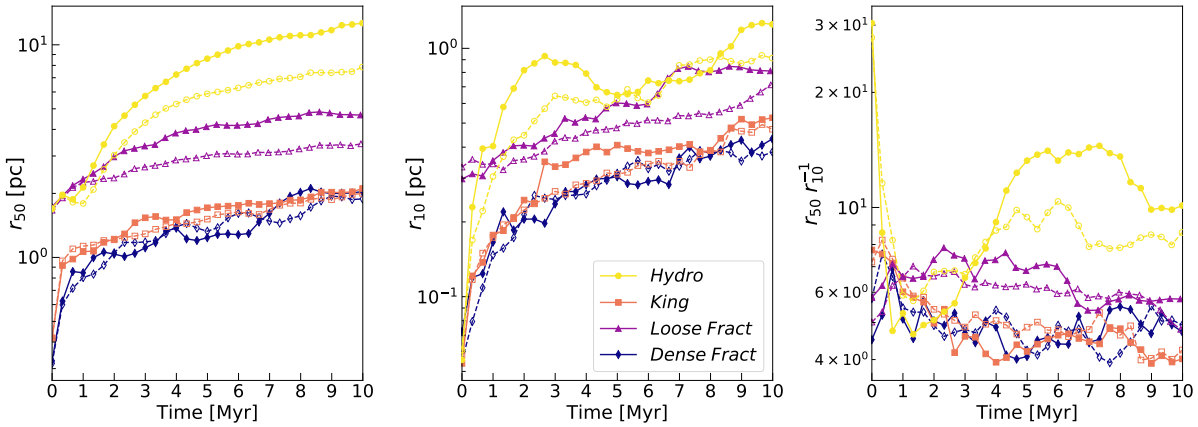

Figure 3.10: Early evolution of the 50% Lagrangian radius (left-hand panel), the 10% Lagrangian radius (central panel), and the concentration of the cluster, quantified by r_{50}/r_{10} (right-hand panel). Different lines represent the medians of different initial phase-space distributions: *Hydro* (yellow circles), *King* (pink squares), *Loose Fract* (magenta triangles), *Dense Fract* (blue diamonds). The solid lines and filled markers represent clusters with original binaries, while the dashed lines and empty markers correspond to clusters without original binaries.

by a factor of 5, see Tab. 3.1) does not allow efficient star-star interactions, that would power a faster expansion. The *King* and *Dense Fract* models, that are set to match the core radius of the initial *Hydro* simulations, undergo a stronger expansion from the very beginning of their evolution. These two different initial conditions display a very similar behaviour.

The peculiarity in the evolution of the *Hydro* case is evident when the evolution of the ratio r_{50}/r_{10} is taken into account. All the cases except the *Hydro* show a monotonic slow decrease for the r_{50}/r_{10} ratio, that indicates that the systems expand at a similar rate at both scales. The *Hydro* initial conditions, instead, show an initial steep decrease of r_{50}/r_{10}, because the growth of r_{50} is balanced by the sub-clump motion (see Fig. 3.4), while at smaller scales the cluster expands rapidly. Even when the cluster has reached a nearly monolithic shape, the evolution of its r_{50}/r_{10} ratio is very different from the other initial conditions: this ratio rapidly increases until it reaches a maximum at about 5 Myr. Such a difference may be explained in terms of the stronger mass segregation that features the *Hydro* simulation (we will discuss this point in Sect. 3.5).

Binding energies

Figure 3.11 shows the evolution of the total binding energy for different initial conditions. In absence of original binaries, every initial configuration creates its own population and the resulting total binding energy is strictly connected to the initial energy scale of the system. In particular, the *Hydro*, *King* and *Dense Fract* final binding energies are similar to each other as they are initialized with similar core radii, whereas the total binding energy of the *Loose Fract* systems is about one order of magnitude lower. Most of the total binding energy is contained in a limited number of binaries (from 2 to 5) that go on hardening as the simulation proceeds. This relation between the total binding energy

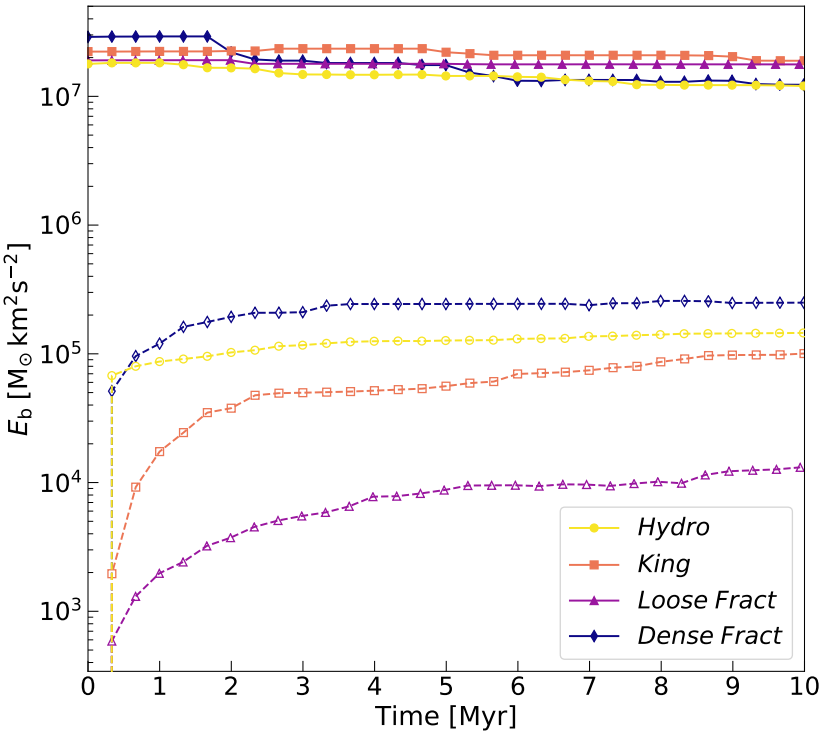

Figure 3.11: Evolution of the total binding energy of the binary systems. Lines and colours are the same as Fig. 3.10.

and the global scales of the clusters confirms that star clusters are self-regulating systems with respect to their binary populations (Goodman & Hut 1989; Goodman et al. 1993): in absence of binaries, each system creates its own population of binaries, with binding energies of the order of its global energy scales.

3.5 Discussion

The *Hydro* star clusters show a very distinctive evolution of the r_{50}/r_{10} ratio. We studied what factor determines the growth of this ratio during the monolithic phase. In particular, we focus on the impact of the initial degree of mass segregation. In fact, a high degree of mass segregation would allow the most massive stars to rapidly form a centrally concentrated core that is dynamically separated from the rest of the cluster, the scenario usually referred to as Spitzer instability (Spitzer 1969). If this happens, the distribution of massive stars is hotter than the rest of the cluster, because they remain more concentrated and the local value of the velocity dispersion decreases with the distance from the center.

Previous $N-$body simulations have found evidence that, for a wide range of initial conditions, the most massive stars in a system do not move slower than the low-mass stars (Parker & Wright 2016; Spera et al. 2016; Webb & Vesperini 2017), as one would expect based on the tendency of stellar systems towards energy equipartition (Trenti & van der Marel 2013; Bianchini et al. 2016). A confirmation that the most massive stars can have higher velocities has also been found in proper motion observations of the open

cluster NGC 6530 (Wright et al. 2019). Wright & Parker (2019) showed that this aspect can be explained by the combination of Spitzer instability and a cool collapse. If the most massive stars remain more concentrated than the rest of cluster, then the core, that is mostly populated by these massive stars, is expected to expand slower than the rest of the cluster.

To quantify the impact of mass segregation on the evolution of the cluster, we selected the 30 most massive stellar particles[3] and evaluated the ratio between their velocity dispersion $\sigma_{\rm mass}$ and the velocity dispersion of all the stellar particles $\sigma_{\rm all}$. For these calculation, only stars inside two half-mass radii are considered, as done in Wright & Parker (2019). The evolution of the ratio between these two velocity dispersions is shown in the upper panel Fig. 3.12. In all the phase-space configurations except the *Hydro*, the velocity dispersion ratio is about one and does not change very much with time. In the *Hydro* case, instead, the high initial value of the velocity dispersion ratio suggests that the stellar cluster has a strong initial mass segregation. Also, during the monolithic phase, the velocity dispersion ratio grows because, after the merger of the two main sub-clumps, their most massive stars rapidly segregate towards the center, while the system globally expands. The segregation of the massive stars towards the center of the potential well may be enhanced by the fact that, in each sub-clump, the stars have already formed a massive core that segregates as one single, very massive particle (see also Fujii et al. 2012). In the case with original binaries, the velocity dispersion value grows enough to match the observed value for NGC 6530.

The connection between the growth of the velocity dispersion ratio and the degree of mass segregation is confirmed by the trend shown by the ratio of the half-mass radii of the 30 most massive stellar particles $r_{\rm mass}$ and the overall half-mass radius r_{50}, shown in the bottom panel of Fig. 3.12. The *Hydro* simulations show an initial strong degree of mass segregation. The initial small scale expansion makes this ratio instantly grow; but, then, it rapidly decreases because of the strong segregation at the center of the cluster. The initial degree of mass segregation seems to be the most important factor in the growth of the velocity dispersion ratio in the *Hydro* case: a stronger initial degree of mass segregation triggers the rapid formation of a dense core that expands more slowly than the rest of the cluster. Also, the rapid formation of a dense core could influence the interaction rate between binaries and the host cluster. If the original hard binaries live in a denser environment, they are more likely to interact: this explains why the *Hydro* initial conditions present different expansions for the cases with and without binaries (Fig. 3.10).

3.6 Summary and Conclusions

We studied the early dynamical evolution ($t < 10\,$Myr) of young stellar clusters with realistic populations of binaries and different initial phase-space distributions. The initial conditions for our $N-$body simulations are obtained by combining a new algorithm to generate realistic stellar and binary distributions (Sana et al. 2012; Moe & Di Stefano 2017) with the joining/splitting algorithm defined in Ballone et al. (2021), to derive initial conditions from hydrodynamical simulations.

[3]In the case of a binary, we consider the particle with a mass equal to the total mass of the binary and place in the center of mass of the binary.

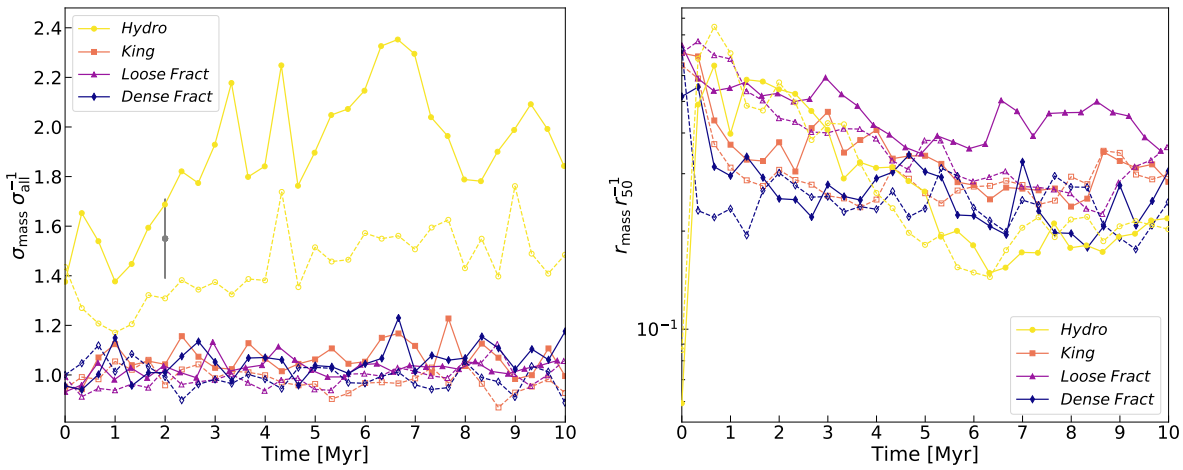

Figure 3.12: **Left panel:** evolution of the ratio between the velocity dispersion of the 30 most massive star particles $\sigma_{\rm mass}$ and the velocity dispersion of all the stars inside inside $2\,r_{50}$, $\sigma_{\rm all}$. The grey data point with error bar is the observed value for NGC 6530 (Wright et al. 2019). **Right panel:** evolution of the ratio between the half-mass radius of the 30 most massive star particles ($r_{\rm mass}$) and the overall half-mass radius, r_{50}. Lines and colours are the same as Fig. 3.10.

For the hydrodynamical initial conditions (*Hydro* cluster), we considered different evolutionary cases by switching on and off the presence of original binary stars and stellar evolution in order to weight their contribution to the dynamical evolution. Our results show that the evolution of the cluster is characterized by two distinct evolutionary phases: first, the global expansion of the cluster is balanced by the approaching of its main sub-clumps, while at small scales the cluster expands instantaneously. After 1 Myr, the cluster has reached a nearly monolithic shape and expands as a whole, following a post-core collapse expansion. Binaries tend to speed up the expansion of the cluster in this phase, making the half-mass radius expand faster, while stellar evolution has a minor impact on the early dynamical evolution of the cluster, but has a major impact on mass loss.

We compared the evolution of the *Hydro* star cluster to that of star clusters with spherical distributions of stars (*King*, *Loose Fract*, *Dense Fract*). The main difference between the *Hydro* cluster and the others relies in the evolution of the r_{50}/r_{10} ratio, that measures the concentration of the system. The *Hydro* cluster, in fact, shows a distinctive trend of r_{50}/r_{10}. At the beginning of the simulations, r_{50}/r_{10} is much larger in the *Hydro* cluster than in the other models, because the *Hydro* cluster is an aggregate of several sub-clumps, resulting in a large total half-mass radius, but its core radius is very small, since it basically coincides with the core radius of the densest sub-clump. The r_{50}/r_{10} ratio decreases very fast (< 1 Myr) in the *Hydro* cluster, reaching values similar to the other clusters, because of the hierarchical merger of the sub-clumps, which reduces the total half-mass radius. However, at $t > 1$ Myr the value of r_{50}/r_{10} keeps decreasing in the spherical models, while it grows again in the *Hydro* case. The late growth of r_{50}/r_{10} in the *Hydro* cluster is due to its initial high degree of mass segregation, which allows it to form a centrally concentrated core of massive stars. As this core expands more slowly than the rest of the cluster, the ratio between the velocity dispersion of the most massive

stars and that of all the stars increases. In the case with binaries, it grows enough to match the observed value for NGC 6530 (Wright et al. 2019).

The initial binary stars we set based on observational constraints (Sana et al. 2012; Moe & Di Stefano 2017) are generally too hard to interact in an efficient way with the host environment. The stellar systems recover from the lack of interacting binaries by dynamically creating additional binaries with binding energy of the order of their kinetic energy. The dynamically formed binaries are not hard enough to reproduce the hardest part of the initial distribution of Sana et al. (2012). Also, in the absence of original binaries, the dynamically formed binaries show a binary fraction that increases with the mass of the primary star. This behaviour spontaneously reproduces the relation between binary fraction and stellar mass found in observations (Moe & Di Stefano 2017).

Acknowledgements

We thank the anonymous referee for their useful comments. MM, AB, UNDC, NG and SR acknowledge financial support by the European Research Council for the ERC Consolidator grant DEMOBLACK, under contract no. 770017. NG is supported by Leverhulme Trust Grant No. RPG-2019-350 and Royal Society Grant No. RGS-R2-202004. MP's contribution to this material is supported by Tamkeen under the NYU Abu Dhabi Research Institute grant CAP3. We acknowledge the CINECA-INFN agreement, for the availability of high performance computing resources and support. We also thank Simon Portegies Zwart for useful discussions.

Chapter 4

Dynamics of binary black holes in young star clusters: the impact of cluster mass and long-term evolution

Based on:
Torniamenti S., Rastello S., Mapelli M., Di Carlo U. N., Ballone A., Pasquato M., "Dynamics of binary black holes in young star clusters: the impact of cluster mass and long-term evolution", 2022, MNRAS 517, 2953

Abstract

Dynamical interactions in dense star clusters are considered one of the most effective formation channels of binary black holes (BBHs). Here, we present direct $N-$body simulations of two different star cluster families: low-mass ($\sim 500-800$ $M_\odot$) and relatively high-mass star clusters (≥ 5000 $M_\odot$). We show that the formation channels of BBHs in low- and high-mass star clusters are extremely different and lead to two completely distinct populations of BBH mergers. Low-mass clusters host mainly low-mass BBHs born from binary evolution, while BBHs in high-mass clusters are relatively massive (chirp mass up to ~ 100 $M_\odot$) and driven by dynamical exchanges. Tidal disruption dramatically quenches the formation and dynamical evolution of BBHs in low-mass clusters on a very short timescale ($\lesssim 100$ Myr), while BBHs in high-mass clusters undergo effective dynamical hardening until the end of our simulations (1.5 Gyr). In high-mass clusters we find that 8% of BBHs have primary mass in the pair-instability mass gap at metallicity $Z = 0.002$, all of them born via stellar collisions, while only one BBH with primary mass in the mass gap forms in low-mass clusters. These differences are crucial for the interpretation of the formation channels of gravitational-wave sources.

keywords: black hole physics – binaries: general – galaxies: star clusters: general – stars: kinematics and dynamics - gravitational waves - methods: numerical

4.1 Introduction

Over the last six years, the LIGO (Aasi et al. 2015) and Virgo (Acernese et al. 2015a) interferometers dectected an increasing number of gravitational wave (GW) events (e.g., Abbott et al. 2016b; Abbott et al. 2016; Abbott et al. 2019, 2021f). At the end of the

third observing run, the third GW transient catalog (GWTC-3) consists of 90 GW candidates (Abbott et al. 2021d,e). Most of these events are produced by the inspiral of two black holes (BHs). Among the most peculiar events, the merger remnant of GW190521 (Abbott et al. 2020; Abbott et al. 2020d) is the first intermediate-mass BH (IMBH) ever detected in the mass range $100-1000\,M_\odot$, with a remnant mass of $142^{+28}_{-16}\,M_\odot$. Also, GW190412 (Abbott et al. 2020a) represents the first observation of a BBH with asymmetric masses. The population of mergers in GWTC-3 also includes two binary NS mergers, GW170817 and GW190425 (Abbott et al. 2017b,a, 2020b), and two BH-NS candidates, GW200105_162426 and GW200115_042309 (Abbott et al. 2021a). Furthermore, Nitz et al. (2021) and Olsen et al. (2022) reported several additional GW candidates (see also Venumadhav et al. 2019, 2020; Nitz et al. 2020, 2021).

The abundance of detected GW sources allows us to attempt to reconstruct their formation channels. In fact, thanks to the distinctive features that different formation channels imprint on the merging progenitors, even a few hundreds detections may be sufficient to identify their main formation pathways (Fishbach et al. 2017; Zevin et al. 2017; Stevenson et al. 2017; Farr et al. 2017; Vitale et al. 2017; Bouffanais et al. 2019, 2021a,b; Wong & Gerosa 2019; Wong et al. 2021; Zevin et al. 2021; Ng et al. 2021; Roulet et al. 2021; Mehta et al. 2022). The isolated formation scenario, for example, predicts the formation of BBHs with primary masses up to $40-50\,M_\odot$, mostly equal-mass systems, with preferentially aligned spins and vanishingly small eccentricity in the LIGO–Virgo band (Mandel & de Mink 2016; Gerosa et al. 2018). According to this scenario, the formation of tight enough binary black holes (BBHs) can take place through evolutionary processes like common envelope (Bethe & Brown 1998; Portegies Zwart & Yungelson 1998; Belczynski et al. 2002, 2008, 2010; Dominik et al. 2012, 2013; Mennekens & Vanbeveren 2014; Loeb 2016; Belczynski et al. 2016a; Mapelli & Giacobbo 2018; Mapelli et al. 2019; Giacobbo & Mapelli 2018; Kruckow et al. 2018; Spera et al. 2019; Tang et al. 2020; Belczynski et al. 2020; García et al. 2021), chemically homogeneous evolution (de Mink & Mandel 2016; Mandel & de Mink 2016; Marchant et al. 2016; du Buisson et al. 2020), or stable mass transfer (e.g., Giacobbo et al. 2018; Neijssel et al. 2019; Bavera et al. 2021).

The dynamical formation scenario, instead, involves dynamical processes in dense stellar environments, like young star clusters (YSCs, e.g., Portegies Zwart & McMillan 2002; Banerjee et al. 2010; Mapelli et al. 2013; Ziosi et al. 2014; Goswami et al. 2014; Banerjee 2018; Perna et al. 2019; Di Carlo et al. 2019, 2020a; Banerjee 2021b; Rastello et al. 2020, 2021), open clusters (e.g., Rastello et al. 2019; Kumamoto et al. 2019, 2020), globular clusters (e.g., Downing et al. 2010; Benacquista & Downing 2013; Rodriguez et al. 2015, 2016a; Antonini & Rasio 2016a; Askar et al. 2017; Fujii et al. 2017; Askar et al. 2018; Fragione & Kocsis 2018; Rodriguez et al. 2019), and nuclear star clusters (e.g., O'Leary et al. 2009; Miller & Lauburg 2009; Arca-Sedda & Capuzzo-Dolcetta 2018; VanLandingham et al. 2016; Hoang et al. 2018; Arca-Sedda & Gualandris 2018; Arca Sedda & Benacquista 2019; Arca Sedda et al. 2020). With respect to the isolated channel, this scenario predicts the formation of merging BBHs with larger primary masses (e.g., McKernan et al. 2012; Mapelli 2016; Antonini & Rasio 2016a; Gerosa & Berti 2017; Stone et al. 2017; McKernan et al. 2018; Rodriguez et al. 2019; Yang et al. 2019), with the possibility of hierarchical mergers (e.g., Antonini et al. 2019; Doctor et al. 2020; Kimball et al. 2020; Mapelli et al. 2021a, 2022; Antonini et al. 2022), isotropic spin distributions (e.g., Rodriguez et al. 2016b), and, in some rare cases, non-zero eccentricity in the LIGO–Virgo band (e.g., Samsing 2018; Samsing & D'Orazio 2018; Samsing et al. 2018; Rodriguez

et al. 2018; Zevin et al. 2019; Dall'Amico et al. 2021).

In this work, we will focus on the dynamical formation of BBHs in young and open stellar clusters. These systems are of key importance to interpret the formation of BBHs, because they host the formation of the most massive stars (Lada & Lada 2003; Portegies Zwart et al. 2010; Crowther et al. 2010), which are the progenitors of massive BHs. Thanks to the high initial central density of the host cluster ($\rho \gtrsim 10^3\,\mathrm{M_\odot pc^{-3}}$, Portegies Zwart et al. 2010), binary stars can efficiently interact with the surrounding stars since the very beginning of their life. This leaves a deep imprint on the properties of the population of BBHs and, in turn, merging BBHs. When YSCs are eventually disrupted by the tidal field of their host galaxy, their stellar content is released into the galactic field. Thus, a large fraction of BBHs which are now in the field may have formed in young stellar systems.

The dynamical formation and evolution of BBHs in YSCs are explored in a realistic way by means of direct $N-$body simulations, where up-to-date prescriptions for single and binary stellar evolution are implemented. In many cases, only the first few hundreds Myr of the life of the star cluster are considered. This is due, on the one hand, to their small relaxation timescales, $t_{\rm rlx} \lesssim 100\,\mathrm{Myr}$ (Portegies Zwart et al. 2010). In particular, the rapid decrease of their central density within the first Myr suppresses the interaction rate in later phases, making them less and less important in shaping the BBH properties. On the other hand, producing large sets of $N-$body simulations, which are necessary to explore the population of merging BBHs with sufficient statistics, has high computational costs. Thus, evolving large sets of YSCs for thousands of Myr would turn to be prohibitively expensive. As a consequence, many simulation of YSCs only take into account the first 100 Myr of the star cluster life (Di Carlo et al. 2019, 2020a,b; Rastello et al. 2020, 2021).

The aim of this work is to evaluate the impact of the late phases (up to 1500 Myr) of the dynamical evolution of the star cluster on the population of BBH mergers. To this purpose, we have run two sets of $N-$body simulations of YSCs in different mass regimes and studied the evolution of the population of BBHs. To calculate the impact of the long-term evolution of the cluster, we compared the BBH merger populations at two different snapshots, 100 Myr and 1500 Myr. The paper is organized as follows: in Section 4.2, we describe the details of the $N-$body simulations and our method. In Section 4.3, we report the results for the BBH populations and mergers. Finally, Section 4.4 summarises our conclusions.

4.2 Methods

4.2.1 Direct *N*-body code

We performed our simulations with the $N-$body code NBODY6++GPU (Wang et al. 2015, 2016), coupled with the population synthesis code[1] MOBSE (Mapelli et al. 2017; Giacobbo et al. 2018; Giacobbo & Mapelli 2018). NBODY6++GPU is the GPU parallel version of NBODY6 (Aarseth 2003a). It implements a 4th-order Hermite integrator, individual block time-steps (Makino & Aarseth 1992) and Kustaanheimo-Stiefel regularization of close encounters and few-body systems. The force contributions at short time steps (*irregular forces*) are computed by a neighbour scheme (Nitadori & Aarseth 2012), and for long time

[1] MOBSE is publicly available at this link.

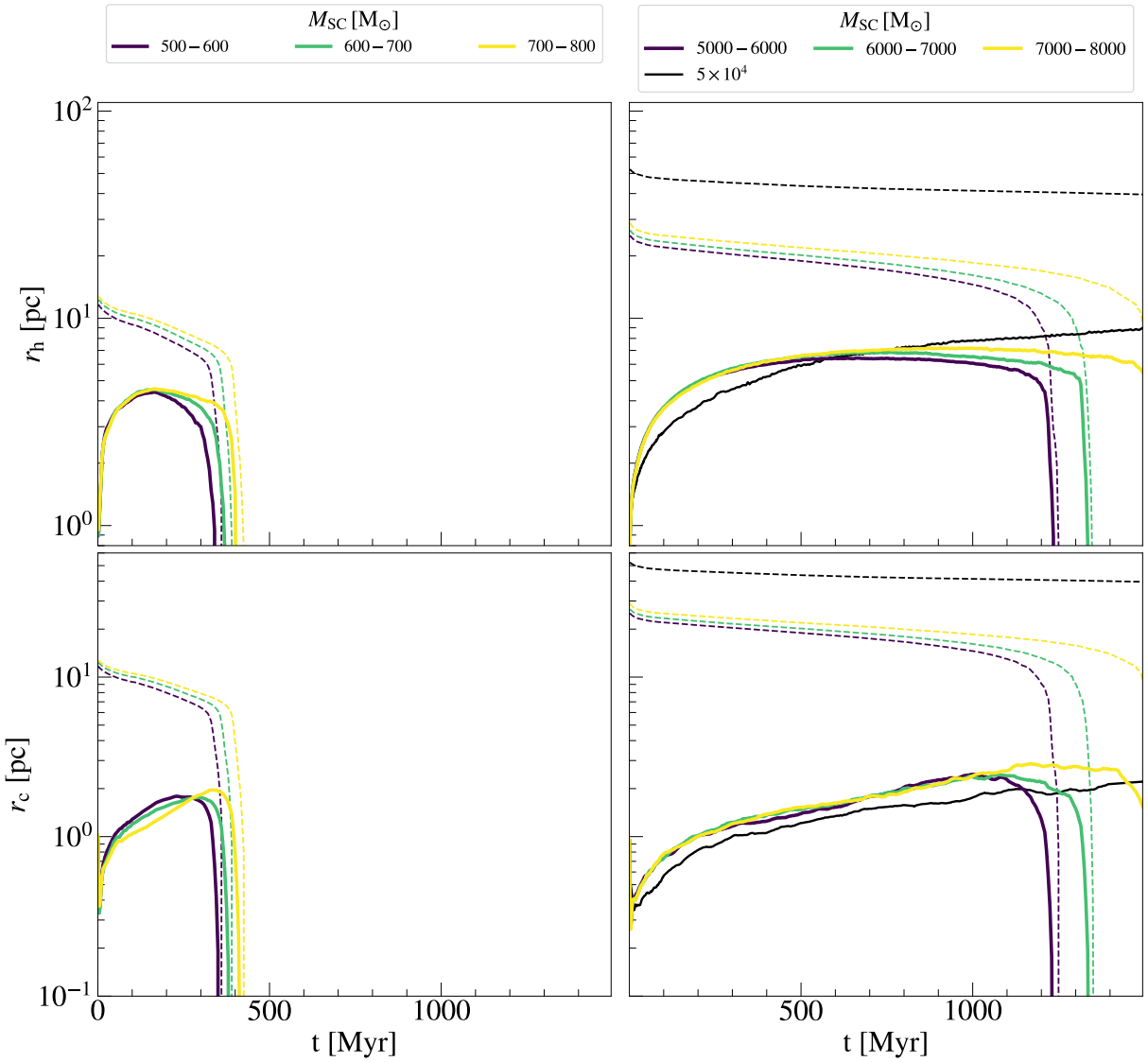

Figure 4.1: Evolution of the half-mass radius r_h (upper panels, solid lines), core radius r_c (lower panels, solid lines), and tidal radius r_t (dashed lines) for low-mass clusters (left) and high-mass clusters (right). Each set is divided into three subsets: for the low-mass clusters $M_{SC} \in [500, 600]$ $M_\odot$ (magenta), [600, 700] $M_\odot$ (green), [700, 800] $M_\odot$ (yellow). For the high-mass clusters $M_{SC} \in [5000, 6000]$ $M_\odot$ (magenta), [6000, 7000] $M_\odot$ (green), [7000, 8000] $M_\odot$ (yellow). Each line shows the median value over the simulated YSCs per each mass bin. The black lines (right panels) refer to the same physical quantities for the star clusters with $M_{SC} = 5 \times 10^4\,M_\odot$.

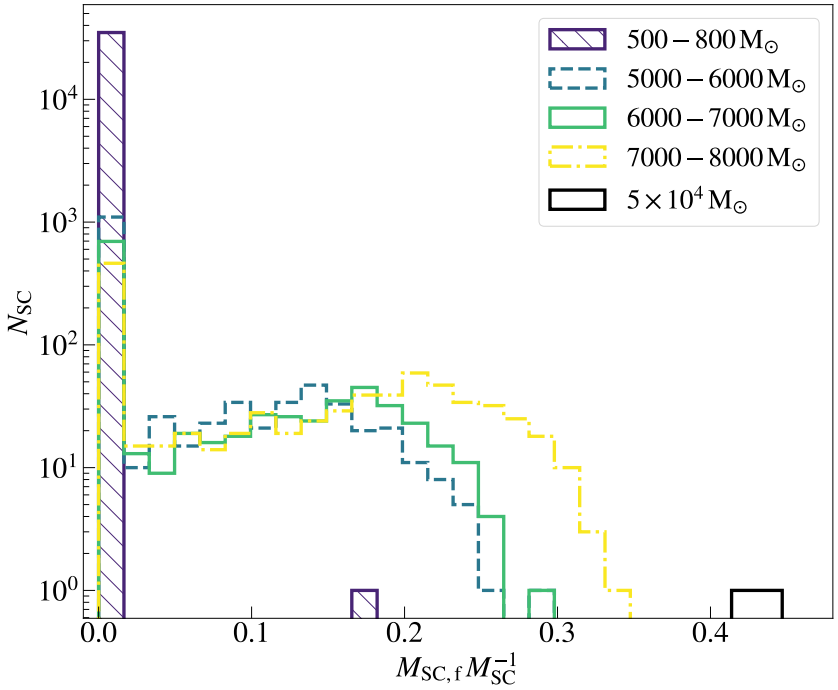

Figure 4.2: Distribution of the ratio between the star cluster bound mass at the end of the simulation, $M_{\rm SC,f}$, and its initial mass $M_{\rm SC}$, for stellar systems with initial mass $M_{\rm SC} \in$ [500, 800] $\rm M_\odot$ (magenta), [5000, 6000] $\rm M_\odot$ (blue), [6000, 7000] $\rm M_\odot$ (green), [7000, 8000] $\rm M_\odot$ (yellow), and $M_{\rm SC} = 5 \times 10^4\,\rm M_\odot$ (black).

steps (*regular* force/timesteps) the force is evaluated by considering all the particles of the system. The irregular-force calculation is performed using CPUs, while the regular forces are evaluated on GPUs using the CUDA architecture. A solar neighbourhood-like static external field (Wang et al. 2016) is included in the force integration. This choice for the tidal field is quite conservative, because the static tidal field does not take into account possible perturbations by disk and bulge shocking, and encounters with molecular clouds, which can accelerate the star cluster disruption (Gieles et al. 2006). Orbital decay and circularization by GW emission are calculated following Peters (1964). Post-Newtonian terms are not included in this version of NBODY6++GPU.

MOBSE is a customized and upgraded version of BSE and includes up-to-date prescription for massive stellar winds (Giacobbo et al. 2018), core-collapse (Fryer et al. 2012) and electron-capture supernovae (Giacobbo & Mapelli 2019), natal kicks (Giacobbo & Mapelli 2020) and (pulsational) pair instability supernovae (Mapelli et al. 2020). Stellar winds are modeled by assuming that the mass loss of hot massive stars depends on metallicity as $\dot{M} \propto Z^\beta$, where β is modelled as in Giacobbo et al. (2018).

For this work, we adopt the delayed model for core-collapse supernovae from Fryer et al. (2012). In this model, there is no mass gap between NSs and BHs: we assume that compact objects more massive than 3 $\rm M_\odot$ are BHs. Natal kicks are modeled according to the prescription by Giacobbo & Mapelli (2020): the magnitude of the kick can be expressed as $v_{\rm kick} \propto f_{\rm H05}\, m_{\rm ej}\, m_{\rm rem}^{-1}$, where $f_{\rm H05}$ is a random number drawn from a Maxwellian distribution with a one-dimensional root mean square velocity $\sigma = 265\,\rm km\,s^{-1}$, $m_{\rm rem}$ is the mass of the remnant, and $m_{\rm ej}$ is the difference between the final mass of the star before the

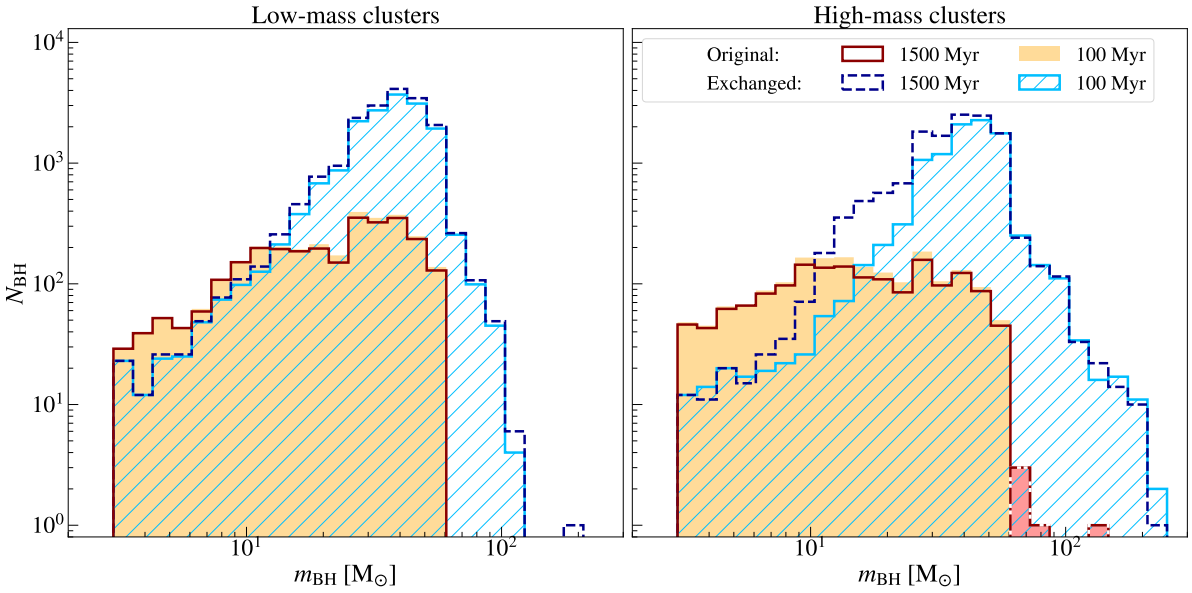

Figure 4.3: Mass distribution of BHs in BBHs, for low-mass clusters (left) and high-mass clusters (right). Red line: original BBHs at 1500 Myr. Orange filled histogram: original BBHs at 100 Myr. Blue dashed line: exchanged BBHs at 1500 Myr. Light blue hatched histogram: exchanged BBHs at 100 Myr. Among the original BHs, we highlight in red those with mass in the PI mass gap at 1500 Myr (red dash-dotted line) and at 100 Myr (red filled histogram). These are anomalous original BBHs in which one of the two stellar components has merged with another star before producing the BBH (see Section 4.3.2 for details).

supernova explosion and the mass of the remnant. Binary evolution processes (tides, mass transfer, common envelope and GW-orbital decay) are implemented as in Hurley et al. (2002). The common envelope process is implemented by adopting the energy formalism (Webbink 1984). In this case, we assume $\alpha = 3$, while the concentration parameter λ is calculated self-consistently as in Claeys et al. (2014).

4.2.2 Initial conditions

Stellar and binary populations

We generate the initial masses of stars (single stars, primary and secondary members of binary systems) according to a Kroupa (2001) initial mass function between 0.1 M$_\odot$ and 150 M$_\odot$. We assume a metallicity $Z = 0.002$, approximately corresponding to 0.1 Z$_\odot$. For binary systems, we assume a distribution of mass ratios $\mathcal{F}(q) \propto q^{-0.1}$, with $q \in [0.1, 1]$ (Sana et al. 2012).

Our algorithm generates a mass-dependent binary fraction f_b, according to Moe & Di Stefano (2017)[2]. The details of the assumed binary fraction per mass bin are shown

[2]Moe & Di Stefano (2017) take their data from different spectroscopic surveys, including binary systems in the field, OB associations, and young star clusters. Ideally, here we should consider only the sub-sample of binary systems in young star clusters (Sana et al. 2012), but this is not feasible, because the lowest-mass stars are missing in such sub-sample.

Mass Bin [$M_\odot$]	Binary fraction f_b
0.1–0.8	0.2
0.8–2.0	0.4
2.0–5.0	0.59
5.0–9.0	0.76
9.0–16.0	0.84
16.0–150.0	0.94

Table 4.1: Adopted values of the original binary fraction f_b (column 2) per each stellar mass bin (column 1). From Moe & Di Stefano (2017).

in Table 4.1. We generate the orbital parameters of binary systems following the observational prescriptions by Sana et al. (2012). In particular, we randomly draw the orbital periods from: $\mathcal{F}(\mathcal{P}) \propto \mathcal{P}^{-0.55}$, with $\mathcal{P} = \log_{10}(P/\text{days}) \in [0.15, 5.5]$, and the eccentricities from $\mathcal{F}(e) \propto e^{-0.45}$, with $e \in [10^{-5}, e_{\max}(P)]$. For a given orbital period, we set an upper limit for the eccentricity distribution according to Moe & Di Stefano (2017): $e_{\max}(P) = 1 - [P/(2\,\text{days})]^{-2/3}$. Our method allows to obtain orbital properties for O-type stars (i.e., the progenitors of BHs) consistent with those observed in young and open clusters and OB associations (Sana & Evans 2011; Sana et al. 2012). Based on population-synthesis simulations by de Mink & Belczynski (2015), we expect that our choice of the initial binary parameters has a mild (negligible) impact on the evolution of BBHs in low-mass (high-mass) clusters, where binary evolution is most (least) important with respect to dynamical interactions. We refer to Torniamenti et al. (2021) for more details on our initial binary population.

Stellar clusters

We initialize stellar positions and velocities in the simulated YSCs with fractal initial conditions, with a fractal dimension $D = 1.6$, in order to mimic the observed clumpiness of embedded star clusters (Cartwright & Whitworth 2004; Sánchez & Alfaro 2009; Kuhn et al. 2019). We generate fractal phase space distributions with McLuster (Küpper et al. 2011).

We uniformly sample the half-mass of our star clusters between 0.5 and 2 pc (e.g., Portegies Zwart et al. 2010; Krumholz et al. 2019). To evaluate the impact of long-term dynamics on the properties of BBH mergers in different dynamical regimes, we consider two sets of star clusters in different mass ranges ($M_{\rm SC}$):

- *Low-mass star clusters*, with mass ranging from $500\,M_\odot$ to $800\,M_\odot$. These clusters present short dynamical evolution timescales at all scales: this reduces the probability of dynamical interactions and, consequently, of dynamical exchanges. Also, YSCs in this mass range typically host a few massive stars, and, consequently, BHs. This further suppresses the rate of dynamical exchanges[3] (Rastello et al. 2021).

[3] An exchange tends to happen when the intruder is more massive than at least one of the members of the binary system, because this leads to a substantial increase of the binary's binding energy, hardening the binary system (Heggie 1975; Hills & Fullerton 1980; Heggie & Hut 2003). Our low-mass clusters lack massive intruders because all of the massive stars are already born in hard binary systems. Thus, exchanges tend to be suppressed.

- *High-mass star clusters*, with mass ranging from $5000\,M_\odot$ to $8000\,M_\odot$. These clusters have a higher rate of dynamical encounters, as a consequence of the higher densities, longer dynamical timescales and larger number of massive stars. Thus, they are expected to produce a larger number of exchanged binaries and BBHs (Rastello et al. 2021). In this sample we also include two star clusters with mass $5 \times 10^4\,M_\odot$.

Here, the terms *low-mass* and *high-mass* clusters are intended only for comparison between the two considered samples. In the literature, low-mass clusters can include even star clusters with much lower mass, down to a few ten $M_\odot$ (e.g., Lada & Lada 2003), while the highest mass clusters can reach $\sim 10^7$ $M_\odot$ (e.g., Georgiev et al. 2016).

In both cases, we sample the mass of star clusters from a power-law distribution $dN/dM_{\rm SC} \propto M_{\rm SC}^{-2}$, following Lada & Lada (2003). The two sets consist in 35578 and 3555 star clusters, respectively. The number of star clusters in the two samples is set to obtain the same total mass. The total kinetic (K) and potential (W) energy of the cluster are set to give a virial ratio $Q = 2\,K/W = 1$.

4.2.3 Impact of long-term evolution

The main goal of this work is to evaluate the impact of dynamics on the population of BBH mergers. In particular, we simulate our star clusters up to $t_{\rm f} = 1500\,$Myr. This corresponds to a total integration time of ~ 150 relaxation timescales ($t_{\rm rlx}$, Spitzer 1987) for low-mass clusters which have, on average, $t_{\rm rlx} \sim 10$ Myr. For high-mass cluster, on average, $t_{\rm rlx} \sim 26$ Myr, and the total integration time is longer than $50\,t_{\rm rlx}$. To be completely sure that we captured all the dynamical encounters relevant for the population of BBHs, we should integrate all our clusters until they become tidally filling, or until the last BH leaves its parent cluster by ejection or evaporation. For the most massive clusters (> 7000 $M_\odot$), our clusters become tidally filling at later times with respect to $t_{\rm f} = 1.5$ Gyr (Figure 4.1). However, integrating our most massive clusters for more than 1.5 Gyr currently requires prohibitive computational resources. Moreover, we found that only 0.01% (6%) of all BBHs are still bound to their parent cluster in our low-mass (high-mass) star clusters. Hence, the vast majority of our BBHs has already been dynamically ejected at 1.5 Gyr and will not be affected by dynamical interactions at later stages.

We compare the population of BBH mergers that form in the first 100 Myr of the evolution of the simulated YSCs with the population of BBH mergers at 1500 Myr. In particular, we first evaluate the population of BBH mergers that we would have obtained if we had integrated the evolution of our YSCs only for the first 100 Myr. This population consists in:

- BBHs that merge within the first 100 Myr, during the $N-$body simulations.

- BBHs that will merge within a Hubble time in absence of further dynamical interactions. To calculate them, we consider the population of existing BBHs at 100 Myr and evolve their orbital eccentricity and semi-major axis by integrating the

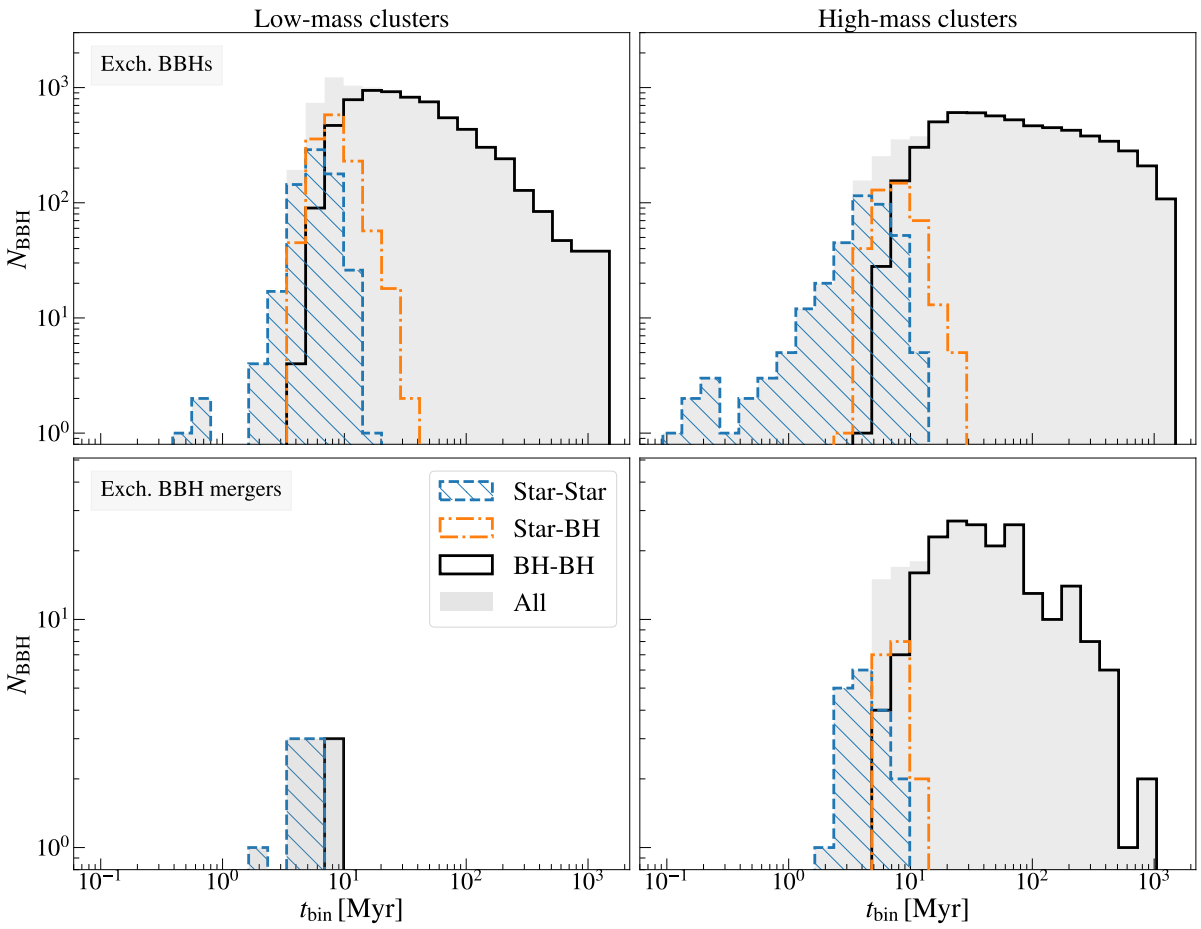

Figure 4.4: Distribution of formation times ($t_{\rm form}$) of binary systems that give birth to exchanged BBHs, in low-mass clusters (left) and high-mass clusters (right). Upper panels: all exchanged BBHs. Lower panels: exchanged BBH mergers. Blue dashed line and hatched area: BBHs that formed when both components were stars. Orange dot-dashed line: BBHs that formed when one component was a star and the other was a BH. Black line: BBHs that formed when both components were BHs. Grey area: all BBHs.

equations of Peters (1964), to calculate the energy loss due to GW emission:

$$\begin{aligned}\frac{{\rm d}a}{{\rm d}t} &= -\frac{64}{5}\frac{G^3\, m_1\, m_2\, (m_1+m_2)}{c^5\, a^3\, (1-e^2)^{7/2}}\, f_1(e),\\ \frac{{\rm d}e}{{\rm d}t} &= -\frac{304}{15}\, e\frac{G^3\, m_1\, m_2\, (m_1+m_2)}{c^5\, a^4\, (1-e^2)^{5/2}}\, f_2(e),\end{aligned} \tag{4.1}$$

where

$$\begin{aligned}f_1(e) &= \left(1+\frac{73}{24}\, e^2+\frac{37}{96}\, e^4\right)\\ f_2(e) &= \left(1+\frac{121}{304}\, e^2\right).\end{aligned} \tag{4.2}$$

All the BBHs that merge within a Hubble time ($t_{\rm H} = 14\,{\rm Gyr}$) are classified as mergers. This is equivalent to assume that the YSCs dissolve at 100 Myr, and their BBHs evolve only via GW emission (no dynamical interactions) after the death of their parent star clusters.

To evaluate how dynamical encounters affect the distribution of BBH mergers in the late phases of the cluster life, we repeat the aforementioned procedure after 1500 Myr, i.e.

- we count how many BBHs merge within 1500 Myr, during the $N-$body simulations;
- we integrate the semi-major axis and eccentricity evolution of the other BBHs that are still bound at 1500 Myr, accounting for GW emission only (Peters 1964), and we count how many of them merge within one Hubble time.

If the dynamical interactions within the cluster are still effective after 100 Myr, they can affect the population of BBHs, and, consequently, of BBH mergers. In particular, dynamical processes can form new BBHs or harden the existing ones, allowing them to merge within an Hubble time, or even before the end of the simulation, thus increasing the population of BBH mergers. In some other cases, dynamical interactions can disrupt existing BBHs, possibly removing them from the population of mergers that we estimated at 100 Myr.

4.2.4 Estimate of relativistic kicks

When two BHs merge, the post-merger remnant receives a kick due to the asymmetric momentum dissipation by GWs (e.g., Favata et al. 2004). This recoil can reach up to thousands km s^{-1}, depending on the symmetric mass ratio and spin orientation (Campanelli et al. 2007). If the kick magnitude is larger than the escape velocity of the host star cluster, the post-merger remnant is ejected. For the star clusters considered in this work (Sect. 4.2.2), the initial escape velocities range from ~ 1 to ~ 10 km s^{-1}, and may rapidly decrease to zero as a consequence of cluster dissolution.

As our simulations do not include relativistic kicks, we evaluated the probability that a post-merger remnant is ejected a posteriori, using the equations reported by Maggiore (2018). In particular, for each BBH merger, we randomly draw a distribution of spin magnitudes for each component from a Maxwellian distribution: we consider two cases: $\sigma_\chi = 0.1$ and $\sigma_\chi = 0.01$ (see, e.g., Bouffanais et al. 2021a, for this assumption). Also, we assume that the spin directions are isotropically distributed over the sphere (e.g., Rodriguez et al. 2016b). We randomly draw 10^5 different spin magnitudes and orientations for each BH, and calculate the resulting relativistic kick distribution. Then, we evaluate the probability that the BH remnant is retained within the cluster, that is the probability to find a kick value lower than the escape velocity at the BBH merger.

For all our BBH mergers, we find a retention probability $p < 2\%$ if $\sigma_\chi = 0.1$ and $p < 5\%$ if $\sigma_\chi = 0.01$. Thus, we can safely assume that all the post-merger remnants are ejected from their host cluster. Therefore, we will remove from our sample any second-generation BBH, i.e. any BBH that has at least one component resulting from a previous BBH merger.

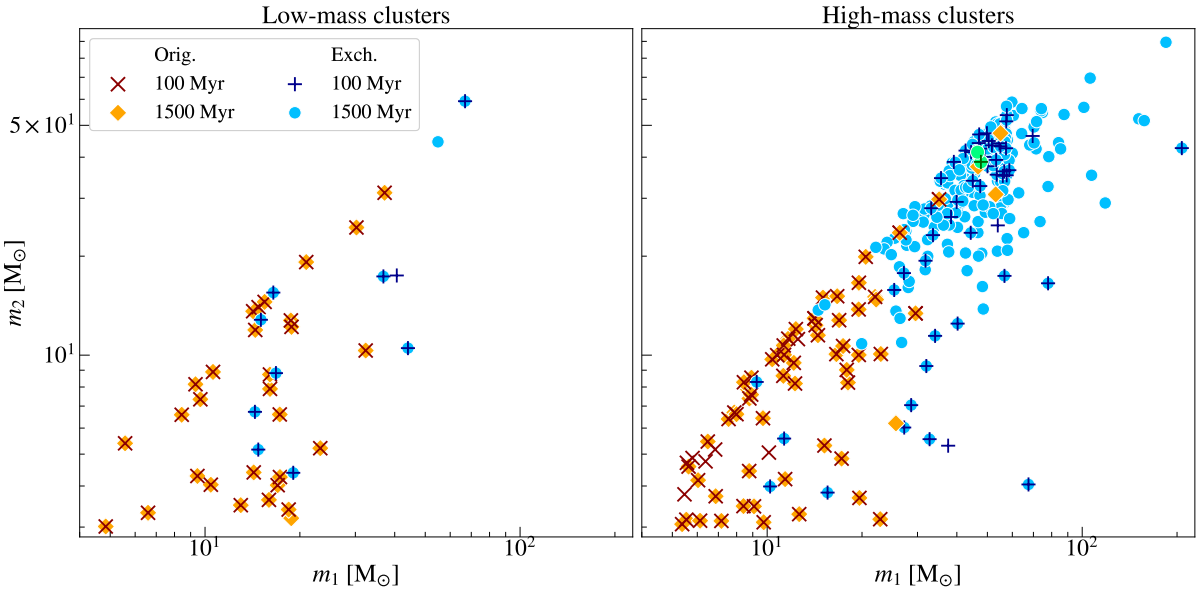

Figure 4.5: Mass of the secondary BH (m_2) versus the primary BH (m_1) of BBH mergers in low-mass clusters (left) and high-mass clusters (right). Orange diamonds: original BBHs at 1500 Myr. Red crosses: original BBHs at 100 Myr. Light blue circles: exchanged BBHs at 1500 Myr. Blue plusses: exchanged BBHs at 100 Myr. Green circles: exchanged BBHs at 1500 Myr in star clusters with mass $5 \times 10^4\,\mathrm{M}_\odot$.

4.3 Results

4.3.1 Global evolution of the cluster

Figure 4.1 shows the evolution of the half-mass radius r_h, tidal radius r_t, and core radius r_c of the two sets of clusters. Each set is split into three sub-sets of different mass in order to better take into account the impact of the cluster mass on its expansion. As a comparison for high-mass clusters, we also show the evolution of the stellar clusters with $5 \times 10^4\,\mathrm{M}_\odot$.

All the clusters show an initial rapid expansion due to the early mass loss caused by stellar and binary evolution (stellar winds and supernovae). This expansion is visible at all scales, but is more pronounced for r_h, consistently with the results of Chattopadhyay et al. (2022). Also, the early mass loss causes the initial steep decrease of the tidal radius.

After the most massive stars have evolved into compact remnants, the cluster enters a slower, relaxation-driven phase, as visible from the change of slope of r_t. In particular, the tendency towards energy equipartition makes the low-mass stars move altogether to the outer regions, approaching the tidal boundary, while the heavier stars and compact remnants sink at the center of the cluster, if they are not already segregated (Spitzer 1987). As a result, stars are progressively removed by the galactic tidal field, leading to cluster dissolution. Eventually, the tidal stripping, further enhanced by the cluster mass loss, and the possible energy generation by massive BBHs within the cluster core lead the stellar cluster out of dynamical equilibrium (Giersz et al. 2019), causing an abrupt disruption of the cluster and a sharp decrease of its relevant radii.

The duration of the relaxation-driven phase depends on the initial cluster mass. For

low mass clusters, the short relaxation timescales (Spitzer 1987), combined with the small initial mass, cause a rapid dissolution. Their typical lifetime is 400 Myr, with no particular distinction among the three subsets. The evolution of high-mass clusters, instead, is characterized by a much milder expansion, where the growth of $r_{\rm h}$ is balanced by tidal stripping. As a result, $r_{\rm h}$ remains almost constant (a similar trend can be seen in Banerjee 2017 for more massive clusters) for the first 1000 Myr. The cluster dissolution happens at different times, depending on the mass subset considered. The typical lifetime spans from 1250 Myr for clusters with mass $< 6000\,{\rm M}_\odot$, up to more than 1500 Myr for clusters more massive than $7000\,{\rm M}_\odot$. In contrast, the $5 \times 10^4\,{\rm M}_\odot$ clusters undergo a far slower expansion and their tidal radius is almost unchanged at the end of the simulation, except for the initial rapid decrease due to stellar evolution mass loss.

In both low- and high-mass clusters, the core radius increases monotonically until the cluster is disrupted, thus lacking a clear core-collapse phase. As shown by Chattopadhyay et al. (2022), this is not unexpected for models with a large original binary population. In this case, original binaries can heat up the cluster since the very beginning of its evolution, preventing a deep core collapse.

Figure 4.2 shows the distribution of the ratio between the star cluster bound mass at 1500 Myr, $M_{\rm SC,f}$, and its initial mass, $M_{\rm SC}$. Low-mass clusters are completely disrupted by the tidal field of the host galaxy at the end of the simulation. In only one case, a core of about $120\,{\rm M}_\odot$, corresponding to 18% of the initial mass, can survive[4].

As for high-mass clusters, one third of the stellar systems are still bound at the end of the simulation. In this set, the number of surviving clusters increases with the initial mass of the cluster. Also, more massive clusters can generally retain a higher fraction of mass. Finally, stellar clusters with $5 \times 10^4\,{\rm M}_\odot$ preserve about half of their initial mass at 1500 Myr.

4.3.2 BBH populations

Figure 4.3 shows the mass distribution of BHs in BBHs in the two considered snapshots: 100 Myr and 1500 Myr. In this section, we analyse both merging and non-merging BBHs. Among the BBH populations, we distinguish between *original BBHs*, whose progenitors were already present as binary stars in the initial conditions of the simulation[5], and *exchanged BBHs*, which have formed as a consequence of dynamical exchanges.

In low-mass clusters, the BH populations in the two snapshots are almost identical, suggesting that, after 100 Myr, dynamical encounters play a negligible role in the evolution of BBHs. In contrast, high-mass clusters are still dynamically active at later phases, as indicated by the increase of the number of exchanged BHs between $7\,{\rm M}_\odot$ and $50\,{\rm M}_\odot$.

The BH populations of low- versus high-mass clusters show several differences. First, low-mass clusters display a larger number of original BBHs with $m_{\rm BH} > 20\,{\rm M}_\odot$. Such

[4]Most of the remaining mass of this interesting survivor consists of a BBH with a total mass of 80 $\rm M_\odot$, composed of two BHs of 44 $\rm M_\odot$ and 36 $\rm M_\odot$, respectively. This BBH formed via dynamical exchange. The rest of the mass is distributed in 50 low-mass stars. This is a unique case in our sample. We may speculate that, because the BBH formed in a relatively loose environment ($\sim 10\,{\rm M}_\odot\,{\rm pc}^{-3}$), its high mass and the poor dynamical interaction rate allowed a number of stars to remain within the tidal radius, without being scattered away by the BBH itself.

[5]In the literature, a binary star that is already present in the initial conditions of a direct N-body simulation is often referred to as a primordial binary star. Here, we use the term *original* instead of *primordial*, to avoid any possible confusion with the concept of primordial BHs (e.g., Carr et al. 2016).

massive original BBHs tend to be suppressed in high-mass clusters, because they undergo stronger dynamical interactions for a longer time, eventually resulting in a dynamical exchange. This leads to the formation of nearly equal-mass, massive exchanged BBHs in the high-mass clusters. This process is also enhanced by the higher initial number of massive stars in high-mass clusters with respect to low-mass clusters. As a consequence, original BBHs in high-mass clusters tend to have lower masses than those in low-mass clusters.

Figure 4.4 displays the distribution of formation times of the binary systems that give birth to exchanged BBHs ($t_{\rm form}$). In low-mass clusters, 8% of these systems form when both components are still stars, and about 15% when only one component is a BH. Most of the binaries that result in BBHs form by the pairing of two BHs, with a peak at formation time $t_{\rm form} = 10 - 20$ Myr. The rapid decrease of the dynamical activity and the dissolution of the stellar cluster cause a steep decrease in the distribution of $t_{\rm form}$, and only 12% of the BBHs form after 100 Myr in low-mass clusters.

In high-mass clusters, about 88% of the binaries resulting in BBHs form from the pairing of two BHs. In this case, the distribution of $t_{\rm form}$ shows a flatter trend, hinting at an efficient dynamical activity of the cluster at later times. In fact, more than one third of the BBHs pair up after 100 Myr. In these clusters, only 5% of the binaries that produce BBH systems form when both components are still stars.

Mass-gap BHs and IMBHs

More than 7% of our simulated BBHs in high-mass clusters (here we consider both merging and non-merging systems) have primary mass $> 60\,{\rm M}_\odot$.

The formation of such massive BHs, with mass ranging from $\sim 60\,{\rm M}_\odot$ to $\sim 120\,{\rm M}_\odot$ is suppressed in single stellar evolution by pair-instability (PI) and pulsational pair instability (PPI). Nonetheless, as shown by Spera et al. (2019), Di Carlo et al. (2019) and Di Carlo et al. (2020a), BHs in the mass gap can form as a consequence of stellar mergers, which produce very massive stars that eventually collapse to BHs.

BHs in this mass range may also be the result of previous BH mergers (e.g., Banerjee 2021a). However, almost all merger remnants are expected to be ejected by relativistic kicks in our simulated star clusters (Sect. 4.2.4). Hence, all the BHs which have a mass $60-120$ ${\rm M}_\odot$ and are members of BBHs form as a result of stellar mergers in our simulated star clusters.

In five cases, a BH with mass > 60 ${\rm M}_\odot$ even forms in an original binary system. These are systems in which the original binary remains bound after the merger of one of its components with a third star, producing an original binary with a mass-gap primary BH (Fig. 4.3).

Low-mass clusters display a lower percentage of mass-gap BHs in BBHs ($\sim$ 4%), because of their lower rate of dynamical interactions as well as the limited initial number of massive stars (Sect. 4.3.2). Also, no mass-gap BH is present in original binary systems.

Furthermore, ~ 1.5% of all BHs that are bainry members in our high-mass clusters are IMBHs (i.e., BHs with mass > 100 ${\rm M}_\odot$). The maximum BH mass we find in BBHs in our high-mass clusters is 250 ${\rm M}_\odot$. As in the case of BHs in the PI mass-gap, all the IMBHs we found form via multiple stellar collisions (e.g., Di Carlo et al. 2021). In contrast, only eight BHs with mass $> 100\,{\rm M}_\odot$ form in low-mass clusters, corresponding to ~ 0.1% of all the BHs born in the low-mass clusters.

	Low-mass clusters		High-mass clusters	
BBH mergers	100 Myr	1500 Myr	100 Myr	1500 Myr
All	40	40	115	307
Original	30	30	64	60
Exchanged	10	10	51	247
Inside YSC	1	1	25	174
IMBHs	1	1	4	47
$m_{\rm tot,max}$ [$\rm M_\odot$]	126	126	249	273

Table 4.2: We report the number of all (first row), original (second row) and exchanged (third row) BBH mergers. We also show the number of BBHs that merge inside the cluster during the simulation (fourth row). Finally, we report the number of IMBHs produced by BBH mergers (merger remnants, fifth row), and their maximum BH mass (last row).

4.3.3 BBH mergers

In this Section, we focus on BBH mergers, i.e. BBHs that reach coalescence in less than 14 Gyr.

Low-mass clusters

Figure 4.5 shows the mass of the secondary BH (m_2) versus the primary BH (m_1) for BBH mergers. In low-mass clusters, the population of BBH mergers mostly consists of original BBHs, as a further proof of the poor dynamical activity of these systems. In general, dynamical exchanges do not affect the population of BBHs after 100 Myr ($\sim 10\,t_{\rm rlx}$), as already suggested by Fig. 4.3, with two exceptions. First, one BBH that is predicted to merge if the simulation is run only for 100 Myr, is later disrupted by dynamical interactions, and no longer exists at 1500 Myr. Also, the second most massive merger (with a final remnant mass $m_{\rm tot} = 99\,\rm M_\odot$) needs to dynamically harden for longer than 100 Myr to enter the regime in which the orbital decay by GWs becomes effective. As shown in Fig. 4.4 (lower panel), 70% of the binaries that give birth to merging BBHs form at early stages, when both components are stars. At later stages, the scarce efficiency of dynamical hardening in low-mass clusters quenches the formation of further BBH mergers.

The properties of BBH mergers are summarized in Table 4.2. In low-mass clusters, almost all the BBHs are no longer bound to their host cluster when they merge. In this work, a BBH merger is labelled as bound if it merges inside the cluster during the simulation.

High-mass clusters

High-mass star clusters host a population of BBH mergers about eight times larger than low-mass clusters, although the total initial mass of the two sets of star clusters is approximately the same. This enhancement of BBH mergers in high-mass clusters is particularly evident for the exchanged systems, which, at 1500 Myr, represent the majority of BBH mergers.

The populations of BBH mergers at 100 and 1500 Myr show notable differences. A number of original BBHs that, at 100 Myr, are predicted to merge are later disrupted (Figure 4.5 and Table 4.2). Some exchanged BBHs are also disrupted after the first 100 Myr.

However, these disrupted exchanged BBHs are compensated by the late formation and/or hardening of other exchanged BBHs: we predict 51 exchanged BBH mergers at 100 Myr ($\sim 4\,t_{\rm rlx}$), while at 1500 Myr ($\sim 60\,t_{\rm rlx}$) we find five times more exchanged BBH mergers, as shown in Table 4.2. Figure 4.4 shows that most of the binaries that result in BBH mergers form via exchange when both components have already collapsed to BHs. As opposed to low-mass clusters, merging BBHs can form at very late stages, up to 1000 Myr.

A large number of BBHs (174) merge during our simulations, while they are still inside their parent cluster. Their post-merger remnant is always ejected from the cluster by gravitational recoil (see Sect. 4.2.4), thus preventing the possibility of second-generation BH mergers.

In high-mass clusters, 47 BBH mergers give birth to IMBHs, with a remnant mass $m_{\rm tot} > 100\,{\rm M}_\odot$. In the eight most massive mergers, the primary BH is itself an IMBH. The most massive merger remnant has a mass $m_{\rm tot} = 273\,{\rm M}_\odot$.

Figure 4.6 shows the distribution of chirp masses of BBH mergers, for the two considered snapshots (100 and 1500 Myr). The changes in the distribution are mostly due to the long-term dynamical activity within high-mass clusters. The late dynamical activity triggers a large increase of the number of mergers with high chirp mass $m_{\rm chirp} \approx 35 - 40\,{\rm M}_\odot$.

4.3.4 BBH orbital properties at formation

To estimate for how long a stellar cluster is dynamically active and can affect the formation of BBH mergers, we evaluated $t_{\rm M}$, defined as the time (since the beginning of the simulation) at which the semi-major axis of the BBH has become sufficiently tight to merge within a Hubble time via GW emission. Figure 4.7 shows $t_{\rm M}$ as a function of the initial orbital properties of the BBH, that is its initial semi-major axis ($a_{\rm BBH}$) and orbital eccentricity ($e_{\rm BBH}$).

In both low-mass and high-mass clusters, the original BBH mergers show typical values of $t_{\rm M} \lesssim 10\,{\rm Myr}$, $a_{\rm BBH} \lesssim 0.1\,{\rm AU}$, and circular orbits. These properties spring from their formation pathway. These BBHs are, in fact, the result of original binaries that hardened as a consequence of a common envelope phase. When the second BH forms, the orbital properties of the BBH already allow it to merge within an Hubble time. For this class of BBH mergers, then, $t_{\rm M}$ mainly coincides with the time at which the second BH in the binary forms. Also, because the common envelope phase leads to a large mass loss, the resulting BH masses are systematically smaller than the exchanged ones.

As a confirmation of this idea, Fig. 4.8 shows $t_{\rm M}$ as a function of the total mass of the merging BBH, $m_{\rm tot}$ and the time at which the BBH forms, $t_{\rm BBH}$. Original BBHs have $t_{\rm BBH} \lesssim 10\,{\rm Myr}$ and, in most cases, $t_{\rm BBH} = t_{\rm M}$. In high-mass stellar cluster, seven original BBHs show $t_{\rm M} > t_{\rm BBH}$, with $t_{\rm M}$ that can be as high as 1000 Myr. In these cases, dynamical hardening allows the binary system to enter the GW regime after the BBH formation. Because these mergers have not undergone a common envelope phase, they can have masses comparable to the exchanged BBHs (up to $m_{\rm tot} = 102\,{\rm M}_\odot$). In contrast, $t_{\rm BBH}$ ranges from 5 Myr to 1100 Myr for exchanged BBHs. In high-mass clusters, more than 20% of all BBHs form after the first 100 Myr. Because exchanged BBHs have not undergone mass loss by a common envelope phase, and because dynamical exchanges favour the formation of massive binaries, their total masses are systematically higher than those of original BBH mergers, with $m_{\rm tot} \gtrsim 40\,{\rm M}_\odot$.

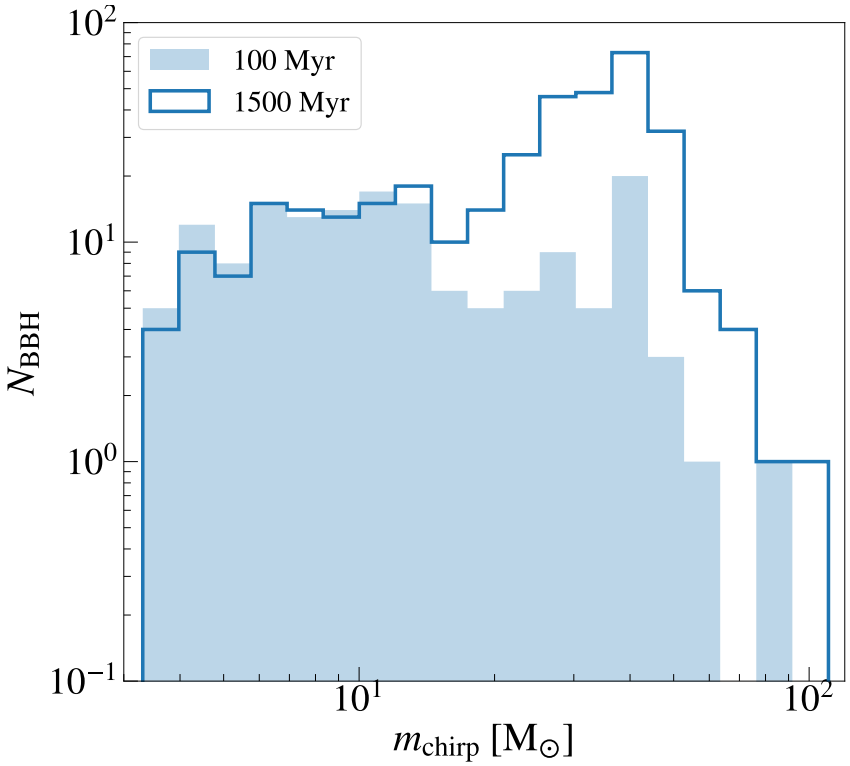

Figure 4.6: Chirp mass distribution of merging BBHs at 100 Myr (light-blue filled histogram) and at 1500 Myr (blue line), for all the simulated clusters.

In low-mass YSCs, only three exchanged BBH mergers have $a_{\rm BBH} \gtrsim 1$ AU. In two cases, these mergers correspond to the two most massive BBHs, which formed in dynamically active environments. As a further proof of their dynamical origin, these BBHs are characterized by eccentric orbits. In high-mass clusters, where dynamical interactions play a major role, the distribution of BBH mergers extends to higher values of $a_{\rm BBH}$ and $t_{\rm M}$. In particular, exchanged binaries, when they form, are generally characterized by large semi-major axes, up to 1.5×10^4 AU, and thus take longer times to enter the regime in which GWs efficiently shrink the semi-major axis. In some cases, $t_{\rm M}$ can be as high as 1400 Myr, indicating that dynamical hardening can play a role even at the very end of the simulation.

Finally, the dynamical encounters that lead to the formation of BBHs leave a distinctive imprint on their eccentricity. The resulting binary systems are, in fact, characterized by larger eccentricities at formation, with $e_{\rm BBH} > 0.1$[6]. Exchanged BBHs that have values of $t_{\rm M} \lesssim 100$ Myr and high eccentricities can be later disrupted by dynamical interactions, and are no longer present at 1500 Myr.

4.3.5 Formation pathway of BHs in the upper mass gap

In high-mass (low-mass) stellar clusters, the primary component of 26 BBH mergers (1 BBH merger) has mass in the PI gap. This corresponds to 8% (2.5%) of all BBH mergers

[6]In this discussion, we refer to the eccentricity at the BBH formation. During the in-spiral phase, the BBH mergers will still be circularized as a consequence of GW emission.

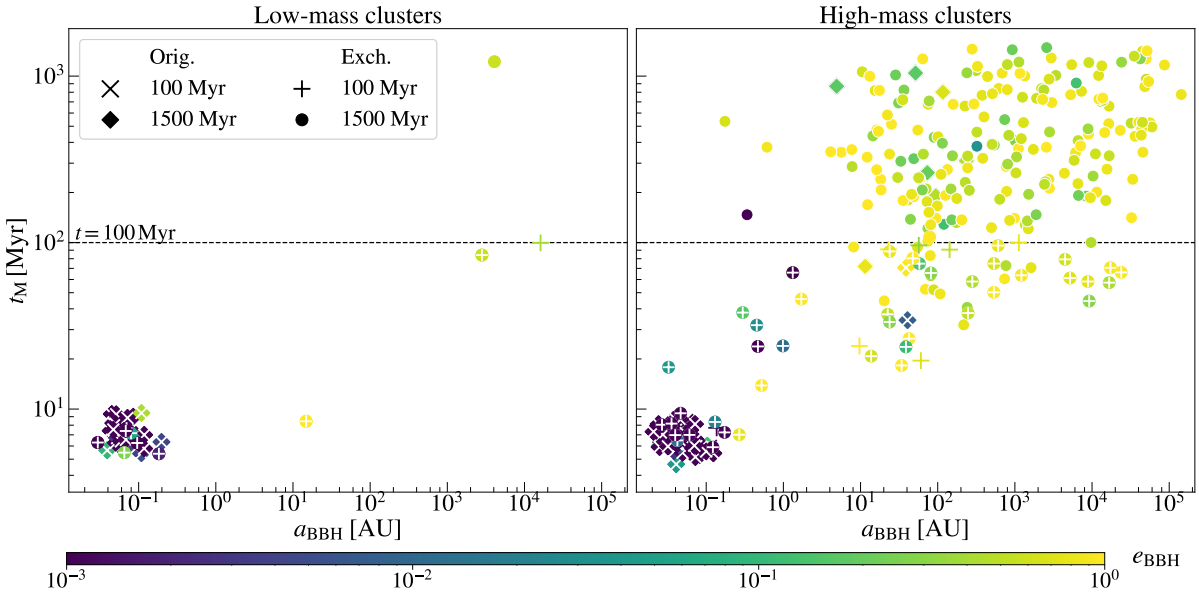

Figure 4.7: Time at which the semi-major axis of the BBH has become sufficiently tight to merge within a Hubble time via GW emission (according to Peters 1964) versus semi-major axis of the BBH when it forms (a_{BBH}), for merging BBHs in low-mass clusters (left) and high-mass clusters (right). The markers are the same as in Figure 4.5. The colour-map encodes the information on the orbital eccentricity at the BBH formation, e_{BBH}. If a BBH at 1500 Myr is also present at 100 Myr, it is marked with a white cross (original) or plus (exchanged).

in high-mass (low-mass) clusters. Figure 4.9 shows the evolution of some BHs in the PI mass gap that become the primary components of BBH mergers. In all cases, the progenitor star undergoes at least one collision with another star. The merger product of such stellar collisions is an exotic star, with an undersized He core with respect to the hydrogen-rich envelope. Such star does not develop PI, because its central properties (temperature and density) do not fall within the PI regime (e.g., Renzo et al. 2020; Costa et al. 2021, 2022; Ballone et al. 2022). At the end of its evolution, the stellar product directly collapses into a BH more massive than 60 $M_\odot$.

In all our simulations, the binary system that eventually results in a BBH merger with primary mass in the PI gap forms via dynamical exchanges, when both components have already collapsed into BHs. We conservatively assume that mergers between a BH and a star do not affect the mass of the BH, because we expect mass accretion onto the BH to be very inefficient (Di Carlo et al. 2020a,b, but see Rizzuto et al. 2021 for a different assumption).

4.4 Summary

We have studied the formation of BBHs in young and open star clusters via direct N-body simulations, exploiting the codes NBODY6++GPU (Wang et al. 2015) and MOBSE (Mapelli et al. 2017). We simulated two different classes of star clusters: low-mass (500–800 $M_\odot$) and relatively high-mass (5000–8000 $M_\odot$) systems. We find that the properties

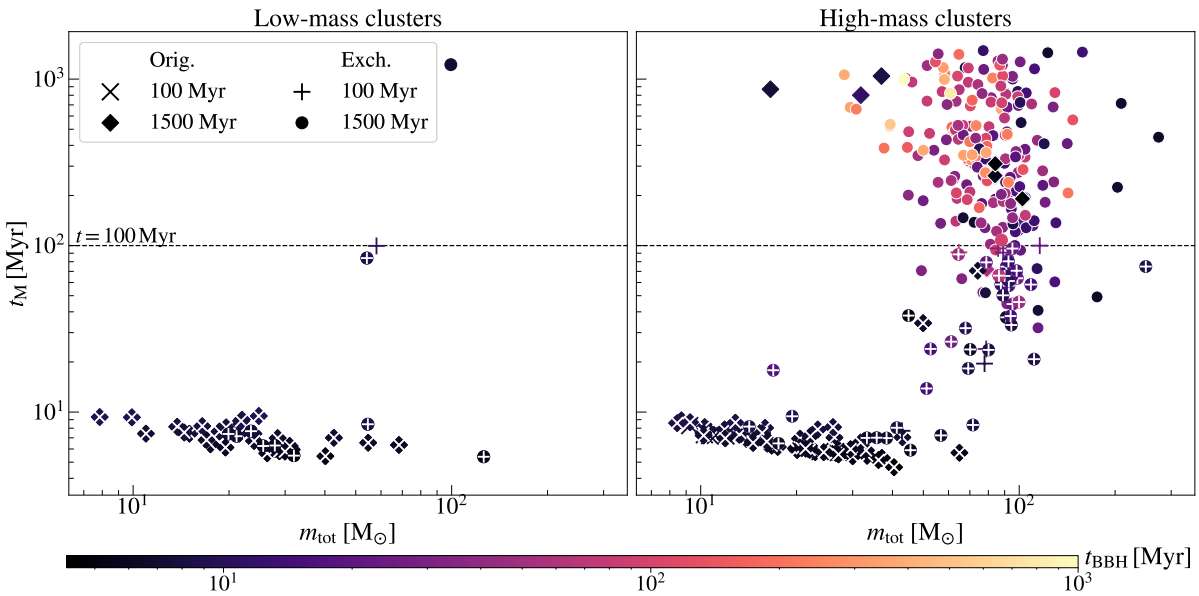

Figure 4.8: Time at which the semi-major axis of the BBH has become sufficiently tight to merge within a Hubble time via GW emission (according to Peters 1964) versus total mass of the BBH merger (m_{tot}), for merging BBHs in low-mass clusters (left) and high-mass clusters (right). The markers are the same as in Figure 4.5. The colour-map encodes the information on the time at which the BBH forms, t_{BBH}. If a BBH at 1500 Myr is also present at 100 Myr, it is marked with a white cross (original) or plus (exchanged).

and timescales of BBH mergers in the two star-cluster families are extremely different.

In low-mass clusters, most BBHs form in the first 100 Myr and are the result of the evolution of original binary stars, which evolve through common envelope. They do not harden significantly after $\sim$ 100 Myr. In contrast, the late evolutionary stages ($>$ 1 Gyr) are crucial for high-mass clusters. Exchanged BBHs (i.e., BBHs that form via dynamical exchanges) are the most common BBH mergers in high-mass clusters (Figures 4.3 and 4.5). While exchanged BBHs form preferentially in the first $\sim$ 100 Myr, they keep hardening significantly until the end of the simulations (1.5 Gyr, Figure 4.4). This confirms the importance of integrating the evolution of relatively massive clusters ($\gtrsim$ 5000 $M_\odot$) for $>$ 1 Gyr.

This difference between the BBH population of low-mass and high-mass star clusters mostly springs from the different two-body relaxation timescale and tidal disruption timescale of the two star cluster families. Our low-mass and high-mass star clusters have an average two-body relaxation timescale (Spitzer 1987) of $\sim$ 10 Myr and $\sim$ 26 Myr, respectively. This means that mass segregation and other dynamical processes happen earlier in low-mass clusters. Furthermore, low-mass clusters dissolve already at $\sim$ 300 Myr because of the galactic tidal field, while our high-mass clusters become tidally filling at $\gtrsim$ 1200 Myr (Figure 4.1). Hence, the dynamical activity of the low-mass clusters is quenched by tidal evaporation about four times earlier than that of high-mass clusters.

In both low-mass and high-mass clusters, the latest BBHs that form (exchanged BBHs) are the most massive ones (primary mass $\gtrsim$ 30 $M_\odot$), because dynamical exchanges favour the pairing of the most massive BHs (Figure 4.5). The distribution of the chirp mass of

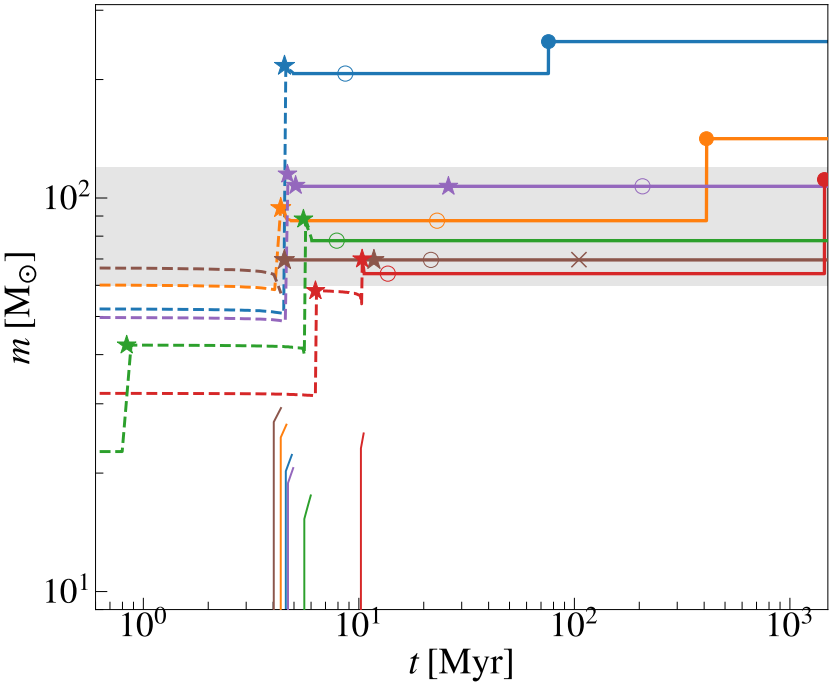

Figure 4.9: Evolution of the total mass (thick lines) and core mass (thin lines), for the progenitors of BHs in the PI mass gap and for the most massive primary component of a BBH merger (blue line). The dashed lines mark the time interval before the star becomes a BH. Different markers indicate: the merger between the progenitor star or the BH and another star (stars), the time when the BBH forms (open circles), the merger between the BH and another BH (filled circle), and the time at which the binary is possibly disrupted (crosses). The grey area encloses the PI mass gap, from $\sim 60\,M_\odot$ to $\sim 120\,M_\odot$.

BBH mergers shows two main peaks: the main peak at $\sim 30-40$ M$_\odot$, and a secondary peak at $\sim 7-15$ M$_\odot$. The high-mass peak develops mainly after 100 Myr (Figure 4.6).

These results confirm that we must integrate the evolution of a star cluster for at least 50 two-body relaxation timescales if we want to probe its BBH population.

BBH mergers in low-mass clusters are driven mostly by binary evolution via common envelope: they form with short semi-major axis (~ 0.1 AU) and low orbital eccentricity (Figure 4.7). In contrast, massive BBHs in high-mass clusters form with larger semi-major axis (> 10 AU) and higher orbital eccentricity ($0.1-1$).

A non-negligible percentage (8%) of our simulated BBH mergers in high-mass clusters have primary component's mass in the pair-instability (PI) mass gap. All of them form via stellar collisions, in which a main-sequence star merges with a more evolved star (core He burning). About 80% of these massive BBHs leave a merger remnant in the IMBH range. In contrast, in low-mass clusters only one dynamical BBH merger produces an IMBH.

Furthermore, in the high-mass clusters, we find a few original BBHs with primary mass in the PI mass gap. These are systems in which one of the two components of the binary star undergoes a collision with a third star and collapses to a BH in the PI mass gap without leading to the ionization of the original binary system.

Overall, our study shows that the formation channels of BBHs in low-mass ($\sim 500-800$

$M_\odot$) and high-mass star clusters ($\geq$ 5000 $M_\odot$) are extremely different and lead to two completely distinct BBH populations. Low-mass clusters host mainly low-mass BBHs born from binary evolution, while BBHs in high-mass clusters are relatively massive and driven by exchanges. This difference is crucial for the interpretation of GW sources.

Acknowledgements

We thank the anonymous referee for the insightful comments, which helped to improve the quality of this manuscript. MM, AB and SR knowledge financial support from the EuropeanResearch Council for the ERC Consolidator grant DEMOBLACK, under contract no. 770017. MP acknowledges financial support from the European Union's Horizon 2020 research and innovation programme under the Marie Sklodowska-Curie grant agreement No. 896248. We thank Nicola Giacobbo and the members of the DEMOBLACK team for useful discussions. ST thanks Mark Gieles and the ICCUB Virgo team for useful comments and discussions. We acknowledge that the results of this research have been achieved using the DECI resource Snellius based in the Netherlands at SURFsara, with support from the PRACE aisbl.

Chapter 5

Hierarchical binary black hole mergers in globular clusters: the impact of cluster evolution

Based on the draft of the manuscript:
Torniamenti S., Mapelli M., et al.
"Hierarchical binary black hole mergers in globular clusters: the impact of cluster evolution", to be submitted to MNRAS.

Abstract

Hierarchical mergers are one of the main proposed channels to form massive binary black holes (BBHs). Here, we explore the process of hierarchical mergers in globular clusters by means of our semi-analytic code FASTCLUSTER. We model the structural evolution of globular clusters by taking into account mass loss by stellar evolution, two-body relaxation, and tidal stripping by the host galaxy. These processes quench the hierarchical assembly of black holes (BHs), by reducing the cluster central density and escape velocity. We find that globular clusters host hierarchical BH mergers up to the third generation when we properly account for cluster evolution, whereas our non-evolving cluster models produce four (or more) generations of BHs. Our third-generation BHs reach a maximum mass of $\sim 200\,M_\odot$ at low metallicity ($Z = 0.0002$), and are produced only if the initial escape velocity is $\gtrsim 30\,\mathrm{km\,s^{-1}}$. The BH spin distribution shows a peak at $\chi_1 = 0.7$ for second-generation BHs, an $\chi_1 = 0.8$ for third-generation BHs, with a spread that depends on the first-generation distribution. In turn, this has also an impact on the precessing spins, whose distribution peaks at $\chi_\mathrm{p} = 0.7$ for second-generation BHs, independently of the first-generation spin distribution.

keywords: gravitational waves – black hole physics – stars: black holes – stars: kinematics and dynamics – galaxies: star clusters: general

5.1 Introduction

The detection of gravitational waves (GWs) by the Advanced LIGO (Aasi et al. 2015) and Virgo (Acernese et al. 2015b) inteferometers has opened new perspectives for our

understanding of compact objects. At the present day, the third gravitational-wave transient catalog (GWTC-3) includes a total of 90 candidate events with a high probability of astrophysical origin (Abbott et al. 2021b,d). Most of them are interpreted as the merger of two black holes (BHs). Also, several additional candidates have been claimed, based on independent pipelines (Zackay et al. 2019; Venumadhav et al. 2020; Nitz et al. 2020). The growing sample of GW detections has made it possible, for the first time, to try to reconstruct the underlying black hole (BH) population, and understand the complex physical processes that affect their formation and evolution.

A fundamental piece of this puzzle is represented by the detection of the most massive BH mergers, namely GW190521 (Abbott et al. 2020; Abbott et al. 2020d), and, possibly, GW190403_051519, GW190426_190642 (Abbott et al. 2021f), and GW200220_061928 (Abbott et al. 2021d). In particular, the remnant of GW190521, which originates from the inspiral of two BHs with masses $m_1 = 85^{+21}_{-14}\,\mathrm{M}_\odot$ and $m_2 = 66^{+17}_{-18}\,\mathrm{M}_\odot$ (Abbott et al. 2020d) is the very first intermediate-mass BH (IMBH) ever detected in the mass range $100 - 1000\mathrm{M}_\odot$. Also, its BH progenitors lie within the (pulsational) pair-instability (PI) mass gap ($60 - 120\,\mathrm{M}_\odot$, Belczynski et al. 2016b; Woosley 2017; Spera & Mapelli 2017; Marchant et al. 2019; Stevenson et al. 2019), where BHs are not expected to form from the collapse of a single star.

The formation pathway of BBH mergers within and above the PI mass gap is still matter of debate, because of the large uncertainties that affect both the lower and the upper boundary (Farmer et al. 2020; Mapelli et al. 2021b; Farrell et al. 2021; Belczynski et al. 2020; Costa et al. 2022). Direct collisions of stars or BHs in dense stellar environments, like young, globular and star clusters might produce BHs that fill the PI mass gap. More specifically, the collision a massive star with a well-developed helium core and a non-evolved companion may lead to the formation of exotic stars with an undersized core, whose temperature and density do not fall within the PI regime, and which directly collapses into a BH more massive than $\sim 60\mathrm{M}_\odot$ (Spera et al. 2019; Renzo et al. 2020; Costa et al. 2022; Ballone et al. 2022). Direct $N-$body simulations show that these collisions are not rare in young and open clusters (Di Carlo et al. 2019, 2020a; Torniamenti et al. 2022b). Also, stellar-origin BHs can undergo repeated mergers with other BHs, a scenario referred to as hierarchical merger scenario (e.g., Miller & Hamilton 2002; Fishbach et al. 2017; Gerosa & Berti 2017; Doctor et al. 2020; see Gerosa & Fishbach 2021 for a recent review on this topic).

The hierarchical assembly of BHs is a complex process, because it involves a non-trivial interplay between the properties of the binary BH (BBH) population (mass ratios, spins) and the structure and evolution of the host cluster (escape velocity, central density). In particular, when two BHs merge, the BH remnant receives a relativistic recoil at birth, due to the asymmetric momentum dissipation by GWs (e.g., Fitchett 1983; Favata et al. 2004; Campanelli et al. 2007; Lousto & Zlochower 2011). This recoil can be as large as thousands of $\mathrm{km\,s^{-1}}$ (Holley-Bockelmann et al. 2008; Moody & Sigurdsson 2009; Fragione & Kocsis 2018; Gerosa & Berti 2019; Arca Sedda et al. 2020), depending on the mass ratio and the spin alignment of the merging BHs, and may lead to the ejection of the BH remnant. This prevents the possibility of successive mergers. For this reason, the stellar environments that mainly favour the hierarchical assembly of BHs are those with larger escape velocities. Also, when the merger remnant is retained in the cluster, the star cluster central density needs to be high enough to allow the merger remnant to pair up again by dynamical exchanges or three-body encounters (e.g., Heggie 1975; Hills &

Fullerton 1980). Massive stellar systems like nuclear star clusters (NSCs) and globular clusters (GCs) are ideal candidates to host hierarchical mergers, because of their high densities ($\gtrsim 10^4\,M_\odot\,pc^{-3}$) and escape velocities ($\gtrsim 10-100\,km\,s^{-1}$).

In this work, we aim to explore the impact of the evolution of the host star cluster on the production of dynamically-formed BBH hierarchical mergers, by simultaneously taking into account mass loss, relaxation, and tidal stripping by the host galaxy . In particular, we will focus on GCs. Exploring the relevant parameter space, for both the BBHs (masses, mass ratios, spins), and the host cluster (total mass, density, metallicity), is not feasible by hybrid Monte-Carlo and/or N-body codes. To avoid this complication, a number of semi-analytic codes has been developed, e.g. `cBHBd` (Antonini et al. 2019; Antonini & Gieles 2020b; Antonini et al. 2022), FASTCLUSTER (Mapelli et al. 2021a, 2022), `B-POP` (Arca Sedda et al. 2021), and `Rapster` (Kritos et al. 2022b,a). In particular, Mapelli et al. (2021a, 2022) introduced a fast and flexible semi-analytic model to integrate the hardening and GW emission in different environments, that is young stellar clusters, globular clusters, and nuclear star clusters. This tool, named FASTCLUSTER, overcomes the numerical challenge of simulating BBHs in massive and long-lived star clusters by integrating the effect of dynamical hardening and GW emission with a fast and semi-analytical approach, calibrated on direct $N-$body models. In this work, we have further improved this tool, by implemented all the relevant aspect of cluster evolution: stellar evolution, two-body relaxation and tidal stripping by the host galaxy. In this way, we can integrate, in the same framework, both the evolution of the host stellar environment (mass, escape velocity, central density) and the orbital properties of the dynamically-formed BBH mergers (BH masses, semi-major axis, eccentricity).

This work is organized as follows. In Sect. 5.2 we introduce the details of the code implementation. In Sect. 5.3 we report our result for the populations of hierarchical mergers. Finally, Sect. 5.4 summarizes our conclusions.

5.2 Methods

In this work, we have implemented the relevant aspects of star cluster evolution in FASTCLUSTER (Mapelli et al. 2021a, 2022), which allows to integrate the hardening and GW emission via semi-analytical recipes. To do this, we have coupled FASTCLUSTER with the semi-analytic code CLUSTERBH (Antonini & Gieles 2020b), which provides recipes for the evolution of the host cluster as a consequence of stellar mass loss and relaxation. Also, we have implemented tidal stripping in our code, by referring to the analytic formulas by Gieles et al. (2011).

In order to achieve a fast but realistic description of the star cluster evolution, our code evolves only the bulk properties of the stellar cluster, that are relevant for the formation and evolution of BBHs, without considering the detailed internal structure. In particular, we will trace the evolution of $M_{\rm tot}$, $M_{\rm BH}$, and the half-mass radius of the cluster $r_{\rm h}$ (Antonini & Gieles 2020b).

5.2.1 Star cluster evolution

The basic assumption of our cluster evolution model is that the star cluster consists in two components, BHs, with a total mass of $M_{\rm BH}$, and all the other members (including

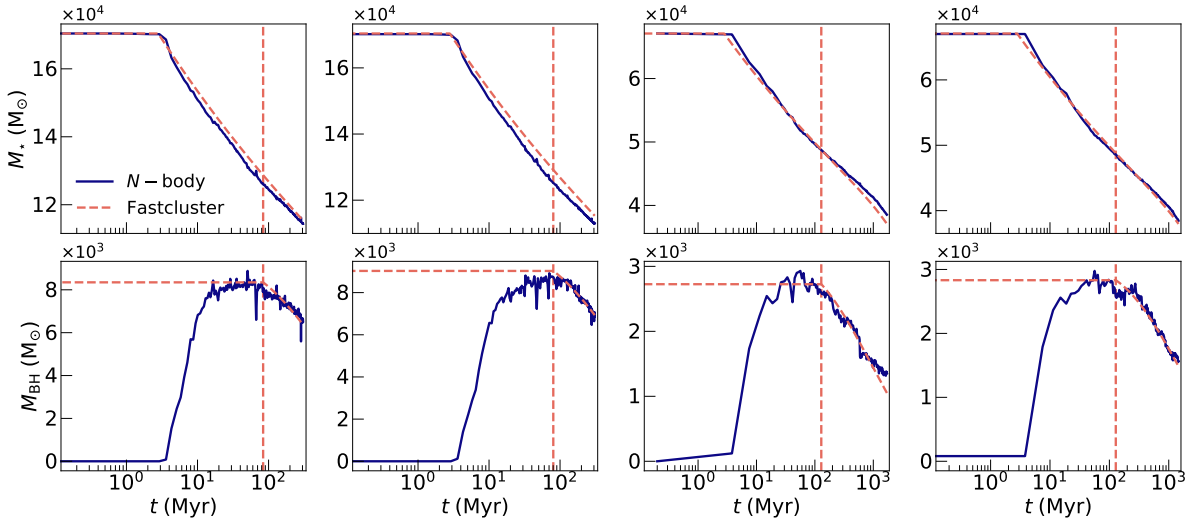

Figure 5.1: Evolution of the mass of the stellar (upper panels) and BH mass (lower panels), for the $N-$body simulations (blue, solid line) and FASTCLUSTER (red dashed line). The red vertical dashed line displays the time of core collapse in FASTCLUSTER.

stars and the other stellar remnants), with a total mass of M_* (Breen & Heggie 2013). The total mass of the cluster is $M_{\rm tot} = M_* + M_{\rm BH}$.

Stellar mass loss

We assume that the mass loss by stellar evolution evolves as a function of time (Antonini & Gieles 2020b):

$$\dot{M}_{*,\rm sev} = \begin{cases} 0 & t < t_{\rm sev}, \\ -\nu \frac{M_*}{t} & t \geq t_{\rm sev}, \end{cases} \tag{5.1}$$

where $t_{\rm sev}$ is the time-scale for mass loss by stellar evolution, which we will calibrate with $N-$body simulations (see Sect. 5.2.2) and $\nu \approx 0.07$ is a free parameter fitted to the results of $N-$body simulations (Antonini & Gieles 2020b). As a result of mass loss by stellar evolution, the cluster is assumed to expand adiabatically:

$$\dot{r}_{\rm h,sev} = -\frac{\dot{M}_{*,\rm sev}}{M_{\rm tot}} r_{\rm h}. \tag{5.2}$$

Two-body relaxation

We model the relaxation processes by considering the case of a two-component stellar cluster hosting a BH sub-system, following Breen & Heggie (2013). As the stellar system evolves towards energy equipartition, the most massive components (the BHs in this case) become more and more segregated at the center. If we assume that the star cluster is Spitzer (1969) unstable, a temperature difference holds between the two components, generating a heat transfer from the center of the cluster towards the outer parts. When several relaxation times have elapsed, the stellar cluster achieves a state of balanced

evolution (Hénon 1961; Breen & Heggie 2013), where energy is produced in the BH sub-system core by dynamical interactions between BHs and BBHs. The produced energy is then conducted via two-body relaxation, and spreads throughout the bulk of the cluster. The energy flux from the core is regulated by the energy demand of the whole cluster (Hénon 1961). As a consequence, the evolution of the BH sub-system can be related to the global evolution of the cluster.

We define the onset of the the balanced evolution as the moment of the BH core collapse (Antonini & Gieles 2020b):

$$t_{\rm cc} = N_{\rm rh}\, t_{{\rm rh},\psi}(t=0), \tag{5.3}$$

where $N_{\rm rh} = 3.21$ is fitted to $N-$body models (Antonini & Gieles 2020b), and $t_{{\rm rh},\psi}$ is the half-mass relaxation time-scale, defined as (Spitzer & Hart 1971b):

$$t_{{\rm rh},\psi} = 0.138\sqrt{\frac{M_{\rm tot}\, r_{\rm h}^3}{G}}\frac{1}{\langle m\rangle\, \psi \ln\Lambda}. \tag{5.4}$$

Here, $\langle m\rangle$ is the mean mass of a star in the cluster, including all the components, and $\ln\Lambda = 10$ is the Coulomb logarithm. The parameter ψ is the heat conduction efficiency of the cluster in presence of a mass spectrum. In fact , $\psi = 1$ for equal-mass systems, but can be as high as 30–100 for young clusters, where very massive stars are present (Gieles et al. 2010). For this work, we refer to the derivation of ψ for a two-component system under the assumption of energy equipartition, given by Spitzer & Hart (1971b):

$$\psi = \left(m_*^{3/2}\, M_* + m_{\rm BH}^{3/2}\, M_{\rm BH}\right)\, N_{\rm tot}^{3/2}/M_{\rm tot}^{5/2}, \tag{5.5}$$

where m_* and $m_{\rm BH}$ are the mean mass of stars and BHs, respectively, and $N_{\rm tot}$ is the total number of particles within the cluster.

In each run, the mean mass of the BH population is set to the mean mass of the BH catalogue used to generate the first-generation BBHs (see Sect. 5.2.4). This allows to incorporate the dependence of the BH mass on metallicity. The total mass of the BH population, $M_{\rm BH}$, is tuned based on the comparison with realistic $N-$body simulations, as described in Sect. 5.2.2

After the onset of balance evolution, the rate of energy from the core to the bulk of the cluster is given by the energy flux at the half-mass radius (Hénon 1961; Breen & Heggie 2013):

$$\dot{E} = \zeta\frac{|E|}{t_{{\rm h},\psi}}, \tag{5.6}$$

where $E = -0.2\, G\, M_{\rm tot}^2/r_{\rm h}$ is the total energy, and $\zeta = 0.1$ quantifies the expansion rate (Gieles et al. 2011). In a BH sub-system, the dynamical interactions that produce heat in the core also result in the ejection of BBHs and BHs. More specifically, a BBH that forms within the cluster hardens as a consequence of dynamical interactions, until the dynamical recoil is high enough to eject it from the cluster (Goodman 1984).

As a consequence, we can couple the energy generation within the core to the BH mass-loss rate, which, in turn, depends on the total energy and the relaxation time-scale (Breen & Heggie 2013; Antonini & Gieles 2020b):

$$\dot{M}_{\rm BH} = \begin{cases} 0, & t < t_{\rm cc} \text{ or } M_{\rm BH} = 0 \\ -\beta\frac{M_{\rm tot}}{t_{\rm rh}} & t \geq t_{\rm cc} \text{ or } M_{\rm BH} > 0, \end{cases} \tag{5.7}$$

where $\beta \approx 0.003$ is fitted to $N-$body models (Antonini & Gieles 2020b). The resulting expansion rate can be derived, under the assumption of virial equilibrium from eq. 5.6:

$$\dot{r}_{\rm h,rlx} = \zeta \frac{r_{\rm h}}{t_{\rm rh}} + 2 \frac{\dot{M}_{\rm tot}}{M_{\rm tot}} r_{\rm h}, \tag{5.8}$$

where $\dot{M}_{\rm tot} = \dot{M}_* + \dot{M}_{\rm BH}$. The combined evolution for the half-mass radius, by including stellar mass-loss and relaxation processes is:

$$\dot{r}_{\rm h} = \begin{cases} 0 & t < t_{\rm sev}, \\ \dot{r}_{\rm h,sev} & t \geq t_{\rm sev} \text{ and } \mathrm{t} < \mathrm{t_{cc}}, \\ \dot{r}_{\rm h,sev} + \dot{r}_{\rm h,rlx} & t \geq t_{\rm cc} \end{cases} \tag{5.9}$$

Tidal mass loss

Tidal stripping brings an additional stellar-mass loss term (Gieles et al. 2011):

$$\dot{M}_{*,\rm tid} = -\xi_{\rm J} \frac{M_{\rm tot}}{t_{\rm rh,\psi=1}}. \tag{5.10}$$

We set the mass-loss time-scale as the relaxation time for $\psi = 1$ (Gieles et al. 2011), because evaporation takes place at the tidal boundary, where almost no BHs are present. Also, $\xi_{\rm J}$ incorporates the cluster evolution at different tidally-filling regimes:

$$\xi_{\rm J} = \frac{3}{5}\zeta \left(\frac{r_{\rm h}/r_{\rm J}}{[r_{\rm h}/r_{\rm J}]_1} \right)^{3/2}, \tag{5.11}$$

where $r_{\rm J}$ is the Jacobi (tidal) radius, and $[r_{\rm h}/r_{\rm J}]_1 = 0.4$ is set following Gieles et al. (2011). In particular (Gieles & Baumgardt 2008):

$$r_{\rm J} = \left(\frac{G}{3\omega^2} \right)^{1/3} M_{\rm tot}^{1/3}, \tag{5.12}$$

where $\omega = V_{\rm C}\, R_{\rm G}^{-1}$ depends on the cluster galactocentric distance $R_{\rm G}$ and its circular velocity $V_{\rm C}$ (Gieles & Baumgardt 2008). To reproduce the Galactic rotational curve at each $R_{\rm G}$, we refer to a Dehnen (1993) profile:

$$V_C = G M_{\rm g} \frac{R^{2-\gamma}}{(R + r_{\rm s})^{3-\gamma}}. \tag{5.13}$$

where the galaxy total mass $M_{\rm g} = 3.18 \times 10^{11}\,\mathrm{M}_\odot$, the galaxy length scale $r_{\rm s} = 5.12$ kpc, and $\gamma = 0.54$ are fitted to reproduce the Milky Way rotational curve (Leveque et al. 2022).

The combined stellar mass loss, by including both stellar evolution and tidal stripping, is then:

$$\dot{M}_* = \begin{cases} \dot{M}_{*,\rm tid} & t < t_{\rm sev}, \\ \dot{M}_{*,\rm tid} + \dot{M}_{*,\rm sev} & t \geq t_{\rm sev}. \end{cases} \tag{5.14}$$

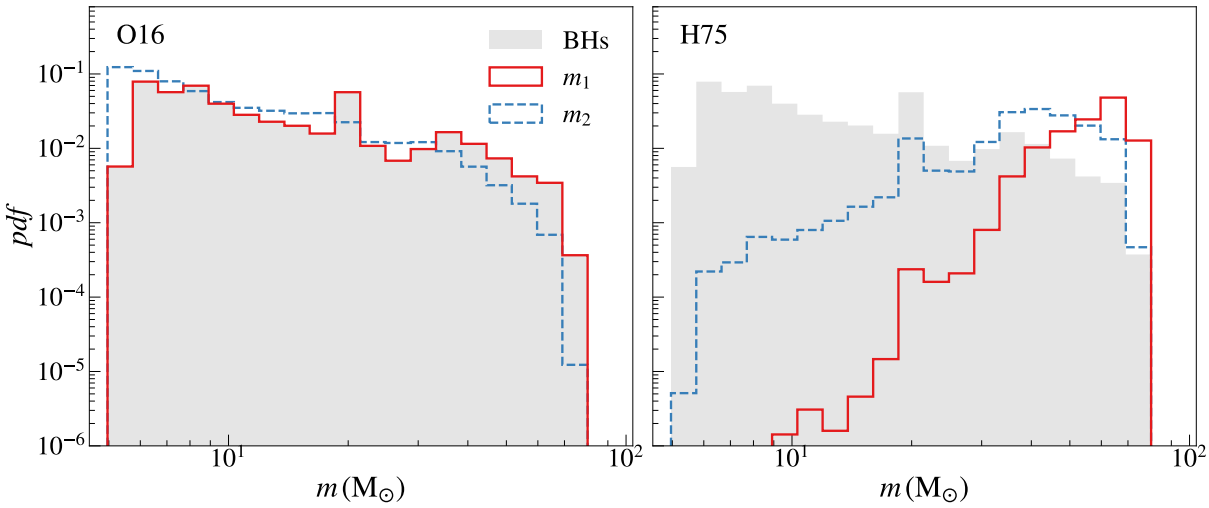

Figure 5.2: First generation (1g) of primary masses (red) and secondary masses (blue) of BBHs given by the mass sampling used in Mapelli et al. (2021a) (left) and by the new mass sampling used for this work (right), at metallicity: $Z = 0.0002$.

5.2.2 Comparison with $N-$body simulations

The relevant scales $t_{\rm sev}$, and $M_{\rm BH}$ depend on the details of the stellar evolutionary processes. In order to tune them to up-to-date stellar-evolution recipes, and to assess the goodness of the cluster evolution given by FASTCLUSTER, we compared the evolution of the stellar and BH component mass to that from the $N-$body simulations of GCs by Arca Sedda et al. (in prep.).

Figure 5.1 shows the comparison between the $N-$body models and FASTCLUSTER. For the stellar component, a value $t_{\rm sev} = 3$ Myr gives a good comparison for all the simulations we considered. Our semi-analytic code is able to reproduce the initial change of the slope in the stellar mass profile, as a consequence of wind mass loss and supernova explosions.

$M_{\rm BH}$ is the total mass of the central BH sub-system (Breen & Heggie 2013), which powers the evolution of the cluster (see Sect. 5.2.1). For this reason, we set its initial value to the total BH mass within the half-mass radius, at the moment of core collapse. For the $N-$body models we considered, the BH mass fraction $f_{\rm BH}$ ranges from 0.42 to 0.5. After core collapse, FASTCLUSTER can reproduce the slope of the evolution of the BH due to the dynamical ejection of BHs. For our runs, we will set $M_{\rm BH}$ by considering, for each cluster, a BH mass fraction $f_{\rm BH} = 0.45$.

5.2.3 Globular cluster properties

In our model, each GC is defined by its total mass $M_{\rm tot}$ and half-mass density ρ. We draw the total masses from a log-normal distribution with mean $\langle \log_{10} M_{\rm tot}/\mathrm{M}_\odot \rangle = 5.6$ (Harris 1996). We assume a fiducial standard deviation $\sigma_{\rm M} = 0.4$ for all star cluster flavours (Mapelli et al. 2021a, 2022).

The densities at the half-mass radius are drawn from a log-normal distribution with mean $\langle \log_{10} \rho/(\mathrm{M}_\odot\,\mathrm{pc}^{-3}) \rangle = 3.7$. We assume a fiducial standard deviation $\sigma_\rho = 0.4$. For each star cluster, we assume a core density $\rho_{\rm c} = 20\,\rho$. The escape velocity is calculated

from the relation (Georgiev et al. 2009b,a; Fragione et al. 2020):

$$v_{\rm esc} = 40\,{\rm km\,s^{-1}} \left(\frac{M_{\rm tot}}{10^5\,{\rm M_\odot}}\right)^{1/3} \left(\frac{\rho}{10^5\,{\rm M_\odot\,pc^{-3}}}\right)^{1/6}. \tag{5.15}$$

We simulate only one BBH per each randomly drawn GC, thus not taking into account possible BBH-BBH interactions. When star cluster evolution is not activated the lifetime of the star cluster is set to 13.6 Gyr. When star cluster evolution is activated, the lifetime of the star cluster is determined by the cluster evolution itself.

5.2.4 Hierarchical BBH mergers

First generation BHs

In this work, we study the BBH mergers in star clusters originating from first-generation (1g) dynamical BBH, which form from either the dynamical interaction between three single BHs or the exchange between a single BH and an existing BBH (Heggie 1975). We draw the masses of first-generation BHs from catalogues produced with the population synthesis code MOBSE[1] (Mapelli et al. 2017; Giacobbo et al. 2018).

We adopt the rapid model by Fryer et al. (2012) for core-collapse supernovae, while for (pulsational) PI supernovae we use the equations reported in the appendix of Mapelli et al. (2020). This yields a minimum BH mass of $\approx 5\,{\rm M_\odot}$ and a maximum BH that depends on metallicity. We consider four metallicities: $Z = 0.02$, 0.006, 0.002, 0.0002, which approximately correspond to ${\rm Z_\odot}$, $0.3\,{\rm Z_\odot}$, $0.1\,{\rm Z_\odot}$, $0.01\,{\rm Z_\odot}$. The maximum BH mass obtained, for each metallicity, is $80\,{\rm M_\odot}$, $60\,{\rm M_\odot}$, and $30\,{\rm M_\odot}$, respectively.

To generate 1g dynamical BBHs, we randomly draw the BH masses from the sample of single BHs or BHs in loose binaries in the MOBSE catalogue. Then, we consider two possible criteria for coupling the BH masses.

BH mass coupling

First, we refer to the mass sampling used in Mapelli et al. (2021a). In this case, the mass of the primary m_1 is uniformly sampled from the list of BHs, while the secondary is sampled from the probability distribution function (O'Leary et al. 2016):

$$p(m_2) \propto (m_1 + m_2)^4, \tag{5.16}$$

in the interval $[m_{\rm min}, m_1)$ where $m_{\rm min} = 5\,{\rm M_\odot}$. Hereafter, we will refer to this mass coupling as to O16.

In this work, we also consider the mass sampling introduced in Antonini et al. (2022). In this approach, the coupling rate for BHs is calculated from the formation rate of hard binaries per unit of volume and energy, given by Heggie (1975):

$$\Gamma_{\rm 3b}(m_1, m_2, m_3, x) = n_1 n_2 n_3\, Q(m_1, m_2, m_3, x), \tag{5.17}$$

where $n_i = n(m_i)$ is the number density for BHs with mass m_i. In this formalism, m_1 and m_2 are the masses of the BHs that form the binary, while m_3 is the mass of the interacting third body. The rate function Q (see eq. 4.14 of Heggie 1975) depends on the

[1] MOBSE is publicly available at https://gitlab.com/micmap/mobse_open.

masses of the three BHs, on the binding energy of the binary, and on the inverse of their mean internal energy $(m_i\sigma_i^2)^{-1}$, where σ_i is the component velocity dispersion. Because massive objects at the cluster center tend to reach a condition of energy equipartition, we assume that $\beta_1 = \beta_2 = \beta_3$.

The binary formation rate per unit volume as a function of the masses of the interacting BHs can be calculated by integrating the rate function over all x from the hard-soft boundary. The resulting formation rate (per unit volume) is (Antonini et al. 2022):

$$\Gamma_{3b}(m_1, m_2, m_3) \propto n_1 n_2 n_3 \frac{(m_1 m_2)^4 m_3^{5/2}}{\sqrt{(m_1 + m_2 + m_3)(m_1 + m_2)}} \beta^{9/2}, \tag{5.18}$$

and the probability density function for the mass of either m_1 or m_2 is (note that eq. 5.18 is symmetric with respect to their masses):

$$p_{1,2}(m_{1,2}) = \int_{m_{low}}^{m_{up}} \int_{m_{low}}^{m_{up}} dm_3\, dm_{2,1}\, \Gamma_{3b}, \tag{5.19}$$

where $m_{\rm low}$ and m_{up} are the lower and upper limit of the mass distribution. To generate 1g BBHs through this mass sampling, we randomly sample from the MOBSE catalogue pairs of masses by using eq. 5.19. Then, we assign m_1 (m_2) to the maximum (minimum) sampled masses. Hereafter, we will refer to this mass coupling as to H75.

Figure 5.2 shows the resulting mass couplings, at a metallicity $Z = 0.0002$. Dynamical BBHs generated through the H75 coupling are skewed towards higher masses, as a consequence to the tendency of dynamical interactions to pair up the most massive objects. As a consequence, the primaries have always masses $m_1 > 10\,{\rm M}_\odot$.

After generating the BH masses, we check that the BBH components are not ejected by supernova kicks. The kick is calculated, like in Mapelli et al. (2021a), based on linear momentum conservation:

$$v_{\rm SN} = v_{\rm H05} \frac{\langle m_{\rm SN} \rangle}{m_{\rm BH}}, \tag{5.20}$$

where $m_{\rm BH}$ is the BH mass, $\langle m_{\rm SN} \rangle = 1.33\,{\rm M}_\odot$ is the average NS mass (Özel & Freire 2016), and $v_{\rm H05}$ is randomly drawn from a Maxwellian distribution with root-mean square $265\,{\rm km s}^{-1}$. If the BBH components receive a kick larger than the escape velocity (eq. 5.15), we do not evolve the BBH.

The dimensionless spin magnitudes (χ_1 and χ_2) of the BHs are sampled from Maxwellian distributions with root-mean square $\sigma_\chi = 0.05$, 0.01, or 0.1. We draw spin directions isotropic over the sphere, because dynamical interactions reset any spin alignments with the orbital angular momentum of the binary system.

The BBH initial eccentricity is drawn from a thermal probability distribution (Heggie 1975):

$$p(e) = 2\,e \quad e \in [0, 1), \tag{5.21}$$

and the semi-major axis is drawn from:

$$p(a) \propto a^{-1} \quad a \in [1, 10^3]\,{\rm R}_\odot. \tag{5.22}$$

Since soft binaries are disrupted by dynamical interactions within the star cluster (Heggie 1975), we first check if the newly-generated binary is hard. If not, we generate a new semi-major axis until we obtain a hard binary, which is then integrated.

Table 5.1: Summary of the models.

ID	1g	Ng	Z	σ_χ	Evol. cases
Ong	O16	ngng	0.0002	0.05	NoEv, Evol, Tidal
O1g	O16	ng1g	0.0002	0.05	NoEv, Evol, Tidal
H1g	H75	ng1g	0.0002	0.05	NoEv, Evol, Tidal

Column 1: Name of the model; column 2: coupling criterion of the BH masses (O16, H75); column 3: coupling of the Ng secondary mass (ngng, ng1g); column 4: metallicity of first-generation BHs (Z = 0.0002, 0.002, 0.02); column 5: root-mean square value of the Maxwellian distribution of spin magnitudes (σ_χ = 0.05, 0.1, 0.01); column 6: evolutionary cases for the stellar cluster (NoEv, Evol, Tidal).

Orbital evolution

Hard BBHs within the star cluster evolve as a consequence of both dynamical hardening and gravitational wave emission. The evolution of their semi-major axis a and eccentricity e can be described as (Mapelli et al. 2021a):

$$\begin{aligned}\frac{\mathrm{d}a}{\mathrm{d}t} &= -2\,\pi\,\xi\,\frac{G\,\rho_\mathrm{c}}{\sigma}\,a^2 - \frac{64}{5}\,\frac{G^3\,m_1\,m_2\,(m_1+m_2)}{c^5\,a^3\,(1-e^2)^{7/2}}\,f_1(e)\\ \frac{\mathrm{d}e}{\mathrm{d}t} &= 2\,\pi\,\xi\,\kappa\,\frac{G\,\rho_\mathrm{c}}{\sigma}\,a - \frac{304}{15}\,e\frac{G^3\,m_1\,m_2\,(m_1+m_2)}{c^5\,a^4\,(1-e^2)^{5/2}}\,f_2(e),\end{aligned} \tag{5.23}$$

where c is the speed of light and (Peters 1964):

$$\begin{aligned}f_1(e) &= 1 + \frac{73}{24}\,e^2 + \frac{37}{96}\,e^4\\ f_2(e) &= 1 + \frac{121}{304}\,e^2.\end{aligned} \tag{5.24}$$

In eqs. 5.23, σ is the 3D velocity dispersion, and ξ and κ are two dimensionless parameters, calibrated with direct $N-$body simulations (Hills 1983; Quinlan 1996; Miller & Hamilton 2002; Sesana et al. 2006). Here, we assume $\xi = 3$ (Quinlan 1996) and $\kappa = 0.1$ (Sesana et al. 2006). Equations 5.23 are composed of two terms. The first ones ($\mathrm{d}a/\mathrm{d}t \propto -a^2$ and $\mathrm{d}e/\mathrm{d}t \propto a$) describe the dynamical hardening and the evolution of eccentricity via Newtonian dynamical scatterings; the second ones ($\mathrm{d}a/\mathrm{d}t \propto -a^{-3}$ and $\mathrm{d}e/\mathrm{d}t \propto -a^{-4}$) describe hardening and circularization via GW emission (Peters 1964).

Equations 5.23 are integrated until the BBH is ejected from the cluster, or it merges, or the star cluster dies by evaporation, or we reach the Hubble time (which one of these cases happens first). If the BBH is ejected from the cluster, FASTCLUSTER integrates only the second terms of eqs. 5.23 (hardening and circularization by GW emission) until either the BBH merges in the field or a Hubble time has elapsed (Mapelli et al. 2021a, 2022).

A binary is assumed to be ejected from the cluster when $a_\mathrm{ej} > a_\mathrm{GW}$ (Baibhav et al. 2020) where

$$a_\mathrm{ej} = \frac{2\,\xi\,{m_*}^2}{(m_1+m_2)^3}\,\frac{G\,m_1\,m_2}{v_\mathrm{esc}^2} \tag{5.25}$$

is semi-major axis below which the BBH is ejected by dynamical recoil and:

$$a_{\rm GW} = \left[\frac{32\,G^2}{5\,\pi\,\xi\,c^5} \frac{\sigma\,m_1\,m_2\,(m_1+m_2)}{\rho_{\rm c}\,(1-e^2)^{7/2}}\,f_1(e) \right]^{1/5} \tag{5.26}$$

is the maximum semi-major axis for the regime of efficient orbital decay via GW emission.

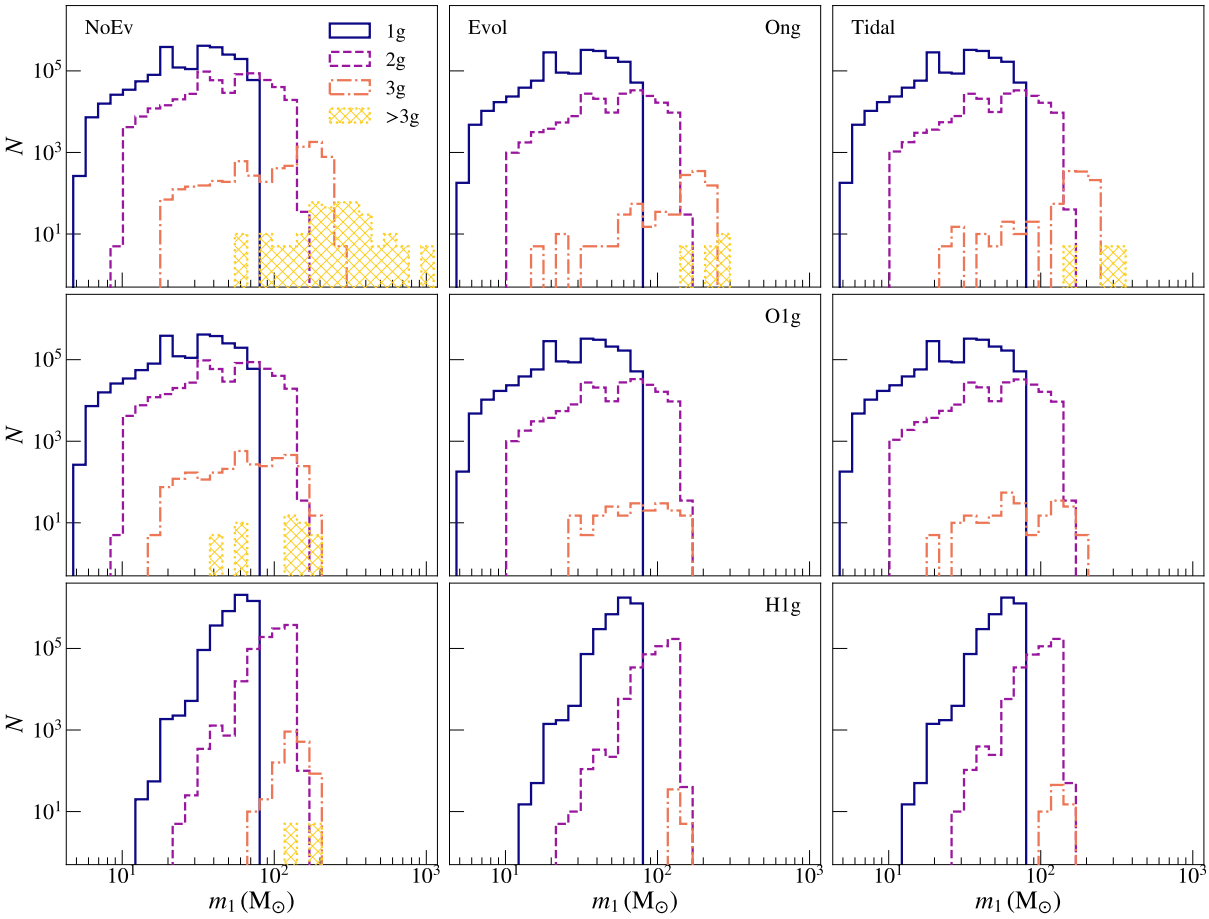

Figure 5.3: Populations of BBH mergers at different generations for the models Ong (upper panels), O1g (middle panels), H1g (lower panels), for different evolutionary cases: NoEv (left), Evol (center), Tidal (right). Different colours show BBH mergers at different generations.

Nth generation (Ng) dynamical BBHs

If the BBH merger time $t_{\rm GW}$ is less than one Hubble time (13.7 Gyr), we estimate the mass and spin of the merger remnant using the fitting formulas by Jiménez-Forteza et al. (2017). Also, if the BBH merges inside its parent star cluster, we calculate the relativistic kick magnitude $v_{\rm K}$ using the fitting formula by Lousto et al. (2012). We assume that the merger remnant remains inside its parent cluster if the relativistic kick magnitude $v_{\rm K} < v_{\rm esc}$, where $v_{\rm esc}$ is given by eq. 5.15. Otherwise, the merger remnant is ejected from the parent cluster and cannot be involved in any further hierarchical merger.

We assume that, even if the merger remnant is not ejected, it is kicked out in the outskirts of the cluster. Thus, the BH must sink back to the core via dynamical friction before it can acquire new companions via three-body encounters or exchanges. The timescale for this to happen is given by the dynamical friction timescale (Chandrasekhar 1943):

$$t_{\rm DF} = \frac{3}{4\,(2\,\pi)^{1/2}\,G^2\ln\Lambda}\,\frac{\sigma^3}{m_{\rm ng}\,\rho}, \tag{5.27}$$

where $m_{\rm ng}$ is the mass of the ng BH. After a time $t_{\rm DF}$, the BH has sunk to the core of the cluster and can acquire a companion by exchange with an existing binary, on a timescale (Miller & Lauburg 2009)

$$t_{12} = 3\,{\rm Gyr}\,\left(\frac{0.01}{f_{\rm bin}}\right)\,\left(\frac{10^6\,{\rm pc}^{-3}}{n_{\rm c}}\right)\,\left(\frac{\sigma}{50\,{\rm km\,s}^{-1}}\right) \left(\frac{12\,{\rm M}_\odot}{m_{\rm ng}+2\,m_{\rm BH}}\right)\,\left(\frac{1\,{\rm AU}}{a_{\rm hard}}\right), \tag{5.28}$$

where $f_{\rm bin}$ is the binary fraction, $m_{\rm ng}$ is the mass of the ng BH, $n_{\rm c}$ is the number central density of the cluster and $a_{\rm hard} = G\,m_{\rm BH}/\sigma^2$ is the minimum semi-major axis of a hard binary system in the BH sub-system. The resulting timescale $t_{\rm dyn,ng}$ for the merger remnant to pair up dynamically with a new companion BH is $t_{\rm dyn,ng} = t_{\rm DF} + t_{12}$. The n-generation BBH will thus form at $t_{\rm ng} = t_{\rm merg} + t_{\rm dyn,ng}$, where $t_{\rm merg} = t_{\rm cc} + t_{\rm GW}$ is the delay time of the first generation (1g) BBH. If $t_{\rm ng}$ is shorter than the Hubble time, we start the loop again by drawing the secondary mass for the given primary mass (following the same procedure described in Sect. 5.2.4) and integrating the second generation (2g) BBH with eqs 5.23. We iterate the hierarchical merger chain until the merger remnant is ejected from the cluster, or the cluster evaporates, or we reach the Hubble time.

At each generation, we sample the new secondary mass depending on the chosen mass coupling. When the O16 mass coupling is considered, we sample the secondary mass from eq. 5.16. In this case, we consider two possible approaches. First, we leave the possibility that the second BH ranges from $[m_{\rm min}, m_{\rm 1,ng})$ (case ngng, as done in Mapelli et al. 2021a, 2022). Second, we limit to the case in which the secondary is always a 1g BH (case ng1g), and $m_2 \in [m_{\rm min}, \max(m_{\rm 1,1g}))$. For the H75 mass coupling, we sample m_2 from eq. 5.19, by setting m_1 to the mass of the ng primary (ng1g).

5.2.5 BBH merger rate

We evaluate the BBH merger rate following Mapelli et al. (2022):

$$\mathcal{R}(z) = \frac{\rm d}{{\rm d}t(z)}\int_{z_{\rm max}}^{z}\psi(z')\,\frac{{\rm d}t(z')}{{\rm d}z'}\,{\rm d}z' \int_{Z_{\rm min}(z')}^{Z_{\rm max}(z')}\eta(Z)\,\mathcal{F}(z',z,Z)\,{\rm d}Z, \tag{5.29}$$

where $t(z)$ is the look-back time at redshift z, $\psi(z')$ is the formation rate density at redshift z' for GCs, $Z_{\rm min}(z')$ and $Z_{\rm max}(z')$ are the minimum and maximum metallicity of stars formed at redshift z', $\eta(Z)$ is the merger efficiency at metallicity Z, and $\mathcal{F}(z',z,Z)$ is the fraction of BBHs that form at redshift z' from stars with metallicity Z and merge at

redshift z, normalized to all BBHs that form from stars with metallicity Z. To calculate the look-back time we take the cosmological parameters (H_0, $\Omega_{\rm M}$ and Ω_Λ) from Ade et al. (2016).

Formation rate density

For the formation rate of GCs as a function of redshift, we assume the Gaussian distribution:

$$\psi_{\rm GC}(z) = \mathcal{B}_{\rm GC}\ \exp\left[-\frac{(z-z_{\rm GC})^2}{(2\,\sigma^2_{\rm GC})}\right], \tag{5.30}$$

where, in the fiducial model, $z_{\rm GC} = 3.2$ is the redshift where the formation rate of GCs is maximum, $\sigma_{\rm GC} = 1.5$ is the standard deviation of the distribution and $\mathcal{B}_{\rm GC}$ is the normalization factor. This distribution is reminiscent of the one estimated by El-Badry et al. (2019) (see also Rodriguez & Loeb 2018). In particular, the fiducial normalization we adopt, $\mathcal{B}_{\rm GC} = 2\times10^{-4}\,{\rm M_\odot\,Mpc^{-3}\,yr^{-1}}$, is consistent with both El-Badry et al. (2019) and Reina-Campos et al. (2019b). The peak redshift $z_{\rm GC} = 3.2$ is calibrated on the distribution of the ages of Galactic GCs, which peaks at $z = 3.2$ (Gratton et al. 1997, 2003; VandenBerg et al. 2013). We refer the reader to Mapelli et al. 2022 for more details on the choice of these parameters.

Merger efficiency

The merger efficiency is the total number of BBHs of a given population that merge within a Hubble time divided by the total initial stellar mass of that population (Giacobbo et al. 2018; Klencki et al. 2018). For dynamical BBHs, we estimate the merger efficiency in star clusters as:

$$\eta_{\rm SC}(Z) = \frac{\mathcal{N}_{\rm merg,\,sim}(Z)}{\mathcal{N}_{\rm sim}(Z)}\,\frac{\mathcal{N}_{\rm BH}(Z)}{M_*(Z)}, \tag{5.31}$$

where $\mathcal{N}_{\rm merg,\,sim}(Z)$ is the number of BHs simulated with FASTCLUSTER that merge within a Hubble time for a given metallicity Z, $\mathcal{N}_{\rm sim}(Z)$ is the number of BHs simulated with FASTCLUSTER for a given metallicity Z, $\mathcal{N}_{\rm BH}$ is the total number of BHs associated with a given metallicity (including the BHs we did not simulate with FASTCLUSTER) and $M_*(Z)$ is the total initial stellar mass for a given metallicity Z. $\mathcal{N}_{\rm merg,\,sim}(Z)$ and $\mathcal{N}_{\rm sim}(Z)$ are directly extracted from the simulations. We calculate $M_*(Z) = \sum M_{\rm TOT}(Z)$, i.e. the sum of the initial total mass of all simulated star clusters with a given Z. We derive $\mathcal{N}_{\rm BH}(Z)$ as the number of BHs we expect from a stellar population following a Kroupa mass function between 0.1 and 150 $\rm M_\odot$, assuming that all stars with zero-age main sequence mass ≥ 20 $\rm M_\odot$ are BH progenitors (Heger et al. 2003). In our definition, $\mathcal{N}_{\rm merg,\,sim}(Z)$ includes even Ng mergers, while $\mathcal{N}_{\rm sim}(Z)$ counts only 1g BHs. Hence, the ratio $\mathcal{N}_{\rm merg,\,sim}(Z)/\mathcal{N}_{\rm sim}(Z)$ can be > 1 if hierarchical mergers are extremely efficient.

Metallicity evolution

Following Bouffanais et al. (2021a), we describe the metallicity evolution through the fit given by Madau & Fragos (2017):

$$\log\langle Z/{\rm Z_\odot}\rangle = 0.153 - 0.074\,z^{1.34} \tag{5.32}$$

To describe the spread around the mass-weighted metallicity, we assume that metallicities are distributed according to a log-normal distribution:

$$p(z', Z) = \frac{1}{\sqrt{2\pi\,\sigma_{\rm Z}^2}}\,\exp\left\{-\frac{\left[\log\left(Z(z')/{\rm Z}_\odot\right) - \left\langle \log Z(z')/Z_\odot\right\rangle\right]^2}{2\,\sigma_{\rm Z}^2}\right\}, \tag{5.33}$$

where

$$\left\langle \log Z(z')/Z_\odot\right\rangle = \log\left\langle Z(z')/Z_\odot\right\rangle - \frac{\ln(10)\,\sigma_{\rm Z}^2}{2}. \tag{5.34}$$

The standard deviation σ_Z is set to 0.3 (Mapelli et al. 2022). Equation 5.33 allows us to estimate the term $\mathcal{F}(z', z, Z)$ of eq. 5.29:

$$\mathcal{F}(z', z, Z) = \frac{\mathcal{N}(z', z, Z)}{\mathcal{N}_{\rm TOT}(Z)}\,p(z', Z), \tag{5.35}$$

where $\mathcal{N}(z', z, Z)$ is the total number of BBHs that form in GCs at redshift z' with metallicity Z and merge at redshift z, while $\mathcal{N}_{\rm TOT}(Z)$ is the total number of BBH mergers with progenitor's metallicity Z.

5.2.6 Description of the runs

We ran different sets of $N = 5\times10^6$ 1g BBHs. In order to test the impact of the star cluster evolution on the population of hierarchical mergers, we consider three cases: absence of star cluster evolution (NoEv), star cluster evolution in isolation (Evol), and in presence of a tidal field (Tidal). In the latter case, the galacto-centric distance is set to 8 kpc. To highlight the impact of star cluster evolution, for each evolutionary case we set the initial seed of our random generations, such that the same BBHs evolve in the same GCs.

5.3 Results

In the following, we will explore how star cluster evolution affects the population of hierarchical mergers. Also, we will quantify how the BBH mass ratio affects the process of hierarchical assembly, by comparing different coupling criteria.

For our comparison, we will focus on selected metallicities and spin distributions, which best match GC observations and GW detections. As shown by Muratov & Gnedin (2010) (see their Fig. 23), GCs display a bimodal metallicity distribution ([Fe/H] $= -1.6, 0.6$, which coincide with $Z = 0.0003$ and $Z = 0.003$), with an overabundance of metal-poor clusters. In the following, we will show the models with metallicity $Z = 0.0002$, which roughly coincides with the main peak of the distribution. As for the spin distribution, we will show the results for the models with $\sigma_\chi = 0.05$, which is reminiscent of the spin distribution inferred from GWTC-3 (Abbott et al. 2021e). Table 5.1 summarizes the details of the models under consideration.

5.3.1 Impact of star cluster evolution

Figure 5.3 shows the populations of BBH mergers at different generations, for different mass couplings and for different evolutionary cases. Independently of the mass coupling considered, the main effect due to star cluster evolution is to quench the BH hierarchical

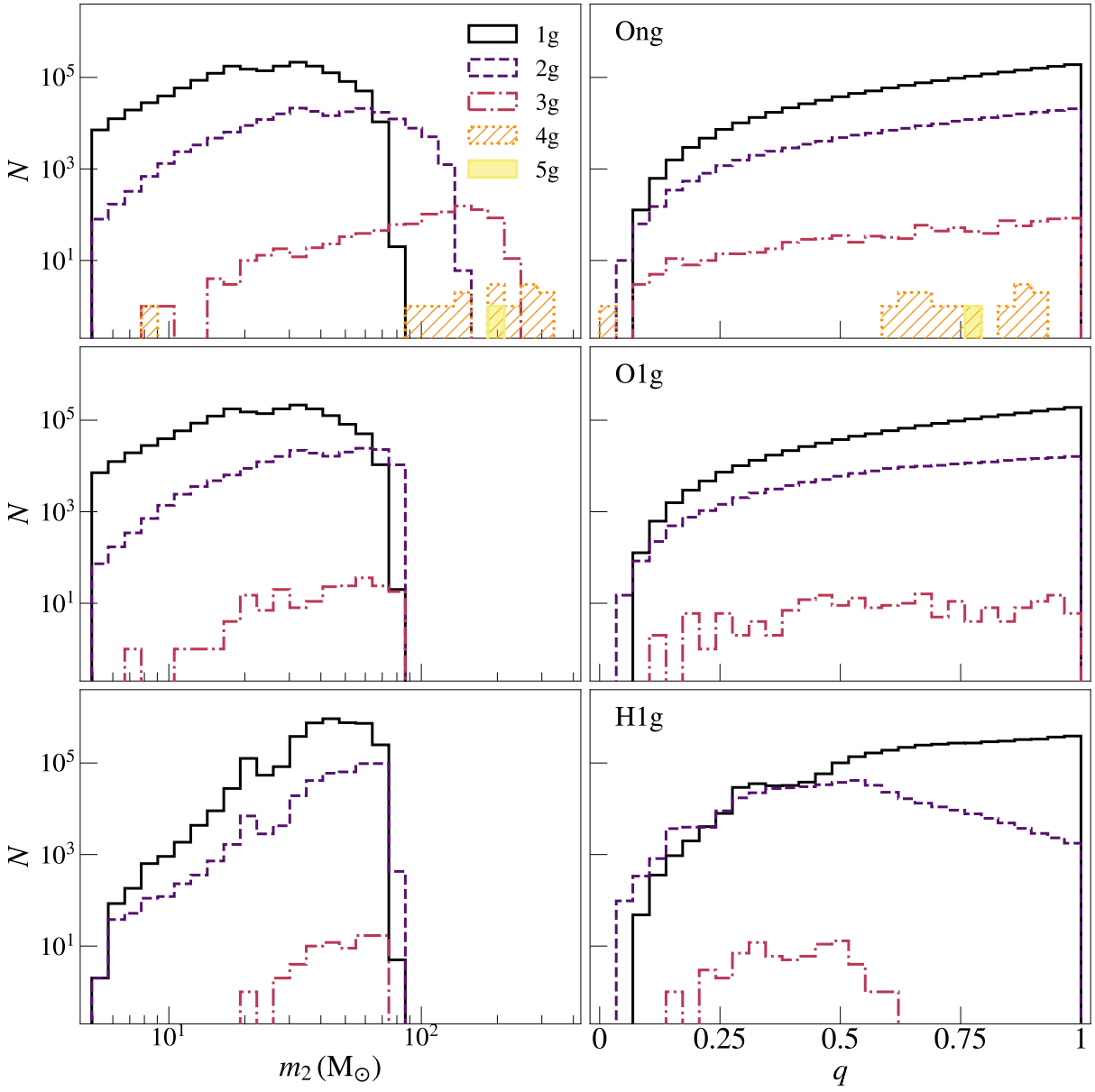

Figure 5.4: Distributions of m_2 (left) and mass ratios q (right), for the models Ong (upper panels), O1g (middle panels), H1g (lower panels). Different colours show BBH mergers at different generations.

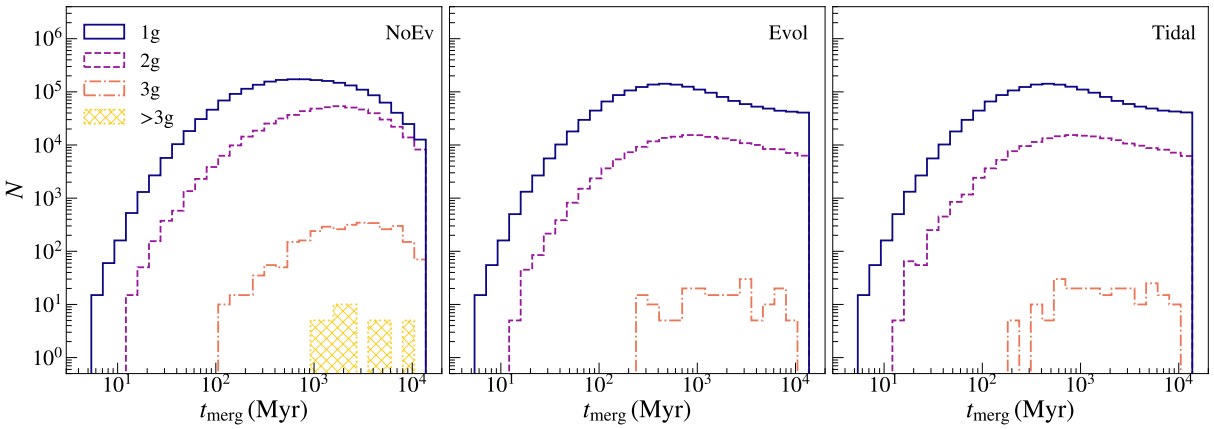

Figure 5.5: Distribution of merger times for the model O1g, for different evolutionary cases: NoEv (left), Evol (center), and Tidal (right). Different colours show BBH mergers at different generations.

chain after the third generation. Only models where ngng BBH mergers are allowed can produce 4g mergers, with an efficiency $N_{4g}/N_{1g} \sim 10^{-5}$. In contrast, when star cluster evolution is not taken into account, the hierarchical process can continue up to the 5th generation, with a 5g efficiency: $N_{5g}/N_{1g} \sim 10^{-5}$.

In our models, the hierarchical process is not affected by the tidal stripping from the host Galaxy. The populations of BBH mergers in clusters that evolve in isolation and in presence of a tidal field show almost identical behaviours, with slight differences due to stochastic fluctuations (e.g., in the kick generation) of the simulations. This suggests that the additional mass loss due to the tidal stripping (at the considered distance) plays a negligible role. The quenching of the hierarchical process is thus mainly due to core expansion as a consequence of two-body relaxation, which produces lower central densities and, in turn, a less efficient hardening rate.

The BBH mass coupling criterion deeply affects the population of BBH mergers since the first generation. In particular, the H1g case produces mass distributions that are skewed towards larger masses, as a consequence of the tendency of dynamical interactions (eq. 5.18) to couple the most massive BHs. In contrast, the O16 coupling criterion results in a more uniform distribution of BBH merger masses. When only ng1g BBH mergers are taken into account, the hierarchical chain stops at the third generation when an accurate star cluster evolution is considered, independently of the coupling criterion considered.

5.3.2 Mass ratios

Figure 5.4 compares the distribution of secondary masses and the resulting mass ratios for different mass couplings. The distributions of m_2 strongly depend on the sampling considered. In the H75 case, the distribution of secondary masses is skewed towards larger masses with respect to the O16 coupling criterion. At the first generation, all the mass ratio distributions show similar distributions, with an increasing trend towards larger values. Also, the fraction of 2g BBH mergers with respect to 1g mergers is similar for all the different couplings, $N_{2g}/N_{1g} \sim 10^{-1}$.

At the higher generation, distinct mass coupling criteria lead to very different mass

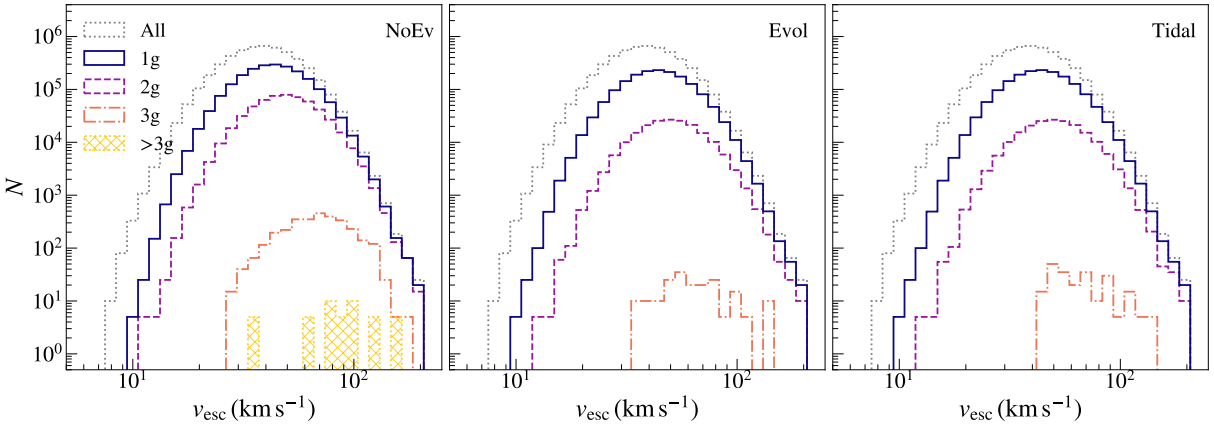

Figure 5.6: Distribution of escape velocities v_{esc} for the model O1g, for different evolutionary cases: NoEv (left), Evol (center), Tidal (right). Different colors show BBH mergers at different generations. The grey dashed line displays the distribution of v_{esc} for all the GCs considered.

ratio distributions. For the H75 case, the sampling criterion again favours the coupling between the most massive stars, and new secondary mass is likely to be $m_2 \sim \max(m_{1,1g})$. Since $m_{1,2g} \sim 2\max(m_{1,1g})$, the second generation mass ratio distribution peaks at ~ 0.5. Still, at the third generation, the distribution of mass ratios ranges between 0.2 and 0.6. The O16 sampling, in contrast, show similar mass ratio distributions at all generations, since m_2 is determined from eq. 5.16. In the ng1g case, the distribution shows a flatter trend at the third generation, because mass ratios close to 1 can no longer be produced as, in general, $m_{1,3g} \gtrsim \max(m_{1,1g})$.

5.3.3 Relevant time and velocity scales

Figure 5.5 shows how star cluster evolution affects the distribution of merger times. At the first generation, all the distributions display a peak at $t_{merg} \sim 500$ Myr. For BBHs that can merger in shorter timescales, the star cluster evolution plays a negligible role. At longer timescales, the lower hardening rate within the core quenches the production of BBH mergers by 20% already at the first generation.

One of the aspects that mainly affect the process of hierarchical mergers is the complex interplay between the relativistic recoil kick at the BBH merger (see Sect. 5.2.4) and the cluster escape velocity, which determines if the host cluster can retain the merger remnant. Figure 5.6 displays the distribution of the initial v_{esc} for globular clusters that host mergers, at different generations. BBH mergers tend to be favoured by larger escape velocities, which result from very dense and/or very massive star clusters (e.g., see eq. 5.15). Also, only star cluster with $v_{esc} \gtrsim 30\,\mathrm{km\,s^{-1}}$ can produce 3g BBH mergers.

5.3.4 Inferred BBH populations at $z = 0$

Figure 5.7 shows the primary BH mass distribution at redshift $z = 0$ obtained from dynamical BBH mergers in GCs according to their merger rate, calculated as described in Sect. 5.2.5. As a qualitative comparison, we show the posterior distribution inferred from

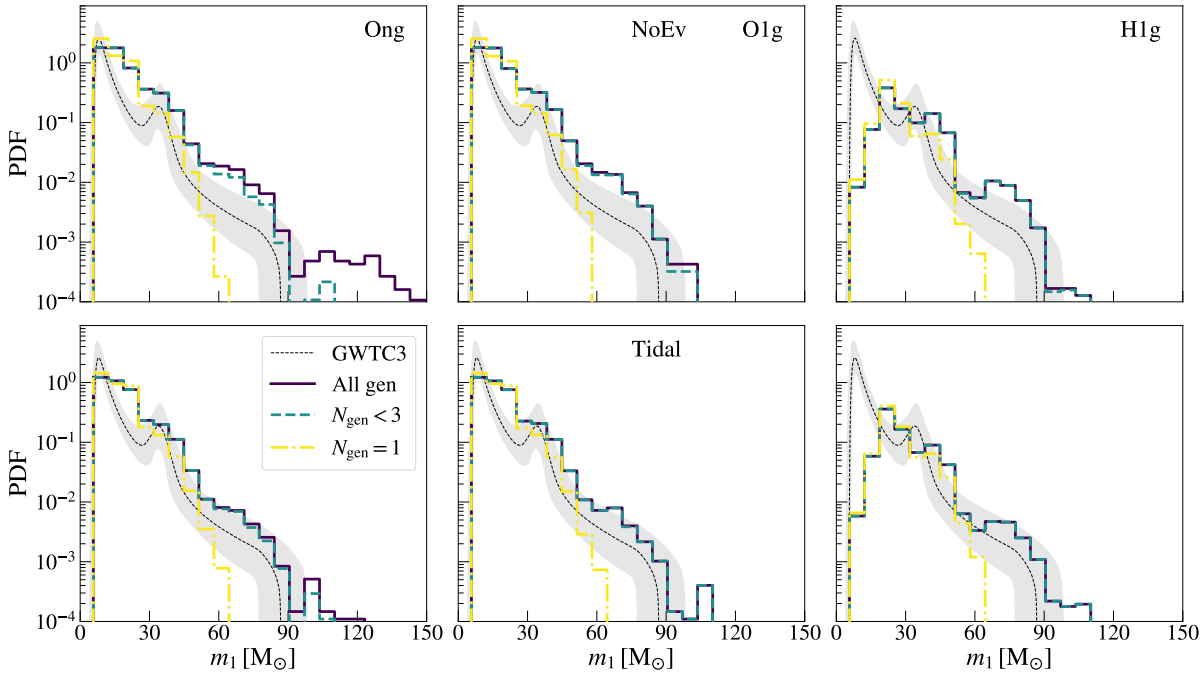

Figure 5.7: Probability distribution functions of primary BH masses of BBHs mergers at redshift $z = 0$, for the models Ong (left), O1g (center), and H1g (right). Upper panels: populations inferred from models without stellar evolution (NoEv). Lower panels: populations inferred from models with stellar evolution in presence of Galactic tidal field (Tidal). The purple solid line is the contribution of mergers of all generations, the green dashed line is the contribution of mergers up to the 2g, and the yellow dot-dashed line is the contribution from only 1g BBH mergers. The dashed black curve shows the posterior population distribution inferred from GWTC-3 events (Abbott et al. 2021e), with the shaded region showing the 90% credible interval. We arbitrarily re-scaled the inferred PDF distributions.

GWTC-3 events (Abbott et al. 2021e). In particular, we estimated the populations of BBH mergers at $z = 0$ in our synthetic Universe, without considering observation biases. The main effect of hierarchical mergers is to extend the distribution of primary masses at values larger than $60\,M_\odot$. Star cluster evolution quenches the inferred distributions in the high mass regime. This is a consequence of the less efficient production of hierarchical mergers due to the GC dissolution, as explained in Sect. 5.3.1.

The BH sampling criterion plays a relevant role in shaping the inferred distribution. In general, all the sampling considered can reproduce the slope of the distribution from GWTC-3 at high masses, where hierarchical mergers take over. The Ong and O1g cases can reproduce the first peak at $\approx 10\,M_\odot$, and then display a monotonically decreasing trend. Also, they match the distribution at the second peak ($\approx 35\,M_\odot$).

The H1g case displays a more sub-structured distribution, with different peaks. This coupling criterion cannot reproduce the first peak of the posterior distribution from GW detections, because it favours the coupling of the most massive BHs. As a consequence, mergers from low-mass BHs are disfavored. In contrast, the H1g case displays a main peak due to 1g BBH mergers, which extends from $\approx 25\,M_\odot$ to $\approx 50\,,M_\odot$ and roughly

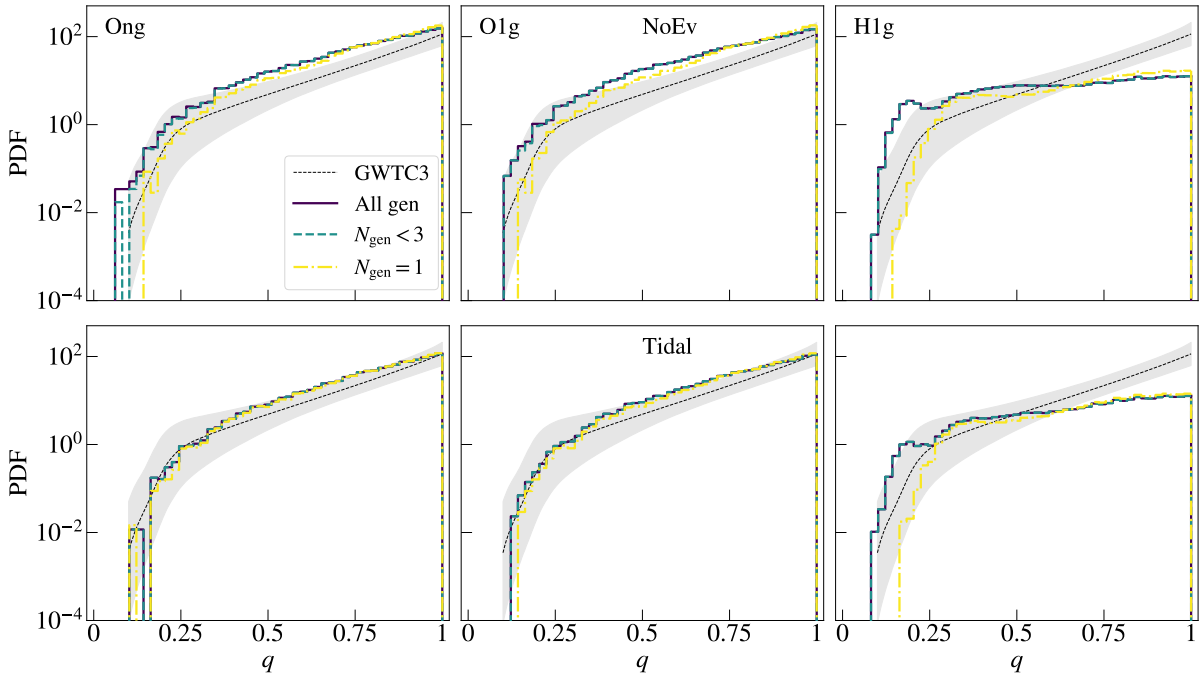

Figure 5.8: Same as Fig. 5.7, but for the probability distribution function of mass ratios of BBHs mergers at redshift $z = 0$.

encloses the one inferred from GW detections. A secondary peak due to 2g BBH mergers is present at $\approx 70 - 80\,M_\odot$. These results are consistent with those from Antonini et al. (2022), who considered the same mass sampling criterion, but different (power-law) initial BH mass functions.

Figure 5.8 shows the inferred distributions for mass ratios from dynamical BBH mergers in GCs, at $z = 0$. The models based on the O16 sampling perform well in matching the trend inferred from GWTC-3 at all values. In the Ong case, the distributions of mass ratios at all generations are the same, because secondary masses are always sampled from eq. 5.16 without any restriction. When only ng1g mergers are considered, successive-generation mergers result in higher rates at low q, because higher values are quenched by the growing mass of the primary BH. At high values, the H1g model shows a flatter trend, and for $q \gtrsim 0.8$ we find a discrepancy of about one order of magnitude with the detected trend, consistently with Antonini et al. (2022).

5.4 Summary

We have studied the process of hierarchical mergers in globular clusters, by considering dynamically-formed BHs. To do this, we have implemented un upgraded version of our semi-analytic code FASTCLUSTER, which includes all the relevant processes that drive the cluster evolution, that is stellar evolution, two-body relaxation and tidal stripping by the host galaxy.

The net effect of star cluster evolution is to reduce the cluster central density and escape velocity, thus quenching the hardening rate of BBHs and the retention of BBH merger remnants from recoil kicks. Our results suggest that star cluster evolution limits

the maximum generation of BBH mergers to the third generation (3g). If the secondary component of the BBH is a first-generation (1g) BH, the maximum mass yielded by hierarchical mergers is at most $\sim 200\,\mathrm{M}_\odot$ for $Z = 0.0002$.

Also, we quantified how the BH spins and the orbital angular momentum build up to increase the spin at successive generations. The peak of the BH spin distribution is $\chi_1 = 0.7$ for 2g BHs, and $\chi_1 = 0.8$ for 3g BHs, with a spread that depends on the 1g BH spin distribution. This, in turn, has an impact on the distribution of the precessing spin, which distribution displays an increasing trend that peaks at $\chi_\mathrm{p} = 0.7$, independently on the intitial spin distribution.

Acknowledgements

MM and ST acknowledge financial support from the European Research Council for the ERC Consolidator grant DEMOBLACK, under contract no. 770017.

Chapter 6

Stellar-mass black holes in the Hyades star cluster?

Based on the draft of the manuscript:
Torniamenti S., Gieles M., Penoyre Z., Jerabkova T., Wang L., Anders F.,
"Stellar-mass black holes in the Hyades star cluster?", to be submitted to MNRAS.

Abstract

Understanding the natal kicks of stellar-mass black holes (BHs) is essential to make reliable predictions for gravitational wave detections. Most models that try to reproduce the binary-black hole merger rate require a significant fraction of BHs to receive low or negligible kicks: in this case BHs should be retained even in star clusters with low escape velocities ($\lesssim 1$ km/s), such as open clusters. In this study, we search for signatures of stellar-mass BHs in the nearest open cluster to the Sun: the Hyades. We compare the mass density profiles of a suite of direct N-body models to data from the *Gaia* space mission. The observations are best reproduced by N-body models with $2-3$ BHs at present times. Models that never possessed BHs have an half-mass radius that is $\sim 30\%$ smaller than the observed value, while those where the last BHs were ejected recently ($\lesssim 150$ Myr ago) can still reproduce the density profile. In these model, the ejected (binary) BHs are at a typical distance of ~ 60 (80) pc from the Hyades (Sun). In 50% of the models hosting BHs, some BHs have a stellar companion. Their period distribution peaks at $\sim 10^3$ yr making them unlikely to be found through velocity variations. We look for potential BH companions through large *Gaia* astrometric and spectroscopic errors, identifying 56 binary candidates and their inferred periods and mass ratios - none of which are consistent with a massive compact object companion. We conclude that the present-day structure of the Hyades requires a significant fraction of BHs to form with low-enough kicks ($v_{\rm esc} \lesssim 3\,{\rm km\,s^{-1}}$ at 20 Myr) to be retained by the host cluster.

keywords: black hole physics – binaries: general – star clusters: individual: Hyades cluster – stars: kinematics and dynamics - methods: numerical

6.1 Introduction

The discovery of binary black holes (BBH) mergers with gravitational wave (GW) detectors (Abbott et al. 2021d) has led to an active discussion on the origin of these systems

(e.g. Belczynski et al. 2016a; Mandel & de Mink 2016; Rodriguez et al. 2016a; Samsing et al. 2022). A popular scenario is that BBHs form dynamically in the centers of globular clusters (GCs, e.g. Portegies Zwart et al. 2001; Antonini & Gieles 2020a) and open clusters (OCs, e.g. Rastello et al. 2019; Di Carlo et al. 2019; Kumamoto et al. 2020; Banerjee 2021a; Torniamenti et al. 2022b). This scenario has gained support from the discovery of accreting BH candidates in an extragalactic GC (Maccarone et al. 2007) and several Milky Way GCs (Strader et al. 2012; Chomiuk et al. 2013; Miller-Jones et al. 2015) as well as the discovery of three detached binaries with BH candidates in the Milky Way GC NGC3201 (Giesers et al. 2018; Kamann et al. 2020) and one in the 100 Myr star cluster NGC1850 in the Large Magellanic Cloud (Saracino et al. 2022, but see El-Badry & Burdge 2022).

Various studies have also pointed out that populations of stellar-mass BHs may be present in GCs, based on their large core radii (Mackey et al. 2007, 2008); the absence of mass segregation of stars in some GCs (Peuten et al. 2016; Alessandrini et al. 2016; Weatherford et al. 2020); the central mass-to-light ratio (for the cases of Omega Centauri and 47 Tucanae see Zocchi et al. 2019; Baumgardt et al. 2019; Hénault-Brunet et al. 2019); the core over half-light radius (Askar et al. 2018; Kremer et al. 2020) and the presence of tidal tails (see Gieles et al. 2021, for the case of Palomar 5).

Recently, Gieles et al. (2021) presented direct N-body models of the halo GC Palomar 5. This cluster is unusually large ($\sim 20\,\mathrm{pc}$) and is best-known for its extended tidal tails. Both these features can be reproduced by an N-body model that has at present $\sim 20\%$ of the total mass in stellar-mass BHs. They show that the half-light radius, $R_{\rm eff}$, is a strong increasing function of the mass fraction in BHs ($f_{\rm BH}$). Because all models were evolved on the same orbit, this implies that the ratio of $R_{\rm eff}$ over the Jacobi radius is the physical parameter that is sensitive to $f_{\rm BH}$.

At the present day, all of the searches for BH populations in star clusters focused on old ($\gtrsim 10\,\mathrm{Gyr}$) and relatively massive ($\gtrsim 10^4\,\mathrm{M}_\odot$) GCs in the halo of the Milky Way and there is thus-far no work done on searches for BHs in young OCs in the disc of the Milky Way. The reason is that most methods that have been applied to GCs are challenging to apply to OCs: for mass-to-light ratio variations, precise kinematics are required, which is hampered by orbital motions of binaries (Geller et al. 2015) and potential escapers (e.g. Fukushige & Heggie 2000; Claydon et al. 2017) at the low velocity dispersions of OCs (few $100\,\mathrm{m/s}$).

In the last few years, the advent of the ESA *Gaia* survey (Gaia Collaboration et al. 2016, see Gaia Collaboration et al. 2022 for the latest release) has allowed us, for the first time, to study in detail the position and velocity space of OCs (e.g., see Cantat-Gaudin 2022 for a recent review), and to identify their members with confidence. Several hundreds of new objects have been discovered (e.g. Cantat-Gaudin et al. 2018b,a; Castro-Ginard et al. 2018, 2020, 2022; Sim et al. 2019; Liu & Pang 2019; Hunt & Reffert 2021), and could be distinguished from non-physical over-densities that were erroneously listed as OCs in the previous catalogues (Cantat-Gaudin & Anders 2020).

The possibility to reveal the full spatial extension of OCs members has made it feasible to describe in detail their radial distributions, up to their outermost regions (Tarricq et al. 2022), and to study them as dynamical objects interacting with their Galactic environment. In particular, OCs display extended halos of stars, much more extended than their cores, which are likely to host a large number of cluster members (Nilakshi et al. 2002; Meingast et al. 2021). Also, evidence of structures that trace their ongoing

disruption, like tidal tails, has been found for many nearby OCs, like the Hyades (Reino et al. 2018; Röser et al. 2019; Lodieu et al. 2019; Meingast & Alves 2019; Jerabkova et al. 2021), Blanco 1 (Zhang et al. 2020), Praesepe (Röser & Schilbach 2019), and even more distant ones like UBC 274 (Piatti 2020; Casamiquela et al. 2022). This wealth of data provides, for the first time, the required information to characterize the structure of OCs in detail and, possibly, to look for the imprints given by the presence of dark components, in the same way as done for GCs.

In this exploratory study, we aim to find constraints on the presence of BHs in the Hyades cluster, the nearest - and one of the most widely studied - open clusters. We use the same approach as in the Pal 5 study of Gieles et al. (2021), hence a good understanding of the behaviour of $R_{\rm eff}$ at the orbit of the Hyades is required, i.e. the model clusters need to be evolved in a realistic Galactic potential. We explore the large suite of $N-$body models by Wang & Jerabkova (2021), conceived to model the impact of massive stars (i.e. the BH progenitors) on the present-day structure of Hyades-like clusters. By comparing these models to the radial profiles of Hyades members with different masses from *Gaia* (Evans & Oh 2022), we aim to constrain if a dark component is required.

The paper is organised as follows. In Section 6.2, we describe the details of the $N-$body models and our method to compare them to observations. In Section 6.3, we report the results for the presence of BHs in the Hyades. In Sect. 6.4 we report a discussion on BH-star candidates in the cluster. Finally, Sect. 6.5 summarises our conclusions.

6.2 Methods

6.2.1 The Hyades cluster

The Hyades is the nearest open cluster to us, at a distance $d \approx 45$ pc (Perryman et al. 1998). By relying on 6D phase-space constraints, Röser et al. (2011) identified 724 stellar members moving with the bulk Hyades space velocity, with a total of mass $435\,{\rm M}_\odot$ (Röser et al. 2011). The tidal radius is estimated to be $r_{\rm t} \approx 10\,{\rm pc}$, and the resulting bound mass is $\approx 275\,{\rm M}_\odot$ (Röser et al. 2011). Also, the cluster displays prominent tidal tails, which extend over a distance of 800 pc (Jerabkova et al. 2021).

The Hyades cluster contains stars with masses approximately between 0.1 $\rm M_\odot$ and 2.6 $\rm M_\odot$. Röser et al. (2011) found that average star mass of the cluster is observed to decrease from the center to the outward regions, as a consequence of mass segregation. Recently, Evans & Oh (2022) performed a detailed study of the Hyades membership and kinematics, with the aim to quantify the degree of mass segregation within the cluster. In particular, they applied a two-component mixture model to the *Gaia* DR2 data (Gaia Collaboration et al. 2018b) and identified the cluster and tail members with masses $m > 0.12\,{\rm M}_\odot$ (brighter than $M_{\rm G} < 14.06$). They assigned a mass value to each observed source by means of a nearest-neighbour interpolation on the *Gaia* colour-magnitude space (BP $-$ RP vs. $M_{\rm G}$). Finally, they defined two components, named "high-mass" and "low-mass" stars, based on a color threshold at BP $-$ RP $= 2$, corresponding to 0.56 $\rm M_\odot$. The component median masses are 0.95 $\rm M_\odot$ and 0.32 $\rm M_\odot$, respectively. These values were taken as nominal masses for the two components.

As a consequence of mass segregation within the cluster, Evans & Oh (2022) showed that this two-component formalism is needed to adequately describe the radial cumulative mass profiles over the entire radius range and within the tidal radius. In particular, the

	Best-fit Plummer model		Stars within 10 pc	
	Low-mass	High-mass	Low-mass	High-mass
M ($M_\odot$)	117.3	207.5	71.9	170.5
$r_{\rm hm}$ (pc)	8.10	4.88	5.67	4.16

Table 6.1: Left: Total mass (M) and half-mass radius ($r_{\rm hm}$) for the two components of the best-fit Plummer model, from Evans & Oh (2022). Right: the resulting parameters for the distribution of stars within 10 pc, given by the best-fit Plummer model, truncated at $r_{\rm t} = 10$ pc.

mass distributions of the stellar components within the tidal radius are well described by a superposition of two Plummer (1911) models. Table 6.1 reports the relevant parameters of the best-fit Plummer model (Evans & Oh 2022). The estimated total mass and half-mass radius of stars within 10 pc are $r_{\rm hm,l} = 5.7$ pc and $M_{\rm l} = 71.9\,{\rm M}_\odot$ for the low-mass stars and $r_{\rm hm,h} = 4.16$ pc and $M_{\rm h} = 170.5\,{\rm M}_\odot$ for the high-mass component displays.

In this work, we will use the density profiles given by the best-fit Plummer models reported in Tab. 6.1 as observational points to compare to our $N-$body models. For this reason, hereafter we will refer to this best-fit profiles as to "observed profiles".

6.2.2 N-body models

We use the sample of $N-$body simulations introduced in Wang & Jerabkova (2021), which aim to describe the present states of the Hyades cluster.

The simulations are generated by using the N-body code PETAR (Wang et al. 2020b,a). The code can provide accurate dynamical evolution of close encounters and binaries. The single and binary stellar evolution are included by using the population synthesis codes, SSE and BSE (Hurley et al. 2000, 2002; Banerjee 2021b). The "rapid" supernova model for the remnant formation and material fallback from Fryer et al. (2012), along with the pulsation pair-instability supernova (Belczynski et al. 2016a) are used. In this prescription, if no material falls back onto the compact remnant after the launch of the supernova explosion, natal kicks are drawn from the distribution inferred from observed velocities of radio pulsars, that is a single Maxwellian with $\sigma = 265\,{\rm km\,s^{-1}}$ (Hobbs et al. 2005). For compact objects formed with fallback, kicks are lowered proportionally to the amount of stellar envelope that falls back ($f_{\rm b}$). In this case $v_{\rm kick,fb} = (1 - f_{\rm b})v_{\rm kick}$, where $v_{\rm kick}$ is the kick velocity without fallback. For the most massive BHs, which are formed via direct collapse ($f_{\rm b} = 1$) of a massive star, no natal kicks are imparted. In this formalism, the kick is a function of the fallback fraction, and not of the mass of the compact remnant.

A metallicity of $Z = 0.02$ was used. The tidal force from the Galactic potential is calculated by the GALPY code (Bovy 2015) with the MWPOTENTIAL2014, which includes a bulge, a disk and a halo.

Initial conditions

The sample of $N-$body models consists of 4500 star clusters, initialized with a grid of different total masses M_0 and half-mass radii $r_{\rm hm,0}$. The initial values for M_0 are set to 800, 1000, 1200, 1400, or 1600 $M_\odot$, while $r_{\rm hm,0}$ takes values 0.5, 1, or 2 pc. The initial positions and velocities are sampled from a Plummer (1911) sphere.

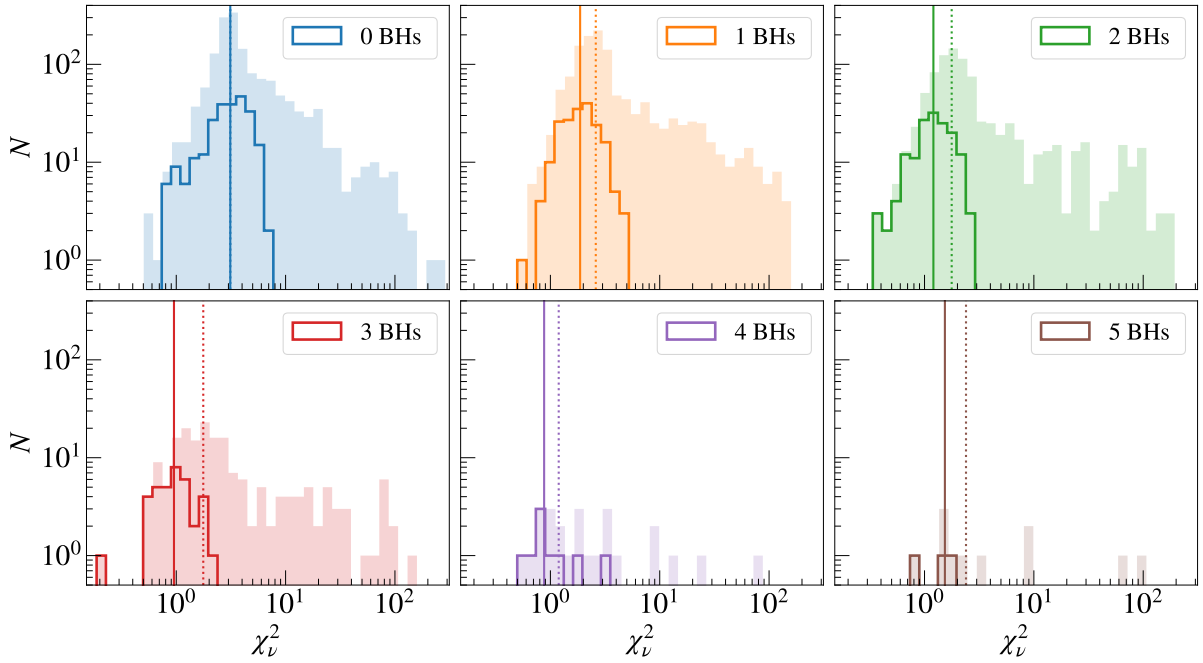

Figure 6.1: Distributions of χ^2_ν from the fits to the density profile for star clusters with different numbers of BHs. The filled area include the entire distributions of star clusters, while the solid line displays the star clusters with $150\,\mathrm{M}_\odot \leq M_\mathrm{h} \leq 190\,\mathrm{M}_\odot$. The vertical lines show the median value of the distributions when all the clusters are considered (dotted line) and when the mass cut is applied (solid line).

The cluster initial mass function (IMF) is sampled from a Kroupa (2001) IMF between $0.08 - 150\,\mathrm{M}_\odot$. For each couple $[M_0, r_{\mathrm{h},0}]$, Wang & Jerabkova (2021) generate 300 models by randomly sampling the stellar masses with different random seeds. On the one hand, this allows to quantify the impact of stochasticity as the result of IMF sampling, which, especially for such clusters with a limited number of particles play a fundamental role (e.g. see Goodman et al. 1993; Boekholt & Portegies Zwart 2015; Wang & Hernandez 2021). On the other hand, different random samplings result in different fractions of O-type stars with $m > 20\,\mathrm{M}_\odot$ (the BH progenitors), which deeply affect the cluster global evolution (see Wang & Jerabkova 2021). In the sample considered, the mass fraction of O-type stars f_O ranges from to 0 to 0.34 (the expected fraction for the chosen IMF is 0.13). The stochasticity of the random sampling of stellar masses may produce $f_\mathrm{O} = 0$, that is the cluster does not contain stars massive enough to form BHs at all. The percentage of clusters with $f_\mathrm{O} = 0$ depends on the initial cluster mass, and varies from 6% for clusters with $M_0 = 800\,\mathrm{M}_\odot$ to 0.7% for clusters with $M_0 = 1600\,\mathrm{M}_\odot$. In total, 2.4% of the clusters do not host stars with $m > 20\,\mathrm{M}_\odot$. No primordial binaries are included in the simulations.

All the clusters are evolved for 648 Myr, the estimated age of the Hyades (Wang & Jerabkova 2021). The initial position and velocity of the cluster are set to match the present-day coordinates in the Galaxy (see Gaia Collaboration et al. 2018a; Jerabkova et al. 2021). For this purpose, the center of the cluster is first integrated backwards for 648 Myr in the MWPotential2014 potential by means of the time-symmetric integrator in Galpy. The final coordinates are then set as initial values for the cluster position and velocity (Wang & Jerabkova 2021).

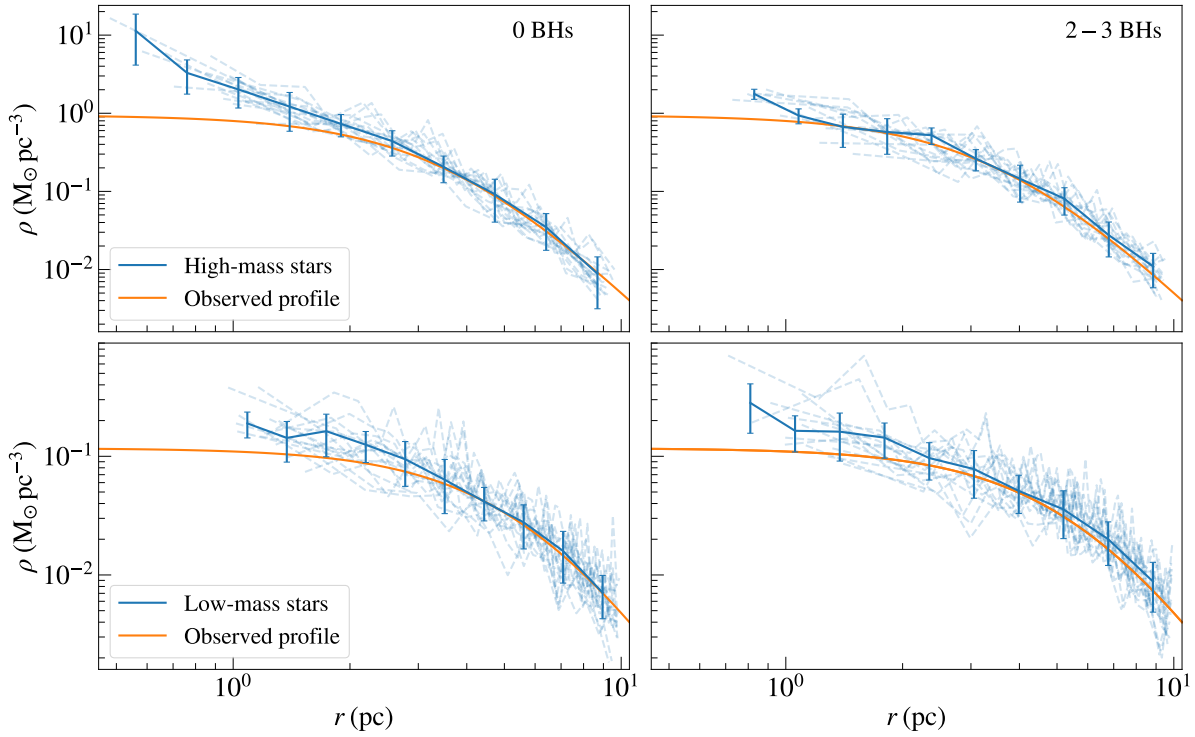

Figure 6.2: Density profiles for high-mass stars (upper panels) and low-mass stars (lower panels), for 16 models drawn from the cases with $N_{\rm BH} = 0$ (left) and $N_{\rm BH} = 2$ or 3 (right). The blue dashed lines are the individual models. The blue solid line is the median of the distribution at selected radial distances, with the associated errors (the Plummer uncertainties are comparable to those of the N-body models). The orange line represents the observed profile (Evans & Oh 2022).

6.2.3 Comparing models to observations

We build the model density profiles from the final snapshots of the $N-$body simulations. First, we center the cluster to the density center, calculated as the square of density weighted average of the positions (Casertano & Hut 1985; Aarseth 2003b). Then, we build the profiles for low-mass and high-mass stars within $r_{\rm t}$, separately. To be consistent with the observed profiles (see Sect. 6.2.1), we define all the stars below $0.56\,{\rm M}_{\odot}$ as low-mass stars, and all the stars above this threshold as high-mass stars. Also, because we want to compare to observable radial distributions, we only include the visible components of the cluster (main sequence and giant stars), without taking into account stellar remnants such as BHs. We divide the stellar cluster into radial shells containing the same number of stars. Due to the relatively low number of stars, we consider $N_{\rm bin} = 10$ stars per shell.

To assess how well the models reproduce the observed profiles, we refer to a chi-squared comparison, where we define the reduced chi-squared (with an expected value near 1) as:

$$\chi^2_\nu = \frac{1}{\nu} \sum_i \frac{(\rho_{{\rm obs},i} - \rho_{{\rm mod},i})^2}{\delta\rho_i^2}, \tag{6.1}$$

where ν is the number of degrees of freedom, which depends on the number of density points obtained with the binning procedure. The quantities $\rho_{\rm obs,i}$ and $\rho_{\rm mod,i}$ are the density in the $i^{\rm th}$ bin, for the observed and model profile respectively. The error $\delta\rho_i^2$ is given by

the sum of the model and the observed bin uncertainties. For the both observed and $N-$body profile, we determine the bin uncertainty as the Poisson error:

$$\delta\rho = \frac{\bar{m}}{4/3\,\pi\,\left(r_f^3 - r_i^3\right)}\sqrt{N_{\rm bin}}, \tag{6.2}$$

where $\bar{m}$ is the mean mass of the bin stars, and r_i^3 and r_f^3 are the bin upper and lower limit. For the $N-$body models, the bin lower (upper) limit is set as the position of the innermost (outermost) star, and $\bar{m}$ is the mean stellar mass in each bin. For the observed profiles, we consider the same bin boundaries as the $N-$body models, and set $\bar{m}$ as the mass of the component under consideration. Then, we estimate analytically from the Plummer (1911) distribution the number of stars between r_i and r_f.

Our comparison is performed by considering the high-mass density profile only. This choice relies on the fact that the observed mass function in figure 2 of Evans & Oh (2022) displays a depletion at low masses, which may hint at possible sample incompleteness below 0.2 $\mathrm{M}_\odot$. We thus focus only on the high-mass range to obtain a more reliable result. Also, high-mass stars, being more segregated, represent better tracers of the innermost regions of the cluster, where BHs are expected to reside, and thus provide more information about the presence of a possible dark component. We emphasize that this is intended as a formal analysis with the objective of determining whether a model is able to give a reasonable description of the observed cluster profile.

In order to filter out the simulations that present little agreement with the observations, we consider only the models with a final high-mass bound mass within $\pm 20\,\mathrm{M}_\odot$ from the observed value $M_{\rm h} = 170.5\,\mathrm{M}_\odot$ (see Tab. 6.1). Among the simulated models, 636 clusters (14%) lie within this mass range.

6.3 Results

As the cluster tends towards a state of energy equipartition, the most massive objects progressively segregate toward its innermost regions, while dynamical encounters push low-mass stars further and further away (Spitzer 1987). BHs, being more massive than most of the other stars, tend to concentrate at the cluster center, quenching the segregation of massive stars. As a consequence, their presence in a given star cluster is expected to affect the radial mass distribution of the cluster' stellar population (Fleck et al. 2006; Hurley 2007; Peuten et al. 2016).

In the star cluster sample under consideration, the number of BHs (within 10 pc), $N_{\rm BH}$, ranges from 0 to 5. Star clusters with $N_{\rm BH} = 0$ can result from the ejection of all the BHs, because of supernovae kicks (50% of the cases) and/or dynamical interactions. Our $N-$body models display initial escape velocities $v_{\rm esc} \lesssim 6\,\mathrm{km\,s^{-1}}$, which decrease to $v_{\rm esc} \lesssim 3\,\mathrm{km\,s^{-1}}$ at 20 Myr. Thus, only BHs formed with almost negligible kicks can be retained within the host cluster. Also, as mentioned earlier, the IMF may not contain massive-enough stars to form BHs (12% of the models that end up with 0 BHs within the mass cut, see Sect. 6.2.2).

In the following, we will assess if $N_{\rm BH} \leq 5$ BHs can produce quantifiable imprints on the radial distributions of stars.

6.3.1 Chi-squared distributions

Fig. 6.1 shows the distributions of χ^2_ν, for different $N_{\rm BH}$. If we apply the mass cut introduced in Sect. 6.2.3, we can select most of the models with χ^2_ν closer to the expected value near 1, and remove those that are highly inconsistent with the observed profiles. The result of our the comparison improves with increasing $N_{\rm BH}$, up to $N_{\rm BH} = 4$, which however exist in only 1% of the cases. If we focus on the cases with a large number of good fits ($N_{\rm BH} \leq 3$), the median value of the reduced chi-squared distributions decrease from $\chi^2_\nu \approx 3$ to $\chi^2_\nu \approx 1$ for $N_{\rm BH}$ increasing from 0 to 3.

When only models within the mass cut are considered, 98% of the clusters have $N_{\rm BH} \leq 3$. This is mainly because star clusters that contain a high initial mass fraction in O-type stars (which evolve into BHs) are easily dissolved by the strong stellar winds (Wang & Jerabkova 2021), and result in present-day total masses far below the one observed for the Hyades. If the initial mass fraction in O-type stars is more than two times higher than that expected from a Kroupa (2001) IMF, our models cannot result in present-day clusters in the selected mass range.

Table 6.2 reports the final total masses and BH mass fractions for different components in the $N-$body models, and for different values of $N_{\rm BH}$. The total mass in high-mass stars is $\approx 170\,{\rm M}_\odot$, independently on the number of BHs, as a consequence of the chosen criterion for filtering out models with little agreement with the observed cluster. Also the total visible mass, $M_{\rm vis} \approx 240\,{\rm M}_\odot$, does not show any dependence on $N_{\rm BH}$, with the only exception of the sample with 5 BHs. For the latter case, as mentioned earlier, the initial larger mass fraction of O-stars brings about a more efficient mass loss across the tidal boundary, and results in lower total stellar masses. In contrast, the total mass $M_{\rm tot}$, increases with $N_{\rm BH}$: the total BH mass spans from $\approx 10\,{\rm M}_\odot$ ($f_{\rm BH} = 0.04$) if only 1 BH is present, up to $\approx 45\,{\rm M}_\odot$ for the case with 5 BHs ($f_{\rm BH} = 0.16$).

6.3.2 Two-component radial distributions

To highlight the difference in the fit performance between models with BHs and without BHs, we randomly drew 16 models from simulations (which have already passed the mass cut) with 0 BHs and from a sample obtained by combining the sets with 2 and 3 BHs. For each distribution, we evaluated the median values for selected bins and the spread, as $1.4 \times {\rm MAD}\,\left(\sqrt{N_{\rm bin}}\right)^{-1}$, where MAD is the median absolute deviation.

Fig. 6.2 displays the density profiles of the high-mass (top) and low-mass (bottom) components of these samples, compared to the observed profiles (see Sect. 6.2.1). The density profiles of the $N-$body models are mostly consistent with the observed distributions. Models with $N_{\rm BH} = 0$ display more concentrated distributions of high-mass stars, due to the absence of a more massive component. For this reason, they tend to overestimate the density in the innermost regions. The selected models also perform a good description of the low-mass stars, although they were not considered in the fitting procedure. This component presents central densities lower than high-mass stars of about an order of magnitude, as a consequence of mass segregation within the cluster.

A better description of the relative concentration of stars with different masses (and thus of the degree of mass segregation) is given by the ratio between their half-mass radii (e.g., see Vesperini et al. 2013, 2018; de Vita et al. 2016; Torniamenti et al. 2019) Fig. 6.3 displays the ratios between high-mass and low-mass stars, for all the models with 0 BHs and with 2−3 BHs. For the latter, BHs suppress the segregation of the high-mass

$N_{\rm BH}$	$M_{\rm vis}$ ($\rm M_\odot$)	$M_{\rm h}$ ($\rm M_\odot$)	$M_{\rm tot}$ ($\rm M_\odot$)	$f_{\rm BH}$	$f_{\rm O}$	M_0 ($\rm M_\odot$)	$r_{h,0}$ (pc)	$P_{\rm cut}$
0 BHs	$233.9^{+21.4}_{-22.1}$	$170.5^{+12.3}_{-15.1}$	$254.0^{+24.4}_{-24.1}$	0	$0.09^{+0.06}_{-0.05}$	$1016.1^{+194.5}_{-16.1}$	$0.98^{+0.99}_{-0.48}$	13.8
1 BHs	$242.5^{+21.0}_{-21.9}$	$170.5^{+15.6}_{-10.7}$	$274.1^{+22.5}_{-25.0}$	$0.04^{+0.02}_{-0.01}$	$0.12^{+0.06}_{-0.06}$	$1201.4^{+200.3}_{-200.6}$	$0.99^{+0.99}_{-0.49}$	13.6
2 BHs	$241.2^{+21.8}_{-22.1}$	$168.1^{+14.5}_{-11.1}$	$280.2^{+22.9}_{-25.4}$	$0.07^{+0.02}_{-0.02}$	$0.15^{+0.05}_{-0.05}$	$1401.4^{+200.3}_{-200.6}$	$1.00^{+0.99}_{-0.50}$	14.2
3 BHs	$242.7^{+27.6}_{-26.2}$	$173.0^{+10.9}_{-18.0}$	$289.6^{+30.8}_{-28.4}$	$0.09^{+0.02}_{-0.01}$	$0.15^{+0.05}_{-0.04}$	$1400.5^{+195.5}_{-197.3}$	$1.96^{+0.03}_{-1.27}$	16.8
4 BHs	$249.3^{+14.2}_{-29.4}$	$167.1^{+14.1}_{-7.2}$	$294.5^{+23.7}_{-22.4}$	$0.11^{+0.02}_{-0.01}$	$0.17^{+0.03}_{-0.04}$	$1400.5^{+195.3}_{-0.2}$	$1.97^{+0.04}_{-0.71}$	27.2
5 BHs	$216.7^{+25.5}_{-8.5}$	$155.6^{+6.0}_{-3.4}$	$281.4^{+18.8}_{-14.2}$	$0.16^{+0.01}_{-0.02}$	$0.18^{+0.02}_{-0.05}$	$1598.5^{+0.3}_{-270.2}$	$1.97^{+0.00}_{-0.02}$	27.2

Table 6.2: Properties of the Hyades models with $150\,\rm M_\odot \leq M_h \leq 190\,M_\odot$, for different values of $N_{\rm BH}$ (column 1): total mass in visible stars (column 2), total mass of high-mass stars (column 3), total mass (column 4), BH mass fraction (column 5), initial mass fraction in O-type stars (column 6), initial total mass (column 7), initial half-mass radius (column 8). The last column reports the percentage of models within the mass cut, for the selected $N_{\rm BH}$. The reported values are the medians of the distributions, while the subscripts and superscripts represent the difference from the 16% and 84% percentiles, respectively.

stars, producing less centrally concentrated distributions and increasing their half-mass radius. As a result, the sample with 2−3 BHs displays less mass segregation among the visible stars with respect to models with 0 BHs. Also, the former case yields a much better agreement with the observed value[1].

6.3.3 Half-mass radii

Figure 6.4 shows the impact of the presence of BHs on $r_{\rm hm}$, defined as the half-mass radius of all the visible stars. The distributions shift towards higher values for increasing numbers of BHs, which is because $r_{\rm h}$ is larger, but also because of the quenching of mass segregation of the visible components. Our models suggest that 3 BHs can produce an increase in the expected value of the half-mass radius for the visible stars of $\sim 40\%$. As a further hint on the presence of a BH component, the observed value almost coincides with the expected value for the case $N_{\rm BH} = 3$.

The distribution of $r_{\rm hm}$ of the $N_{\rm BH} = 0$ sample is mostly inconsistent with the observed value of the Hyades cluster. Unlike the other cases, this distribution shows a more asymmetric shape, with a peak at $r_{\rm hm} \simeq 3\,\rm pc$, and a tail which extends towards larger values, more consistent with the models hosting BHs. We investigated if this tail may come from clusters that have recently ejected all their BHs, and have still memory of them. Figure 6.5 shows the the distribution of half-mass radii for the cases without BHs at the present day. We distinguished between different ranges of $t_{\rm BH}$, defined as the time at which the last BH was present within the cluster. The stellar clusters that have never hosted BHs,

[1]In this study, the half-mass radii are calculated from the distributions of the stars within $r_{\rm t}$, and do not refer to the half-mass radii of the whole Plummer model.

because they are ejected by the supernova kick or because there are not massive stars to produce them (see Sect. 6.3), constitute the bulk of the distribution, and are inconsistent with the observations.

The $N-$body models where all the BHs were ejected in the first 500 Myr show the same distribution as those that have never hosted BHs. For these clusters, the successive dynamical evolution has erased the previous imprints of BHs on the observable structure, because the most massive stars had enough time to segregate to the center after the ejection of the last BH. Finally, star clusters where BHs were present after 500 Myr (i.e. the last $\sim$ 150 Myr) still preserve some memory of the previous BH population, and display larger half-mass radii, in some cases consistent with the observed value. Since the present-day relaxation time (Spitzer 1987) for our $N-$body models is $t_{\rm rlx} \approx 45$ Myr, we find that the only models that have ejected their last BH less than $3\,t_{\rm rlx}$ ago have preserved some memory of their previous presence.

BHs that were ejected from the Hyades in the last 150 Myr display a median distance ~ 60 pc from the cluster (~ 80 pc from the Sun). Only in two cases, the dynamical recoil could eject the BH at a present-day distance > 1000 pc, while in all the other cases the BH is found closer than 200 pc from the cluster center.

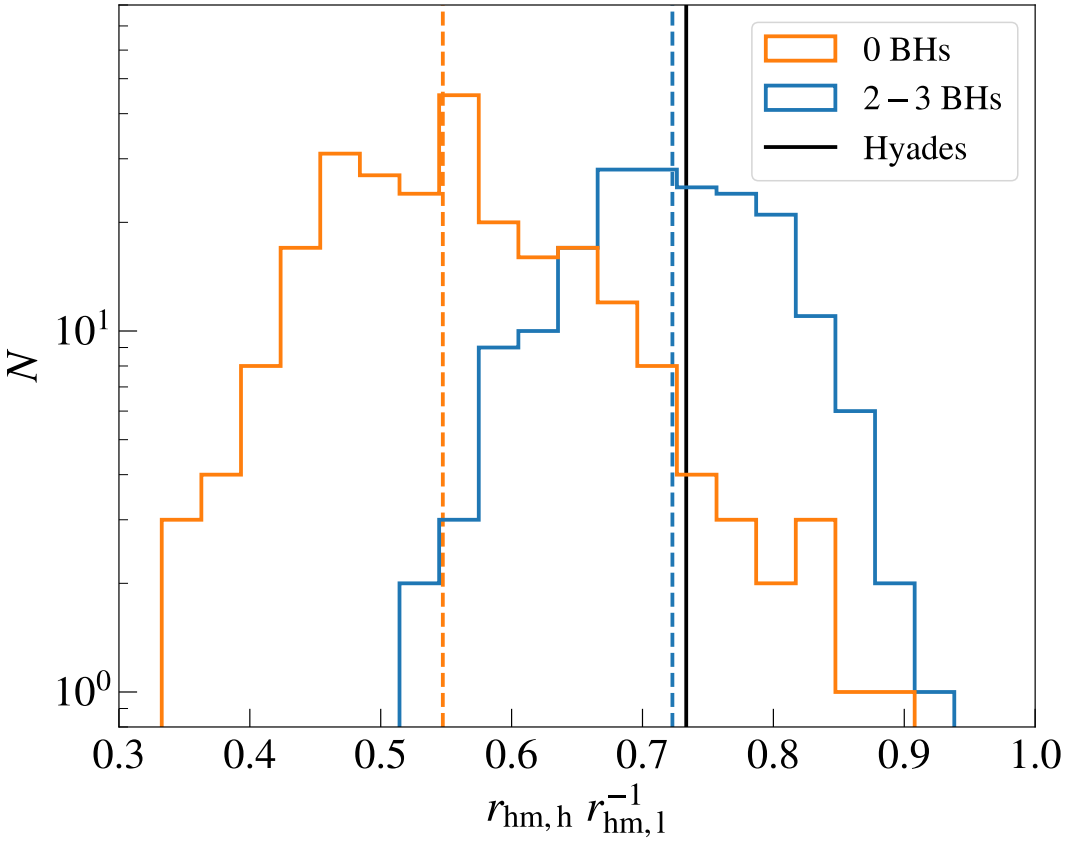

Figure 6.3: Distribution of the ratio between the half-mass radius of the high-mass stars ($r_{\rm hm,h}$) and that of low-mass stars ($r_{\rm hm,l}$), for star clusters with $N_{\rm BH} = 0$ (orange) and $N_{\rm BH} = 2-3$ (blue). The dashed vertical lines represent the medians of the distributions, and the vertical black line displays the observed value for the Hyades (Evans & Oh 2022).

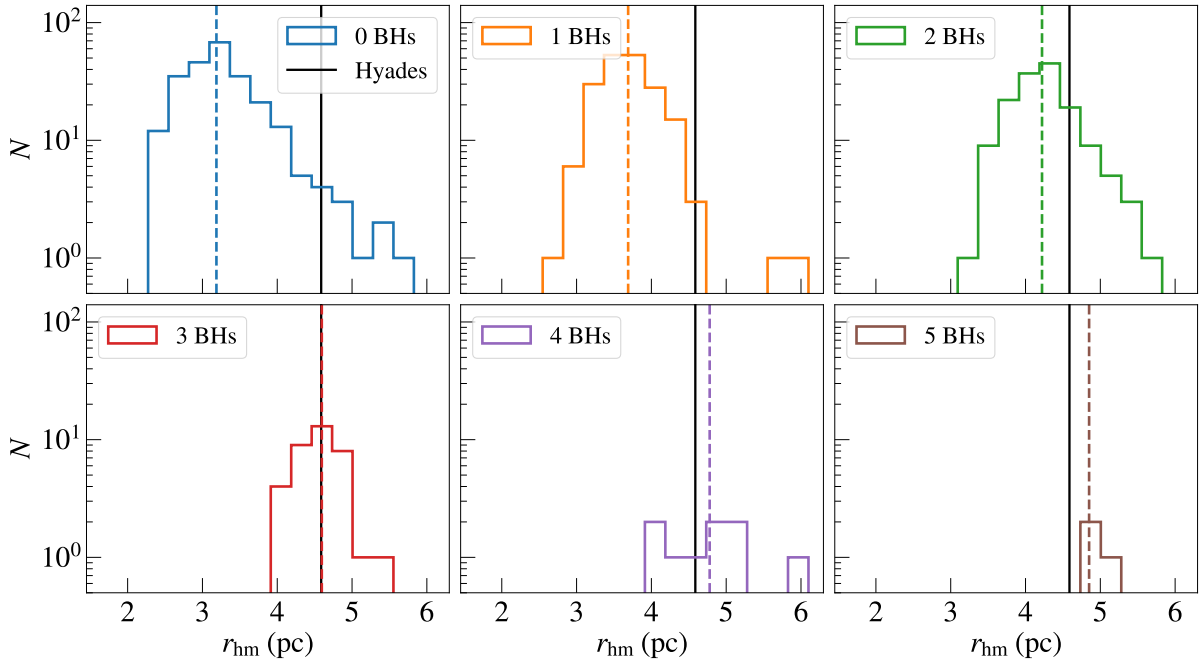

Figure 6.4: Distributions of half-mass radii of visible stars for $N-$body models with different N_{BH}. The dashed vertical lines represent the medians of the distributions, and the vertical black line displays the observed value for the Hyades (Evans & Oh 2022).

6.3.4 High-mass stars parameter space

As explained in Sect. 6.3.3, the presence of even $2-3$ BHs has a measurable impact on the observable structure of such small-mass clusters. High-mass stars are most affected by the presence of BHs, because they are prevented from completely segregating at the cluster core. In Fig. 6.6 we show how the number of BHs within the cluster relates to the total mass in high-mass stars (M_h) and to their half-mass radius ($r_{hm,h}$). In this case, we consider all the simulated models, without any restriction on the high-mass total mass, and we show how the average number of BHs in the $N-$body models varies in the $M_h - r_{hm,h}$ space.

The total mass in high-mass stars can be as high as 400 $M_\odot$, while the half-mass radius takes values from 1 to 8 pc. The most diluted clusters feature the lowest mass, because they are closer to being disrupted by the Galactic tidal field. In contrast, models with higher M_h are characterized by the fewest BHs, because of the absence of massive progenitors, which enhance the cluster mass loss. As explained in Sect. 6.3.2, $r_{hm,h}$ grows for increasing number of BHs at the cluster center. In the mass range of the Hyades, the expected value of $r_{hm,h}$ when $N_{BH} = 3$ is larger by almost $\sim 60\%$ with respect to the case with 0 BHs. The observed values of the Hyades (Evans & Oh 2022) lie in a region of the parameter space between $2-3$ BHs, a further corroboration of the previous results of Sect. 6.3. Finally, higher numbers of BHs are disfavoured by our models, because they predict an even lower degree of mass segregation for high-mass stars.

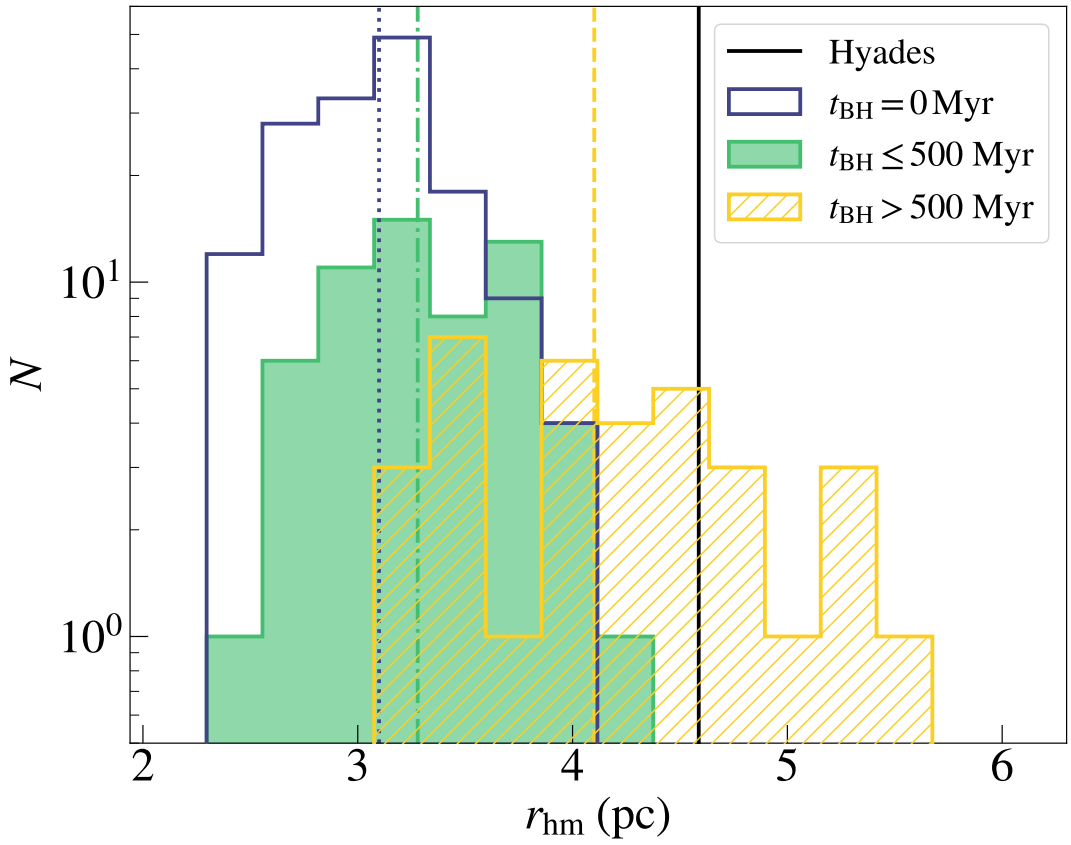

Figure 6.5: Distributions of r_{hm} for star clusters of the noBH sample. We distinguish between $N-$body models where BHs have not formed because there were not stars massive enough in the IMF (magenta, vertical dotted line), star clusters were BHs have been ejected before 500 Myr (red filled area, vertical dash-dotted line), and star clusters were BHs have been ejected after 500 Myr (yellow hatched area, vertical dashed line). The black line displays the value derived from observations (Evans & Oh 2022).

6.3.5 Velocity dispersion profiles

We quantified the impact of a central BH component on the velocity dispersion profile. To this purpose, we compared the same samples of 16 models with $N_{BH} = 0$ and with $N_{BH} = 2 - 3$ as done for the density profiles (see Sect. 6.3.2). Figure 6.7 displays the so-obtained velocity dispersion profiles, calculated as the mean dispersion over the three components. The presence of 2−3 BHs produces a non-negligible increase of 40% in the velocity dispersion in the inner 1 pc. The rise in dispersion is reminiscent of the velocity cusp that forms around a single massive object (Bahcall & Wolf 1976). Such a cusp develops within the sphere of influence of a central mass, which can be defined as $GM_\bullet/\sigma^2$, with $M_\bullet$ the mass of the central object and σ the stellar dispersion. For $M_\bullet = 20\,M_\odot$ and $\sigma = 0.3$ km/s we find that this radius is ~ 1 pc, roughly matching the radius within which the dispersion is elevated. Although a BBH of $20\,M_\odot$ constitutes $\sim 10\%$ of the total cluster mass, the mass with respect to the individual stellar masses is much smaller (factor of 20) compared to the case of an intermediate-mass BH in a GC (factor of 10^4) or a super-massive BH in a nuclear cluster (factor of 10^6). As a result, a BBH in Hyades makes larger excursions from the center due to Brownian motions.

From eq. 90 in Merritt (2001) we see that the wandering radius of a BBH of 20 $M_\odot$ in Hyades is ~ 0.15 pc. Although this is smaller than the sphere of influence, it is still a significant fraction of this radius. Also, in presence of a BBH with massive components ($> 50\,M_\odot$) stars may tend to align their orbital angular momentum that of the BBH (Mapelli et al. 2005). In our $N-$body models, however, where BBH components have lower masses, stars show isotropic distribution with respect to the direction of the central BBH angular momentum, independently of the distance from the cluster center. Thus, no signature of angular momentum alignment is found. We therefore conclude that the elevated dispersion is due to the combined effect of stars bound to the BBH, stars being accelerated by interaction with the BBH (Mapelli et al. 2005) and the Brownian motion of its center of mass.

We calculated the total mass of the cluster by referring to the commonly used dynamical estimation:

$$M_{\rm dyn} \simeq \frac{10\langle\sigma^2_{\rm 1D}\rangle R_{\rm eff}}{G}. \tag{6.3}$$

To be consistent with observational estimations, we defined $\sigma_{\rm 1D}$ as the line-of-sight velocity dispersion of high-mass stars and the effective radius $R_{\rm eff}$ as the radius containing half the number of high-mass stars. We find a systematic bias between $M_{\rm dyn}$ and $M_{\rm tot}$. In particular, $M_{\rm dyn}$ always overestimates the total mass of the cluster of a typical factor ~ 1.6 for $N_{\rm BH} = 0$ and ~ 2 if $N_{\rm BH} > 0$. This is mainly due to the presence of unbound stars that are still associated with the cluster, which velocities are enhanced by the tidal heating (e.g., see also Oh & Evans 2020).

6.3.6 Tidal tails

Star clusters are subject to an evolutionary mass loss from stellar evolution and $N-$body relaxation processes. The relaxation process may increase the kinetic energy of a star sufficiently to be able to escape the cluster and find its own orbit in the Galactic potential. Numerical simulations show that stellar escapers form a symmetrical S-shaped stellar distribution of stars slowly drifting away from the cluster. Given the nature of the orbits of tails members within the Galactic potential, along which they vary their velocity, the distribution of stars in tidal tails is not uniform. As described by Küpper et al. (2010, 2012), there are so-called epicyclic overdensities whose properties and position in the tail mainly depend on cluster mass and the Galactic potential.

Before *Gaia* DR2 it was not possible to detect tidal tails of OCs (e.g. Röser et al. 2019; Meingast & Alves 2019). Further studies, for example Jerabkova et al. (2021) or Boffin et al. (2022), showed that $N-$body models are essential for the search of the tidal tails of OCs and for interpreting the recovered members. This is because tidal tails are large-scale ($100 - 1000$ pc) structures dissolving into the Galactic stellar field making tail members surrounded by stellar contaminants. Since the *Gaia* mission only provides radial velocity values for bright stars (Cropper et al. 2018), the search for tidal tail members mostly relies on on-the-sky projected parameters as proper motions which have complex shapes. Despite the difficulties connected with the search for tidal tails of open star clusters, they provide constraints on the evolution of the star clusters, but also its interplay with the Galactic potential.

Wang & Jerabkova (2021) show that the details of the massive OB star population affect the evolution of a cluster. This means that the initial conditions of star clusters

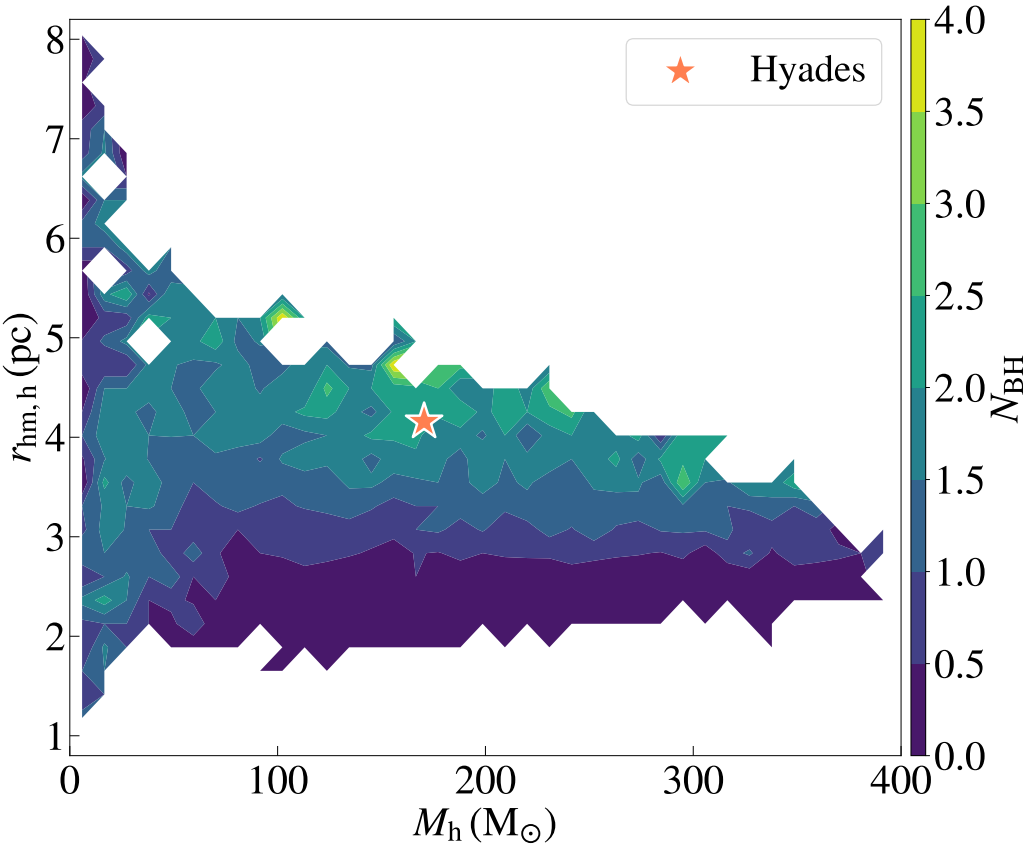

Figure 6.6: Contour plot of the total mass (M_{h}) and the half-mass radius ($r_{\mathrm{hm,h}}$) of the high-mass stars. The colormap encodes the local mean number of BHs in that region of the parameter space. The orange star displays the values derived from observations (Evans & Oh 2022).

cannot be constrained unless the initial content of massive stars is known. In this work, we specifically compare the best-fit models with different BH content and study their tidal tails. The overall tidal tail shape and its kinematics signatures are not sensitive on the cluster initial conditions. We find no evidence that the BH content affects the phase space distribution of the tails and the position of the epicyclic over-densities is not significantly affected, as shown in Fig. 6.8. We notice the density profile of the tail varies from model to model.

Future studies might specifically target the epicyclic over-densities in more detail and establish their phase-space properties for mode models to provide large statistical grounds. While the current observational data are not sufficient to provide such information (see the bottom panel of Fig. 6.8), this will likely change with the future *Gaia* data releases and the complementary spectroscopic surveys SDSS-V (Almeida et al. 2023), 4MOST (de Jong et al. 2019) and WEAVE (Dalton et al. 2012).

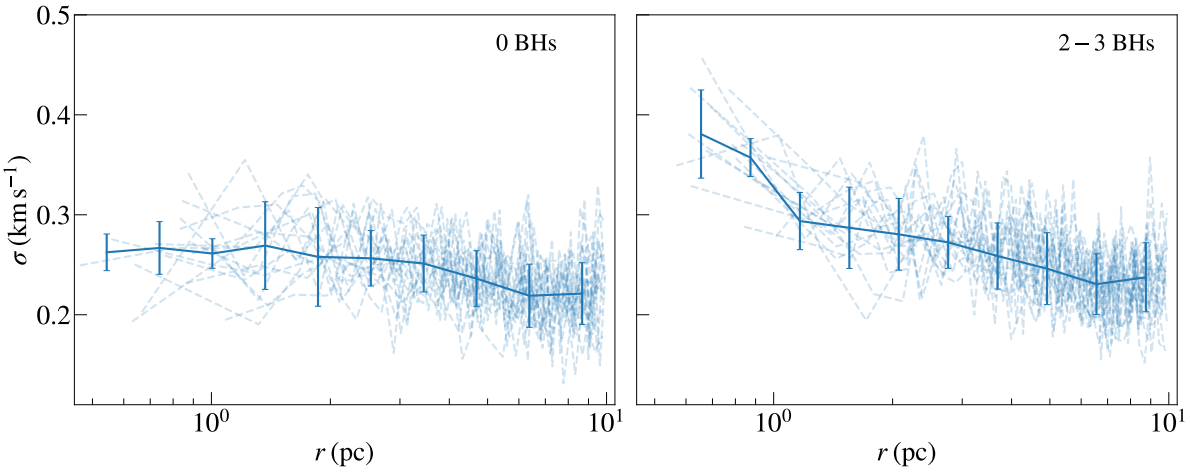

Figure 6.7: One-dimensional velocity dispersion profiles for 16 models drawn from the cases with $N_{\rm BH} = 0$ (left) and $N_{\rm BH} = 2 - 3$ (right). The blue dashed lines are the single models. The blue solid line is the median of the distribution at selected radial distances, with the associated errors.

6.4 Discussion: observational tests

6.4.1 BH companions

Three-body interactions within a stellar cluster strongly favour the formation of binary systems, mainly composed of the most massive objects (Heggie 1975). As a consequence, BHs tend to form binaries preferentially with other BHs, and when in binaries with a lower-mass stellar companion, they rapidly exchange the companion for another BH (Hills & Fullerton 1980). In general, the result is a growing BBH population in the cluster core (Portegies Zwart et al. 2001). In OCs, however, given the limited number of BHs by the initial low number of massive stars, a non-negligible fraction of BH-star binary systems may form and survive.

Binary stars in dynamically-active clusters are expected to display semi-major axis distributions that depend on the cluster properties. Soft binaries (with binding energy lower than the average cluster kinetic energy) are easily disrupted by any strong encounter with another passing star or binary. The upper limit for the semi-major axis is thus given by the hard-soft boundary of the cluster:

$$a_{\rm max} = \frac{G m_1 m_2}{2 \langle m\sigma^2 \rangle}, \tag{6.4}$$

where $m_{1,2}$ are the masses of the binary components, and $E_{\rm b} = \langle m\sigma^2 \rangle$ is the hard-soft boundary (Heggie 1975). For an OC with $\sigma \approx 0.5\,{\rm km\,s^{-1}}$, the upper limit for a binary composed of a black-hole ($m_1 = 10\,{\rm M_\odot}$) and a star ($m_2 = 1\,{\rm M_\odot}$) is of the order of $a_{\rm max} \sim 10^{-1}$ pc.

When a hard binary is formed, it becomes further tightly bound through dynamical encounters with other cluster members (Heggie 1975; Goodman 1984; Kulkarni et al. 1993; Sigurdsson & Phinney 1993. Each encounter causes the binary to recoil, until the binary becomes so tight that the recoil is energetic enough to kick it out from the cluster.

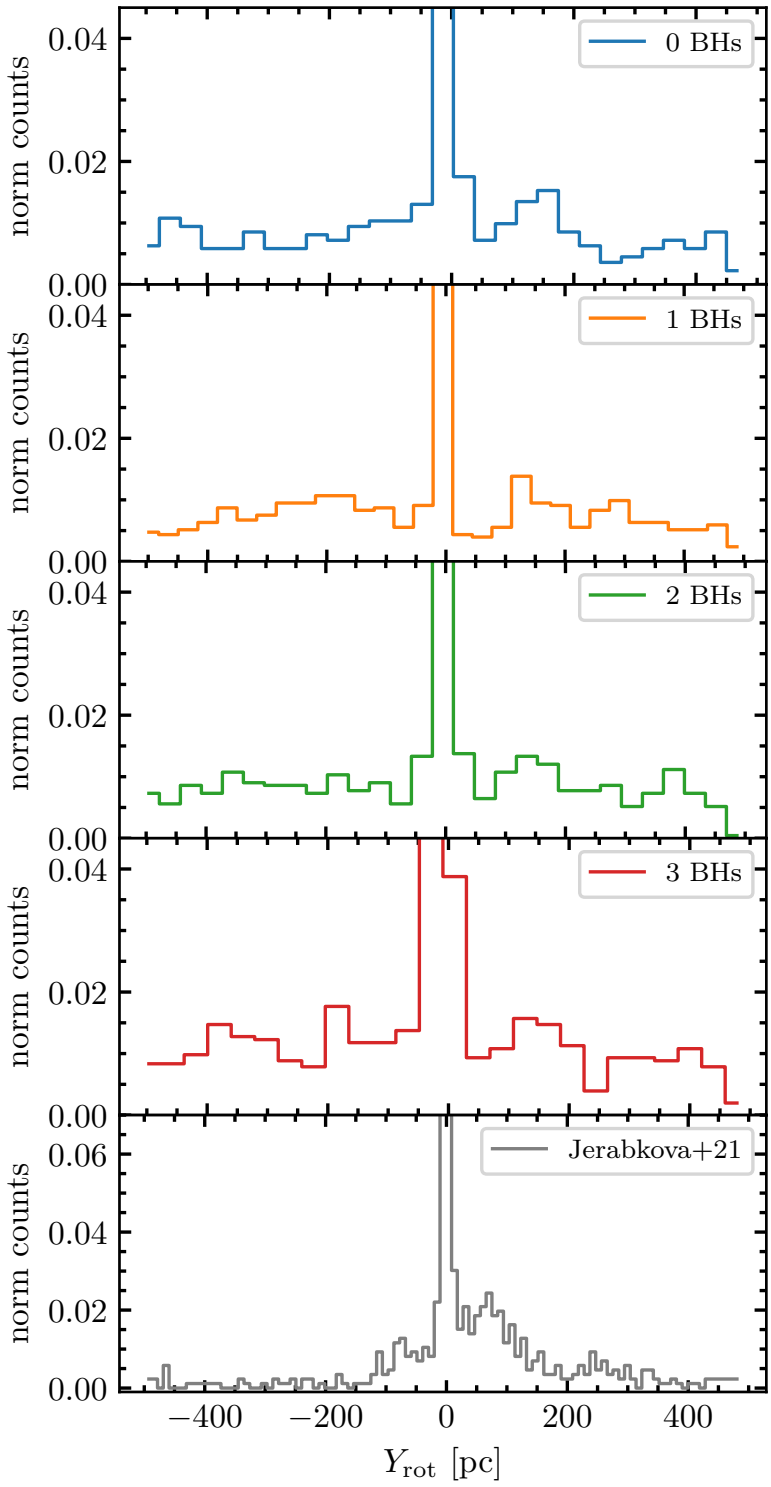

Figure 6.8: The individual panels show histogram along the tidal tails in Y Galactic coordinates rotated so that the VY component is horizontal. The panels 1-4 (from top) show N-body simulations with (0,1,2,3) BHs, and the bottom panel shows *Gaia* data from Jerabkova et al. (2021). Histogram bins were optimised using Knuth's rule (Knuth 2006).

$N_{\rm BH}$	$f_{\rm BH-Star}$	$f_{\rm BH-Remn.}$	$f_{\rm BH-BH}$
1 BHs	0.78	0.22	0.0
2 BHs	0.15	0.02	0.83
3 BHs	0.02	0.07	0.91
4 BHs	0.07	0.07	0.86
5 BHs	0.2	0.0	0.8

Table 6.3: Fractions of binary systems hosting BHs, for different number of BHs within 10 pc (column 1). We distinguish between different types of BH companions, specifically stars (column 2), white dwarfs or NSs (column 3), and BHs (column 4).

For this, the lower limit $a_{\rm min}$ can be assumed to be the semi-major axis at which the binary that produces a recoil equal to the escape velocity $v_{\rm esc}$. Following Antonini & Rasio (2016b):

$$a_{\rm min} = 0.2 \frac{G m_1 m_2}{v_{\rm esc}^2} \frac{m_3^2}{m_{12}^2 m_{123}}, \tag{6.5}$$

where $m_3 = \langle m \rangle$, $m_{12} = m_1 + m_2$, and $m_{123} = m_1 + m_2 + m_3$. For an open cluster with $v_{\rm esc} \approx 0.5\,{\rm km\,s^{-1}}$, $m_1 = m_2 = 10\,{\rm M_\odot}$ and $m_3 = 0.5\,{\rm M_\odot}$, we obtain $a_{\rm min} \sim 10^{-5}$ pc (2 AU). For a BH-star binary system ($m_2 = 1\,{\rm M_\odot}$) $a_{\rm min} \sim 10^{-4}$ pc.

BHs in our $N-$body models, as expected, show a tendency to dynamically couple with other objects, and form binary and triple systems. When $N_{\rm BH} > 0$, only in 6% of the cases the BH is not bound in a binary or multiple systems. Even in models where only 1 BH is present, the single BH tends to form binaries with (mainly) stars or other remnants (white dwarfs of NSs). Fig. 6.9 shows the distribution of semi-major axes and periods for binaries and triple systems of clusters with $N_{\rm BH}$ ranging from 1 to 4. Independently of $N_{\rm BH}$, most of the binaries display semi-major axes from 10^{-5} pc to 10^{-1} pc, consistently with our approximate calculation. When more than 1 BH is present, dynamical interactions tend to favour the formation of BBHs. As reported in Tab. 6.3, the fraction of BBHs represents by far the largest fraction of binary systems hosting BHs, if more than 1 BHs is hosted by the cluster.

6.4.2 Binary candidates in the Hyades

In this section we present a search for possible massive companions to MS stars in the Hyades. We identify binary candidates by searching for members with enhanced *Gaia* astrometric and spectroscopic errors (following Penoyre et al. 2020; Belokurov et al. 2020, and Andrew et al. 2022).

Selecting cluster members

We start with all *Gaia* DR3 sources with $\varpi > 5$ mas, RA between 62 and 72 degrees, Dec between 13 and 21 and *RUWE* greater than 0 (effectively enforcing a reasonable 5-parameter astrometric solution) - giving 5640 sources as shown in Fig. 6.10. We also apply an apparent G-band magnitude cut of $m_{\rm G} < 15$ above which the astrometric accuracy of *Gaia* starts to degrade rapidly due to Poisson noise. Analysis beyond this magnitude is eminently possible, but for such a nearby population of stars this cut excludes a minority of the cluster (even more so the likely binary systems, as binary fraction increases with

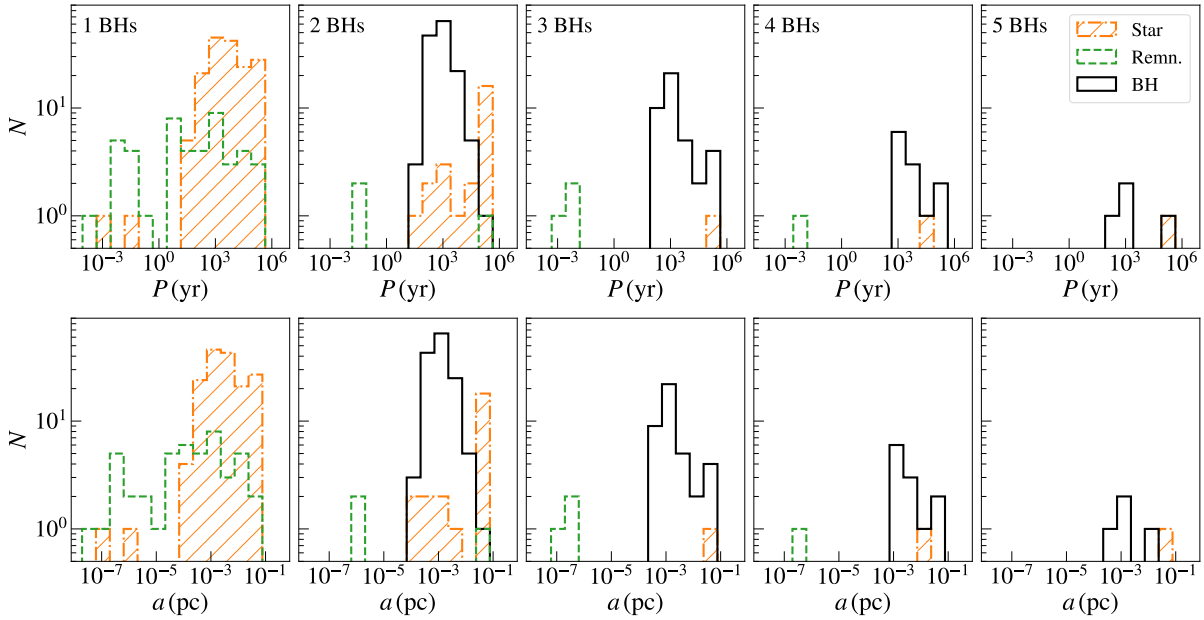

Figure 6.9: Distributions of periods (upper panels) and semi-major axes (lower panels) of the binary and triple systems hosting BHs, for $N-$body models with different numbers of BHs. We distinguish between different types of BH companions, specifically stars (orange dash-dot line, hatched area), white dwarfs or NSs (green dashed line), and BHs (black)

mass) and means that *Gaia* should have a near constant (∼0.2 mas, Lindegren et al. 2021) precision per observation and thus allows uncomplicated comparison of sources.

To select cluster members we use the position, proper motion, and parallax to construct an (unnormalized) simple membership probability:

$$p_{\rm member} = e^{-\sum_x \left(\frac{x-x_0}{\sigma'_x}\right)^2} \tag{6.6}$$

where

$$\sigma'^2_x = \sigma^2_x + \sigma^2_{AEN} + \sigma^2_{x_0} \tag{6.7}$$

with x denoting each of the parameters of RA, Dec, $\mu_{RA^*}(=\mu_{RA}\cos(Dec))$, μ_{Dec} and ϖ. σ_x is the reported uncertainty on each parameter in the *Gaia* catalog and σ_{AEN} is the `astrometric_excess_noise` of the fit. x_0 and σ_{x_0} are the assumed values and spread of values expected for the cluster as listed in Tab. 6.4. The inclusion of the AEN ensures that potentially interesting binaries, which may have a significantly larger spread in their observed values and thus fall outside of the expected variance of the cluster, are not selected against.

The value of $p_{\rm member}$ for stars in the field is shown in Fig. 6.11 from which we choose a critical value of $\log_{10}(p_{\rm member}) = -1.75$ giving 229 members which can be seen and identified on the Hertzsprung-Russell diagram shown in figure 6.12.

Astrometric and spectroscopic noise

Following the method introduced in Andrew et al. (2022) we can use the astrometric and spectroscopic noise associated with the measurements in the *Gaia* source catalog (which assumes every star is single) to identify and characterize binary systems. This is possible

for binaries with periods from days to years, as these can show significant deviations from expected single-body motion. As *Gaia* takes many high-precision measurements the discrepancy between the expected and observed error behavior is predictable and, as we will do here, can be used to estimate periods, mass ratios and companion masses.

The first step is to select systems with significant excess noise. For astrometry, we can use a property directly recorded in the catalog `ruwe` which stands for the renormalized unit-weight error. This is equal to the square root of the reduced chi-squared of the astrometric fit and should, for well-behaved observations, give values clustered around 1. Values significantly above 1 suggest that either the model is insufficient, the error is underestimated, or there are one or more significant outlying data points.

Given that binary systems are ubiquitous (a simple rule-of-thumb is that around half of most samples of sources host more than one star, see e.g. Offner et al. 2022) these will be the most common cause of excess error, especially in nearby well-characterized systems outside of very dense fields.

It is possible to compute a reduced-chi-squared for any quantity where we know the observed variance, expected precision, and the degrees of freedom - and thus we can find the $RUWE$ associated with spectroscopic measurements as well. To do this we need to estimate the observational measurement error, which we do as a function of the stars' magnitude and color (as detailed in Andrew et al. 2022) giving $\sigma_{spec}(m_G, m_{BP} - m_{RP})$, the uncertainty expected for a single measurement for each source. Thus we can construct a spectroscopic renormalized unit-weight error, which we'll call $RUWE_{spec}$ to use alongside the astrometric which we'll denote as $RUWE_{ast}$. These values are shown for Hyades candidate members in Fig. 6.13.

Only a minority of *Gaia* sources have radial-velocity observations, which can be missing because sources are too bright ($m_G \lesssim 4$, as seen at the top of the HR diagram), too dim ($m_G \gtrsim 14$, as seen at the bottom), in too dense neighborhoods, or if they are double-lined (with visible absorption lines in more than one of a multiple system, as may be the case with some likely multiple stars above the main-sequence). We use only systems with `rv_method_used = 1` as only these are easily invertible to give binary properties (Andrew et al. 2022 for more details).

The particular value at which $RUWE$ is deemed significant must be decided pragmatically, and we adopt the values from Andrew et al. (2022) of $RUWE_{ast} > 1.25$ and $RUWE_{spec} > 2$, where the higher criteria for spectroscopic measurements stems from the smaller number of measurements per star and thus the wider spread in $RUWE$. We select sources satisfying both of these criteria as candidate Hyades binaries, giving 56 systems.

There are some sources that exceed one of these criteria and not the other, and these are interesting potential candidates, but they cannot be used for the next step in the analysis. Using both (generally independent) checks should significantly reduce our number of false positives. It is worth noting that radial-velocity signals are largest for short-period orbits, whereas astrometric signals are largest for systems whose periods match the time baseline of the survey (34 months for *Gaia* DR3). This both tells us about which systems we might miss or might meet one criterion and not the other. It also gives the explanation for one of the largest sources of contaminants in this process: triples (or higher multiples) where each significant excess noise comes from a different orbit and thus the two cannot be easily combined or compared.

If we know the $RUWE$ and the measurement error, and assume that all excess noise comes from the contribution of the binary we can invert to find specifically the contribution

of the binary:

$$\sigma_{b,spec} = \sqrt{RUWE^2_{spec} - 1} \cdot \sigma_{spec}(m_G, m_{BP} - m_{RP}). \tag{6.8}$$

and

$$\sigma_{b,ast} = 2\sqrt{RUWE^2_{ast} - 1} \cdot \sigma_{ast}(m_G) \tag{6.9}$$

where the factor of 2 comes from the fact that *Gaia* takes one-dimensional measurements of the stars 2D position.

Binary properties from excess error

The contributions in equations (6.8) and (6.9) can be mapped back to the properties of the binary and inverted to give the period and (after estimating the mass of the primary) the mass of the companion, as detailed in Andrew et al. (2022). For binary periods less than or equal to the time baseline of the survey the period is approximately:

$$P = \frac{2\pi A}{\varpi} \frac{\sigma_{b,ast}}{\sigma_{b,spec}}, \tag{6.10}$$

and the mass ratio follows:

$$q^3 - \alpha q^2 - 2\alpha q - \alpha = 0, \tag{6.11}$$

where

$$\alpha = \frac{A}{GM\varpi} \sigma^2_{b,spec} \sigma_{b,ast} \tag{6.12}$$

and $A = 1$ AU. M is the mass of the primary star which can be estimated via:

$$M = 10^{0.0725(4.76 - M_G)}, \tag{6.13}$$

where M_G is the absolute magnitude of the star (Pittordis & Sutherland 2019). This is only strictly relevant for MS stars - but all evolved systems in the Hyades are too bright for *Gaia* spectroscopic measurements and thus will not be included in later analysis (with the exception of WDs, which are too dim).

These equations assume the companion has negligible luminosity of its own. If this assumption doesn't hold then the period is slightly overestimated and the mass ratio (and companion mass) are slightly underestimated (see Fig. 3 of Andrew et al. 2022 for more detailed behaviour). The inferred properties of all 56 systems are shown in Fig. 6.14 and recorded in Tab. 6.5.

There are some simple consistency checks we can apply to these results. Primarily we know that astrometric measurements should only be discerning for binaries with periods from months to decades (Penoyre et al. 2022) - thus any deep blue or deep red points are likely spurious solutions - though there are only a handful that have erroneous seeming periods.

As we are searching for significant-mass BHs it is interesting to interrogate the sources with the highest values of q and M_c, but we should be careful as this is equivalent to selecting those with the largest errors and thus possibly those most likely to truly be erroneous (rather than caused by a binary). For example, the highest mass ratio ($q > 1$) sources are amongst the dimmest (and thus least reliably measured) in the sample - these could be physical, most likely white dwarf companions - but could also be random error.

	ϖ	RA	Dec	μ_{RA^*}	μ_{Dec}
x_0	22	66.9	16.4	105	-25
σ_{x_0}	7	3.2	3.2	35	30

Table 6.4: Values for ϖ, RA, Dec, μ_{RA^*}, μ_{Dec}, and their reported uncertainty in the *Gaia* catalog.

The brighter stars that show evidence of companions have relatively modest properties - mass ratios below 1 and companion masses significantly below those of a clear BH companion.

Given the period constraints on binaries including BHs present in the simulations, as presented in Fig. 6.9, it is not shocking that we do not find any likely companions. We certainly cannot rule out that these or other stars in the Hyades might have massive compact companions on smaller or wider orbits that *Gaia* would be insensitive to. Instead, we are pleased to be able to present a list of candidate binaries whose companions are most likely similar main-sequence stars or WDs.

Stars with massive companions may still be identifiable via their velocity offset. The orbital velocity of a $1.5\,M_\odot$ star in a binary with a companion of $15\,M_\odot$ and a period of $10^3(10^4)\,$yr has an orbital velocity of $\sim 7(3)\,$km/s. Searching for these systems from velocity offsets is beyond the scope of this work but is an interesting avenue for future exploration.

6.4.3 Implications for gravitational waves

Given the vicinity of the Hyades, it is interesting to ask the question whether a BBH in the Hyades would be observable as a continuous gravitational wave source with ongoing or future experiments. Let us therefore adopt a BBH with component masses of $m_1 = m_2 = 10\,M_\odot$, an average stellar mass of $\langle m \rangle = 0.5\,M_\odot$ and an escape velocity from the center of the cluster of $v_{\rm esc} = 0.5\,$km/s. Then we assume that the semi-major axis is $a = a_{\rm min} = 2$ AU, i.e. the minimum before it is ejected in an interaction with a star (equation 6.4.1). This is the most optimistic scenario, because it results in the smallest a, but since the interaction time between stars and the BBH goes as $1/a$, a BBH spends a relatively long time at this final, high binding energy. For an average energy increase of 20% (Spitzer 1987) a binary spends approximately 20% of its life cycle in the highest binding energy state. An estimate of the absolute duration can be obtained from the required energy generation rate (Antonini & Gieles 2020c), from which we find $\sim 5\,$Gyr. Because this is much longer than the Hyades' age, it is a reasonable assumption that a putative BBH is near this highest energy state. For the adopted parameters, $a_{\rm min} \simeq 2$ AU. For a typical eccentricity of ~ 0.7, the peak frequency ($\sim 5 \times 10^{-4}\,$mHz, equation 37 in Wen 2003), i.e. below the lower frequency cut-off of LISA (~ 0.1mHz) and the orbital period of ~ 0.7 yr is comparable to the maximum period that can be found by LISA ($\sim 0.7\,$yr, Chen & Amaro-Seoane 2017). Only for eccentricities $\gtrsim 0.99$ (2% probability for a thermal distribution) the peak frequency is $\gtrsim 0.1$ mHz. BH masses ($\gtrsim 30\,M_\odot$) result in orbital periods comfortably in the regime that LISA could detect ($\lesssim 0.08$ yr), but such high masses are extremely unlikely given the high metallicity of the Hyades.

Perhaps a BBH might be observable with the Pulsar Timing Array (PTA). Jenet et al. (2005) show that a BBH at a minimum distance to the sight line to a millisecond pulsar

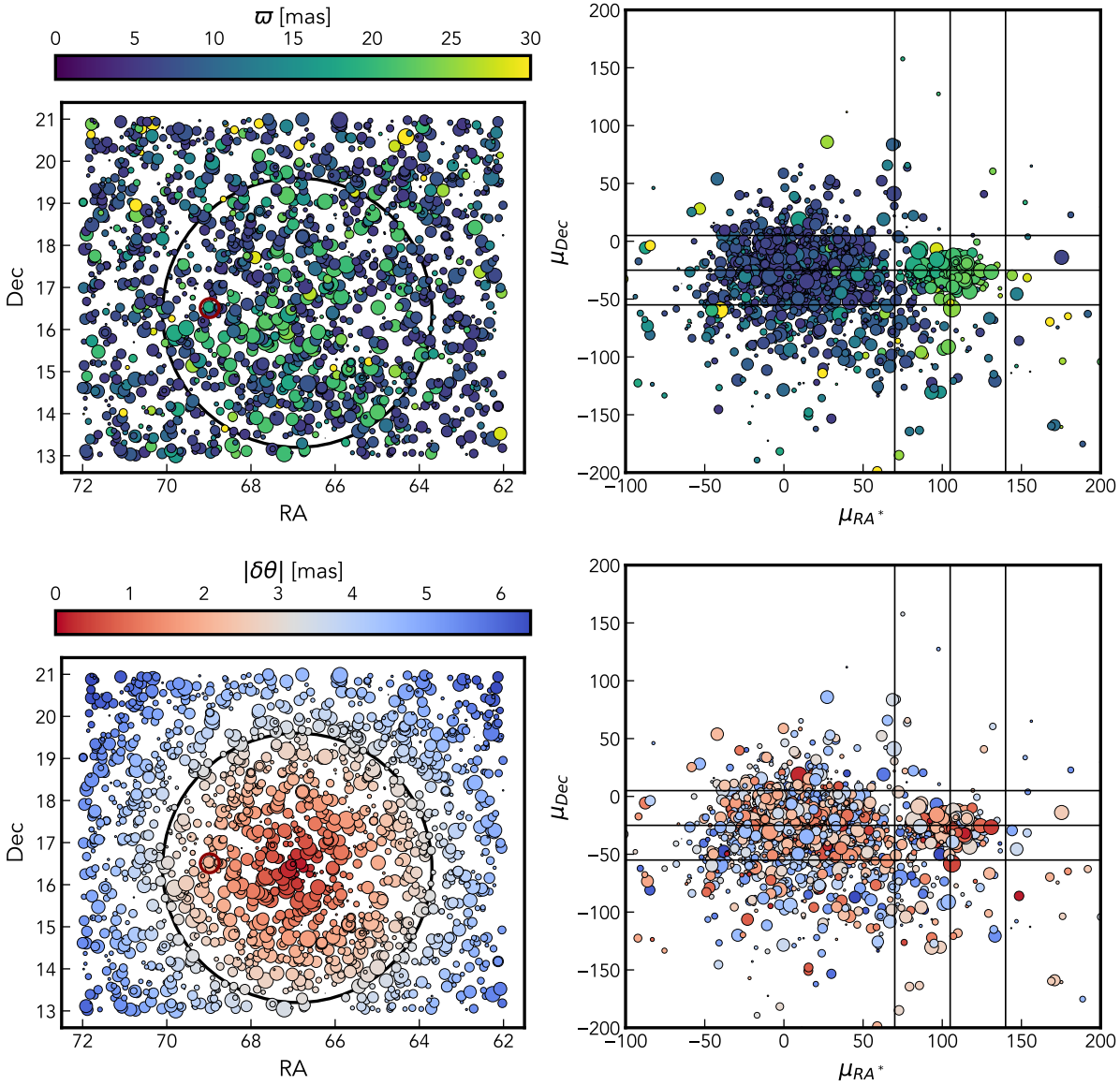

Figure 6.10: Position on sky (left) and proper motion (right) of sources in the field of the Hyades (with $\varpi > 5$ mas). We show the parallax (top row) and angular offset from the center of the cluster (bottom row). Aldebaran, a foreground star too bright for *Gaia*, is shown as a red open circle. The size of each point is set by their apparent magnitude and only sources with $m_G < 15$ are shown (see Fig. 6.12 for reference). We also show an angular offset of 3.2 mas (black circle, left) and lines denoting $\mu_{RA^*} = 105$ mas yr^{-1} and ± 35 mas yr^{-1} from this (black vertical lines, right) and $\mu_{Dec} = -25$ mas yr^{-1} and ± 30 mas yr^{-1} (black horizontal lines, right).

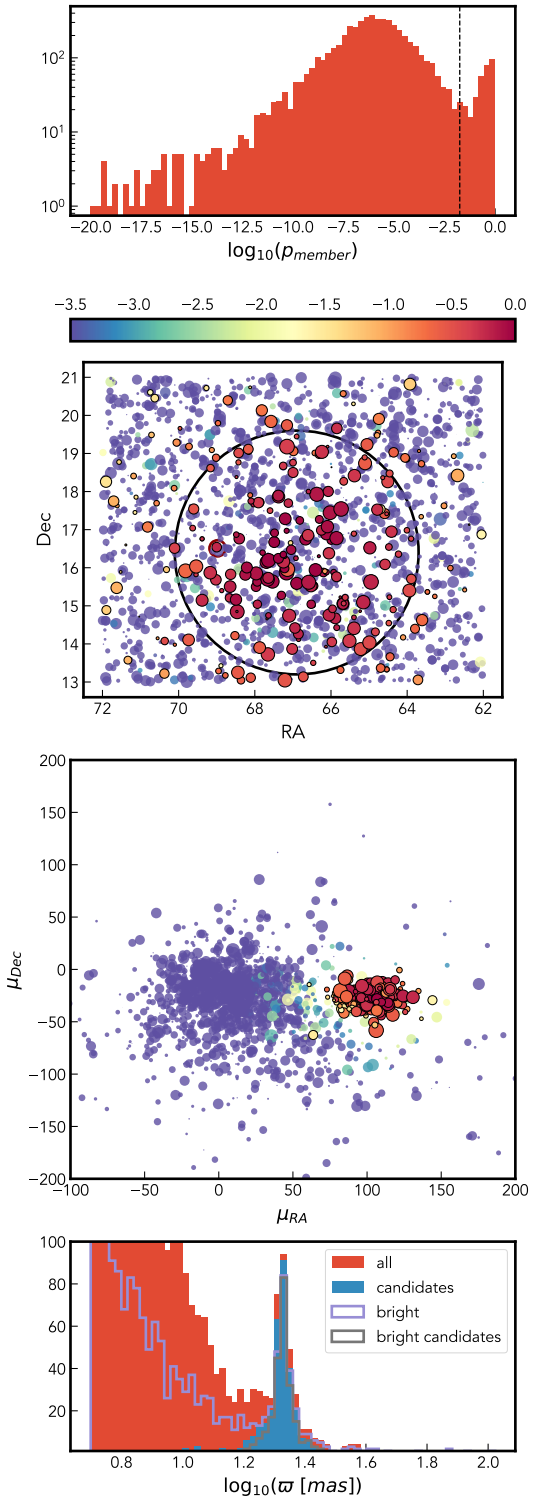

Figure 6.11: The cluster membership probability for stars in the Hyades field based on equation 6.6. We show the distribution of probabilities for all stars (top) and based on this make a cut at $\log_{10}(p_{member}) = -1.75$ (vertical dashed line). We then show the position and proper motion distribution (middle two panels, similar to Fig. 6.10) colored by $\log_{10}(p_{member})$, stars with values greater than -1.75 are shown with black outlines. Finally, we show the parallax distribution of all stars in our field and our candidates (bottom).

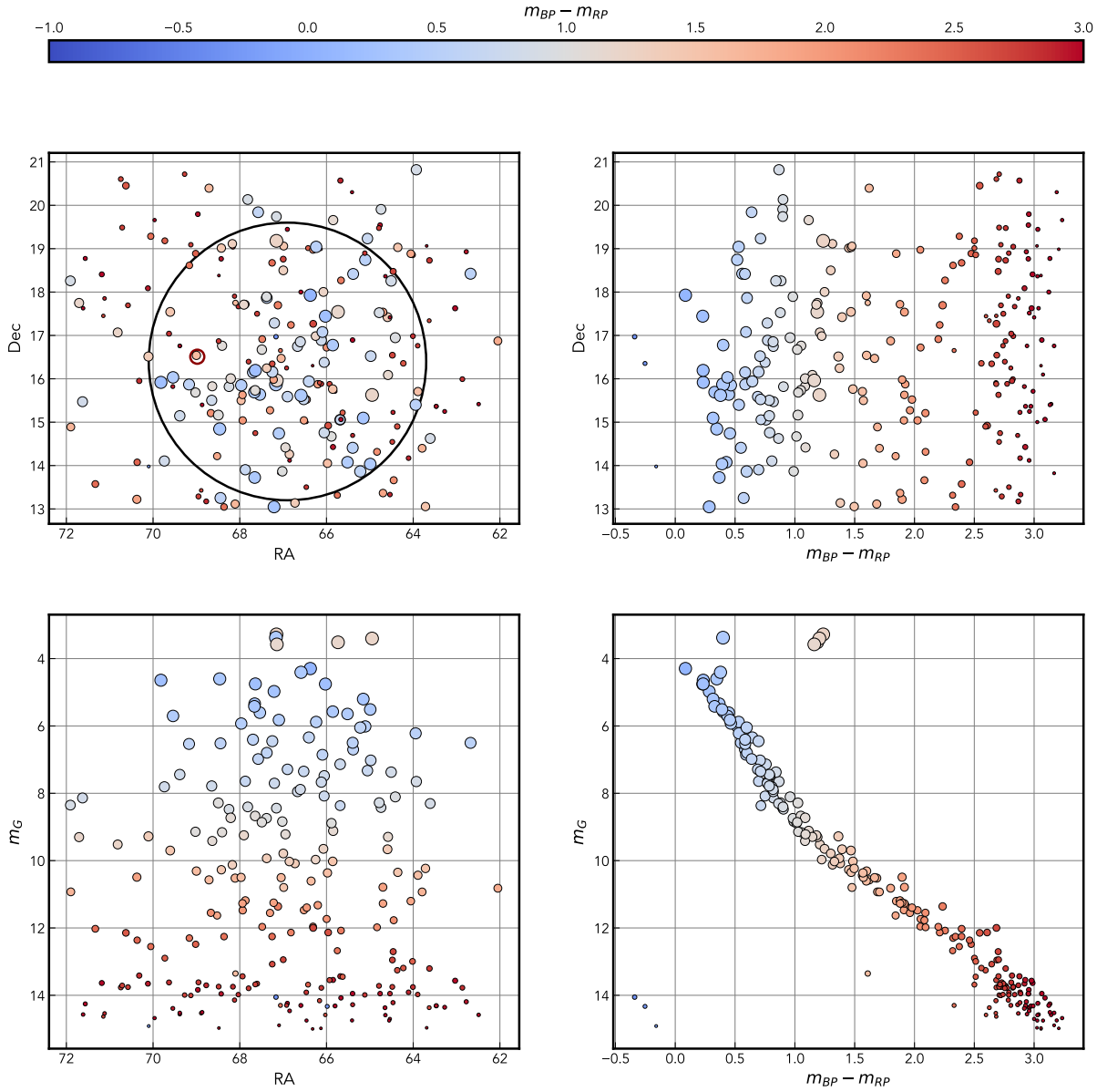

Figure 6.12: Sky maps and color-magnitude diagrams for Hyades candidates, colored by *Gaia* color. Axes are shared moving horizontally and vertically between panels such that any individual star can be traced between plots.

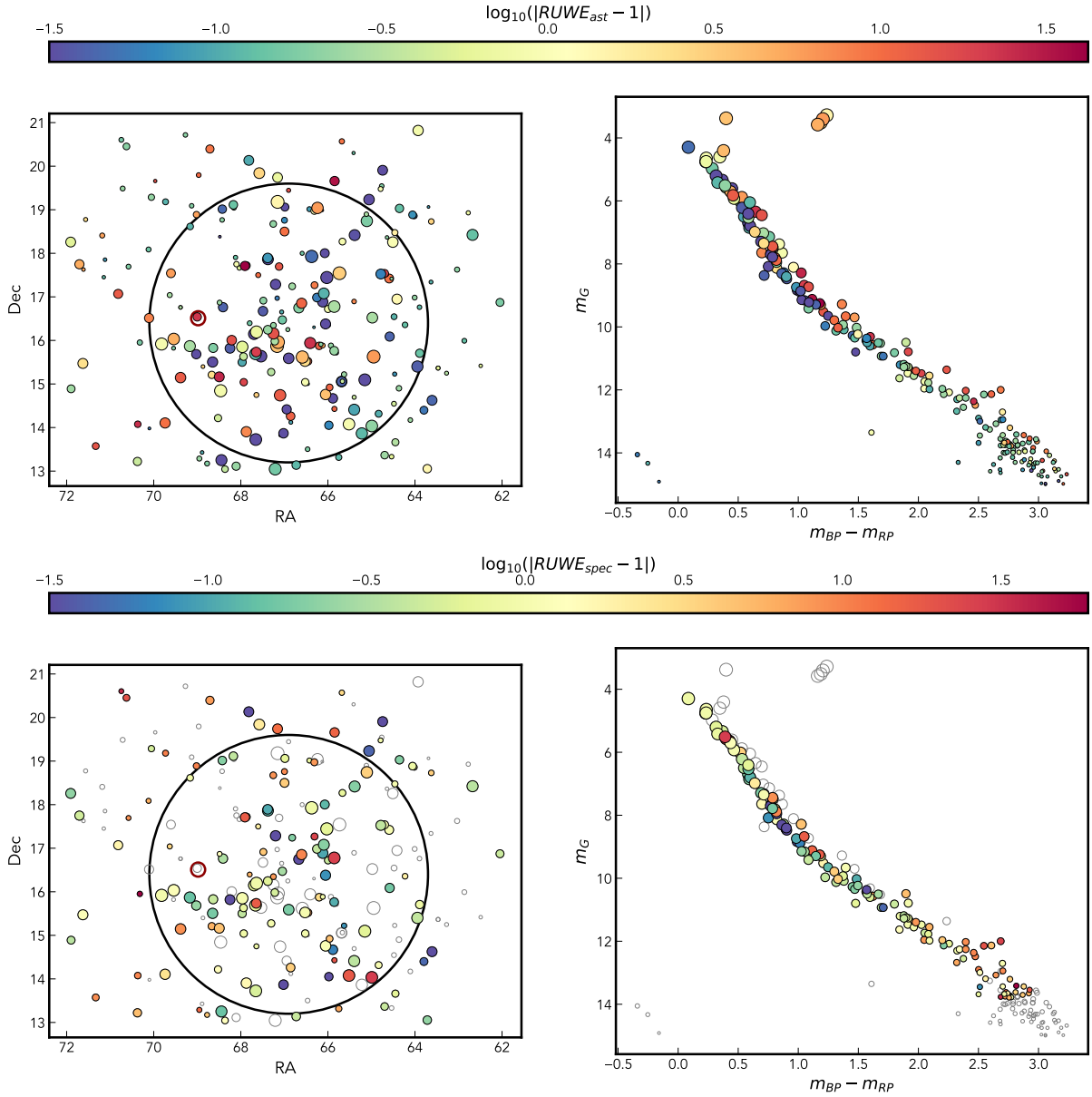

Figure 6.13: Hyades candidates colored by astrometric (top) and spectroscopic (bottom) renormalized-unit-weight-error ($RUWE$). Values significantly above 1 suggest that the system has an extra source of noise, most ubiquitously a binary companion. Many sources don't have radial velocity measurements in the *Gaia* source catalog, and these are denoted with empty grey circles in the bottom plot.

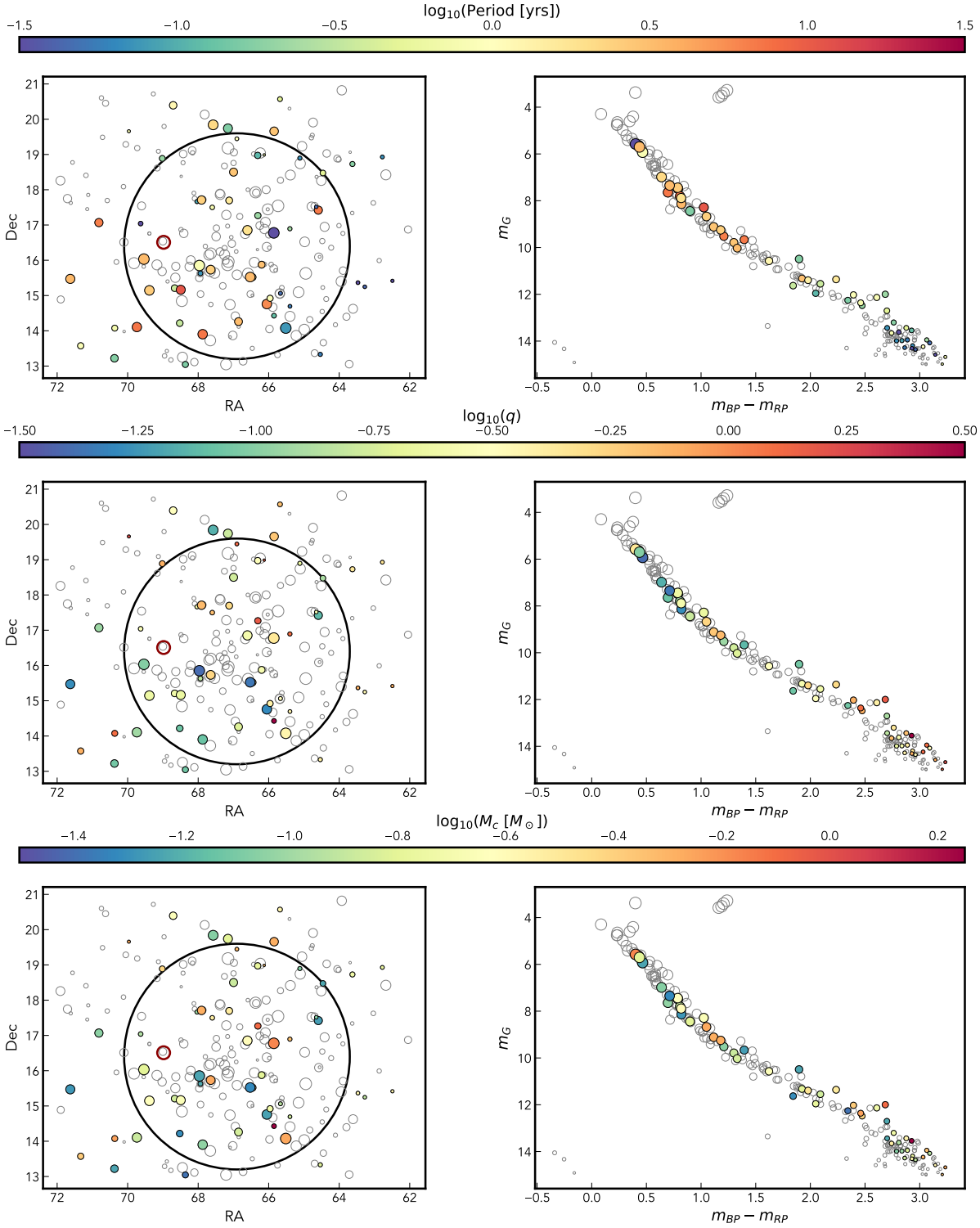

Figure 6.14: Periods, mass ratios (q) and companion masses (M_c) of Hyades candidates inferred from astrometric and spectroscopic $RUWE$. Only sources with significantly high $RUWE$ in both measurements are included here, and all others are shown with empty grey circles.

(MSP) of 0.03 pc ($\sim$ 3 arcmin for the Hyades' distance) causes a time-of-arrival fluctuation of 0.2-20 ns, potentially observable (van Straten et al. 2001). Unfortunately, the nearest MSP in projection is PSR J0407+1607 at 5.5 deg[2]. If the BBH was recently ejected, it may be close to a MSP in projection, but the maximum distance a BBH could have travelled is $\sim$ 1 deg (Section 6.3.2) and there are only 4 pulsars within a distance of 10 deg, so this is unlikely as well. In conclusion, it is unlikely that (continuous) gravitational waves from a BBH in or near the Hyades will be found.

6.4.4 Gravitational microlensing

Because of the vicinity of the Hyades, BHs have a relatively large Einstein radii and we may detect a BH or a BBH through lensing. For a BH mass of $10\,M_\odot$ at a distance of 45 pc the Einstein angle is $\theta_E \simeq 42$ mas. Assuming that background stars in the galaxy are distant enough to act as a source, we find from the *Gaia* catalogue that the on-sky density of background sources is $\Sigma_S \simeq 10^{-9}\,\mathrm{mas}^{-2}$. The Hyades moves with an on-sky velocity of $v_H \simeq 100\,\mathrm{mas\,yr}^{-1}$ relative to the field stars. This gives us a rough estimate of the microlensing rate of $R \simeq N_{BH}\theta_E\Sigma_S v_H \simeq 10^{-5}\,\mathrm{yr}^{-1}$, where we used $N_{BH} = 2$. Unfortunately, the expected rate is too low. Even for a 10^3 higher density of background sources (e.g. with LSST) we are in a regime that it is unlikely to detect dormant BHs with microlensing.

6.5 Conclusions

In this study, we present a very first attempt to find dynamical imprints of stellar-mass black holes (BHs) in Milky Way open clusters. In particular, we focused on the closest open cluster to the Sun, the Hyades cluster. We compared the mass density profiles from a suite of direct $N-$body models, conceived with the precise intent to model the present-day state of Hyades-like clusters (Wang & Jerabkova 2021), to radial mass distributions of stars with different masses, derived from *Gaia* data (Evans & Oh 2022).

Our comparison favors $N-$body models with $2-3$ BHs at present. In these models, the presence of a central BH component quenches the segregation of visible stars, and leads to less concentrated distributions. Star clusters with 3 BHs (and a BH mass fraction $f_{BH} \simeq 0.1$) best reproduce the observed value, while those that never possessed BHs have an half-mass radius that is $\sim 40\%$ smaller. This result is further confirmed by the radial distribution of high-mass stars ($m \geq 0.56\,M_\odot$), which, being more segregated, are more affected by the presence of central BHs. Models in which the last BH was ejected recently ($\leq$ 150 Myr ago) can still reproduce the density profile. For these model, we estimate that the ejected (binary) BHs are at a typical distance of $\sim$ 60 pc from the Hyades.

In absence of primordial binaries, about 94% of the BHs in the present-day state of our $N-$body models dynamically couple with other objects and form binary and triple systems. Among them, 50% of the clusters with BHs host BH-star binary systems. Their period distribution peaks at $\sim 10^3$ yr making it unlikely to find BHs through velocity variations. We explored the possible candidate stars with a BH companion, based on their excess error in the *Gaia* singe-source catalog but otherwise high membership probability.

[2]ATNF Pulsar Catalog by R.N. Manchester et al., at http://www.atnf.csiro.au/research/pulsar/psrcat

We found 56 possible binaries candidates, but none which show strong evidence of sufficient companion mass to be a likely BH. Also, we explored the possibility to detect binary BHs through gravitational waves with Pulsar Timing Array. We found that (continuous) gravitational waves from a BBH in or near the Hyades is unlikely to be found. Finally, we estimated that detecting dormant BHs with gravitational microlensing is unlikely too.

Our study suggests that, at the present day, the radial mass distribution of stars provides the most promising discriminator to find signatures of BHs in open clusters. In particular, the most massive stars within the cluster, and their degree of mass segregation, represent the best tracers for the presence of central BHs. For the case of the Hyades, its present-day structure requires a significant fraction of BHs to form with kicks that are low enough to be retained by the host cluster.

Our approach of detailed modelling of individual OCs can be applied to other OCs to see whether Hyades is an unique cluster, or that BHs in OCs are common. Charting the demographics in OCs in future studies will be a powerful way to put stringent constraints on BH kicks and the contribution of OCs to gravitational wave detections.

Acknowledgements

ST acknowledges financial support from the European Research Council for the ERC Consolidator grant DEMOBLACK, under contract no. 770017. MG acknowledges support from the Ministry of Science and Innovation (EUR2020-112157, PID2021-125485NB-C22) and from Grant CEX2019-000918-M funded by MCIN/AEI/10.13039/501100011033 and from AGAUR (SGR-2021-01069). ZP acknowledges that this project has received funding from the European Research Council (ERC) under the European Union's Horizon 2020 research and innovation programme (Grant agreement No. 101002511 - VEGA P). LW thanks the support from the one-hundred-talent project of Sun Yat-sen University, the Fundamental Research Funds for the Central Universities, Sun Yat-sen University (22hytd09) and the National Natural Science Foundation of China through grant 12073090 and 12233013. FA acknowledges financial support from MCIN/AEI/10.13039/501100011033 through grants IJC2019-04862-I and RYC2021-031638-I (the latter co-funded by European Union NextGenerationEU/PRTR). ST thanks Michela Mapelli for useful comments and suggestions.

sourceid	RA	Dec	parallax	pmra	pmdec	mg	bprp	RUWEast	sigmabast	RUWEspec	sigmabspec	Pinf	qinf	Mcinf
3313842529024545664	65.85493019594335	16.777147465731876	20.795046	106.97092	-26.247469	5.573977	0.40038252	1.2823561	0.41557395	27.358295	23.794285	0.025030272	0.44117424	0.6805129
3311000119668435200	65.51518023603637	14.077103275227195	22.026937	113.774475	-21.321016	5.6442456	0.42680836	1.8872856	0.7889371	19.065733	14.198232	0.075180255	0.3714967	0.5546593
3309990523179108480	69.53972879902068	16.03321720295417	17.820915	84.96662	-8.793861	5.7026787	0.4365778	5.6922646	2.4559207	2.1845562	1.2523471	3.2795131	0.09720816	0.15520167
3312637842237882880	67.96612153925633	15.851471350184573	21.005054	99.49563	-34.32999	5.928877	0.46518755	1.5450443	0.47656766	2.0089986	0.8186548	0.82594234	0.039998896	0.057937805
144130516816579200	67.57532736919829	19.84041406012967	19.89243	86.11872	-26.106121	6.9827037	0.6383934	3.7624655	1.3966898	3.2055814	0.9599861	2.179701	0.069570266	0.08619921
3312751882209460864	66.52490368958763	15.524230392191061	23.521027	124.196014	-25.313429	7.3494782	0.7129674	3.4419775	1.343747	2.0151875	0.5174881	3.2901115	0.044089917	0.04835587
3309493720019304576	69.38373895275495	15.146378860785259	25.64366	101.49229	-18.512648	7.4436464	0.7864218	13.72717	5.776902	9.669819	2.558703	2.6238859	0.2289321	0.23954499
3311151233797884416	66.05246947657736	14.758157583423541	20.856197	110.226265	-12.401878	7.4817166	0.7890749	4.709577	1.9607697	2.121658	0.4972577	5.634556	0.05053243	0.056626927
3307815006281475200	67.87268564180225	13.903399057854472	20.276747	86.607285	-6.108541	7.643193	0.69734	8.31893	3.525965	2.614277	0.7415865	6.9882374	0.083096355	0.09157219
3309170875916905856	69.73925748852255	14.105477042258816	18.390837	91.53597	-20.422842	7.8071556	0.80762196	10.741918	4.6240096	3.6913257	1.0178571	7.361735	0.118229695	0.1313378
3313743710417140864	66.60303643900508	16.853180488088583	26.757921	95.673996	-38.761845	7.8861456	0.81799173	12.058122	5.1952686	10.748748	3.0819666	1.8774892	0.25809193	0.24698886
3309006602007842048	71.62700947833584	15.471931785895292	20.5006	87.325676	-25.352728	8.138844	0.8205805	3.2997699	1.3771452	2.1922784	0.5878727	3.40549	0.052342582	0.052890003
3309540170088830464	68.49438499286096	15.16352719505778	20.641268	108.03673	-33.110138	8.2856655	1.0252385	27.214418	11.50729	5.577302	1.5087116	11.012355	0.22136614	0.2177251
48061409893621248	67.1555527872302	19.74051990049017	20.810343	102.9064	-38.101357	8.441752	0.89888763	1.6440603	0.53488284	14.239208	4.5749774	0.16743268	0.16246925	0.15522723
3312631623125272448	67.64578394363194	15.733880135447295	17.485168	100.58648	-25.256905	8.67361	1.0493889	21.024082	7.626148	18.202843	5.276344	2.4634974	0.55225676	0.54067534
48197783694869760	65.84566930782594	19.658531350570186	21.598646	97.3178	-37.780178	9.1158905	1.1155329	34.355576	10.966481	16.315971	5.2403026	2.887581	0.62754923	0.52858657
3314151251273992832	67.9051025367819	17.70963694563987	28.507998	98.723816	-22.038061	9.247976	1.1795635	43.27126	13.478946	17.999285	5.767014	2.443363	0.70073265	0.5220939
3406216383523959936	70.81584857548913	17.068982088574	22.40773	84.4349	-41.66873	9.519791	1.2086744	14.337425	4.4526625	2.7862427	0.90990114	6.508449	0.11398687	0.08856268
47319858019739264	64.59216618931373	17.421415275740294	23.752161	104.46378	-50.567753	9.66315	1.3945608	10.326841	3.221443	2.0533266	0.5846881	6.9130993	0.07403989	0.054991435
3314484094059409408	66.99617799986078	18.500100518411095	19.760468	108.59516	-40.885216	9.7873955	1.2999792	10.631993	3.3175225	4.8615503	1.7125669	2.9215875	0.1696449	0.13192531
3310876802567157248	66.85605547720428	14.260578556388577	20.42228	102.45836	-19.95602	10.026131	1.33076	12.669773	3.9585905	4.7959375	1.7974386	3.2138977	0.18906817	0.13960828
3308127405023027328	70.3740966937844	13.221124178946916	22.662909	99.23287	-18.63009	10.491406	1.8964214	1.4050351	0.29435474	5.7457695	2.2721488	0.1703603	0.08793274	0.057852447
3410898202818634624	68.70917414686971	20.394419352148518	18.76046	110.18581	-22.617853	10.571909	1.6212931	9.876004	2.8892152	8.526632	3.900182	1.1767963	0.32126498	0.2233311
3313526556869575296	66.20070596676636	15.874649203665436	20.678333	100.34452	-12.269188	11.324224	1.9229269	12.951795	4.8260064	3.9638534	2.295628	3.0298467	0.2657315	0.15727599
3314185129975960448	67.12038862642493	17.695791947186837	20.918434	109.48695	-44.22729	11.360385	2.2351828	15.092351	5.5574145	8.521062	4.8796754	1.6225665	0.52000636	0.3046414
3312751229374292864	66.45571421241527	15.521152733202104	19.244942	118.904	-10.06363	11.395764	1.9788427	13.038091	4.7377243	8.969254	5.425513	1.3522661	0.54579365	0.32762027
3309541170817293824	68.66689038204488	15.208964911975178	21.075073	103.15689	-35.85557	11.549942	2.0912971	3.344131	1.0991819	6.668379	4.2592897	0.36493292	0.2443392	0.13831078
3309336867813205760	68.52256353868661	14.21747714186208	18.199448	85.34915	-16.904617	11.629388	1.8422108	1.4415438	0.34694323	2.4431305	1.6714453	0.3399052	0.08429948	0.049661882
47917816253918720	66.31113667576857	18.973455972926324	18.569708	97.28108	-28.887608	11.957183	2.0487833	2.0377967	0.5246777	8.945428	7.500937	0.11225916	0.30151984	0.16694689
3313958046465282304	66.30695338557209	17.268076545714347	19.312836	107.2612	-27.188425	11.998245	2.6850185	9.333254	2.704557	26.169952	19.287603	0.2163822	1.5024871	0.81455195
3308152208457011072	71.33211010053422	13.574216271157622	19.19447	87.72377	-9.913272	12.024581	2.3941412	15.202123	4.3817663	9.862589	7.8390193	0.86788297	0.77107835	0.41712388
3311162843092490496	65.96041133865042	14.921402707495972	25.659887	113.94731	-28.725637	12.134732	2.6072578	11.986289	3.3206553	5.654087	4.5110784	0.85494554	0.39180115	0.18730214
3307489031146701696	68.36303444839065	13.045385968619557	23.333511	110.45561	-21.440964	12.256755	2.342475	1.363789	0.2545818	2.3844779	2.0315888	0.16005203	0.08510464	0.041261565
3308428877366857728	70.36635522147463	14.076016738839469	26.182947	99.25034	-33.95699	12.363147	2.4602451	25.720503	7.026489	10.856859	10.731864	0.745237	1.2423422	0.56752026
3410409886514680064	69.01782417867581	18.888423253705223	20.245579	84.23755	-22.036737	12.484824	2.47365	6.511168	1.7505827	11.434649	12.022853	0.21433577	0.76413935	0.3754725
47729215646206080	64.46150286122511	18.475053544960033	21.640215	113.170876	-30.777138	12.703422	2.6998405	2.711683	0.7202027	2.0415013	2.0097606	0.49351305	0.12772296	0.059066143
48455894049191424	63.624805023608	18.729881346946026	20.680376	110.10128	-30.568058	13.204377	2.7620544	3.769246	0.98915327	4.831599	7.9032397	0.18036395	0.43028054	0.18605632
49157794785448192	65.67911798706223	20.56998136359179	22.204473	109.14224	-37.47773	13.435896	2.8771925	10.13076	2.8767006	4.160689	7.6917205	0.50197315	0.66635245	0.2701574
3312613000147191680	67.93658293586253	15.630149907181586	21.92811	104.99937	-31.718637	13.436778	2.7022161	1.2680652	0.22256374	2.1944704	4.0981297	0.073810354	0.14576809	0.059358526
3311038666998173184	65.84974595899124	14.427849817287893	21.160046	110.94352	-21.135527	13.543492	2.9259453	12.498561	3.6824527	20.370281	41.5711	0.12476101	5.761253	2.334608
3313207698500079360	69.63189917287164	17.04055509824066	22.853317	106.24673	-31.3891	13.618415	2.808816	1.2659032	0.23495989	4.2582116	9.578849	0.031987548	0.282138	0.109801285
3314140599755959424	67.60020695729807	17.499587834144798	18.23571	78.77907	-28.804348	13.654834	2.7426186	10.872717	3.3146904	2.9538498	6.8027906	0.79631144	0.6842594	0.28725055
3313839574086963712	65.39849909000245	16.894192274532255	24.33773	125.71914	-40.65925	13.948855	3.064352	8.383781	2.817	5.9499407	14.526592	0.23746127	1.244193	0.44788775
3310478710637066752	64.53629289150157	13.331259196596612	20.93439	111.15798	-14.546099	13.949699	2.8872652	1.5854778	0.4164988	4.107172	10.453021	0.056723293	0.3978708	0.15124361
3314137846679343872	68.0336649745617	17.6643440638911	21.075275	99.88685	-30.655151	13.979582	2.8372974	1.5255272	0.3941187	2.4364855	6.2334156	0.08940822	0.25801963	0.097356565
47760521664503296	65.11560537190881	18.89705576636259	19.672964	104.719475	-32.569706	13.988257	2.7881794	1.2785263	0.27335688	2.2563696	5.902441	0.070158176	0.21893603	0.08457476
3311221258944195200	65.66660974089085	15.062399584369444	23.376665	84.40576	-23.434784	14.077939	3.0911245	1.3902847	0.34179467	3.8369422	9.311588	0.046796	0.32785812	0.11720649
4850918600340416	62.776059616737115	18.928963628615932	19.93843	109.657745	-28.472279	14.192208	2.9350224	1.7115903	0.5110402	3.5404887	11.017797	0.069329664	0.46646634	0.17331943
48048902948906368	66.90245867179468	19.445767441293732	19.231146	96.80087	-38.773808	14.238761	3.0310307	16.237202	6.0698442	3.4705567	9.437445	0.99670756	1.3147694	0.4911199
3311102820926310784	65.39669553192954	14.695153868168017	20.326693	106.496574	-19.731718	14.278773	2.862668	1.3977338	0.3713231	2.7254941	9.875319	0.05512948	0.37344685	0.1358137
3311810047420637568	63.46857579356195	15.36487063340007	22.387419	123.95292	-13.587856	14.308949	2.9282503	1.5574532	0.4591437	5.319673	20.914965	0.029223839	0.7675065	0.26816785
3311804515502788352	63.273952149488956	15.247700118856342	22.357246	122.44951	-18.603453	14.355454	2.9613495	1.3029861	0.32675368	2.5205526	10.018484	0.04347603	0.35185495	0.12204755
47322297561027712	64.65025269592638	17.51585330705525	27.013884	64.83592	-61.09387	14.369595	2.959774	1.2812126	0.31491673	2.0114625	7.8232236	0.04440918	0.27206907	0.08790898
45198178534988672	62.49039974488908	15.416883616520483	21.22679	118.5227	-21.854282	14.58098	3.1423988	1.5162789	0.48248684	4.441856	20.385468	0.03322999	0.7961063	0.27099073
3410559832411244160	69.96546164739077	19.6593898461387	23.499067	87.291985	-34.15228	14.677451	3.234291	16.270372	7.1377497	3.6114807	11.025825	0.8210118	1.6573471	0.5350476
47959705067457152	66.12800628155945	18.986786982710726	20.498665	111.01914	-43.00263	14.982163	3.2060423	10.618676	5.2158256	2.239869	10.304867	0.7358764	1.3935447	0.44927633

Table 6.5: Candidate binaries in the Hyades with significant astrometric and spectroscopic excess noise. RA and Dec are in degrees - sigmabspec is in kms^{-1} - all other quantities are expressed in the appropriate combinations of mas, yr and $M_{\odot}$.

Chapter 7

Conclusions and outlook

In this thesis, I have explored the interplay between young stellar clusters and their populations of binary stars, black holes (BHs), and binary black holes (BBHs). Specifically, I have made use of advanced numerical models to study how the host cluster shapes the properties of these populations and, in turn, how their presence affects the evolution and the present-day state of the environment where they live.

First, I introduced a new approach to generate a number of star clusters from a given set of stellar distributions (particle masses, positions and velocities) obtained from hydro-dynamical simulations of collapsing molecular clouds (Torniamenti et al. 2022a), which incorporate the observed complexity of star forming regions. My novel method relies on applying a hierarchical clustering algorithm (Pedregosa et al. 2011) to inform a tree representation of the cluster phase-space. This is then turned into new realizations by modifying the initial branches of the tree (encoding the relations between the biggest sub-clumps in the simulation). The new realizations display a different large scale structure, but share similar properties at smaller scales, preserving in particular the fractal dimension of the original simulation. I have shown that the new generations yield a comparable evolution to the original cluster at different scales. This analysis suggests that my method is a promising way to generate new mass and phase-space distributions from existing hydro-dynamical simulations. The speedup in computation time is tremendous: generating initial conditions from hydro-dynamical simulations requires about 1.5×10^5 core hours per simulation, while our procedure takes about 10 core seconds to train the initial tree distribution and generate a new realization.

Second, I focused on the description of the early phases of the star cluster life. In particular, I studied the impact of primordial binary populations on the early dynamical evolution ($t < 10\,\mathrm{Myr}$) of young stellar clusters. To do this, I generated initial conditions that reproduce the observed phase-space distributions of star forming regions from hydro-dynamical simulations. Then, I associated an observation-based primordial population of binaries to these stellar distributions. My results show that the evolution of the cluster is characterized by two distinct phases: first, the global expansion of the cluster is balanced by the approaching of its main sub-clumps, while at small scales the cluster expands instantaneously. When the cluster reaches a nearly monolithic shape, it expands as a whole (Torniamenti et al. 2021). Primordial binaries tend to speed up the expansion of the cluster in this phase, making the half-mass radius expand like in a post-core collapse expansion. Also, they trigger the formation of a hot core, which temperature contrast can grow enough to match the observed value for NGC 6530 (Wright et al. 2019).

Primordial binary populations (Sana et al. 2012; Moe & Di Stefano 2017) are generally too hard to undergo dynamical exchanges. The stellar system recovers from the lack of interacting binaries by dynamically creating additional binary systems with binding energy of the order of its kinetic energy. In the absence of primordial binaries, the dynamically-formed binaries show a binary fraction that spontaneously reproduces the trend with the primary stellar mass found in observations (Moe & Di Stefano 2017).

A second theme I largely addressed is the interplay between the host star cluster and its BH population. First, I studied the dynamical formation of BBHs in young and open star clusters via direct N-body simulations. I considered two different star cluster families: low-mass ($\sim 500 - 800\,\mathrm{M}_\odot$) and relatively high-mass star clusters ($\geq 5000\,\mathrm{M}_\odot$), characterized by different degrees of dynamical activity. I found that the properties of BBH merger populations are extremely different in the two sets. In low-mass clusters, most BBHs mergers are the result of the evolution of original binary stars, which evolve through common envelope. In contrast, in high-mass clusters dynamical exchanges are effective also at late evolutionary stages (> 1 Gyr) for coupling and hardening BBHs (Torniamenti et al. 2022b). This has an impact on the chirp mass distribution of BBH mergers, which shows two main peaks: a main peak at $\sim 30 - 40\,\mathrm{M}_\odot$, due to dynamically-formed BBH mergers, and a secondary peak at $\sim 7 - 15\,\mathrm{M}_\odot$. Finally, a non-negligible percentage (8%) of the BBH mergers in high-mass clusters have primary component's mass in the pair-instability (PI) mass gap, all of them form via stellar collisions. About 80% of these massive BBHs leave a merger remnant in the IMBH range. Overall, this study shows that the formation channels in dynamically-active star clusters are extremely different from nearly-isolated environments and lead to two completely distinct BBH populations. These differences are crucial for the interpretation of GW sources.

Also, I have studied the process of hierarchical mergers in globular clusters (Torniamenti et al., in prep.). To explore the relevant parameter space that this process requires, I have implemented an upgraded version of the semi-analytic code FASTCLUSTER (Mapelli et al. 2021a), by including all the relevant processes that drive the cluster evolution, namely stellar evolution, two-body relaxation and tidal stripping by the host galaxy. My results indicate that globular clusters can only host hierarchical BH mergers up to the third generation, i.e. at least one generation less than what previously thought.

Finally, I explored the signatures that the presence of stellar-mass BHs leave in open clusters, by considering the nearest open cluster to the Sun: the Hyades (Torniamenti et al., in prep.). To do this, I compared the mass density profiles of a suite of direct N-body models, conceived to model the present-day state of the cluster (Wang et al. 2016), to accurate radial profiles obtained from *Gaia* data (Evans & Oh 2022). In the $N-$body models, the number of BHs within the cluster ranges between $N_{\rm BH} = 0$ and $N_{\rm BH} = 5$. Star clusters with $N_{\rm BH} = 0$ result from either the ejection of all the BHs, due to supernova kicks or dynamical scattering, or the absence of stars massive enough to collapse into BHs. The number of BHs has an impact on the half-mass radius of the cluster: more BHs produce less concentrated distributions of stars. In particular, models that never possessed BHs have typically an half-mass radius that is $\sim 30\%$ smaller than the observed value. This feature is even more evident from the distribution of high-mass stars ($m > 0.56\,\mathrm{M}_\odot$), which do not segregate completely at the cluster core because of the presence of BHs.

The observed profiles of the Hyades are best reproduced by N-body models with ~ 3 BHs at present, corresponding to a total mass fraction $f_{\rm BH} \sim 0.1$. Also, models in which

the last BHs were ejected recently ($\lesssim 150$ Myr ago) can reproduce the density profile. In these models, the ejected (B)BHs are at a typical distance of ~ 60 pc from the Hyades. Our results suggest that the present-day structure of the Hyades requires a significant fraction of BHs to form with low-enough natal kicks to be retained within the cluster.

In summary, this thesis added several pieces of information to the dynamical modelling of young and open clusters and their binary stars, BHs, and BBHs. This provided a clue on both our comprehension of the early evolution of young star clusters, and of the formation channels gravitational wave sources. Also, I performed a first attempt to find signatures of the presence of BHs in open clusters, from the impact that these objects have on the distribution of visible stars. My work strongly supports the idea that the interaction between dense stellar environments and their binary and BH populations plays a fundamental role in shaping their mutual evolution. In turn, this leaves imprints that we can now test with gravitational wave detections as well as observations of visible distributions of stars in stellar clusters.

In perspective, the growing number of detected gravitational waves (Abbott et al. 2021d) - and the count is expected to increase at even faster rates thanks to the improved sensitivity of the current ground-based detectors and to the advent of the next generation ground-based interferometers (Punturo et al. 2010; Reitze et al. 2019) - will provide new test-beds for our models on the formation channels of BBHs. As suggested by many authors, about few hundreds of detections may be sufficient to say something on the formation channels of BBHs, thanks to the distinctive imprints the produce (e.g. Fishbach et al. 2017; Gerosa & Berti 2017; Stevenson et al. 2017; Bouffanais et al. 2019, 2021a,b.

At the same time, we have now the opportunity to combine this information with the exquisite astrometric and photometric measurements offered by *Gaia* (Gaia Collaboration et al. 2022) and ground-based spectroscopic surveys, like *Gaia*-ESO and the upcoming WEAVE, 4MOST, MOONS (Gilmore et al. 2022; Dalton et al. 2012; de Jong et al. 2019; Cirasuolo et al. 2014). This synergy will contribute to overcome the degeneracies that still affect our models for BH formation. In particular, signatures of BHs in open clusters, given their low escape velocities ($\lesssim 1\,\mathrm{km\,s^{-1}}$), would provide important information about low SN kicks for BHs. My study on the Hyades suggests that, at the present day, the radial mass distribution of stars provides the most promising discriminator to find signatures of BHs in open clusters. In particular, the most massive stars within the cluster, and their degree of mass segregation, represent the best tracers for the presence of central BHs. This approach can be applied to other open clusters to see whether Hyades is an unique cluster, or that BHs in open clusters are common. Charting the BH demographics in open clusters in future studies will be a powerful way to put stringent constraints on BH kicks and the contribution of open clusters to gravitational wave detections.

List of Figures

List of Tables

Bibliography

Aarseth, S. J. 2003a, Gravitational N-Body Simulations (Cambridge University Press), 430

Aarseth, S. J. 2003b, Gravitational N-Body Simulations (Cambridge University Press, November 2003.)

Aasi, J., Abadie, J., Abbott, B. P., et al. 2015, Classical and Quantum Gravity, 32, 115012

Aasi, J., Abbott, B. P., Abbott, R., et al. 2015, Classical and Quantum Gravity, 32, 074001

Abbott, B. P., Abbott, R., Abbott, T. D., et al. 2016, Phys. Rev. Lett., 116, 061102

Abbott, B. P., Abbott, R., Abbott, T. D., et al. 2016a, ApJ, 818, L22

Abbott, B. P., Abbott, R., Abbott, T. D., et al. 2016b, Physical Review X, 6, 041015

Abbott, B. P., Abbott, R., Abbott, T. D., et al. 2020a, Phys. Rev. D, 102, 043015

Abbott, B. P., Abbott, R., Abbott, T. D., et al. 2020b, ApJ, 892, L3

Abbott, B. P., Abbott, R., Abbott, T. D., et al. 2019, Physical Review X, 9, 031040

Abbott, B. P., Abbott, R., Abbott, T. D., et al. 2017a, ApJ, 848, L13

Abbott, B. P., Abbott, R., Abbott, T. D., et al. 2017b, ApJ, 848, L12

Abbott, B. P., Abbott, R., Abbott, T. D., et al. 2017c, Physical Review Letters, 119, 161101

Abbott, B. P., Abbott, R., Abbott, T. D., et al. 2017d, ApJ, 848, L12

Abbott, R., Abbott, T. D., Abraham, S., et al. 2021a, ApJ, 915, L5

Abbott, R., Abbott, T. D., Abraham, S., et al. 2021b, Physical Review X, 11, 021053

Abbott, R., Abbott, T. D., Abraham, S., et al. 2021c, ApJ, 913, L7

Abbott, R., Abbott, T. D., Abraham, S., et al. 2020c, ApJ, 896, L44

Abbott, R., Abbott, T. D., Abraham, S., et al. 2020d, ApJ, 900, L13

Abbott, R., Abbott, T. D., Abraham, S., et al. 2020, Phys. Rev. Lett., 125, 101102

Abbott, R., Abbott, T. D., Acernese, F., et al. 2021d, arXiv e-prints, arXiv:2111.03606

Abbott, R., Abbott, T. D., Acernese, F., et al. 2021e, arXiv e-prints, arXiv:2111.03634

Abbott, R., Abbott, T. D., Acernese, F., et al. 2021f, arXiv e-prints, arXiv:2108.01045

Acernese, F., Agathos, M., Agatsuma, K., et al. 2015a, Classical and Quantum Gravity, 32, 024001

Acernese, F., Agathos, M., Agatsuma, K., et al. 2015b, Classical and Quantum Gravity, 32, 024001

Ade, P. A. R., Aghanim, N., & Zonca, A. e. a. 2016, A&A, 594, A13

Alessandrini, E., Lanzoni, B., Ferraro, F. R., Miocchi, P., & Vesperini, E. 2016, ApJ, 833, 252

Allison, R. J., Goodwin, S. P., Parker, R. J., Portegies Zwart, S. F., & de Grijs, R. 2010, MNRAS, 407, 1098

Almeida, A., Anderson, S. F., Argudo-Fernández, M., et al. 2023, arXiv e-prints, arXiv:2301.07688

An, J. H. & Evans, N. W. 2006, AJ, 131, 782

Anders, E. & Grevesse, N. 1989, GCA, 53, 197

Andrew, S., Penoyre, Z., Belokurov, V., Evans, N. W., & Oh, S. 2022, MNRAS, 516, 3661

Antonini, F. & Gieles, M. 2020a, Phys. Rev. D, 102, 123016

Antonini, F. & Gieles, M. 2020b, MNRAS, 492, 2936

Antonini, F. & Gieles, M. 2020c, MNRAS, 492, 2936

Antonini, F., Gieles, M., Dosopoulou, F., & Chattopadhyay, D. 2022, arXiv e-prints, arXiv:2208.01081

Antonini, F., Gieles, M., & Gualandris, A. 2019, MNRAS, 486, 5008

Antonini, F. & Rasio, F. A. 2016a, ApJ, 831, 187

Antonini, F. & Rasio, F. A. 2016b, ApJ, 831, 187

Arca Sedda, M. & Benacquista, M. 2019, MNRAS, 482, 2991

Arca-Sedda, M. & Capuzzo-Dolcetta, R. 2018, Monthly Notices of the Royal Astronomical Society, 483, 152

Arca-Sedda, M. & Gualandris, A. 2018, MNRAS, 477, 4423

Arca Sedda, M., Mapelli, M., Benacquista, M., & Spera, M. 2021, arXiv e-prints, arXiv:2109.12119

Arca Sedda, M., Mapelli, M., Spera, M., Benacquista, M., & Giacobbo, N. 2020, ApJ, 894, 133

Askar, A., Arca Sedda, M., & Giersz, M. 2018, MNRAS, 478, 1844

Askar, A., Szkudlarek, M., Gondek-Rosińska, D., Giersz, M., & Bulik, T. 2017, MNRAS, 464, L36

Atri, P., Miller-Jones, J. C. A., Bahramian, A., et al. 2019, MNRAS, 489, 3116

Bahcall, J. N. & Wolf, R. A. 1976, ApJ, 209, 214

Baibhav, V., Gerosa, D., Berti, E., et al. 2020, Phys. Rev. D, 102, 043002

Ballone, A., Costa, G., Mapelli, M., & MacLeod, M. 2022, arXiv e-prints, arXiv:2204.03493

Ballone, A., Mapelli, M., Di Carlo, U. N., et al. 2020, MNRAS, 496, 49

Ballone, A., Torniamenti, S., Mapelli, M., et al. 2021, MNRAS, 501, 2920

Banerjee, S. 2017, MNRAS, 467, 524

Banerjee, S. 2018, MNRAS, 473, 909

Banerjee, S. 2021a, arXiv e-prints, arXiv:2109.14612

Banerjee, S. 2021b, MNRAS, 500, 3002

Banerjee, S., Baumgardt, H., & Kroupa, P. 2010, MNRAS, 402, 371

Banerjee, S. & Kroupa, P. 2011, ApJ, 741, L12

Banerjee, S. & Kroupa, P. 2013, ApJ, 764, 29

Banerjee, S. & Kroupa, P. 2015, MNRAS, 447, 728

Bastian, N., Gieles, M., Ercolano, B., & Gutermuth, R. 2009, MNRAS, 392, 868

Bate, M. R. 2009a, MNRAS, 397, 232

Bate, M. R. 2009b, MNRAS, 392, 1363

Bate, M. R., Bonnell, I. A., & Price, N. M. 1995, MNRAS, 277, 362

Baumgardt, H., He, C., Sweet, S. M., et al. 2019, MNRAS, 488, 5340

Baumgardt, H. & Kroupa, P. 2007, MNRAS, 380, 1589

Baumgardt, H. & Makino, J. 2003, MNRAS, 340, 227

Bavera, S. S., Fragos, T., Zevin, M., et al. 2021, A&A, 647, A153

Beaumont, D. & Stepney, S. 2009, in 2009 IEEE Congress on Evolutionary Computation, IEEE, 2446–2453

Belczynski, K., Bulik, T., Fryer, C. L., et al. 2010, ApJ, 714, 1217

Belczynski, K., Holz, D. E., Bulik, T., & O'Shaughnessy, R. 2016a, Nature, 534, 512

Belczynski, K., Kalogera, V., & Bulik, T. 2002, ApJ, 572, 407

Belczynski, K., Kalogera, V., Rasio, F. A., et al. 2008, ApJS, 174, 223

Belczynski, K., Klencki, J., Fields, C. E., et al. 2020, A&A, 636, A104

Belczynski, K., Ryu, T., Perna, R., et al. 2016b, ArXiv e-prints [arXiv:1612.01524]

Belokurov, V., Penoyre, Z., Oh, S., et al. 2020, MNRAS, 496, 1922

Benacquista, M. J. & Downing, J. M. B. 2013, Living Reviews in Relativity, 16, 4

Bertin, G. 2014, Dynamics of Galaxies

Bertin, G. & Stiavelli, M. 1984, A&A, 137, 26

Bethe, H. A. & Brown, G. E. 1998, ApJ, 506, 780

Bianchini, P., Sills, A., van de Ven, G., & Sippel, A. C. 2017, MNRAS, 469, 4359

Bianchini, P., van de Ven, G., Norris, M. A., Schinnerer, E., & Varri, A. L. 2016, MNRAS, 458, 3644

Bianchini, P., van der Marel, R. P., del Pino, A., et al. 2018, MNRAS, 481, 2125

Bianchini, P., Varri, A. L., Bertin, G., & Zocchi, A. 2013, ApJ, 772, 67

Binney, J. & Tremaine, S. 2008, Galactic Dynamics: Second Edition

Blaauw, A. 1952, Bulletin of the Astronomical Institutes of the Netherlands, 11, 405

Blaauw, A. 1964, ARA&A, 2, 213

Boekholt, T. & Portegies Zwart, S. 2015, Computational Astrophysics and Cosmology, 2, 2

Boffin, H. M. J., Jerabkova, T., Beccari, G., & Wang, L. 2022, MNRAS, 514, 3579

Boley, A. C. 2009, ApJ, 695, L53

Boley, A. C., Hayfield, T., Mayer, L., & Durisen, R. H. 2010, Icarus, 207, 509

Bonnell, I. A., Bate, M. R., & Vine, S. G. 2003, MNRAS, 343, 413

Bouffanais, Y., Mapelli, M., Gerosa, D., et al. 2019, ApJ, 886, 25

Bouffanais, Y., Mapelli, M., Santoliquido, F., et al. 2021a, MNRAS, 507, 5224

Bouffanais, Y., Mapelli, M., Santoliquido, F., et al. 2021b, MNRAS, 505, 3873

Bovy, J. 2015, ApJS, 216, 29

Breen, P. G. & Heggie, D. C. 2013, MNRAS, 432, 2779

Burgers, J. M. 1948, Advances in Applied Mechanics, 1, 171

Campanelli, M., Lousto, C. O., Zlochower, Y., & Merritt, D. 2007, Phys. Rev. Lett., 98, 231102

Cantat-Gaudin, T. 2022, Universe, 8, 111

Cantat-Gaudin, T. & Anders, F. 2020, A&A, 633, A99

Cantat-Gaudin, T., Donati, P., Vallenari, A., et al. 2016, A&A, 588, A120

Cantat-Gaudin, T., Jordi, C., Vallenari, A., et al. 2018a, A&A, 618, A93

Cantat-Gaudin, T., Jordi, C., Wright, N. J., et al. 2019, A&A, 626, A17

Cantat-Gaudin, T., Vallenari, A., Sordo, R., et al. 2018b, A&A, 615, A49

Carr, B., Kühnel, F., & Sandstad, M. 2016, Phys. Rev. D, 94, 083504

Cartwright, A. 2009, MNRAS, 400, 1427

Cartwright, A. & Whitworth, A. P. 2004, MNRAS, 348, 589

Casamiquela, L., Olivares, J., Tarricq, Y., et al. 2022, A&A, 664, A31

Casertano, S. & Hut, P. 1985, ApJ, 298, 80

Castro-Ginard, A., Jordi, C., Luri, X., et al. 2020, A&A, 635, A45

Castro-Ginard, A., Jordi, C., Luri, X., et al. 2022, A&A, 661, A118

Castro-Ginard, A., Jordi, C., Luri, X., et al. 2018, A&A, 618, A59

Chandrasekhar, S. 1943, ApJ, 97, 255

Chatterjee, S., Umbreit, S., Fregeau, J. M., & Rasio, F. A. 2013, MNRAS, 429, 2881

Chattopadhyay, D., Hurley, J., Stevenson, S., & Raidani, A. 2022, MNRAS, 513, 4527

Chen, X. & Amaro-Seoane, P. 2017, ApJ, 842, L2

Chevance, M., Kruijssen, J. M. D., Hygate, A. P. S., et al. 2020a, MNRAS, 493, 2872

Chevance, M., Kruijssen, J. M. D., Krumholz, M. R., et al. 2020b, arXiv e-prints, arXiv:2010.13788

Chomiuk, L., Strader, J., Maccarone, T. J., et al. 2013, ApJ, 777, 69

Chomsky, N. 1959, Information and Control, 2, 137

Cirasuolo, M., Afonso, J., Carollo, M., et al. 2014, in Society of Photo-Optical Instrumentation Engineers (SPIE) Conference Series, Vol. 9147, Ground-based and Airborne Instrumentation for Astronomy V, ed. S. K. Ramsay, I. S. McLean, & H. Takami, 91470N

Claeys, J. S. W., Pols, O. R., Izzard, R. G., Vink, J., & Verbunt, F. W. M. 2014, A&A, 563, A83

Clarke, C. J., Bonnell, I. A., & Hillenbrand, L. A. 2000, in Protostars and Planets IV, ed. V. Mannings, A. P. Boss, & S. S. Russell, 151

Claydon, I., Gieles, M., Varri, A. L., Heggie, D. C., & Zocchi, A. 2019, MNRAS, 487, 147

Claydon, I., Gieles, M., & Zocchi, A. 2017, MNRAS, 466, 3937

Corsaro, E., Lee, Y.-N., García, R. A., et al. 2017, Nature Astronomy, 1, 0064

Costa, G., Ballone, A., Mapelli, M., & Bressan, A. 2022, MNRAS, 516, 1072

Costa, G., Bressan, A., Mapelli, M., et al. 2021, MNRAS, 501, 4514

Cournoyer-Cloutier, C., Tran, A., Lewis, S., et al. 2021, MNRAS, 501, 4464

Cropper, M., Katz, D., Sartoretti, P., et al. 2018, A&A, 616, A5

Crowther, P. A., Schnurr, O., Hirschi, R., et al. 2010, MNRAS, 408, 731

Daffern-Powell, E. C. & Parker, R. J. 2020, MNRAS, 493, 4925

Dale, J. E., Ercolano, B., & Bonnell, I. A. 2015, MNRAS, 451, 987

Dale, J. E., Ngoumou, J., Ercolano, B., & Bonnell, I. A. 2014, MNRAS, 442, 694

Dalessandro, E., Raso, S., Kamann, S., et al. 2021, MNRAS, 506, 813

D'Alessio, P., Calvet, N., & Hartmann, L. 2001, ApJ, 553, 321

Dall'Amico, M., Mapelli, M., Di Carlo, U. N., et al. 2021, MNRAS, 508, 3045

Dalton, G., Trager, S. C., Abrams, D. C., et al. 2012, in Society of Photo-Optical Instrumentation Engineers (SPIE) Conference Series, Vol. 8446, Ground-based and Airborne Instrumentation for Astronomy IV, ed. I. S. McLean, S. K. Ramsay, & H. Takami, 84460P

Daniel, K. J., Heggie, D. C., & Varri, A. L. 2017, MNRAS, 468, 1453

Davis, M., Efstathiou, G., Frenk, C. S., & White, S. D. M. 1985, ApJ, 292, 371

de Jong, R. S., Agertz, O., Berbel, A. A., et al. 2019, The Messenger, 175, 3

de Mink, S. E. & Belczynski, K. 2015, ApJ, 814, 58

de Mink, S. E. & Mandel, I. 2016, MNRAS, 460, 3545

de Vita, R., Bertin, G., & Zocchi, A. 2016, A&A, 590, A16

Dehnen, W. 1993, MNRAS, 265, 250

Di Carlo, U. N., Giacobbo, N., Mapelli, M., et al. 2019, MNRAS, 487, 2947

Di Carlo, U. N., Mapelli, M., Bouffanais, Y., et al. 2020a, MNRAS, 497, 1043

Di Carlo, U. N., Mapelli, M., Giacobbo, N., et al. 2020b, MNRAS, 498, 495

Di Carlo, U. N., Mapelli, M., Pasquato, M., et al. 2021, MNRAS, 507, 5132

Di Cintio, P. & Casetti, L. 2019, MNRAS, 489, 5876

Di Cintio, P. & Casetti, L. 2020, in Star Clusters: From the Milky Way to the Early Universe, ed. A. Bragaglia, M. Davies, A. Sills, & E. Vesperini, Vol. 351, 426–429

Dib, S. & Henning, T. 2019, A&A, 629, A135

Diemand, J., Kuhlen, M., & Madau, P. 2006, ApJ, 649, 1

Doctor, Z., Wysocki, D., O'Shaughnessy, R., Holz, D. E., & Farr, B. 2020, ApJ, 893, 35

Dominik, M., Belczynski, K., Fryer, C., et al. 2012, ApJ, 759, 52

Dominik, M., Belczynski, K., Fryer, C., et al. 2013, ApJ, 779, 72

Downing, J. M. B., Benacquista, M. J., Giersz, M., & Spurzem, R. 2010, MNRAS, 407, 1946

du Buisson, L., Marchant, P., Podsiadlowski, P., et al. 2020, MNRAS, 499, 5941

Ebisuzaki, T., Makino, J., Tsuru, T. G., et al. 2001, ApJ, 562, L19

Eddy, S. R. 2004, Nature biotechnology, 22, 1315

Eggleton, P. 2006, Evolutionary Processes in Binary and Multiple Stars

El-Badry, K. & Burdge, K. B. 2022, MNRAS, 511, 24

El-Badry, K., Quataert, E., Weisz, D. R., Choksi, N., & Boylan-Kolchin, M. 2019, MNRAS, 482, 4528

Elmegreen, B. G. 2004, MNRAS, 354, 367

Elmegreen, B. G. 2008, ApJ, 672, 1006

Elmegreen, B. G., Elmegreen, D. M., Chandar, R., Whitmore, B., & Regan, M. 2006, ApJ, 644, 879

Ester, M., Kriegel, H.-P., Sander, J., & Xu, X. 1996, in (AAAI Press), 226–231

Evans, N. W. & Oh, S. 2022, MNRAS, 512, 3846

Fabricius, M. H., Noyola, E., Rukdee, S., et al. 2014, ApJ, 787, L26

Farmer, R., Renzo, M., de Mink, S. E., Fishbach, M., & Justham, S. 2020, ApJ, 902, L36

Farr, W. M., Sravan, N., Cantrell, A., et al. 2011, ApJ, 741, 103

Farr, W. M., Stevenson, S., Miller, M. C., et al. 2017, Nature, 548, 426

Farrell, E., Groh, J. H., Hirschi, R., et al. 2021, MNRAS, 502, L40

Favata, M., Hughes, S. A., & Holz, D. E. 2004, ApJ, 607, L5

Federrath, C. 2013, MNRAS, 436, 1245

Feng, Y. & Modi, C. 2017, Astronomy and Computing, 20, 44

Ferraro, F. R., Mucciarelli, A., Lanzoni, B., et al. 2018, ApJ, 860, 50

Fishbach, M., Holz, D. E., & Farr, B. 2017, ApJ, 840, L24

Fitchett, M. J. 1983, MNRAS, 203, 1049

Fleck, J. J., Boily, C. M., Lançon, A., & Deiters, S. 2006, MNRAS, 369, 1392

Fragione, G. & Kocsis, B. 2018, Phys. Rev. Lett., 121, 161103

Fragione, G., Loeb, A., & Rasio, F. A. 2020, ApJ, 902, L26

Fraley, G. S. 1968, Astrophysics and Space Science, 2, 96

Fryer, C. L., Belczynski, K., Wiktorowicz, G., et al. 2012, ApJ, 749, 91

Fryer, C. L., Woosley, S. E., & Heger, A. 2001, ApJ, 550, 372

Fujii, M. S. 2015, PASJ, 67, 59

Fujii, M. S. & Portegies Zwart, S. 2011, Science, 334, 1380

Fujii, M. S. & Portegies Zwart, S. 2014, MNRAS, 439, 1003

Fujii, M. S. & Portegies Zwart, S. 2015, MNRAS, 449, 726

Fujii, M. S. & Portegies Zwart, S. 2016, ApJ, 817, 4

Fujii, M. S., Saitoh, T. R., Hirai, Y., & Wang, L. 2021, PASJ [arXiv:2103.02829]

Fujii, M. S., Saitoh, T. R., & Portegies Zwart, S. F. 2012, ApJ, 753, 85

Fujii, M. S., Tanikawa, A., & Makino, J. 2017, PASJ, 69, 94

Fukushige, T. & Heggie, D. C. 2000, MNRAS, 318, 753

Gaia Collaboration, Babusiaux, C., van Leeuwen, F., et al. 2018a, A&A, 616, A10

Gaia Collaboration, Brown, A. G. A., Vallenari, A., et al. 2018b, A&A, 616, A1

Gaia Collaboration, Prusti, T., de Bruijne, J. H. J., et al. 2016, A&A, 595, A1

Gaia Collaboration, Vallenari, A., Brown, A. G. A., et al. 2022, arXiv e-prints, arXiv:2208.00211

García, F., Simaz Bunzel, A., Chaty, S., Porter, E., & Chassande-Mottin, E. 2021, A&A, 649, A114

Gavagnin, E., Bleuler, A., Rosdahl, J., & Teyssier, R. 2017, MNRAS, 472, 4155

Geen, S., Hennebelle, P., Tremblin, P., & Rosdahl, J. 2016, MNRAS, 463, 3129

Geller, A. M., Latham, D. W., & Mathieu, R. D. 2015, AJ, 150, 97

Georgiev, I. Y., Böker, T., Leigh, N., Lützgendorf, N., & Neumayer, N. 2016, MNRAS, 457, 2122

Georgiev, I. Y., Hilker, M., Puzia, T. H., Goudfrooij, P., & Baumgardt, H. 2009a, MNRAS, 396, 1075

Georgiev, I. Y., Puzia, T. H., Hilker, M., & Goudfrooij, P. 2009b, MNRAS, 392, 879

Gerosa, D. & Berti, E. 2017, Phys. Rev. D, 95, 124046

Gerosa, D. & Berti, E. 2019, Phys. Rev. D, 100, 041301

Gerosa, D., Berti, E., O'Shaughnessy, R., et al. 2018, Phys. Rev. D, 98, 084036

Gerosa, D. & Fishbach, M. 2021, Nature Astronomy, 5, 749

Giacobbo, N. & Mapelli, M. 2018, MNRAS, 480, 2011

Giacobbo, N. & Mapelli, M. 2019, MNRAS, 482, 2234

Giacobbo, N. & Mapelli, M. 2020, ApJ, 891, 141

Giacobbo, N., Mapelli, M., & Spera, M. 2018, MNRAS, 474, 2959

Gieles, M. & Baumgardt, H. 2008, MNRAS, 389, L28

Gieles, M., Baumgardt, H., Heggie, D. C., & Lamers, H. J. G. L. M. 2010, MNRAS, 408, L16

Gieles, M., Erkal, D., Antonini, F., Balbinot, E., & Peñarrubia, J. 2021, Nature Astronomy, 5, 957

Gieles, M., Heggie, D. C., & Zhao, H. 2011, MNRAS, 413, 2509

Gieles, M., Portegies Zwart, S. F., Baumgardt, H., et al. 2006, MNRAS, 371, 793

Gieles, M. & Zocchi, A. 2015, MNRAS, 454, 576

Giersz, M., Askar, A., Wang, L., et al. 2019, MNRAS, 487, 2412

Giersz, M., Heggie, D. C., & Hurley, J. R. 2008, MNRAS, 388, 429

Giersz, M., Leigh, N., Hypki, A., Lützgendorf, N., & Askar, A. 2015, MNRAS, 454, 3150

Gies, D. R. 1987, ApJS, 64, 545

Giesers, B., Dreizler, S., Husser, T.-O., et al. 2018, MNRAS, 475, L15

Gilmore, G., Randich, S., Worley, C. C., et al. 2022, A&A, 666, A120

Ginat, Y. B. & Perets, H. B. 2023, MNRAS, 519, L15

Gondán, L., Kocsis, B., Raffai, P., & Frei, Z. 2018, ApJ, 860, 5

Goodfellow, I. J., Pouget-Abadie, J., Mirza, M., et al. 2014, arXiv e-prints, arXiv:1406.2661

Goodman, J. 1984, ApJ, 280, 298

Goodman, J., Heggie, D. C., & Hut, P. 1993, ApJ, 415, 715

Goodman, J. & Hut, P. 1989, Nature, 339, 40

Goodman, J. & Hut, P. 1993, ApJ, 403, 271

Goodwin, S. P. & Bastian, N. 2006, MNRAS, 373, 752

Goodwin, S. P. & Whitworth, A. P. 2004, A&A, 413, 929

Goswami, S., Kiel, P., & Rasio, F. A. 2014, ApJ, 781, 81

Gratton, R. G., Bragaglia, A., Carretta, E., et al. 2003, A&A, 408, 529

Gratton, R. G., Fusi Pecci, F., Carretta, E., et al. 1997, ApJ, 491, 749

Gunn, J. E. & Ostriker, J. P. 1970, ApJ, 160, 979

Harris, W. E. 1996, AJ, 112, 1487

Harris, W. E. 2010, arXiv e-prints, arXiv:1012.3224

Heger, A., Fryer, C. L., Woosley, S. E., Langer, N., & Hartmann, D. H. 2003, ApJ, 591, 288

Heggie, D. & Hut, P. 2003, The Gravitational Million-Body Problem: A Multidisciplinary Approach to Star Cluster Dynamics

Heggie, D. C. 1975, MNRAS, 173, 729

Hemsendorf, M. & Merritt, D. 2002, ApJ, 580, 606

Hénault-Brunet, V., Gieles, M., Evans, C. J., et al. 2012, A&A, 545, L1

Hénault-Brunet, V., Gieles, M., Sollima, A., et al. 2019, MNRAS, 483, 1400

Hénon, M. 1961, Annales d'Astrophysique, 24, 369

Hills, J. G. 1980, ApJ, 235, 986

Hills, J. G. 1983, AJ, 88, 1269

Hills, J. G. & Fullerton, L. W. 1980, AJ, 85, 1281

Hoang, B.-M., Naoz, S., Kocsis, B., Rasio, F. A., & Dosopoulou, F. 2018, ApJ, 856, 140

Hobbs, G., Lorimer, D. R., Lyne, A. G., & Kramer, M. 2005, MNRAS, 360, 974

Holley-Bockelmann, K., Gültekin, K., Shoemaker, D., & Yunes, N. 2008, ApJ, 686, 829

Hunt, E. L. & Reffert, S. 2021, A&A, 646, A104

Hurley, J. R. 2007, MNRAS, 379, 93

Hurley, J. R., Pols, O. R., & Tout, C. A. 2000, MNRAS, 315, 543

Hurley, J. R., Tout, C. A., & Pols, O. R. 2002, MNRAS, 329, 897

Hut, P. 1981, A&A, 99, 126

Hut, P. 1983, ApJ, 272, L29

Jelinek, F., Lafferty, J. D., & Mercer, R. L. 1992, in Speech Recognition and Understanding, ed. P. Laface & R. De Mori (Berlin, Heidelberg: Springer Berlin Heidelberg), 345–360

Jenet, F. A., Creighton, T., & Lommen, A. 2005, ApJ, 627, L125

Jerabkova, T., Boffin, H. M. J., Beccari, G., et al. 2021, A&A, 647, A137

Jiménez-Forteza, X., Keitel, D., Husa, S., et al. 2017, Phys. Rev. D, 95, 064024

Kamann, S., Giesers, B., Bastian, N., et al. 2020, A&A, 635, A65

Kamann, S., Husser, T. O., Dreizler, S., et al. 2018, MNRAS, 473, 5591

Kandrup, H. E. & Sideris, I. V. 2003, ApJ, 585, 244

Kaufman, L. & Rousseeuw, P. J. 1990, Finding groups in data. an introduction to cluster analysis (Wiley Series in Probability and Statistics)

Kharchenko, N. V., Berczik, P., Petrov, M. I., et al. 2009, A&A, 495, 807

Kimball, C., Talbot, C., Berry, C. P. L., et al. 2020, ApJ, 900, 177

King, I. R. 1966, AJ, 71, 64

Klencki, J., Moe, M., Gladysz, W., et al. 2018, A&A, 619, A77

Klessen, R. S. & Burkert, A. 2000, ApJS, 128, 287

Knuth, K. H. 2006, arXiv e-prints, physics/0605197

Kolmogorov, A. 1941, Akademiia Nauk SSSR Doklady, 30, 301

Kounkel, M., Covey, K., Suárez, G., et al. 2018, AJ, 156, 84

Kremer, K., Ye, C. S., Rui, N. Z., et al. 2020, ApJS, 247, 48

Kritos, K., Berti, E., & Silk, J. 2022a, arXiv e-prints, arXiv:2212.06845

Kritos, K., Strokov, V., Baibhav, V., & Berti, E. 2022b, arXiv e-prints, arXiv:2210.10055

Kroupa, P. 2001, MNRAS, 322, 231

Kruckow, M. U., Tauris, T. M., Langer, N., Kramer, M., & Izzard, R. G. 2018, MNRAS, 481, 1908

Kruijssen, J. M. D. 2012, MNRAS, 426, 3008

Krumholz, M. R., Klein, R. I., & McKee, C. F. 2012, ApJ, 754, 71

Krumholz, M. R., McKee, C. F., & Bland-Hawthorn, J. 2019, ARA&A, 57, 227

Kudritzki, R. P. 2002, ApJ, 577, 389

Kuhn, M. A., Hillenbrand, L. A., Sills, A., Feigelson, E. D., & Getman, K. V. 2019, ApJ, 870, 32

Kulkarni, S. R., Hut, P., & McMillan, S. 1993, Nature, 364, 421

Kumamoto, J., Fujii, M. S., & Tanikawa, A. 2019, MNRAS, 486, 3942

Kumamoto, J., Fujii, M. S., & Tanikawa, A. 2020, MNRAS, 495, 4268

Küpper, A. H. W., Kroupa, P., Baumgardt, H., & Heggie, D. C. 2010, MNRAS, 401, 105

Küpper, A. H. W., Lane, R. R., & Heggie, D. C. 2012, MNRAS, 420, 2700

Küpper, A. H. W., Macleod, A., & Heggie, D. C. 2008, Astronomische Nachrichten, 329, 1061

Küpper, A. H. W., Maschberger, T., Kroupa, P., & Baumgardt, H. 2011, MNRAS, 417, 2300

Lada, C. J. & Lada, E. A. 2003, ARA&A, 41, 57

Larson, R. B. 1995, MNRAS, 272, 213

Lee, Y.-N. & Hennebelle, P. 2016, A&A, 591, A30

Lee, Y.-N. & Hennebelle, P. 2019, A&A, 622, A125

Leveque, A., Giersz, M., Arca-Sedda, M., & Askar, A. 2022, MNRAS, 514, 5751

Li, H., Vogelsberger, M., Marinacci, F., & Gnedin, O. Y. 2019, MNRAS, 487, 364

Lindegren, L., Klioner, S. A., Hernández, J., et al. 2021, A&A, 649, A2

Lindenmayer, A. 1968a, Journal of Theoretical Biology, 18, 280

Lindenmayer, A. 1968b, Journal of Theoretical Biology, 18, 300

Liu, L. & Pang, X. 2019, ApJS, 245, 32

Lodieu, N., Smart, R. L., Pérez-Garrido, A., & Silvotti, R. 2019, A&A, 623, A35

Loeb, A. 2016, ApJ, 819, L21

Lousto, C. O. & Zlochower, Y. 2011, Phys. Rev. Lett., 107, 231102

Lousto, C. O., Zlochower, Y., Dotti, M., & Volonteri, M. 2012, Phys. Rev. D, 85, 084015

Lupton, R. H. & Gunn, J. E. 1987, AJ, 93, 1106

Lynden-Bell, D. 1962, MNRAS, 123, 447

Maccarone, T. J., Kundu, A., Zepf, S. E., & Rhode, K. L. 2007, Nature, 445, 183

Maciejewski, M., Colombi, S., Springel, V., Alard, C., & Bouchet, F. R. 2009, MNRAS, 396, 1329

Mackey, A. D., Wilkinson, M. I., Davies, M. B., & Gilmore, G. F. 2007, MNRAS, 379, L40

Mackey, A. D., Wilkinson, M. I., Davies, M. B., & Gilmore, G. F. 2008, MNRAS, 386, 65

Madau, P. & Fragos, T. 2017, ApJ, 840, 39

Maggiore, M. 2018, Gravitational Waves: Volume 2: Astrophysics and Cosmology, Gravitational Waves (Oxford University Press)

Makino, J. & Aarseth, S. J. 1992, PASJ, 44, 141

Mandel, I. & de Mink, S. E. 2016, MNRAS, 458, 2634

Manwadkar, V., Trani, A. A., & Leigh, N. W. C. 2020, MNRAS, 497, 3694

Mapelli, M. 2016, MNRAS, 459, 3432

Mapelli, M. 2017, MNRAS, 467, 3255

Mapelli, M. 2021, in Handbook of Gravitational Wave Astronomy, 16

Mapelli, M., Bouffanais, Y., Santoliquido, F., Arca Sedda, M., & Artale, M. C. 2022, MNRAS, 511, 5797

Mapelli, M., Colpi, M., Possenti, A., & Sigurdsson, S. 2005, MNRAS, 364, 1315

Mapelli, M., Colpi, M., & Zampieri, L. 2009, MNRAS, 395, L71

Mapelli, M., Dall'Amico, M., Bouffanais, Y., et al. 2021a, MNRAS, 505, 339

Mapelli, M. & Giacobbo, N. 2018, MNRAS, 479, 4391

Mapelli, M., Giacobbo, N., Ripamonti, E., & Spera, M. 2017, MNRAS, 472, 2422

Mapelli, M., Giacobbo, N., Santoliquido, F., & Artale, M. C. 2019, MNRAS, 487, 2

Mapelli, M., Santoliquido, F., Bouffanais, Y., et al. 2021b, Symmetry, 13, 1678

Mapelli, M., Spera, M., Montanari, E., et al. 2020, ApJ, 888, 76

Mapelli, M., Zampieri, L., Ripamonti, E., & Bressan, A. 2013, MNRAS, 429, 2298

Marchant, P., Langer, N., Podsiadlowski, P., Tauris, T. M., & Moriya, T. J. 2016, A&A, 588, A50

Marchant, P., Renzo, M., Farmer, R., et al. 2019, ApJ, 882, 36

Marks, M. & Kroupa, P. 2011, MNRAS, 417, 1702

Marks, M. & Kroupa, P. 2012, A&A, 543, A8

McKernan, B., Ford, K. E. S., Bellovary, J., et al. 2018, ApJ, 866, 66

McKernan, B., Ford, K. E. S., Lyra, W., & Perets, H. B. 2012, MNRAS, 425, 460

Mehta, A. K., Buonanno, A., Gair, J., et al. 2022, ApJ, 924, 39

Meingast, S. & Alves, J. 2019, A&A, 621, L3

Meingast, S., Alves, J., & Rottensteiner, A. 2021, A&A, 645, A84

Mel'nik, A. M. & Dambis, A. K. 2017, MNRAS, 472, 3887

Mennekens, N. & Vanbeveren, D. 2014, A&A, 564, A134

Merritt, D. 2001, ApJ, 556, 245

Michie, R. W. & Bodenheimer, P. H. 1963, MNRAS, 126, 269

Mikkola, S. & Aarseth, S. J. 1993, Celestial Mechanics and Dynamical Astronomy, 57, 439

Miller, M. C. & Hamilton, D. P. 2002, MNRAS, 330, 232

Miller, M. C. & Lauburg, V. M. 2009, ApJ, 692, 917

Miller-Jones, J. C. A., Strader, J., Heinke, C. O., et al. 2015, MNRAS, 453, 3918

Moe, M. & Di Stefano, R. 2017, ApJS, 230, 15

Moeckel, N. & Bate, M. R. 2010, MNRAS, 404, 721

Moeckel, N., Holland, C., Clarke, C. J., & Bonnell, I. A. 2012, MNRAS, 425, 450

Moody, K. & Sigurdsson, S. 2009, ApJ, 690, 1370

Moyano Loyola, G. R. I. & Hurley, J. R. 2013, MNRAS, 434, 2509

Muratov, A. L. & Gnedin, O. Y. 2010, ApJ, 718, 1266

Murphy, D. N. A., Geach, J. E., & Bower, R. G. 2012, MNRAS, 420, 1861

Neijssel, C. J., Vigna-Gómez, A., Stevenson, S., et al. 2019, MNRAS, 490, 3740

Neumayer, N., Seth, A., & Böker, T. 2020, A&A Rev., 28, 4

Ng, K. K. Y., Vitale, S., Farr, W. M., & Rodriguez, C. L. 2021, ApJ, 913, L5

Nilakshi, Sagar, R., Pandey, A. K., & Mohan, V. 2002, A&A, 383, 153

Nitadori, K. & Aarseth, S. J. 2012, MNRAS, 424, 545

Nitz, A. H., Capano, C. D., Kumar, S., et al. 2021, ApJ, 922, 76

Nitz, A. H., Dent, T., Davies, G. S., et al. 2020, ApJ, 891, 123

Offner, S. S. R., Moe, M., Kratter, K. M., et al. 2022, arXiv e-prints, arXiv:2203.10066

Oh, S. & Evans, N. W. 2020, MNRAS, 498, 1920

Oh, S. & Kroupa, P. 2016, A&A, 590, A107

Oh, S., Kroupa, P., & Pflamm-Altenburg, J. 2015, ApJ, 805, 92

O'Leary, R. M., Kocsis, B., & Loeb, A. 2009, MNRAS, 395, 2127

O'Leary, R. M., Meiron, Y., & Kocsis, B. 2016, ApJ, 824, L12

Olsen, S., Venumadhav, T., Mushkin, J., et al. 2022, Phys. Rev. D, 106, 043009

Özel, F. & Freire, P. 2016, ARA&A, 54, 401

Özel, F., Psaltis, D., Narayan, R., & McClintock, J. E. 2010, ApJ, 725, 1918

Pancino, E., Galfo, A., Ferraro, F. R., & Bellazzini, M. 2007, ApJ, 661, L155

Pang, X., Li, Y., Tang, S.-Y., Pasquato, M., & Kouwenhoven, M. B. N. 2020, ApJ, 900, L4

Parker, R. J. & Dale, J. E. 2013, MNRAS, 432, 986

Parker, R. J. & Goodwin, S. P. 2007, MNRAS, 380, 1271

Parker, R. J. & Meyer, M. R. 2012, MNRAS, 427, 637

Parker, R. J. & Wright, N. J. 2016, MNRAS, 457, 3430

Parker, R. J., Wright, N. J., Goodwin, S. P., & Meyer, M. R. 2014, MNRAS, 438, 620

Pasquato, M. & Milone, A. 2019, arXiv e-prints, arXiv:1906.04983

Pavlík, V., Jeřábková, T., Kroupa, P., & Baumgardt, H. 2018, A&A, 617, A69

Pedregosa, F., Varoquaux, G., Gramfort, A., et al. 2011, Journal of Machine Learning Research, 12, 2825

Pelupessy, F. I., van Elteren, A., de Vries, N., et al. 2013, A&A, 557, A84

Penoyre, Z., Belokurov, V., & Evans, N. W. 2022, MNRAS, 513, 2437

Penoyre, Z., Belokurov, V., Wyn Evans, N., Everall, A., & Koposov, S. E. 2020, MNRAS, 495, 321

Perna, R., Wang, Y.-H., Farr, W. M., Leigh, N., & Cantiello, M. 2019, ApJ, 878, L1

Perryman, M. A. C., Brown, A. G. A., Lebreton, Y., et al. 1998, A&A, 331, 81

Peters, P. C. 1964, Physical Review, 136, 1224

Peuten, M., Zocchi, A., Gieles, M., Gualandris, A., & Hénault-Brunet, V. 2016, MNRAS, 462, 2333

Pfalzner, S. 2009, A&A, 498, L37

Pfalzner, S., Parmentier, G., Steinhausen, M., Vincke, K., & Menten, K. 2014, ApJ, 794, 147

Piatti, A. E. 2020, A&A, 639, A55

Pittordis, C. & Sutherland, W. 2019, MNRAS, 488, 4740

Plummer, H. C. 1911, MNRAS, 71, 460

Portegies Zwart, S. F., Baumgardt, H., Hut, P., Makino, J., & McMillan, S. L. W. 2004, Nature, 428, 724

Portegies Zwart, S. F. & McMillan, S. L. W. 2000, ApJ, 528, L17

Portegies Zwart, S. F. & McMillan, S. L. W. 2002, ApJ, 576, 899

Portegies Zwart, S. F., McMillan, S. L. W., & Gieles, M. 2010, ARA&A, 48, 431

Portegies Zwart, S. F., McMillan, S. L. W., Hut, P., & Makino, J. 2001, MNRAS, 321, 199

Portegies Zwart, S. F. & Verbunt, F. 1996, A&A, 309, 179

Portegies Zwart, S. F. & Yungelson, L. R. 1998, A&A, 332, 173

Prendergast, K. H. & Tomer, E. 1970, AJ, 75, 674

Press, W. H. & Schechter, P. 1974, ApJ, 187, 425

Prusinkiewicz, P. & Hanan, J. 2013, Lecture notes in Biomathematics, Vol. 79, Lindenmayer systems, fractals, and plants (Springer Science & Business Media)

Punturo, M., Abernathy, M., Acernese, F., et al. 2010, Classical and Quantum Gravity, 27, 194002

Quinlan, G. D. 1996, New Astron., 1, 35

Rabiner, L. & Juang, B. 1986, IEEE ASSP Magazine, 3, 4

Rakavy, G. & Shaviv, G. 1967, ApJ, 148, 803

Rastello, S., Amaro-Seoane, P., Arca-Sedda, M., et al. 2019, MNRAS, 483, 1233

Rastello, S., Mapelli, M., Di Carlo, U. N., et al. 2020, MNRAS, 497, 1563

Rastello, S., Mapelli, M., Di Carlo, U. N., et al. 2021, MNRAS, 507, 3612

Reina-Campos, M., Kruijssen, J. M. D., Pfeffer, J. L., Bastian, N., & Crain, R. A. 2019a, MNRAS, 486, 5838

Reina-Campos, M., Kruijssen, J. M. D., Pfeffer, J. L., Bastian, N., & Crain, R. A. 2019b, MNRAS, 486, 5838

Reino, S., de Bruijne, J., Zari, E., d'Antona, F., & Ventura, P. 2018, MNRAS, 477, 3197

Reitze, D., Adhikari, R. X., Ballmer, S., et al. 2019, in Bulletin of the American Astronomical Society, Vol. 51, 35

Renzo, M., Cantiello, M., Metzger, B. D., & Jiang, Y. F. 2020, ApJ, 904, L13

Repetto, S., Davies, M. B., & Sigurdsson, S. 2012, MNRAS, 425, 2799

Repetto, S. & Nelemans, G. 2015, MNRAS, 453, 3341

Rizzuto, F. P., Naab, T., Spurzem, R., et al. 2021, MNRAS, 501, 5257

Rodriguez, C. L., Amaro-Seoane, P., Chatterjee, S., et al. 2018, Phys. Rev. D, 98, 123005

Rodriguez, C. L., Chatterjee, S., & Rasio, F. A. 2016a, Phys. Rev. D, 93, 084029

Rodriguez, C. L. & Loeb, A. 2018, ApJ, 866, L5

Rodriguez, C. L., Morscher, M., Pattabiraman, B., et al. 2015, Physical Review Letters, 115, 051101

Rodriguez, C. L., Zevin, M., Amaro-Seoane, P., et al. 2019, Phys. Rev. D, 100, 043027

Rodriguez, C. L., Zevin, M., Pankow, C., Kalogera, V., & Rasio, F. A. 2016b, ApJ, 832, L2

Rodriguez-Gomez, V., Genel, S., Vogelsberger, M., et al. 2015, MNRAS, 449, 49

Röser, S. & Schilbach, E. 2019, A&A, 627, A4

Röser, S., Schilbach, E., & Goldman, B. 2019, A&A, 621, L2

Röser, S., Schilbach, E., Piskunov, A. E., Kharchenko, N. V., & Scholz, R. D. 2011, A&A, 531, A92

Roulet, J., Chia, H. S., Olsen, S., et al. 2021, Phys. Rev. D, 104, 083010

Ruthotto, L. & Haber, E. 2021, arXiv e-prints, arXiv:2103.05180

Sabbi, E., Lennon, D. J., Gieles, M., et al. 2012, ApJ, 754, L37

Salpeter, E. E. 1955, ApJ, 121, 161

Samsing, J. 2018, Phys. Rev. D, 97, 103014

Samsing, J., Askar, A., & Giersz, M. 2018, ApJ, 855, 124

Samsing, J., Bartos, I., D'Orazio, D. J., et al. 2022, Nature, 603, 237

Samsing, J. & D'Orazio, D. J. 2018, MNRAS, 481, 5445

Sana, H., de Mink, S. E., de Koter, A., et al. 2012, Science, 337, 444

Sana, H. & Evans, C. J. 2011, in IAU Symposium, Vol. 272, Active OB Stars: Structure, Evolution, Mass Loss, and Critical Limits, ed. C. Neiner, G. Wade, G. Meynet, & G. Peters, 474–485

Sánchez, N. & Alfaro, E. J. 2009, ApJ, 696, 2086

Saracino, S., Kamann, S., Guarcello, M. G., et al. 2022, MNRAS, 511, 2914

Schmeja, S. & Klessen, R. S. 2006, A&A, 449, 151

Seifried, D., Walch, S., Girichidis, P., et al. 2017, MNRAS, 472, 4797

Sesana, A., Haardt, F., & Madau, P. 2006, ApJ, 651, 392

Shapiro, S. L. & Teukolsky, S. A. 1983, Black holes, white dwarfs, and neutron stars : the physics of compact objects

Shenar, T., Sana, H., Mahy, L., et al. 2022, Nature Astronomy, 6, 1085

Sigurdsson, S. & Phinney, E. S. 1993, ApJ, 415, 631

Sim, G., Lee, S. H., Ann, H. B., & Kim, S. 2019, Journal of Korean Astronomical Society, 52, 145

Spera, M. & Mapelli, M. 2017, MNRAS, 470, 4739

Spera, M., Mapelli, M., & Bressan, A. 2015, MNRAS, 451, 4086

Spera, M., Mapelli, M., Giacobbo, N., et al. 2019, MNRAS, 485, 889

Spera, M., Mapelli, M., & Jeffries, R. D. 2016, MNRAS, 460, 317

Spera, M., Trani, A. A., & Mencagli, M. 2022, Galaxies, 10, 76

Spina, L., Ting, Y. S., De Silva, G. M., et al. 2021, MNRAS, 503, 3279

Spitzer, Lyman, J. & Hart, M. H. 1971a, ApJ, 164, 399

Spitzer, Lyman, J. & Hart, M. H. 1971b, ApJ, 164, 399

Spitzer, L. 1987, Dynamical evolution of globular clusters

Spitzer, Jr., L. 1969, ApJ, 158, L139

Steinle, N. & Kesden, M. 2021, Phys. Rev. D, 103, 063032

Stevenson, S., Berry, C. P. L., & Mandel, I. 2017, MNRAS, 471, 2801

Stevenson, S., Sampson, M., Powell, J., et al. 2019, ApJ, 882, 121

Stiefel, E. L., Rheinboldt, W. C., Rheinboldt, C. J., & Hagger, H. J. 1965, Physics Today, 18, 110

Stone, N. C., Metzger, B. D., & Haiman, Z. 2017, MNRAS, 464, 946

Strader, J., Chomiuk, L., Maccarone, T. J., Miller-Jones, J. C. A., & Seth, A. C. 2012, Nature, 490, 71

Takahashi, K. & Baumgardt, H. 2012, MNRAS, 420, 1799

Takahashi, K. & Portegies Zwart, S. F. 2000, ApJ, 535, 759

Tang, P. N., Eldridge, J. J., Stanway, E. R., & Bray, J. C. 2020, MNRAS, 493, L6

Tanikawa, A. & Fukushige, T. 2009, PASJ, 61, 721

Tarricq, Y., Soubiran, C., Casamiquela, L., et al. 2022, A&A, 659, A59

Torniamenti, S. 2022, arXiv e-prints, arXiv:2210.04848

Torniamenti, S., Ballone, A., Mapelli, M., et al. 2021, MNRAS, 507, 2253

Torniamenti, S., Bertin, G., & Bianchini, P. 2019, A&A, 632, A67

Torniamenti, S., Pasquato, M., Di Cintio, P., et al. 2022a, MNRAS, 510, 2097

Torniamenti, S., Rastello, S., Mapelli, M., et al. 2022b, MNRAS, 517, 2953

Trani, A. A., Tanikawa, A., Fujii, M. S., Leigh, N. W. C., & Kumamoto, J. 2021, MNRAS, 504, 910

Trenti, M. & Bertin, G. 2005, A&A, 429, 161

Trenti, M. & van der Marel, R. 2013, MNRAS, 435, 3272

van Leeuwen, F., Le Poole, R. S., Reijns, R. A., Freeman, K. C., & de Zeeuw, P. T. 2000, A&A, 360, 472

van Straten, W., Bailes, M., Britton, M., et al. 2001, Nature, 412, 158

VandenBerg, D. A., Brogaard, K., Leaman, R., & Casagrand e, L. 2013, ApJ, 775, 134

VanLandingham, J. H., Miller, M. C., Hamilton, D. P., & Richardson, D. C. 2016, ApJ, 828, 77

Varri, A. L. & Bertin, G. 2012, A&A, 540, A94

Vázquez-Semadeni, E., Colín, P., Gómez, G. C., Ballesteros-Paredes, J., & Watson, A. W. 2010, ApJ, 715, 1302

Venumadhav, T., Zackay, B., Roulet, J., Dai, L., & Zaldarriaga, M. 2019, Phys. Rev. D, 100, 023011

Venumadhav, T., Zackay, B., Roulet, J., Dai, L., & Zaldarriaga, M. 2020, Phys. Rev. D, 101, 083030

Vesperini, E., Hong, J., Webb, J. J., D'Antona, F., & D'Ercole, A. 2018, MNRAS, 476, 2731

Vesperini, E., McMillan, S. L. W., D'Antona, F., & D'Ercole, A. 2013, MNRAS, 429, 1913

Vesperini, E., McMillan, S. L. W., & Portegies Zwart, S. 2009, ApJ, 698, 615

Vink, J. S., de Koter, A., & Lamers, H. J. G. L. M. 2001, A&A, 369, 574

Vitale, S., Lynch, R., Raymond, V., et al. 2017, Phys. Rev. D, 95, 064053

Wadsley, J. W., Keller, B. W., & Quinn, T. R. 2017, MNRAS, 471, 2357

Wadsley, J. W., Stadel, J., & Quinn, T. 2004, New Astron., 9, 137

Wall, J. E., McMillan, S. L. W., Mac Low, M.-M., Klessen, R. S., & Portegies Zwart, S. 2019, ApJ, 887, 62

Wang, L. & Hernandez, D. M. 2021, arXiv e-prints, arXiv:2104.10843

Wang, L., Iwasawa, M., Nitadori, K., & Makino, J. 2020a, MNRAS, 497, 536

Wang, L. & Jerabkova, T. 2021, A&A, 655, A71

Wang, L., Nitadori, K., & Makino, J. 2020b, MNRAS, 493, 3398

Wang, L., Spurzem, R., Aarseth, S., et al. 2016, MNRAS, 458, 1450

Wang, L., Spurzem, R., Aarseth, S., et al. 2015, MNRAS, 450, 4070

Ward, J. L. & Kruijssen, J. M. D. 2018, MNRAS, 475, 5659

Ward, J. L., Kruijssen, J. M. D., & Rix, H.-W. 2020, MNRAS, 495, 663

Weatherford, N. C., Chatterjee, S., Kremer, K., & Rasio, F. A. 2020, ApJ, 898, 162

Webb, J. J. & Vesperini, E. 2017, MNRAS, 464, 1977

Webbink, R. F. 1984, ApJ, 277, 355

Wen, L. 2003, ApJ, 598, 419

Wilson, C. P. 1975, AJ, 80, 175

Wong, K. W. K., Breivik, K., Kremer, K., & Callister, T. 2021, Phys. Rev. D, 103, 083021

Wong, K. W. K. & Gerosa, D. 2019, Phys. Rev. D, 100, 083015

Wongwathanarat, A., Janka, H. T., & Müller, E. 2013, A&A, 552, A126

Woosley, S. E. 2017, ApJ, 836, 244

Wright, N. J. 2020, New A Rev., 90, 101549

Wright, N. J., Jeffries, R. D., Jackson, R. J., et al. 2019, VizieR Online Data Catalog, J/MNRAS/486/2477

Wright, N. J. & Parker, R. J. 2019, MNRAS, 489, 2694

Yang, Y., Bartos, I., Haiman, Z., et al. 2019, ApJ, 876, 122

Zackay, B., Venumadhav, T., Dai, L., Roulet, J., & Zaldarriaga, M. 2019, Phys. Rev. D, 100, 023007

Zamora-Avilés, M., Vázquez-Semadeni, E., González, R. F., et al. 2019, MNRAS, 487, 2200

Zevin, M., Bavera, S. S., Berry, C. P. L., et al. 2021, ApJ, 910, 152

Zevin, M., Pankow, C., Rodriguez, C. L., et al. 2017, ApJ, 846, 82

Zevin, M., Samsing, J., Rodriguez, C., Haster, C.-J., & Ramirez-Ruiz, E. 2019, ApJ, 871, 91

Zhang, Y., Tang, S.-Y., Chen, W. P., Pang, X., & Liu, J. Z. 2020, ApJ, 889, 99

Ziosi, B. M., Mapelli, M., Branchesi, M., & Tormen, G. 2014, MNRAS, 441, 3703

Zocchi, A., Gieles, M., & Hénault-Brunet, V. 2019, MNRAS, 482, 4713